Transition Metal Oxides for Sustainable Fuels Production via Solar Chemical Looping Reforming

Xiang Gao

August 2018

A THESIS SUBMITTED FOR THE DEGREE OF DOCTOR OF PHILOSOPHY OF THE AUSTRALIAN NATIONAL UNIVERSITY

Research School of Engineering

College of Engineering and Computer Science

The Australian National University

Declaration

This dissertation reports the research I conducted from February 2015 to July 2018 at the Research School of Engineering, College of Engineering and Computer Science, the Australian National University, Canberra, Australian Capital Territory, Australia.

To the best of my knowledge, the materials included in this thesis are originally my own work except where acknowledged and referenced in appropriate manner. They have not been previously published by others, or submitted in whole or in part for the purpose of obtaining a degree from any university or tertiary education institution.

Xiang Gao

August 2018

Abstract

Energy storage by chemical looping steam/dry reforming is a promising alternative for the utilization of solar energy in the industrial and transport sectors. Efficient oxygen carriers with a facile and scalable synthesis method are crucial to achieve economic competitiveness for this solar thermochemical process. In this thesis, a comprehensive overview of solar chemical looping reforming is provided and the state of the art research its associated oxygen carriers is discussed. Improvement in syngas yields and production rates in solar chemical looping reforming were then explored via morphological and structural enhancements of the oxygen carriers.

Firstly, the impact of ceria structural features on its syngas production performance during two-step isothermal redox cycles for four different nano and micro morphologies was investigated. Highly porous flame-made agglomerates composed of small crystalline particles were determined as the best performing morphology with initial production rates of H_2 and CO up to 167% higher than that of commercial sub-micro ceria. Upon 10 isothermal redox cycles at 1173 K, these flame-made structures still maintained at up to 57% faster production rates. It was shown that the high porosity of the flame-made agglomerates was important in inhibiting sintering and grain growth. Notably, higher specific surface area flower-like morphologies collapsed and densified rapidly, and exhibited the slowest kinetics. These findings provide a robust set of structural properties to engineer efficient materials for enhanced solar fuel production by high temperature thermochemical cycles.

Secondly, a first-time investigation of using an earth-abundant manganese-based oxygen carrier in solar chemical looping dry methane reforming was demonstrated and revealed a manganese carbide/oxide redox cycle that resulted in high mass-specific syngas yields and production rates when the oxygen carrier's matrix was incorporated

with fractional amount of cerium ions. In particular, 15 times higher CO_2 splitting rates than the undoped manganese oxide, and also 8 times higher CO yields than cerium oxide was achieved. The long-term performance with 100 cycles revealed that this is not a short-lived enhancement and that the synergetic contribution by cerium ions were highlighted. A thorough investigation of this manganese carbide/oxide redox mechanism was experimentally pursued further with a series of custom-synthesized Ce-Mn oxygen carriers via solar chemical looping steam methane reforming cycles. Interesting discoveries of 3% Ce showing its intense surface distribution of ceria-rich nanoparticles that efficiently dissociate the chemisorbed species into H_2 and CO during methane reforming and water splitting, and the abundance of Ce ions in the bulk lattice that effectively unlock the oxygen carrier's reversible diffusion of oxygen and carbon was revealed in this vacancy-based redox mechanism.

Acknowledgements

I would like to firstly acknowledge my primary supervisor A/Prof. Antonio Tricoli and my co-supervisor Prof. Wojciech Lipiński, who guided me to shape the scope of my field and encouraged me to explore the exhilarating unknown. The technical advice and experimental expertise provided by my advisor, Dr. Alicia Bayon, has been vital in realising project outcomes, especially in my first year of PhD candidature. The numerous discussions with them have helped me to secure the technological foundations of my research and equipped me to become an independent researcher. I am especially thankful for their practical advice in scientific writing and communication, without which my work would have only been instrumental. I would also like to acknowledge the help and support from my colleagues and advisors, in particular, Dr. Peter Kreider, Dr. Roman Bader, Dr. Jim Hinkley, Dr. Guanyu Liu, and Dr. William Wong, for their efficient and effective advice on the research issues I encountered.

My gratitude also extends to my excellent collaborators, both in Australia and around the globe, including Dr. Ye Zhu and his group from the Hong Kong Polytechnic University, Dr. Thomas Gengenbach from the Commonwealth Scientific and Industrial Research Organisation, Prof. Yun Liu and her group from the Research School of Chemistry in ANU, Ms. Iolanda Di Bernardo from Sapienza University of Rome, and the friendly staff in the Centre of Advanced Microscopy in ANU. Their assistance was indispensable for my research and it was a privilege to work with them.

I would like to acknowledge my group for their invaluable friendship and support, and for facilitating an enthusiastic and inquisitive environment. It was with their presence by my side every day that I was able to cope with the seemingly insurmountable life of research. I thank them for transferring their resilience and fortitude onto me.

The assistance provided by our technical support staff, Colin Carvolth, Neal Kaines, and Jason Chen, is also gratefully acknowledged.

I would like to thank the scholarship support from the Research Training Program of the Australian Government, without which none of my endeavours would have been possible. Additionally, I am proud to be a contributing member of the Australian Solar Thermal Research Initiative, a national project supported by the Australian Renewable Energy Agency.

Last but not least, I would like to thank my family for their enduring love and allowing me to travel to this beautiful land of Australia to pursue my dream. Equally important are the gracious friends that I have made in this country, whose support was irreplaceable during my troubled times.

List of Publications

1. **X. Gao**, A. Vidal, A. Bayon, R. Bader, J. Hinkley, W. Lipiński and A. Tricoli, (2016), *Efficient ceria nanostructures for enhanced solar fuel production via high-temperature thermochemical redox cycles*. Journal of Materials Chemistry A, 4(24), 9614-9624.

2. **X. Gao**, A. Vidal, A. Bayon, R. Bader, J. Hinkley, W. Lipiński and A. Tricoli, (2015), *Structural Performance of Micro and Nano-structured Ceria for Solar Thermochemical Fuel Production*. 2015 Asia-Pacific Solar Research Conference, ed. R. Egan, R. Passey, Australian Photovoltaic Institute, Canberra.

3. **X. Gao**, G. Liu, Y. Zhu, P. Kreider, A. Bayon, T. Gengenbach, T. Lu, Y. Liu, J. Hinkley, W. Lipiński and A. Tricoli, (2018), *Earth-Abundant Transition Metal Oxides with Extraordinary Reversible Oxygen Exchange Capacity for Efficient Thermochemical Synthesis of Solar Fuels*. Nano Energy, 50, 347-358.

4. **X. Gao**, I. di Bernardo, P. Kreider, T. Tran-Phu, W. S. Y. Wong, G. Zhao, Y. Zhu, X. Cai, N. Wang, N. Motta, A. Bayon, W. Lipiński and A. Tricoli, *Role of Cerium Ions in Activating Solar Fuels Production by Manganese-based Oxygen Carriers via Chemical Looping Steam Methane Reforming.* (internal review, submission to *Journal of Materials Chemistry A* soon).

5. W. S. Y. Wong, T. Gengenbach, H. T. Nguyen, **X. Gao**, V. S. J. Craig, A. Tricoli, (2017), *Dynamically Gas-Phase Switchable Super(de)wetting States by Reversible Amphiphilic Functionalization: A Powerful Approach for Smart Fluid Gating Membranes.* Advanced Functional Materials, 28, 1704423.

6. H. Manabu*, **X. Gao***, W. Lipiński and A. Tricoli, *Initial Sintering Behaviours of Micron-sized Ceria in Chemical Looping Dry Methane Reforming Redox Cycles.* (in preparation). *co-first authorship

Table of Contents

Chapter One

Solar Chemical Looping Reforming via Transition Metal Oxides

1.1 Introduction

Solar energy is estimated to be technically capable to deliver all of the world energy needs at the cost of utilizing only a few percent of the desert area on the earth.[1, 2] With the ever increasing global demand for energy supply today, it is imperative for modern society to develop processes that help us capitalize on the intermittent yet vast solar resource base. In this context, the storage of solar energy into dispatchable liquid fuels is an attractive alternative to offset the demands.[3, 4] Such synthesized fuels obtained via sustainable conversion processes employing solar energy as the source are termed "solar fuels".[5] The pressing global concerns of climate change have urged the world of a swift transition towards exploiting solar fuels that help us mitigate industrial pollutions and carbon emissions which are conventionally generated by direct consumption of fossil fuels. The typical high market value of liquid fuels relative to the average price of electricity also ensures a strong economic justification for mass production of solar fuels to any country that seeks long-term export revenues.[6]

So far, numerous approaches via thermochemical methods have been explored in search for efficient and scalable synthesis of solar fuels to store solar energy.[7] One approach that stands out to be environmentally and economically feasible is to use concentrated solar radiation for production of synthesis gas or syngas, a mixture of hydrogen and carbon monoxide, and subsequently convert the syngas into liquid fuels via well-established industrial processes such as Fischer-Tropsch synthesis.[8, 9] Solar chemical looping reforming,[10-12] as a process similar to two-step solar thermochemical cycles[4, 13-15] that currently attract intensive research efforts, has recently emerged as a potential candidate promised with further development of materials and reactors designs because of its high efficiency and flexibility of the products. This process, based on redox reactions of oxygen-carrying materials, harnesses high-temperature heat

converted from solar irradiation to drive highly endothermic reforming reactions, mostly reforming of natural gas, and subsequently splits H_2O and/or CO_2 to produce syngas components H_2 and/or CO. Material studies of the oxygen carriers are currently limited and suggest avenues for more complete characterizations of physico-chemical evolutions over a broad range of transition metal oxides under practical solar chemical looping reforming operating conditions.[16, 17]

1.2 Current methods for production of solar fuels

Today, there are three basic pathways – and their hybridization technologies – to produce syngas from solar energy: electrochemical, photochemical and thermochemical.[18] Their reaction mechanisms, forms of energy input, engineering components, process efficiencies and potentials for scalable productions all vary significantly and are detailed below.

1.2.1 Electrochemical processes

Water electrolysis powered by solar-generated electricity is currently more mature than other technologies to produce hydrogen.[19] During electrolysis, water is decomposed into oxygen and hydrogen when an electric current converted from solar energy is passing through. The oxidation reaction at the anode (Equation 1.1) and the reduction reaction at the cathode (Equation 1.2) are shown below:[20]

$$2H_2O(l) \rightarrow O_2(g) + 4H^+(aq) + 4e^- \quad (1.1)$$

$$2H^+(aq) + 2e^- \rightarrow H_2(g) \quad (1.2)$$

The theoretical minimum requirement of electric potential to split water molecules is 1.23 V according to the standard potential of the anode.[21, 22]

As shown in Figure 1.1, apart from the two electrodes, the basic components of an electrolyser also include an external power supply sourced from solar energy. Ideally, hydrogen is produced twice the amount of oxygen. A diaphragm is used between the anode and cathode to separate the product gases while allowing protons to pass through from anode to cathode to be reduced to hydrogen gas.

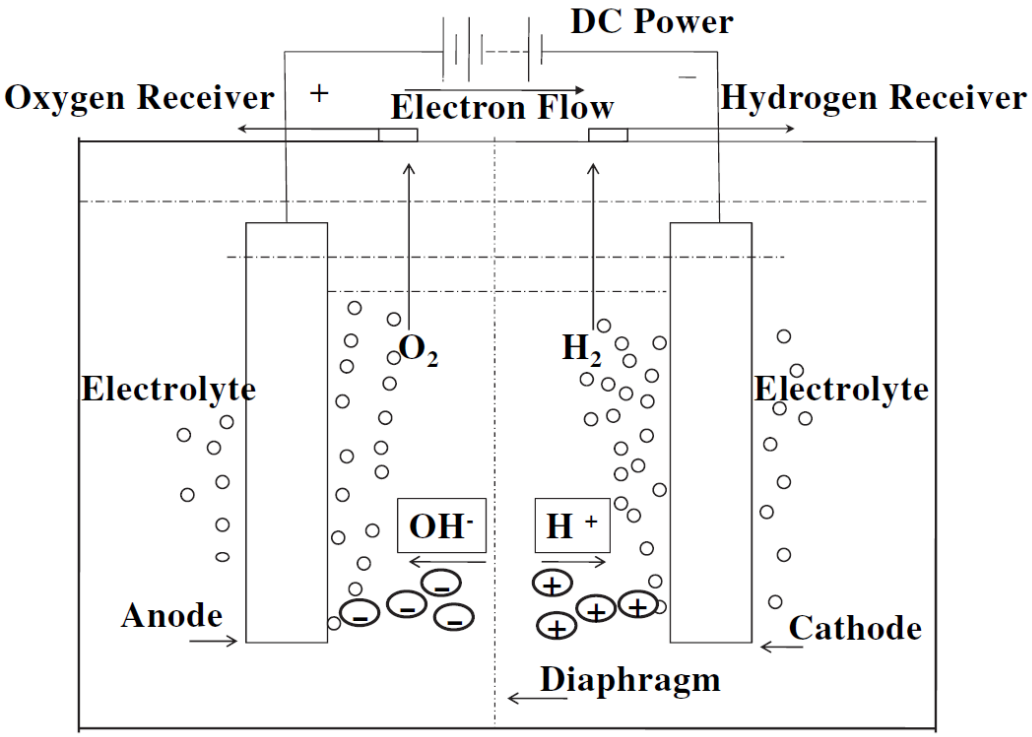

Figure 1.1 Schematic diagram of an electrolyser.[21]

The efficiency of the electrolysis process is dependent on the solar-to-electricity conversion efficiency of the power source and electricity-to-fuel efficiency of the electrolyser.[23] As a mature technology, commercial electrolysers such as alkaline or polymer electrolyte membrane electrolysers can achieve conversion efficiencies up to 80%.[24] However, the electricity generation is the main limitation in the overall efficiency because of its typically low conversion of solar irradiation. PV panels produce solar electricity with about 10–20% efficiency,[25, 26] while that of a solar thermal power plant operated with high-temperature working fluids is in the range of 30–60%[25].

As a result, a higher estimate of the overall theoretical efficiency with the integration of an electrolyser and a solar thermal power plant yields 16–32%.[26-28]

The electricity used for water electrolysis can also be sourced from a sunlight-absorbing electrode instead of external supplies. Such electrode is typically made or coated with an n-type or p-type semiconductor and the associated electrolysis device is called a photoelectrolysis or photoelectrochemical (PEC) water splitting unit.[20, 29, 30] A PEC unit is usually arranged with a window that allows the light absorber to capture sufficient solar irradiation to generate electric potentials. The counter electrode, typically made of metals, is connected to the light absorbing electrode through either external or internal wiring. The reaction mechanism is the same as described in Equations 1.1 and 1.2, and requires a minimum theoretical potential of 1.23 eV from the band gap of the electrode material to split water molecules.[31, 32]

Currently, there are quite a few limitations that PEC systems need to address in order to become more competitive with water electrolysis using external power sources. One major challenge is the complexity of the unit to efficiently track the sun without introducing excess auxiliary components or interrupting the contact between the electrode and water.[20, 24, 33] Additionally, the relatively large bandgaps provided by the electrode materials, typically greater than 3.2 eV, render inefficient utilization of solar irradiance as larger wavelengths such as infrared become less available.[34, 35] Therefore, PEC water splitting units rarely achieve solar-to-fuel conversion efficiencies of more than 16%.[36-38]

1.2.2 Photochemical processes

Photochemical water splitting or CO_2 reduction utilizes the concept of quantum solar energy conversion. The energy quanta or excitation energy is induced from absorption of light on a semiconductor, where electron-hole pairs are created by the

incident photons.[39] Due to the presence of an electric field inside the semiconductor, the generated electrons and holes are separated from each other. The electrons are transferred towards the conducting back-contact, and reach the counter-electrode via external wiring. In the case of photochemical H_2O splitting, a more leading area of research compared to CO_2 reduction, hydrogen gas is generated due to reduction of water by the electrons on the surface of the cathode. Meanwhile, the holes move towards the semiconductor/electrolyte interface and oxidize water to form oxygen gas.

$$H_2O + 2(h^+) \longrightarrow \tfrac{1}{2}\, O_2 + 2H^+ \qquad \text{(HER)}$$

$$2H^+ + 2e^- \longrightarrow H_2 \qquad \text{(OER)}$$

$$H_2O \longrightarrow \tfrac{1}{2}\, O_2 + H_2 \qquad \Delta G = +237.2 \text{ kJ/mol}$$

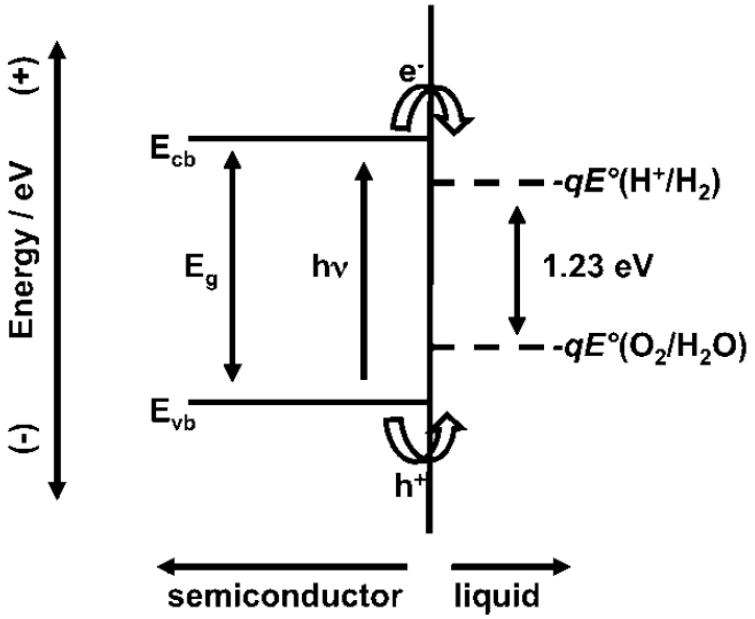

Figure 1.2 Water splitting mechanism using semiconductor photocatalysts.[20]

The electronic properties of a material is generally determined by the energy levels of the highest occupied and the lowest unoccupied orbitals, namely the valence band and the conduction band.[40] In Figure 1.2, the energy gap between the upper edge of the valence band (E_{vb}) and the lower edge of the conduction band (E_{cb}) is termed a bandgap

(E_g).[20] For semiconductors, the bandgap needs to be relatively narrow to allow electrons to move from the valence band to the conduction band upon receiving sufficient external excitation. Splitting H_2O requires a theoretical minimum bandgap of 1.23 eV (Figure 1.2) that corresponds to a photon wavelength of 1000 nm. However, considering the energy losses and the activation barriers, the ideal bandgap of a single semiconductor is in practice much larger, in the range of 1.9–3.5 eV.[41]

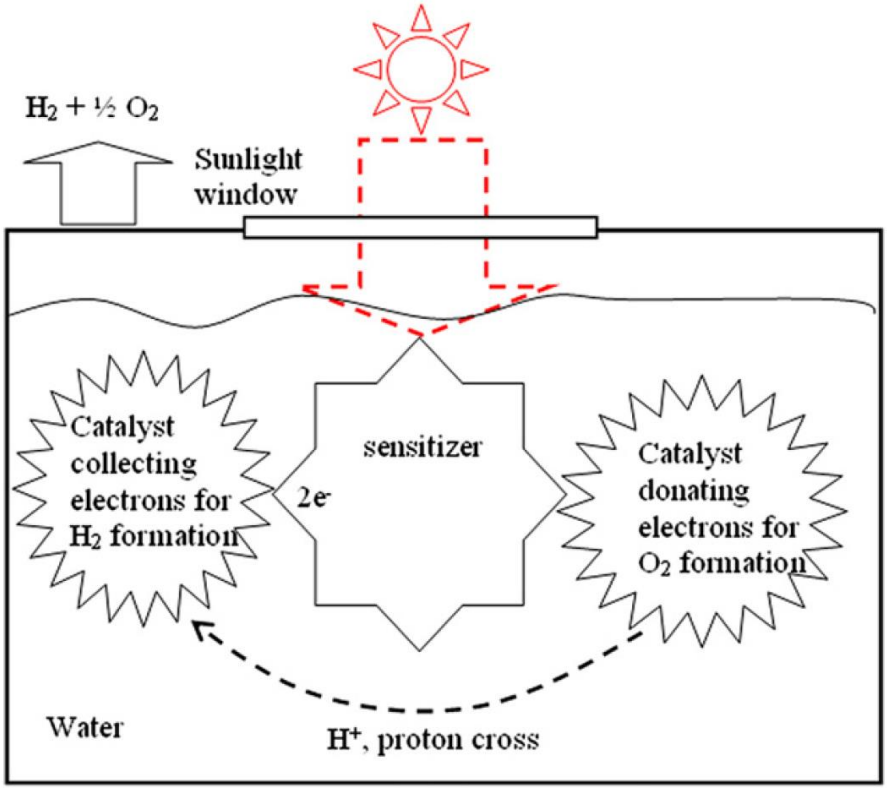

Figure 1.3 Schematic diagram of a photochemical water splitting unit.[18]

The basic components required by a photochemical water splitting cell are shown in Figure 1.3, which includes a window to receive sunlight, a sensitizer and at least one photocatalyst. To intercept more sunlight and approach sufficient contact with water, the sensitizer and catalyst are ideally distributed homogeneously in the water. As a consequence, hydrogen is not produced separately in the cell, although each hydrogen molecule is formed separately from a unit reaction site point of view. The mixture of hydrogen and oxygen is quite sensitive to sparks that may potentially lead to explosion.

Therefore, separation of hydrogen and oxygen is a major engineering challenge in solar photochemical water splitting.[32] However, the simplicity of the system design compared to externally powered electrolysers or thermochemical reactors means that photochemical solar fuel production can be readily distributed in hydrogen fuelling stations or remote areas with reduced auxiliary requirements.

In photochemical hydrogen production, the photocatalyst is utilized to lower the activation energy for the oxygen and hydrogen evolution, and its performance greatly influences the overall efficiency and economics of the water splitting unit. This is the same concern in CO_2 reduction reactions, in which the redox potentials are close to that of hydrogen. Therefore, many scientists and engineers focus on the development of highly efficient, low-cost and long-lifetime catalytic materials, mostly in the form of molecular or solid-state heterogeneous catalysts.[42, 43] Since the first proposal of direct solar water splitting by Fujishima and Honda in 1972 using titanium dioxide (TiO_2),[44] a wide range of semiconductors have been developed for photochemical water splitting or CO_2 reductions, including metals, metal oxides, (oxy)nitrides, sulphides and phosphides.[45, 46]

Similar to photoelectrolysis, the photochemical units also have difficulty in efficiently making use of the entire solar irradiance due to the wavelength selectivity of the catalysts.[34] Current photochemical water splitting units rarely reach an overall efficiency of 10%, even though the quantum efficiency at a certain wavelength could reach 56%.[47] Additionally, the sunlight tracking auxiliary components may further complicate the structure and operations of the process. Therefore, photocatalytic solar fuel production still requires significant research and development before approaching commercialization.

1.2.3 Thermochemical processes

The thermochemical production of solar fuels uses concentrated solar radiation as the energy source in the form of high-temperature heat to drive highly endothermic reactions, and inherently utilizes the entire solar spectrum. As such, they provide thermodynamically favourable paths to produce solar fuels compared to solar electrochemical or photochemical processes.[5] Concentrating solar technologies are currently well underway to commercialization to provide large-scale power generation. When coupled with high-temperature thermochemical reactors, they have the potential of producing solar fuels at large scale and at competitive costs with high solar-to-fuel efficiencies in the short-term future.[7, 48]

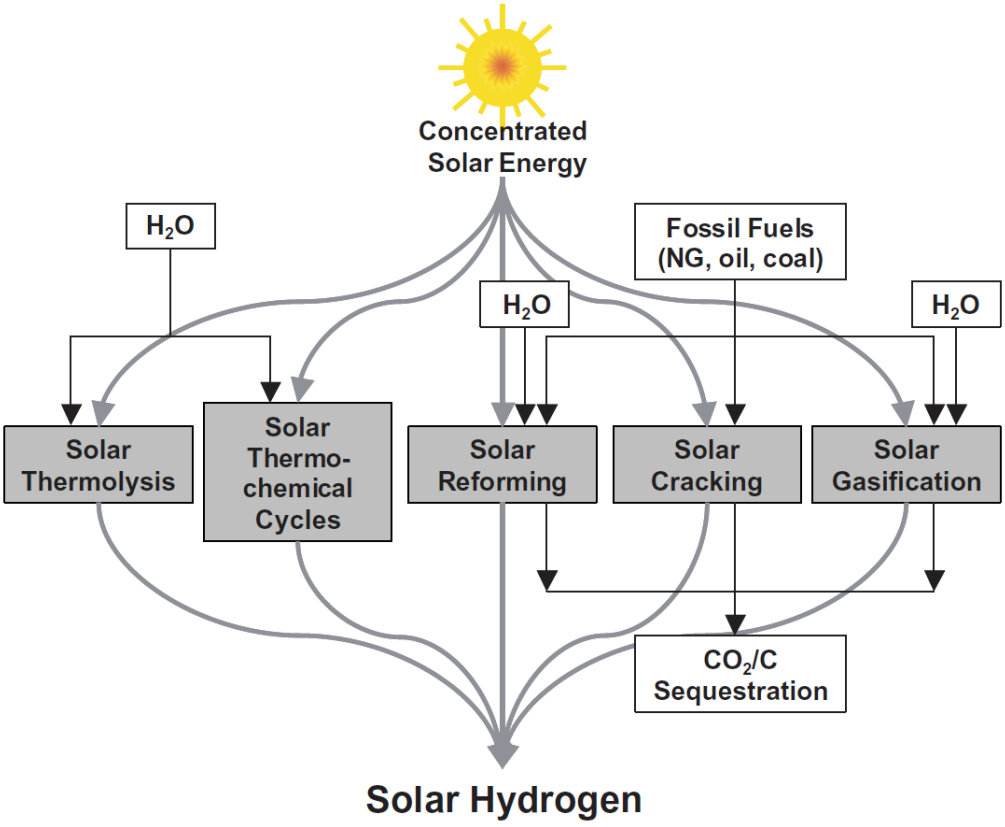

Figure 1.4 Contemporary routes for solar hydrogen production.[3]

Today, there are five major thermochemical routes to produce solar fuels. Figure 1.4 illustrates the case for solar hydrogen production from H_2O splitting, which also applies to solar thermochemical CO_2 reduction when using CO_2 as feedstock. Solar thermolysis

and solar thermochemical cycles ideally have no or negative carbon emissions but requires higher temperatures and still need to resolve some technical barriers before reaching full technical maturity for large-scale demonstration.[3, 13, 14, 49] Solar gasification, cracking or reforming refers to processes using fossil fuels such as natural gas, oil, biomass, or biogas besides zero-energy chemicals (H_2O and CO_2) as feedstock source.[50] Compared to conventional non-solar processes, syngas products from these solar decarbonisation processes have energetic upgrades compared to the feedstock and emit less carbon when combusted.[51, 52] These technologies can be directly integrated into well-known commercial processes such as steam reforming or coal gasification, paving the way for a swift transition towards a low-carbon and renewable-based economy.

1.2.3.1 Solar thermolysis

Solar thermolysis refers to the direct splitting of H_2O (or CO_2) into O_2 and H_2 (or CO) via solar energy. Despite of its single-step simplicity, the high reaction temperatures (> 2500 K for H_2O thermolysis,[49, 53] and > 2650 K for CO_2 thermolysis[54]) render the process impractical for even minimum extent of reaction. The simultaneous co-production of H_2/O_2 or CO/O_2 also requires high-temperature separation steps to prevent product recombination and an explosive mixture.[48] Furthermore, the very high temperatures demanded by the thermodynamics of the process (e.g. 3000 K for 64% dissociation of H_2O at 1 bar) pose severe material and engineering challenges and can lead to significant re-radiation losses from the reactor, lowering the absorption efficiency.[49] Therefore, current research efforts in this area are scarce and a pilot-scale demonstration has not been recommended so far.

1.2.3.2 Solar thermochemical cycles

Solar fuels production via water or carbon dioxide splitting thermochemical cycles bypasses the problem of H_2/O_2 or CO/O_2 separation and further allows operations at

lower temperatures (< 1800 K) than the thermolysis process.[7, 13, 14, 49, 55] The key feature of solar thermochemical cycles is the utilization of intermediate reactions and substances to indirectly split H_2O or CO_2 into syngas components from the solar source, and recycle the intermediate substances within the process to ensure sustainability.[56-60] That is, the sum of all the step-wise reactions is equivalent to the dissociation of H_2O or CO_2, with heat from solar irradiance as the only theoretical energy input. Recently, with the significant progress accomplished in the development of large-scale optical systems capable of achieving mean solar concentration ratios exceeding 5000 suns, essentially corresponding to thermal reservoirs at over 2000 K after conversion, solar thermochemical cycles have been presented with promising potentials for further large-scale demonstration.[3, 61-66] As such, considerable research efforts targeted towards commercializing this technology are currently devoted to reactor designs and material explorations.[2, 4, 13, 67, 68]

Today, research interests have largely shifted towards a two-step H_2O/CO_2 splitting redox cycle, where a redox pair based primarily on metal oxides is used as the intermediate to cyclically release oxygen in an endothermic reduction step (Equation 1.3) and absorb oxygen in an exothermic oxidation step (Equations 1.4a, 1.4b).[13, 69-71] Water (and/or carbon dioxide) is consumed in the oxidation step to re-oxidize the metal oxide and simultaneously produce H_2 (and/or CO),[62, 64, 72-75] as represented below:

Reduction step:

$$MO_x \rightarrow MO_{x-\delta} + 0.5\delta O_2, \quad \Delta H^o_{298} > 0 \tag{1.3}$$

Oxidation step:

$$MO_{x-\delta} + \delta H_2O \rightarrow \delta H_2 + MO_x, \quad \Delta H^o_{298} < 0 \tag{1.4a}$$

and/or

$$MO_{x-\delta} + \delta CO_2 \rightarrow \delta CO + MO_x, \quad \Delta H^o_{298} < 0 \tag{1.4b}$$

The first proposal of this two-step redox approach was investigated by Nakamura in 1977 using Fe_3O_4/FeO redox pair[76]. The reduction temperature was required to be more than 2273 K, at which severe sintering, melting and vaporization was reported during thermal dissociation of Fe_3O_4.[76, 77] A reasonable conversion was achieved during oxidation by H_2O after milling and granulation of FeO. Since then, substantial advances have been made in pursuit of redox materials that have high fuel production capacity, low reduction temperature, fast kinetics, long lifetime, low toxicity and low cost. Systematic reviews of the redox materials were detailed by Scheffe and Steinfeld,[14] Agrafiotis et al.[4] and Muhich et al.[13] that represented the research status up till 2015. In general, two categories were identified for the two-step redox cycles: volatile and non-volatile. Volatile redox cycles consist of metal oxides that undergo gas-to-solid phase transitions during reduction,[78, 79] while non-volatile cycles use metal oxides that remain condensed during the entire process[70, 80]. Despite the higher oxygen exchange capacity (i.e. higher fuel production capacity) and higher thermodynamic favourability of the volatile reactions, the demanding rapid quenching process to avoid product recombination significantly hinders the energy efficiency of volatile redox cycles.[81, 82] Non-volatile cycles bypass the recombination issue and are further categorized into stoichiometric and non-stoichiometric cycles. In stoichiometric cycles, metal oxides generally form solid solutions resulting in altered crystallographic structures during reduction.[76, 83-87] In non-stoichiometric cycles, metal oxides are capable to accommodate variations of the oxygen vacancies within the lattice without inducing crystallographic changes.[62, 72-74, 88-90] Stoichiometric materials generally have higher oxygen exchange capacity than non-stoichiometric materials, but suffer more from slower reaction kinetics and poor stability, essentially leading to lower solar-to-fuel conversion efficiency.[2, 91] A summary of the most commonly investigated redox pairs in two-step thermochemical redox cycles are shown in Table 1.1. Today, ceria and its doped

counterparts still remain to be the state-of-the-art benchmark material because of its rapid reaction kinetics, crystallographic stability, favourable oxidation thermodynamics and higher demonstrated performance.[62, 66, 70, 92] Efforts are also focused on many perovskite materials that operate several hundred degrees lower than ceria during reduction.[72, 90, 93] However, their lower entropy change usually results in consistently less efficient oxidation reactions due to less thermodynamic favourability.[94-96]

Table 1.1 Common redox pairs for two-step thermochemical redox cycles.[14]

Category	**Cycle name**	**Simplified reduction reaction**
Volatile	Zinc oxide	$ZnO(s) \rightarrow Zn(g)$
	Tin oxide	$SnO_2(s) \rightarrow SnO(g)$
Non-volatile (stoichiometric)	Iron oxide	$Fe_3O_4 \rightarrow FeO$
	Ferrite	$M_xFe_{3-x}O_4 \rightarrow xMO + (3-x)FeO$
	Hercynite	$Fe_3O_4 + 3Al_2O_3 \rightarrow 3FeAl_2O_4$ $M_xFe_{3-x}O_4 + 3Al_2O_3 \rightarrow (3-x)FeAl_2O_{4-x} + xMAl_2O_4$
Non-volatile (non-stoichiometric)	Ceria	$CeO_2 \rightarrow CeO_{2-\delta}$
	Doped ceria	$M_xCe_{1-x}O_2 \rightarrow M_xCe_{1-x}O_{2-\delta}$
	Perovskite	$ABO_3 \rightarrow ABO_{3-\delta}$

Reactor designs targeted specifically for solar thermochemical cycles that seek to optimize thermodynamics, kinetics and durability while minimizing parasitic losses from heat and mass transport in an economic and efficient fashion have also advanced significantly in recent years.[97] Under such context, two categories of reactor designs were investigated: monolithic reactors and particle reactors. Monolithic reactors rely on self-supporting active materials and the reduction and oxidation steps are spatially separated either by mechanical motion of the materials or redirection of the solar beam.[62, 98, 99] Depending on the configuration, these reactors may suffer from issues related to low heat recuperation, mechanical failures due to thermal stress, or poor thermal transport.[62, 100, 101] Particle reactors utilize moving particles to facilitate product transport away from the solids.[102-104] These designs are generally beneficial to mass and heat transport but requires efficient direct solar irradiation, leading to size limitations associated with the use of quartz windows.[105]

Additionally, debate over isothermal or non-isothermal operation modes of the redox cycles still continues today. Pure isothermal operation is simpler, but theoretically less efficient as the favourable temperatures for oxidation reactions (exothermic) are at least 400 K lower than those of reduction reactions (highly endothermic).[15, 64] Nevertheless, solar-to-fuel conversion efficiencies of more than 20%[13] are projected for solar thermochemical cycles and a very recent lab-scale demonstration in 2017 using ceria-based dual-scale reticulated porous structure for CO_2 splitting in a second generation cavity reactor has already achieved an efficiency of 5.25%,[66] comparable to the highest value reported to date using PV-electrolyser. This makes solar thermochemical path a stride closer towards being economically and energetically competitive to other production paths of solar fuels with zero carbon emissions.

1.2.3.3 Solar gasification

Gasification of solid-state carbonaceous feedstocks such coal, coke, biomass, bitumen, and carbon-containing wastes for the power and chemical industries is a mature fossil-fuel-based technology to efficiently produce clean and energy-rich syngas. However, conventional autothermal gasification requires up to 40% of the injected feedstock to be combusted internally with O_2 to supply high-temperature process heat for the endothermic reaction.[51] This leads to decrease in feedstock utilization, contaminants in the product gases with combustion products, and requires an energy-demanding air separation unit to supply high-purity oxygen gas for combustion. In contrast, solar gasification has the potential to produce syngas with higher quality, higher output per unit of feedstock and lower specific CO_2 emissions, as the calorific value of the feedstock is upgraded through the solar energy input by an amount equal to the enthalpy change of the reaction.[50] The elimination of an air separation unit also facilitates further economic competitiveness.

In the case of steam gasification of coal, which is a well-developed commercial process attributing to 18% of hydrogen production today,[50] the following reaction is applied:

$$C(s) + H_2O \rightarrow CO + H_2, \quad \Delta H^{o}_{298} = 131 \text{ kJ mol}^{-1} \tag{1.5}$$

At 1300 K, the syngas product of an equimolar mixture can achieve up to 33% energetic upgrade from the coal feedstock only when driven by solar energy.[50] Such syngas, when applied to combined Brayton-Rankine power cycles, can double the specific electric output per unit mass of coal and consequently achieve specific CO_2 intensities approximately half that of conventional coal-fired power plants.

Experimental demonstrations of steam gasification into syngas using prototype directly irradiated solar reactors has yielded feedstock conversions higher than 85%, selectivity to syngas of more than 65%, and projected solar-to-fuel conversion

efficiencies higher than 20%.[106, 107] Further research and development of the solar reactor technology is warranted and new-generation industrial pilot plants are well underway to demonstrate operations approaching mega-watt scale.

1.2.3.4 Solar cracking

Solar cracking almost exclusively refers to the thermal decarburation of methane, the major component of nature gas that is estimated to have 580 Gton yet to be utilized worldwide and expected to last for another two centuries based on current consumption rate of 2.9 Gton per year.[108] The reaction proceeds endothermically below:

$$CH_4 \rightarrow C(s) + 2H_2, \quad \Delta H^{o}_{298} = 75 \text{ kJ mol}^{-1} \tag{1.6}$$

With the potential to produce high-purity hydrogen and condense carbon into solid-state filaments, solar methane cracking bypasses auxiliary product separation and conversion processes that would otherwise be required in other hydrogen production systems seeking CO_2-free operations.[109, 110] However, significant difficulties have been encountered when several groups were trying to practically implement this reaction. The main technical issue is the coke formation and deposition that either blocks the system, or deactivates the catalysts rapidly, making the process very difficult to scale up by industrial standards.[111] The rapid deactivation of the most effective catalysts based on metallic components (e.g. Ni-based) burdens its economic viability. Additionally, the regeneration of the catalyst is based on carbon oxidation, producing CO_2 during the life cycle of the process.[112]

Compared to coal gasification or steam methane reforming, the mild endothermic reaction (1.6) per unit mole of converted C indicates lower energetic upgrade for syngas production by solar methane cracking. Preliminary cost estimates also suggest twice as much production cost for hydrogen (USD 3 $/kg),[110] making it less competitive at the

current state-of-the-art of the solar tower technology, which is the only system able to reach the temperatures needed for direct solar thermal cracking (> 1273 K). Therefore, despite scientific viability, there is still a long path to cover the gap between laboratory and industrial implementation of solar methane cracking.

1.2.3.5 Solar reforming

Presently, traditional reforming industry, particularly steam reforming of methane, is supplying approximately half of the global hydrogen consumption and is likely to remain the technology of choice for some time.[1] Depending on the feed gas and product requirements, key processing steps of steam reforming of methane are shown in Figure 1.5:

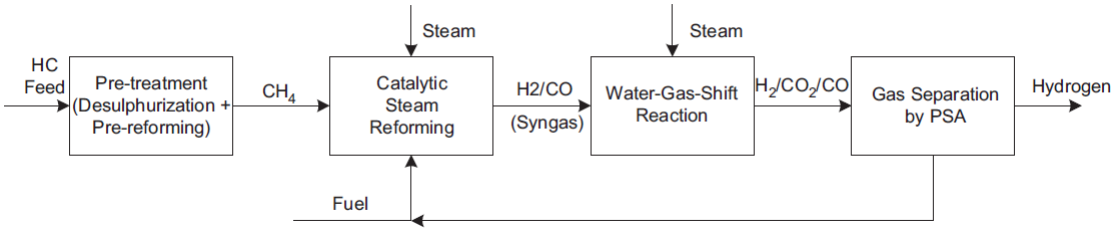

Figure 1.5 Traditional process flow of hydrogen production via steam reforming of methane.[113]

Feed gas purification/pre-treatment is essential to remove certain contaminants (mostly sulphur-containing compounds) that would otherwise poison the catalyst even at a concentration of a few ppb in the feed gas stream.[113] The subsequent key reactions of steam (H_2O) and dry (CO_2) reforming of methane are shown individually below:[114]

$$CH_4 + H_2O \rightarrow 3H_2 + CO,\ \Delta H^o_{298} = +206\ \text{kJ mol}^{-1} \quad (1.7)$$

$$CH_4 + CO_2 \rightarrow 2H_2 + 2CO,\ \Delta H^o_{298} = +247\ \text{kJ mol}^{-1} \quad (1.8)$$

Notably, the heat for the required processes is commonly supplied by gas heaters that burn up to 41% of the methane feedstock or product mixture to maintain the temperature of the endothermic reactions.[10, 115] This results in a 24% reduction in energy content compared to the initial feedstock.[10] Utilizing concentrated solar energy to drive methane reforming processes can completely supplement that fossil-fuel energy demands to run the process and simultaneously store solar energy in the syngas product stream. This solar methane upgrading process can reduce carbon emissions by 41% while storing up to 28% of solar energy as chemical potential.[10, 116] Recently, significant progress has been made in solar steam methane reforming and technologies for directly irradiated volumetric receiver-reactors and tubular reactors are planned for small commercial scale installation.[1] Under this context, plants in the 1-5MW range are expected to be constructed in Australia and Europe in the next couple of years, with pre-commercial stage to be reached within a decade.[1, 117]

Despite significant technical advance, one of the main issues with the steam and dry methane reforming process is that they do not result in a flexible H_2/CO ratio, which is ideal for the subsequent Fischer-Tropsch synthesis of liquid fuels.[6, 118, 119] As a result, the steam methane reforming process needs to be operated at 15-35 bar,[120] and the product gases have to go through additional water-gas shift reactions (Figure 1.5), commonly performed downstream through two additional reactors operated at 583-723 K and 483-513 K.[121] Furthermore, efficient and carbon-resistant catalysts for steam and dry reforming are based on noble metals resulting in significant costs.[122-124] As an economic compromise, catalysts in commercial steam reforming plants are Ni-based and suffer from relatively rapid deactivation and poor selectivity to syngas.[125-127] In order to mitigate catalyst deactivation, conventional steam reformers must operate with excess oxidizer with a H_2O/CH_4 ratio ≥ 3,[114] as opposed to a ratio of 1 suggested by Equation 1.7. The parasitic energy requirement to evaporate and heat the extra water for

reforming and water gas shift is significant (ca. 15% extra energy).[114] Investigation of other low-cost transition metal based catalysts has not yielded a commercially viable substitute to Ni-based catalysts.[128] The commercial Ni-based catalysts also suffer from sintering and coking issues,[123, 129-131] which render them not very suitable for solar thermochemical processes, where large temperature and pressure swings are expected due to intermittent solar thermal loads. Variations of temperature and pressure are particularly problematic for gas-gas reactions such as steam methane reforming as they change the equilibrium conditions and essentially product selectivity and H_2/CO ratios during operation.[1]

Therefore, although it is widely used in hydrogen generation, steam methane reforming is a complex process that involves many essential catalytic steps. Additional energy and equipment is needed to separate CO_2 from the exhaust gas, and this process cannot achieve a complete CO_2 capture. The heat transfer coefficient of the internal tube in the reformer is the rate-limiting factor.[52] Along with the catalyst performance issues, current steam methane reforming process is still not fully ready to be directly transferred to solar demonstrations at large scales.

1.3 Fundamentals of solar chemical looping reforming

Chemical looping reforming is essentially a hybrid approach between thermochemical cycles and steam/dry reforming of methane, in which reactions 1.7 or 1.8 are split into two steps as shown in Equations 1.9 and 1.10 below:[10, 11]

Reduction step:

$$\delta CH_4 + MO_x \rightarrow MO_{x-\delta} + \delta CO + 2\delta H_2, \quad \Delta H^o_{298} > 0 \qquad (1.9)$$

Oxidation step:

$$MO_{x-\delta} + \alpha\delta H_2O + (1-\alpha)\delta CO_2 \rightarrow \alpha\delta H_2 + (1-\alpha)\delta CO + MO_x, \quad \Delta H^o_{298} < 0 \qquad (1.10)$$

In the endothermic partial oxidation (reduction) step, methane reacts with oxygen released from a metal oxide to produce syngas. In the exothermic oxidizer splitting (oxidation) step, H_2O and/or CO_2 react with the reduced metal oxide to produce H_2 and/or CO. In comparison to reduction of a metal oxide by an inert sweep gas or sub-atmospheric pressure, the utilization of methane in reaction (1.9) lowers the thermodynamic barrier before splitting water or carbon dioxide, such that the thermodynamics of chemical looping reforming are those of methane reforming rather than the less favourable thermodynamics of thermolysis.[115] The net products of chemical looping reforming match those of steam and dry reforming for $\alpha=1$ and $\alpha=0$ in reaction (1.10), respectively, with the additional advantage of producing H_2:CO ratio of 2:1 in reaction (1.9) as opposed to 3:1 in reaction (1.7) or 1:1 in reaction (1.8). The syngas from reaction (1.10) can also be tuned by controlling the steam fraction α to obtain any H_2:CO ratio. With $\alpha=1$ or water splitting, the process yields separate streams of syngas ready for Fischer-Tropsch synthesis of liquid fuels and high-purity hydrogen to directly feed in fuel cells, as shown in Figure 1.6. With $\alpha=0$ or carbon dioxide splitting, the potential to convert CO_2 into syngas component CO can provide significant environmental benefits.[114] Chemical looping reforming does not require excess oxidizer that would otherwise be essential in conventional reforming reactors to prevent catalyst deactivation by carbon deposition. Instead, the carbon deposition can be managed by limiting the extent of the reduction of the metal oxide.[132-134]

In this section, a brief summary of the chemical and process thermodynamics of solar chemical looping reforming will be reviewed.

1.3.1 Chemical thermodynamics

To be commercially relevant, the following key metrics of chemical looping reforming are often considered in thermodynamics calculations: methane conversion,

syngas (H_2 and/or CO) selectivity, carbon deposition and oxidizer (H_2O and/or CO_2) conversion.[116, 135-138]

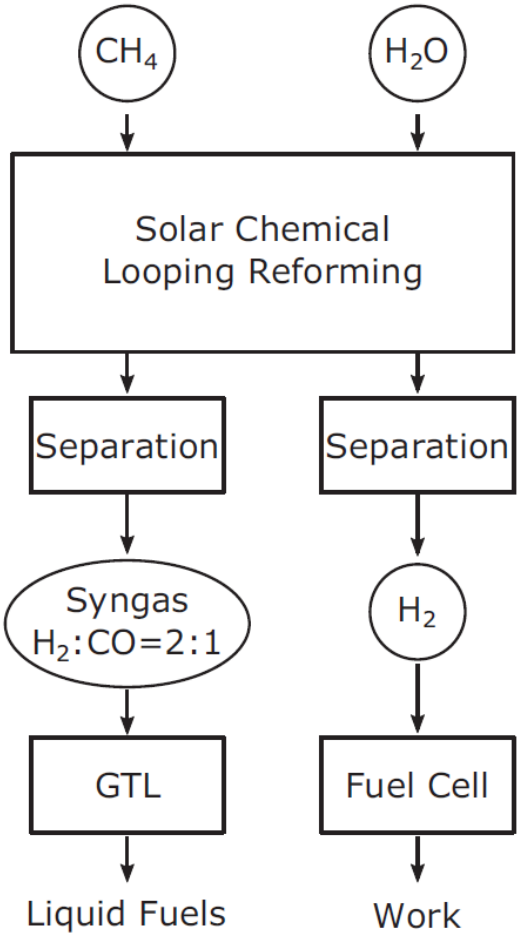

Figure 1.6 Solar chemical looping reforming with H_2O as oxidizer.[10]

Previous equilibrium analysis of the reaction between a 2:1 ratio of CH_4 and O_2 (Figure 1.7) reveals that the converted CH_4 favours complete oxidation products H_2O and CO_2 up to 373 K. From 373 K to 1373 K, the oxygen mole fraction remains below 10^{-16}, much lower than what could be achieved by inert gas sweeping or vacuum pumping. Partial oxidation products (H_2 and CO) comprise more than 95% above 1100 K and over 99% above 1223 K.

However, Figure 1.7 presents only the ideal case where a syngas stream of 2:1 ratio (H_2:CO) can be maintained and a high methane conversion can be achieved with a constant CH_4:O_2 = 2:1 feedstock supply. In terms of reaction (1.9), the equilibrium products will be more complicated to predict as the rate of oxygen supply will be dependent on the extent of reduction of the metal oxide (oxygen carrier).[135] As such, the methane to oxygen ratio will not be constant during the reduction step. This leads to an actual scenario of a gas-solid reaction by (1.9) that upon reaching the thermodynamically preferable temperature of above 1100 K, methane will be firstly converted to H_2O and CO_2, followed by production of H_2 and CO as lattice oxygen from the metal oxide begins to be consumed.[133, 135, 139-141] Upon reaching certain reduction extent, methane to oxygen ratio falls below 2:1 and unreacted methane and solid carbon will be present. This analysis is consistently confirmed by experimental demonstrations of reaction (1.9).[139, 140, 142-145] Deposition of carbon on the metal oxide can block the reaction sites. In certain cases, the issue can be mitigated by using CO_2 during the oxidation step (Equation 1.10, α=0), as the Boudouard reaction alleviates the carbon deposition while enriching the CO product stream:[114, 139, 146, 147]

$$2CO \leftrightarrow C\,(s) + CO_2, \quad \Delta H^{o}_{298} = -172.2 \text{ kJ mol}^{-1} \qquad (1.11)$$

However, in the case of H_2O splitting, the hydrogen product stream is contaminated by carbon oxides mostly dictated by reaction (1.5). In terms of syngas selectivity, previous studies have indicated that higher methane to oxygen ratios always lead to higher H_2 selectivity. However, CO selectivity is maximized at CH_4:O_2 = 2:1. This is because when CH_4:O_2 > 2:1, the formation of solid carbon is promoted instead of CO. Improving kinetics and heat transfer of reaction (1.9) may help suppress carbon formation.[129, 148]

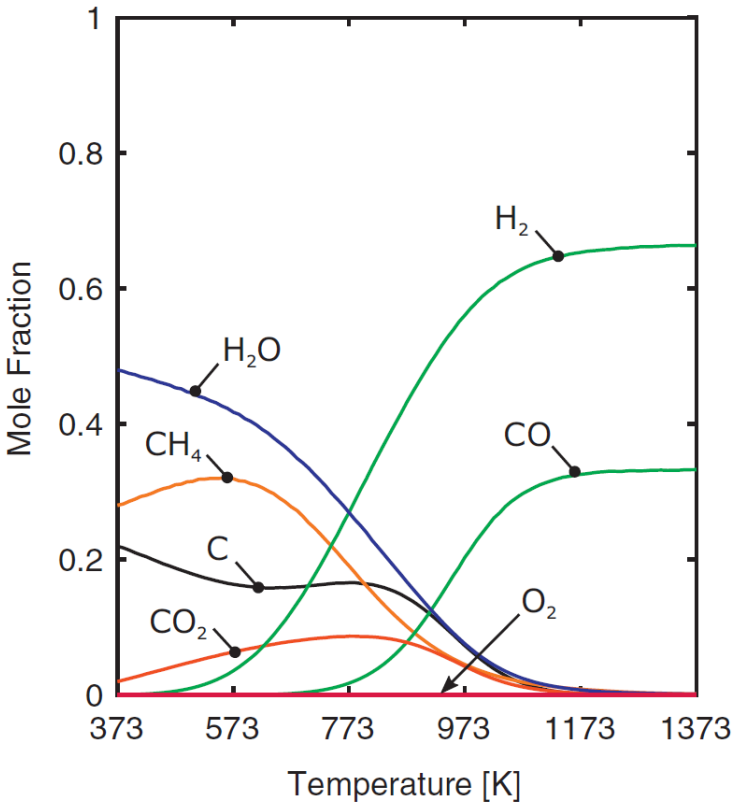

Figure 1.7 Equilibrium product distribution of methane partial oxidation at CH_4:O_2 = 2:1.[10]

The extent of reduction of the metal oxide that can be achieved in reaction (1.9) will also directly influence its capability to split water or carbon dioxide in reaction (1.10). As such, the equilibrium oxygen partial pressure was previously studied as a function of temperature of the oxidizer conversion ranging from 0.01 to 0.99 in Figure 1.8.[10] For isothermal cycles, it is observed that a very high oxidizer conversion of greater than 0.99 can be achieved at 1273 K with CH_4:O_2 = 2:1 in reaction (1.9).[116] However, this temperature is approximately 200 K higher than the thermodynamically favoured temperature for reaction (1.10). It requires further thermodynamic evaluations to see whether the two-temperature cycling is more energetically competitive than the isothermal cycling.

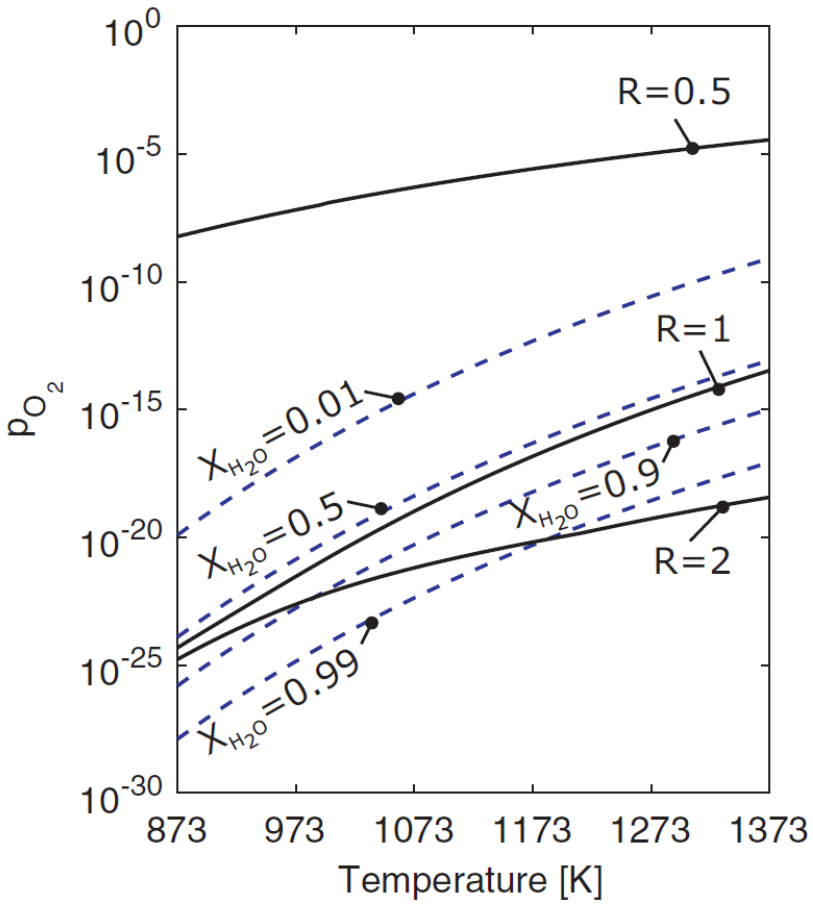

Figure 1.8 Equilibrium partial pressure of oxygen (dashed curves) as a function of temperature for oxidizer conversions between 0.01 and 0.99. Equilibrium partial pressure of oxygen in reaction (1.9) is shown (solid curves) for comparison. R is the CH_4:O_2 ratio.[10]

1.3.2 Process thermodynamics

There are relatively few process thermodynamic analyses of solar chemical looping reforming[135-138] compared to solar thermochemical redox cycles driven by inert gas sweeping or vacuum pumping[63-65, 67, 75, 149-151]. However, the framework for analysis is transferrable. The studies of energy requirements and solar-to-fuel conversion efficiency in solar chemical looping reforming are summarized here. The results suggest the dependence of process efficiency on methane conversion, syngas selectivity and oxidizer conversion.[116, 135, 136, 138] Future work that seeks to optimize the efficiency

towards the projected upper limit should address the improvement of these performance metrics in practice.

A previously presented framework to project the solar-to-fuel efficiency of solar chemical looping reforming for an isothermal open system by Krenzke et al. was defined below:[10, 135]

$$\eta = \frac{\sum_i (n_{i,OUT} - n_{i,IN}) HHV_i}{Q_{SOLAR} + W/\eta_{S\rightarrow E}} \quad (1.12)$$

It denotes the net gain in the higher heating value (HHV) of the gases divided by the direct solar thermal power input to the reactor, Q_{SOLAR}, and the solar thermal power required to provide parasitic work, $W/\eta_{S\rightarrow E}$, including that required for pumping the gases and extracting pure hydrogen or carbon monoxide. Based on this, an expanded analysis with inclusion of the work to extract syngas from the products of the reduction reaction (1.9) is defined below:[135]

$$Q_{SOLAR} + W/\eta_{S\rightarrow E} = Q_{RAD} + Q_{LOSS} + Q_{GAS} + Q_{REJECT} + W_{\Delta P}/\eta_{S\rightarrow E} + W_{SEP}/\eta_{S\rightarrow E} \quad (1.13)$$

On the left hand side, the solar input (Q_{SOLAR}) is that available at the aperture of the reactor. The work input ($W/\eta_{S\rightarrow E}$) is supplied by solar thermal electricity with a solar-to-electricity efficiency ($\eta_{S\rightarrow E}$) of 25%.[152]

On the right hand side, the heat loss by radiation, Q_{RAD}, is estimated by assuming the receiver approaches blackbody behaviour and that there are no reflection losses. In a central tower receiver system, a concentration ratio of 1000 can be assumed.

$$Q_{RAD} = \frac{\sigma T_{CAVITY}^4}{IC} Q_{SOLAR} \quad (1.14)$$

Q_{LOSS}, which is the conduction through the insulation and convection losses from the aperture of the solar reactor, is estimated to be 5% of Q_{SOLAR} according to predictions

for solar reactors at commercial scales.[153] Q_{GAS} is the energy requirement associated with mass flows crossing the system boundary, and it is defined by the difference in enthalpy entering and exiting the system:

$$Q_{GAS} = \sum_i n_{i,OUT} h_i(T) - \sum_i n_{i,IN} h_i(T_\infty) \quad (1.15)$$

Both chemical and sensible energy storage are included in Q_{GAS}. Q_{REJECT} is tied to the energy balance in the splitting reactor, where heat may be rejected during a two-temperature cycle as reaction (1.10) is exothermic.[63, 154, 155] With respect to isothermal solar chemical looping reforming, Q_{REJECT} is assumed to be zero and the released heat from reaction (1.10) remains with the system and offsets the endotherm of reaction (1.9). $W_{\Delta P}$ represents the work for pumping the gases:

$$W_{\Delta P} = \frac{(n_{CH4,IN}+n_{H2O,IN})RT_\infty \ln(\frac{P_\infty+\Delta P}{P_\infty})}{\eta_P} \quad (1.16)$$

W_{SEP} represents the separation work for both reactions (1.9) and (1.10) and is directly related to methane conversion and H_2 or CO selectivity. For water splitting, $W_{SEP,H2O}$ is zero as water condensation requires no extra energy input. In the case of carbon dioxide splitting, the separation work is estimated from commercial processes with second law efficiencies ranging from 10 to 25%. Additionally, the efficiency of separating CH_4 from syngas is estimated to be 10%.[156]

Based on the above framework, the ideal solar-to-fuel efficiency of a chemical looping reforming process is 54% with complete conversion of methane,[10] which is up to two times higher than thermochemical redox cycles driven by inert gas sweeping or vacuum pumping[63, 154]. This efficiency is most sensitive to methane and oxidizer conversions. Key performance parameters also include H_2 selectivity and CO selectivity during reduction reaction (1.9). Further analysis suggests the reactor mass is proportional to efficiency, and decreases as the rates of syngas production increase. Additionally, the optimized efficiency indicates that a mass loading of the metal oxide

at the scale of tens of kilograms per MW of solar thermal input to convert methane (supplied at approximately 10 mL min^{-1} g^{-1}) is required in a chemical looping reforming solar reactor.[10] Therefore, to approach the practicality of implementing a solar chemical looping reforming reactor setup, the task to find a metal oxide that is abundant and inexpensive, and has fast reaction kinetics in reactions (1.9) and (1.10) has become crucial. Furthermore, the material's effect on improving the feedstock conversion and syngas selectivity needs to be addressed.

1.4 Materials for solar chemical looping reforming

Previous reviews have established important properties that are sought after for redox materials in solar thermochemical redox cycles.[4, 13, 14] Most of these properties still hold valid for ideal metal oxides in solar chemical looping reforming. Combined with the key performance parameters identified in Section 1.2.2, these properties are listed below:

- High oxygen exchange capacity: Metal oxides with high oxygen exchange capacities allow more active materials involved in the chemical looping reforming redox cycles, improving the utilisation of the massive amount of oxygen carriers loaded into the reactor required by high solar-to-fuel conversion efficiencies.[80, 140, 157, 158]
- Fast reaction kinetics: Materials with fast reaction kinetics effectively reduce the reactor size requirements, implying significant reduction in capital costs of the reactor setup.[159]
- Carbon resistance: During reduction, carbon deposition blocks the gas-solid reaction interface and induces deviation of the syngas product ratio towards undesirable values. Therefore, materials with higher carbon resistance contribute to higher process efficiency.[135, 141, 160]

- High methane and oxidizer conversion and high H_2 and CO selectivity: As described in Section 1.2.2, these key parameters directly influence the conversion efficiency of the system.
- Non-volatile at the working temperatures: Materials that only show reactivity at high vapour pressures require extra separation to avoid recombination and quenching for recovery. This induces significant energetic penalty and leads to lower process efficiency.
- Retention of high surface area and porosity: Deactivation of the redox material by the loss of surface area and porosity is especially significant in gas-solid reactions such as (1.9) and (1.10). Mitigating this effect is crucial.
- High thermal conductivity: The large mass loading requires the redox materials to have high thermal conductivity in order to achieve high utilization.
- Mechanical and structural stability: Materials should provide large thermal-shock and mechanical resistance to facilitate their use in long periods of working time. Stable microstructural properties including composition, particle size and morphology are also essential in maintaining the redox performance in cyclic operations.[97, 159, 161]
- Stable cyclic performance: Predictable and stable long-term performance of the materials is directly related to the cost for their replacement and quality of the syngas products.
- High abundance, low toxicity and low cost: Metal oxides must be abundant and inexpensive to reduce the capital and replacement cost. In addition, the associated risks during material handling and accidental leaks require the materials to have low toxicity.[80]

A review of the materials that so far address at least some of the above screening criteria is presented below, with the state-of-the-art research highlighted.

1.4.1 Pristine and supported metal oxides

Due to the capability to be fully reduced to the metallic states (ZnO/Zn[78], SnO_2/Sn[81]) or stable low-valency states (Fe_3O_4/FeO[162]), stoichiometric pristine metal oxides, especially transition metal oxides,[45, 123, 163] were the first oxygen carriers studied for chemical looping reforming. To mitigate sintering, non-volatile metal oxides are often supported on inert structures.

The first solar chemical looping reforming was studied by Steinfeld et al. using Fe oxides.[162] The results suggest a stepwise reduction and oxidation in the sequence of $Fe_2O_3 \leftrightarrow Fe_3O_4 \leftrightarrow FeO \leftrightarrow Fe$. Among all the possible iron oxide pairs examined, Fe_3O_4/FeO was later identified as a suitable redox pair due to its relatively less carbon formation, more syngas yields, and faster re-oxidation kinetics (Figure 1.9).[144, 164, 165] However, compared to other stoichiometric metal oxides, Fe_3O_4/FeO still exhibits low oxidizer conversion (< 30%) and low selectivity towards syngas.[77, 144, 162, 166]

Steinfeld et al. also investigated ZnO for solar chemical looping reforming.[78, 136, 167] However, methane conversion with ZnO was only 25% at 1273 K and required up to 1573 K to achieve nearly full conversion with severe carbon deposition observed.[168] This reduction was further demonstrated in a vortex flow solar reactor with a CH_4:ZnO feed ratio greater than 10:1 to maximize the more valuable Zn yields (83-100%), which led to low methane conversion.[78, 167]

Later, Kodama et al. compared the performance of WO_3, Fe_3O_4, ZnO, In_2O_3, SnO_2, V_2O_5 and MoO_2 with methane-driven reduction at 1173 K.[169] ZnO, In_2O_3 and SnO_2 showed phase transition towards gas or liquid upon reduction, and was considered not suitable for cycling. Among the rest, WO_3 provided a good combination of methane conversion (19%), syngas selectivity (55% for H_2 and 92% for CO) and capability for

water splitting. From there, Kodama et al. also conducted further studies of WO_3 with SiO_2, Al_2O_3 and ZrO_2 supports at 1273 K and observed the synergetic interaction between WO_3 and inert ZrO_2 that increased the methane conversion (40% to 70%), water conversion (7% to 30%) and H_2 selectivity (69% to 97%).[170] However, the support reduced CO selectivity (97% to 86%) and tungsten carbide (WC) was formed during reduction. 50 wt% WO_3/ZrO_2 was later investigated in a solar simulator up to 1350 K (Figure 1.10).[171] Despite high methane conversion (93%), the syngas selectivities were low (46% for H_2 and 71% for CO) and the water conversion was poor (< 20%), limiting its potential for achieving high efficiencies. Additionally, the formation of WC during reduction hinders the cycling lifetime of the material, as it is not thermodynamically favourable to split water below 1273 K.

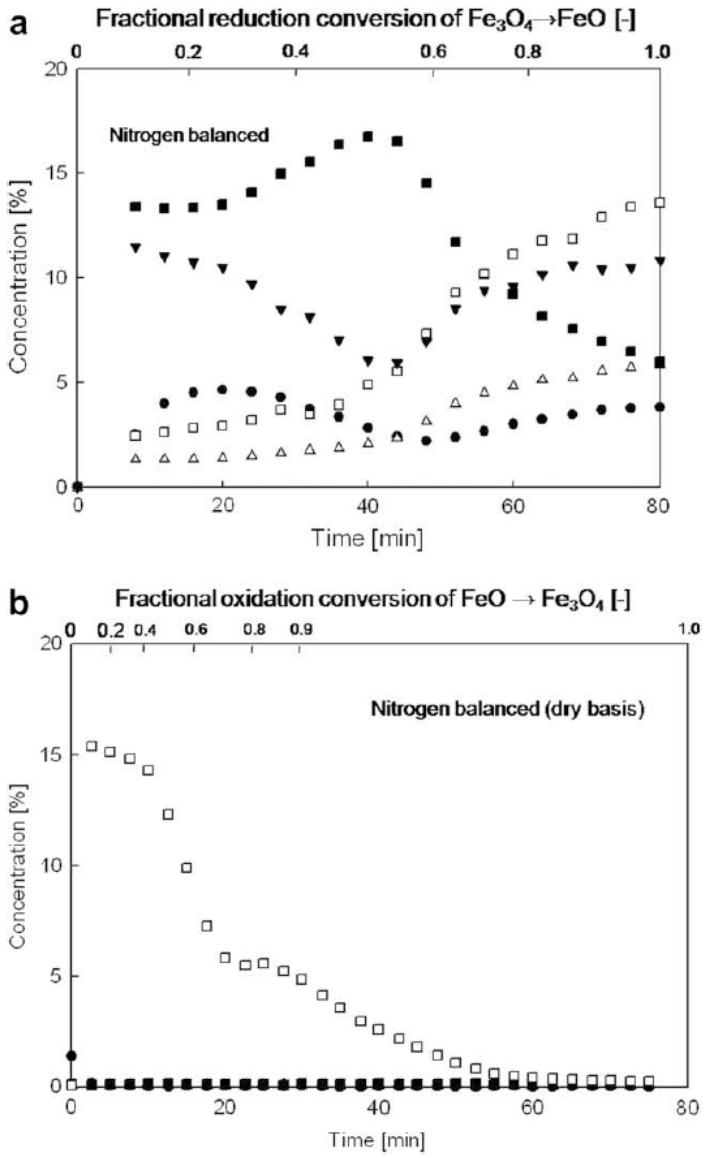

Figure 1.9 Gas concentration from the fluidized bed reactor (a) reducing with methane (C_{CH4} = 25%; U_g = 0.0287 m/s), (b) oxidizing with steam (C_{H2O} = 50%; U_g = 0.0402 m/s) of iron oxides at 1173 K, Δ: CO, ●: CO_2, ■: CH_4, □: H_2, ▼: H_2O.[144]

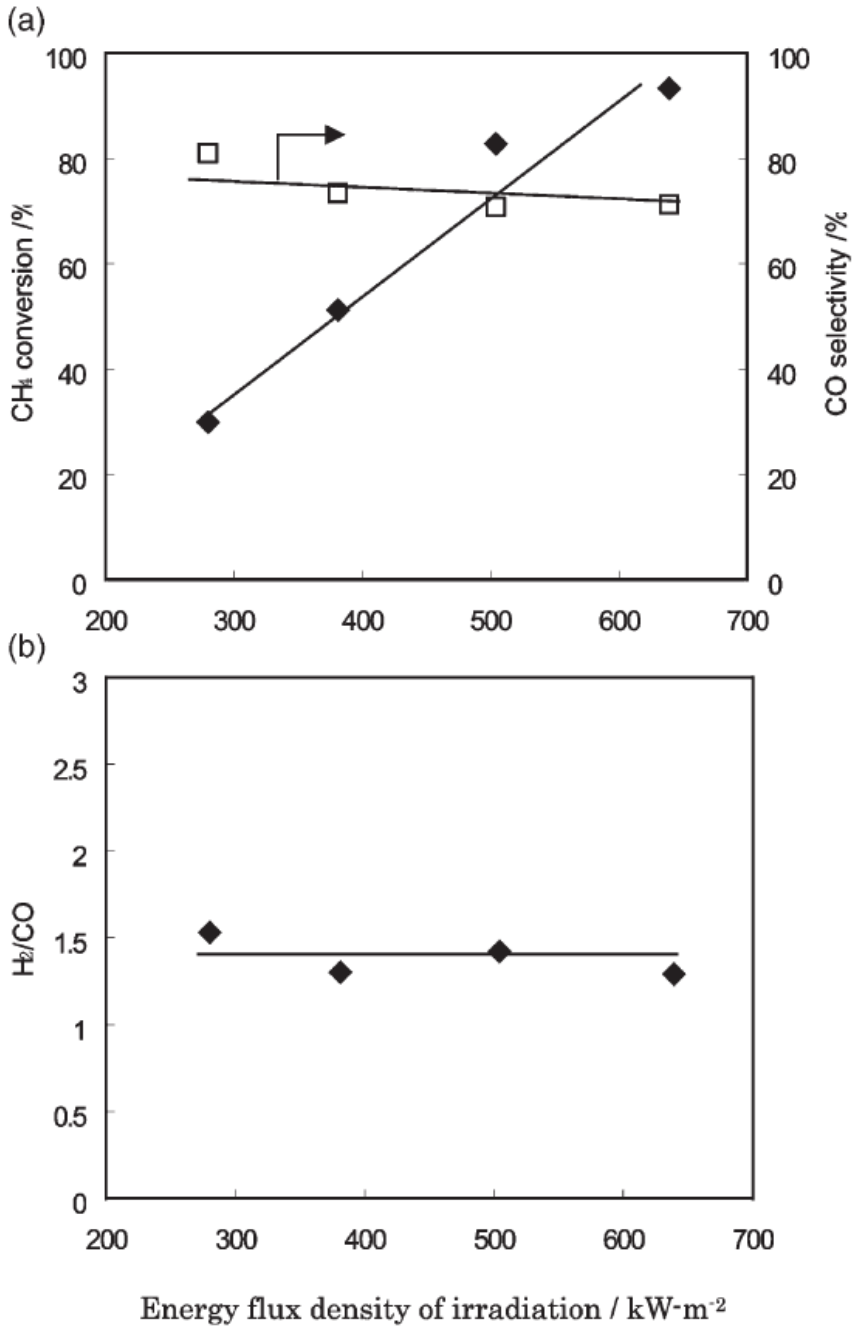

Figure 1.10 Variations of (a) methane conversion and CO selectivity, and (b) the H_2/CO ratio in the product syngas for the flux density of the solar-simulated, visible light of irradiation in the syngas-production process using a solar furnace simulator. 2 g of the WO_3/ZrO_2 catalyst was used. A 50% CH_4-N_2 gas mixture was fed to the light-irradiated catalyst at a flow rate of 12 Ncm^3 min^{-1} for 6 min. The residence time of the feed gas was set to 7.7 s.[171]

Similar to Fe, Mn oxides also have several merits such as toxic-free, low cost and potentially high oxygen exchange capacity. As a common first-row transition metal, Mn has several oxidation states: $MnO_2 \leftrightarrow Mn_2O_3 \leftrightarrow Mn_3O_4 \leftrightarrow MnO \leftrightarrow Mn$.[172] MnO_2 is the highest oxidation state of Mn, but it is not considered to be suitable in a solar reactor powered in a central tower receiver setup due to its decomposition in air at above 773 K. Similarly, Mn_2O_3 is thermodynamically not stable above 1173 K in air. Only Mn_3O_4 is the species stable in air at above 1073 K, limiting the redox pairs suitable for investigation in chemical looping applications. Mn oxides were initially investigated in chemical looping combustion but resulted in low reactivity towards methane. Mn-based oxygen carriers were further supported by TiO_2, Al_2O_3, SiO_2 and $MgAl_2O_4$, but yielded very limited success due to the formation of highly irreversible and unreactive phases.[173] The use of sepiolite as support showed low mechanical strength. When using ZrO_2 as support, the material showed good reactivity and stability over consecutive redox cycles. However, cracks were formed within the oxygen carrier structure as a consequence of thermal treatment and redox reactions.[172] The agglomeration of particles was also observed. To avoid these problems, further stabilisation by introducing MgO and CaO into the ZrO_2 support not only increased the reactivity of Mn oxides, but also inhibited the structural changes and particle agglomeration during redox cycles. These investigations, however, did not extend to oxidation of the reduced Mn-based oxygen carriers by water or carbon dioxide, mostly due to the unfavourable thermodynamics from MnO to Mn_3O_4.[58, 60, 174] Therefore, addressing this challenge by introducing low-cost Mn-based compounds that can overcome the thermodynamic barrier for oxidation will instate significant potential of Mn in solar chemical looping reforming.

Another transition metal Co was also considered in a few works for chemical looping applications. Co-based oxygen carriers have high oxygen exchange capacities, but the relatively high cost and environmental concerns generally make them less

attractive to other transition metal oxides.[175] During redox transformations, Co can have a few oxidation states including Co_3O_4, CoO and Co, among which Co_3O_4 is unstable above 1173 K and easily converted to CoO. Therefore, CoO/Co redox pair was considered in preliminary chemical looping studies but the results suggested unsatisfactory reactivity.[176] As such, TiO_2, MgO and Al_2O_3 were investigated as supports but suffered from strong interaction with CoO forming unreactive compounds, $CoTiO_3$, $Mg_{0.4}Co_{0.6}O$, and $CoAl_2O_4$, respectively. Yttrium-stabilised ZrO_2 demonstrated to be an effective support and increased the reactivity of Co oxide to methane while having a low tendency to carbon formation. However, so far Co-based oxygen carriers have not been reported to be effective in thermochemical H_2O or CO_2 splitting.

1.4.2 Ferrites and mixed metal oxides

To improve the redox performance and stability, Fe_3O_4 was further evaluated in various doping studies.[83, 164, 177-180] Kodama et al. investigated $M_{0.39}Fe_{2.61}O_4$ (M = Ni, Zn, Co) at 1173 K and found Ni-ferrite showed the highest methane conversion (31%) and syngas selectivities (75% for H_2 and 72% for CO).[164] ZrO_2-supported Ni-ferrite was further demonstrated up to 5 chemical looping reforming cycles (Figure 1.11).[164] The support suppressed sintering, improved methane conversion (> 90%) but decreased syngas selectivity (< 60% for H_2 and < 53% for CO).

Cha et al. investigated Cu-ferrites at 1173 K and observed that an increase in Cu content led to an increase in methane conversion and a composition of $Cu_{0.7}Fe_{2.3}O_4$ supported with ZrO_2 had the highest CO selectivity (Figure 1.12).[179] Compared to Fe_3O_4/ZrO_2, Cu-ferrite/ZrO_2 showed much higher carbon resistance, but the overall methane conversion (< 38%) and H_2 selectivity (< 72%) were lower. Similar study by Kang et al. with $CuFe_2O_4/ZrO_2$ achieved methane conversions of up to 83%, possibly due to much lower feed gas (CH_4) flow rate.[178] The syngas selectivities were in

agreement to those obtained by Kodama et al. As for the oxidizer conversion, so far the highest reported with ferrites is 22% demonstrated by Ni-ferrite in water splitting,[164] making them less competitive in solar chemical looping reforming process requiring high oxidizer conversion efficiency.

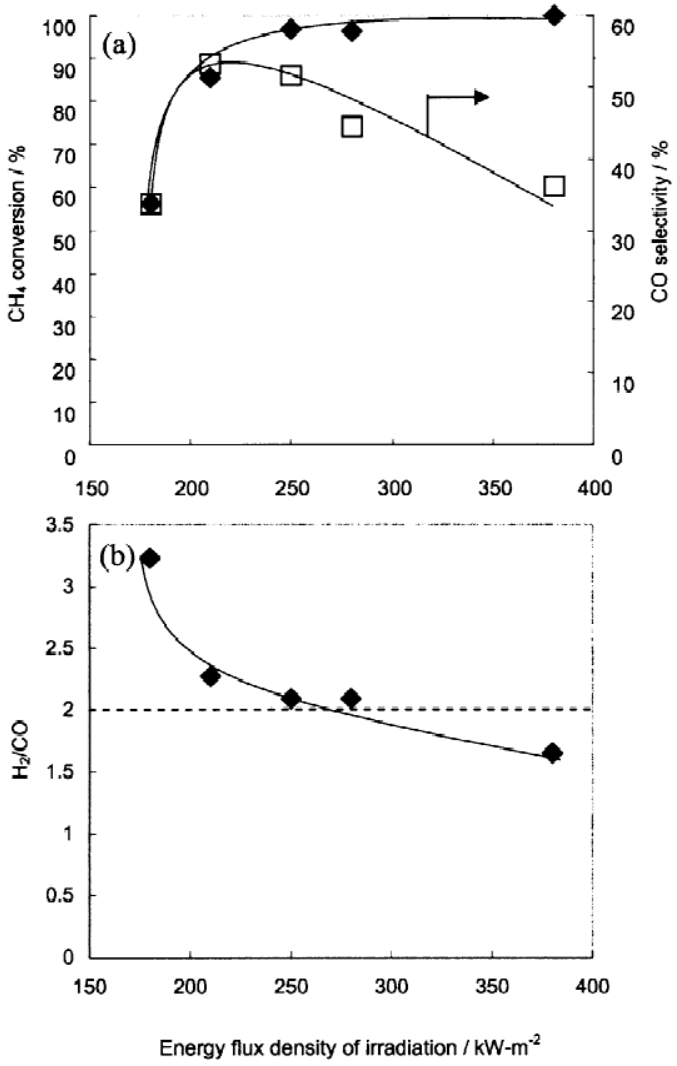

Figure 1.11 Variations of (a) methane conversion and CO selectivity, and (b) the H_2/CO ratio in the product syngas for the flux density of the solar-simulated, visible light of irradiation in the syngas-production process using a solar furnace simulator. 1.5 g of the $Ni_{0.39}Fe_{2.61}O_4/ZrO_2$ catalyst was used. A 52% CH_4-N_2 gas mixture was fed to the light-irradiated catalyst at a flow rate of 12 Ncm^3 min^{-1} for 6 min. The residence time of the feed gas was set to 7.7 s.[164]

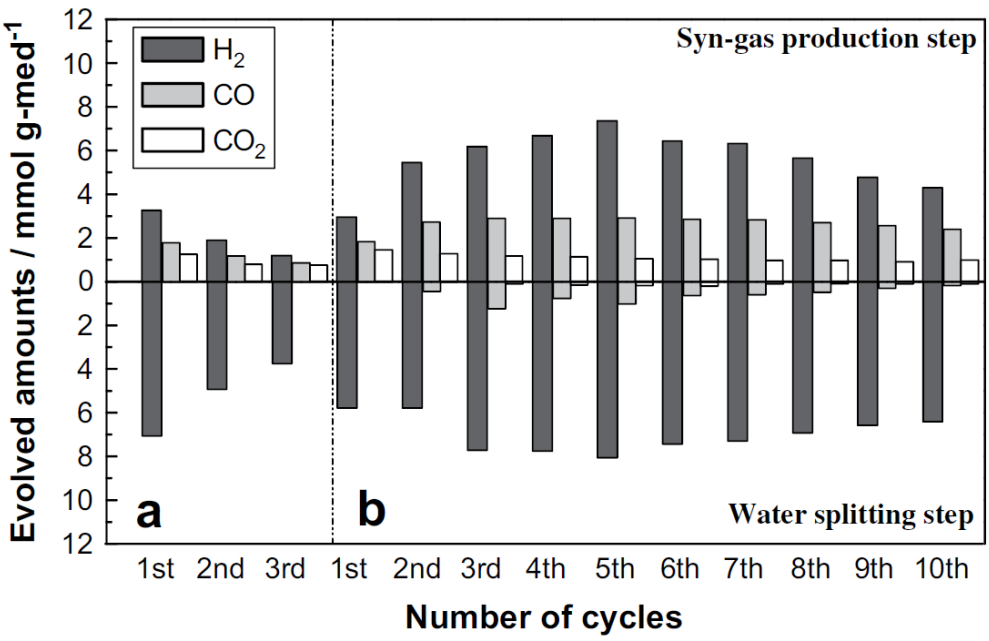

Figure 1.12 Variations in the amounts of evolved gaseous products in the repeated cyclic test for two-step methane reforming over (a) Fe-oxide/ZrO_2 and (b) $Cu_{0.7}Fe_{2.3}O_4/ZrO_2$. The reaction times were 56 min (a) or 104 min (b) for the syngas production step and 120 min for the water splitting step.[179]

Methane-driven reduction studies of mixed metal oxides including NiO, Fe_2O_3 and Mn_3O_4 yielded low syngas selectivity.[181] NiO-based oxides were reported to have higher methane conversion and syngas selectivity than Fe_2O_3-based mixed oxides.[166] Investigation of Ni-Cr-MgO oxides also yielded promising performance if carbon deposition can be mitigated.[182] These studies of mixed metal oxides, however, did not include H_2O or CO_2 splitting for oxidation.

1.4.3 Ceria-based metal oxides

Ceria and its doped counterparts are currently regarded as the benchmark metal oxides used in two-step solar thermochemical cycles with inert sweep gas or sub-atmospheric pressures to drive reduction, because of its capability to retain a stable cubic fluorite structure with a nonstoichiometry up to 0.25, and the extremely fast

kinetics of oxygen diffusion.[62-64, 66, 67, 71, 88, 104, 149-151, 155, 183-192] One of the most notable properties of ceria, however, is its thermodynamic and kinetic favourability towards H_2O or CO_2 splitting after reduction, which is a barrier that many candidate oxygen carriers still need to pass before becoming competitive. These beneficial characteristics of ceria were also confirmed to be significantly helpful in solar chemical looping reforming redox cycles.[93, 116, 132, 133, 135, 137, 139, 141, 147, 193-202]

Cerium (Ce), the second in the lanthanide series, is the most abundant element in the rare earth family, approaching levels of major metals such as Cu and Zn. It is also the first element in the periodic table to possess a ground state electron in a 4f orbital (Xe $4f^1 5d^1 6s^2$), which is responsible for its powerful redox behaviour when cycling between its two ionic states, Ce^{4+} (the Xe ground state) and Ce^{3+} (Xe $4f^1$). Ce^{4+} has an ionic radius of 0.97 Å, smaller than the less oxidized Ce^{3+} (1.14 Å).[203] In the ceria ($CeO_{2-\delta}$) lattice, the much lighter O^{2-} anion is much larger in ionic radius, 1.35 Å, than both of the cerium ions. In the ceria crystal, each cerium atom is bonded to eight oxygen atoms (eight-fold coordinated), while each oxygen atom is four-fold coordinated (Figure 1.13). The complete unit cell, Ce_4O_8 measures 5.1 Å on an edge, and is a face-centred cubic (fcc) fluorite lattice.[204]

Depending on the synthesis conditions, crystallites can be comprised of several or many unit cells. For example, a 1.1 nm particle, the smallest ceria nanoparticle theoretically possible would contain 8 unit cells (2×2×2).[205] The assessment of crystallite size is usually performed by analysis of an X-ray diffractogram and the use of the Scherrer equation.[206] Crystallites are the elementary building blocks for nanoparticles in general. Ceria nanoparticles can be either mono- or polycrystalline with the latter being more common. This leads to several descriptions of particle size, based upon the analytical method employed. X-ray diffraction (XRD) techniques can be

utilized to determine crystallite size, while transmission electron microscopy (TEM) can determine nanoparticle shape and constituent particle size. It is instructive to compare TEM geometric size to XRD crystallite size to obtain an estimate of the number of crystallites per particle. The hierarchal assembly of unit cells into crystallites and crystallites into particles can be extended even further by self-assembly (oriented attachment at particular surfaces) of particles into larger structures, such as rods, sheets, cubes and hollow or porous variants, which can vary in size within the 1–100 nm range. Additional polymorphs of ceria, such as nanowires, nanocubes, hollow plates, and tabular triangular grains have also been synthesized.[207-209] Theoretical models based on simulated crystallisation and self-assembly can be investigated to predict a variety of properties such as crystal strain. Crystal strain is the displacement of atoms from their equilibrium lattice positions that results in particle energy in excess of the equilibrium value. This strain energy can be exploited to modulate chemical reactivity (strain-tuneable reactivity).[210] The unique chemistry and commercial potential of these novel ceria structures is still an active area of research and development.

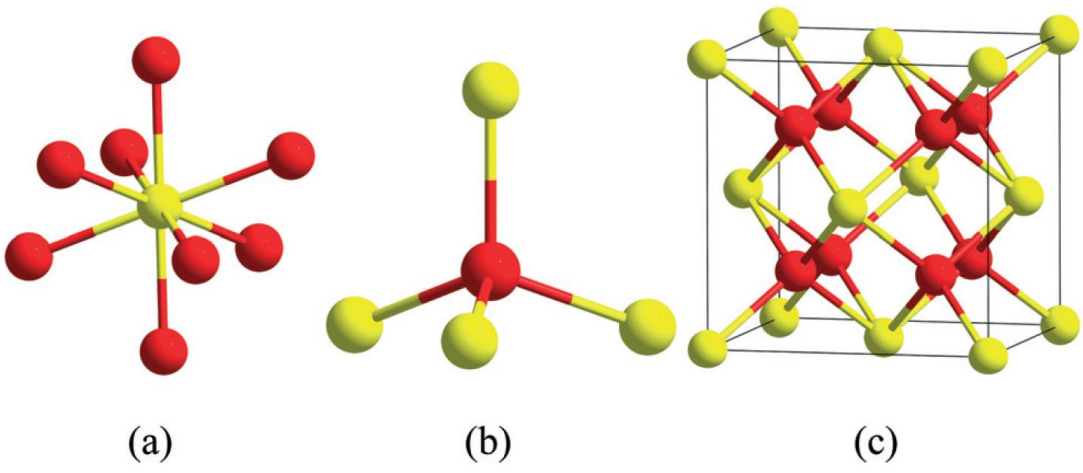

Figure 1.13 Structural analysis of ceria crystals and unit cells. Eight-fold coordinated cerium atoms (yellow) with four-fold coordinated oxygen atoms (red) in ceria crystals (a and b) and the primitive unit cell (c).[211]

Current studies have related the high redox capability of ceria to its labile lattice oxygen, or formation of oxygen vacancies. The concept of the oxygen vacancy is that of a missing oxygen atom (or atoms for a di or tri vacancy) in one or more of the eight octants in a ceria unit cell.[212] The oxygen vacancy can be quantified by a number called the oxygen storage capacity (OSC). This number is expressed as micromoles of oxygen liberated per gram of starting material. The OSC for molecular cerium dioxide (gas phase) is 1452.47 μmol O_2 g^{-1}. However, commonly used ceria is produced as micro- or nano-scale crystals and may only approach a fraction of the theoretically calculated OSC when fully reduced. Indeed, solid particle ceria can be thought of as an "oxygen buffer" that either provides or removes oxygen to/from the surrounding environment by responding to a lack or excess of oxygen in that environment.[204] Solar thermochemical cycles and chemical looping reforming utilizes this ability of ceria to reversibly extract oxygen atoms from the lattice for production of renewable fuels. Based on the OSC concept, atomistic simulations have predicted the topographical factors influencing surface activity in ceria. For instance, edges, steps and corners are generally more reactive than flat featureless planes. The activity also depends on microstructure and strain in the nanocrystals.

In addition to topographical features, nanoparticle size is also a critical parameter in determining particle reactivity. Unlike most nano-structures, nanoceria is unique in that the lattice expands as the particle becomes smaller. This lattice expansion leads to a decrease in oxygen release and reabsorption. Hailstone et al. explained that in smaller ceria nanocrystals, a larger fraction of the cerium atoms are in the fully reduced state, even though the ceria nanoparticles retain a cubic lattice, and not the predicted hexagonal lattice.[205] They further suggested that a nanoceria size of 2-3 nm, corresponding to a $Ce_{80}O_{160}$ particle, provides the maximum OSC. In such a configuration, 24 corner oxygen atoms on the (100) face[213] are only two and not four

coordinated to adjacent cerium atoms and are therefore quite labile. Vacancy formation from these 24 atoms would produce $CeO_{1.7}$ (and not $CeO_{1.5}$) as the lower practical limit, with an inherent OSC of 872.1 μmol O_2 g^{-1}. It is worth noting that this OSC is unlikely to be observed in practice as the OSC at this size is not limited by oxygen atom availability but perhaps by other factors such as the ability to accommodate only a certain number of reduced cerium atoms or co-located vacancies or perhaps energetics of formation of twelve corresponding reduced cerium atoms.

In light of ceria's complex physical and interesting properties, it is perhaps not surprising that numerous methods have been developed to synthesize these materials. Broadly speaking these synthetic methods can be categorized into two temperature regimes: lower temperatures here defined as less than 250 °C and higher temperature regimes that can extend to combustion, flame synthesis and even plasma arc temperatures that can reach several thousand degrees Celsius.[214]

The most numerous and commonly employed lower temperature wet-chemical synthetic methods for the production of nanoceria are: co-precipitation,[215, 216] hydrothermal,[217, 218] solvothermal,[209, 219] sol–gel,[220, 221] Pechini[88] (a modified sol–gel method using citric acid), micro emulsion and reversed micelle methods.[222, 223] These methods are favoured for small scale and research quantities of materials. Typically these techniques rely on a source of Ce^{3+} and an oxidant to convert the Ce^{3+} ion to the more insoluble Ce^{4+} ion, and one or more stabilizers, which may also play the dual role of both stabilizer and oxidizer.

Higher temperature processes for the production of ceria and doped ceria composition, such as the aerosol processes, can operate at very high combustion temperatures, 1000 to 2500 °C. These processes employ ceria precursors such as cerium alkoxide or carboxylate aerosols that are fed into a reaction chamber in a continuous

manner. Physical vapour synthesis represents another technique utilizing an argon plasma arc operating at several thousand degrees Celsius. At these very high temperatures, the direct synthesis of ceria provides very prismatic (i.e. sharp edges and corners), five to several thousand nm agglomerates. These stand in marked contrast to the particle morphologies produced at temperatures <250 °C, more commonly <100 °C where well-differentiated sub 5 nm spherical and star-like nanoparticles can be made.[224]

Calcination is a commonly employed high temperature technique for the industrial scale production of ceria in which the as-made cerium composition is not yet an oxide. This process involves high temperature treatment below the melting point of the material in an oxygen atmosphere. Particle size is usually controlled by gas phase temperature and velocity conditions.

The first study by Otsuka et al. suggested that reduction of ceria by methane can be kinetically limited.[133] This observation is supported by demonstrations showing increasing rates of syngas production with increased surface area. The reduction mechanism is suggested to proceed via a modified Mars-van Krevelen model,[133, 202, 225] as shown in Figure 1.14. At the initiation of the reduction, the production of CO_2 and H_2O is dominant as the surface adsorbed oxygen is abundant and chemisorbed carbon and hydrogen are readily oxidized to complete oxidation products. This leads to high methane conversions but low syngas selectivities at the initial stage. The surface adsorbed oxygen is depleting faster than it can be replenished by lattice oxygen, which diffuses from the bulk to the surface. The decrease of available surface oxygen leads to a decrease in methane conversion, but an increase in syngas selectivity. The rate of bulk lattice oxygen diffusion decreases as nonstoichiometry increases. When it is slower than methane dissociation, chemisorbed carbon starts to accumulate on the surface. Studies suggest that carbon deposition tends to occur when more than 80% of the available

oxygen has been consumed in the oxygen carrier.[132, 134, 139] During water splitting, oxidizer conversion is highest at the initiation of oxidation when the surface and bulk oxygen in ceria are depleted. As the oxygen vacancies in the lattice are filled and the surface and bulk oxygen become more abundant, the oxidizer conversion decreases.

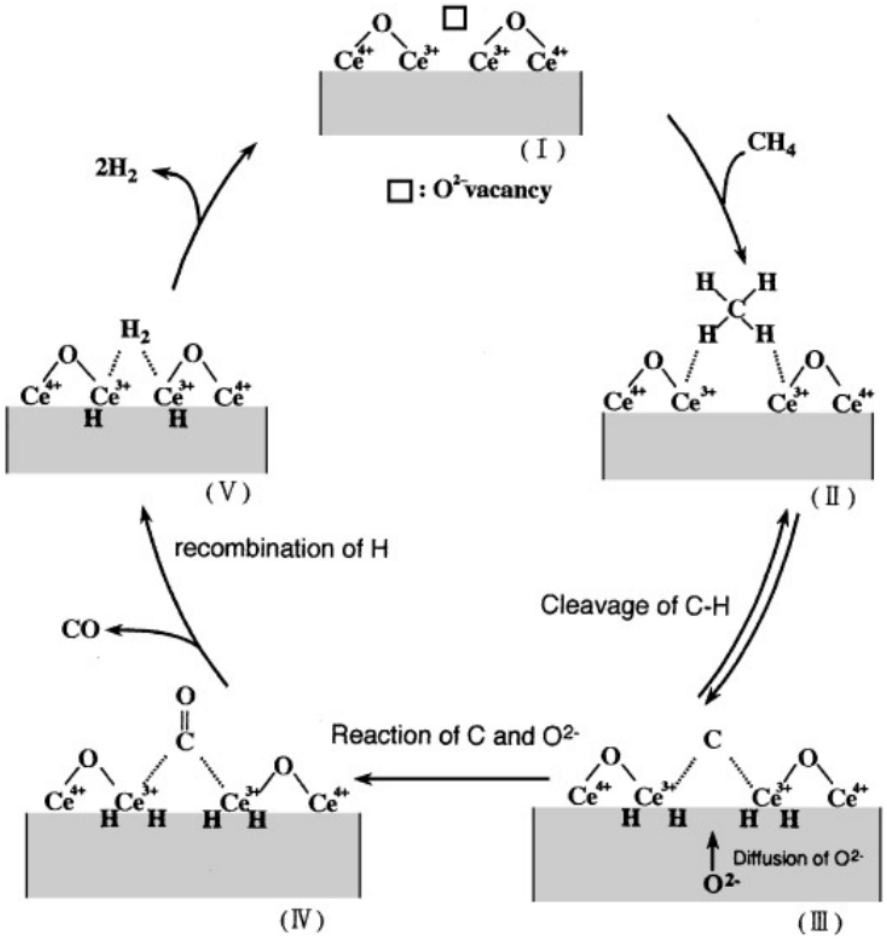

Figure 1.14 Reaction mechanism of ceria reduction by methane.[133]

The reaction mechanisms indicate that the morphology of ceria and operating conditions will influence feedstock (methane and oxidizer) conversions and syngas selectivity. Higher specific surface area and porosity are likely to yield higher rates of the surface reactions and higher methane and oxidizer conversions. However, so far morphology studies dedicated to ceria-based chemical looping reforming cycles are

scarce and further experimental evaluations are required to validate and quantify this hypothesis.[133, 135, 139, 226-229]

Thermodynamic studies suggest reduction of ceria by methane is viable at as low as 873 K with a high syngas selectivity of over 94%.[193] However, the kinetics at this low temperature range is limited, resulting in low methane conversion demonstrated by Ostuka et al.[132, 133, 193] Therefore, future studies have all shifted towards temperature range 250-400 K higher than the thermodynamic threshold, which is also more compatible to typical temperature outputs from central tower systems.[7] Recently, Krenzke et al. investigated the effect of temperature on methane conversion, syngas selectivity, and oxidizer conversion with fibrous ceria particles from 1173 K to 1273 K.[135] Modest improvements were observed for methane and oxidizer (CO_2) conversion as well as syngas selectivity by increasing the temperature. Carbon deposition was not significant until 1373 K. Additionally, by increasing the methane flow rate of 15 times, higher bed-average nonstoichiometries were obtained, leading to higher syngas selectivity and higher oxidizer conversion. However, methane conversion dropped significantly (20% to 2%). The trade-off to maintain high performance of all the key parameters (feedstock conversion and product selectivity) is a critical issue to be addressed in practical solar chemical looping reforming demonstrations. This trade-off is in agreement with the projected solar-to-fuel efficiencies measured by Krenzke et al. in Figure 1.15.[135] The highest projected efficiency at 1273 K is 27% for reduction in 5 mL min^{-1} g^{-1} CH_4, resulting in 25% methane conversion, 84% oxidizer conversion, 62% H_2 selectivity and 66% CO selectivity.

A parallel study was conducted by Warren et al. using 1.13 kg of ceria in a solar-simulated fixed bed reactor.[137] Solar chemical looping reforming with CO_2 was measured at 1393 K. Reduction was performed with 10 vol% methane diluted with Ar,

and achieved a methane conversion of 52%, H_2 selectivity of 83%, and CO selectivity of 59%. Due to high operating temperature, carbon deposition was significant (26%), and the subsequent CO_2 conversion was low (21%). The measured and projected efficiencies are shown in Figure 1.16. Warren et al. claimed that an efficiency of 7.5% could be reached if the full capacity of the reactor (equivalent to a loading of 15.8 kg ceria) can be utilized. Deviation of this projection from Krenzke et al. is tentatively attributed to operating with diluted methane, high thermal losses in the reactor prototype, and limited consideration of the performance trade-off when selecting operating temperature, feedstock flow rates and cycling times.

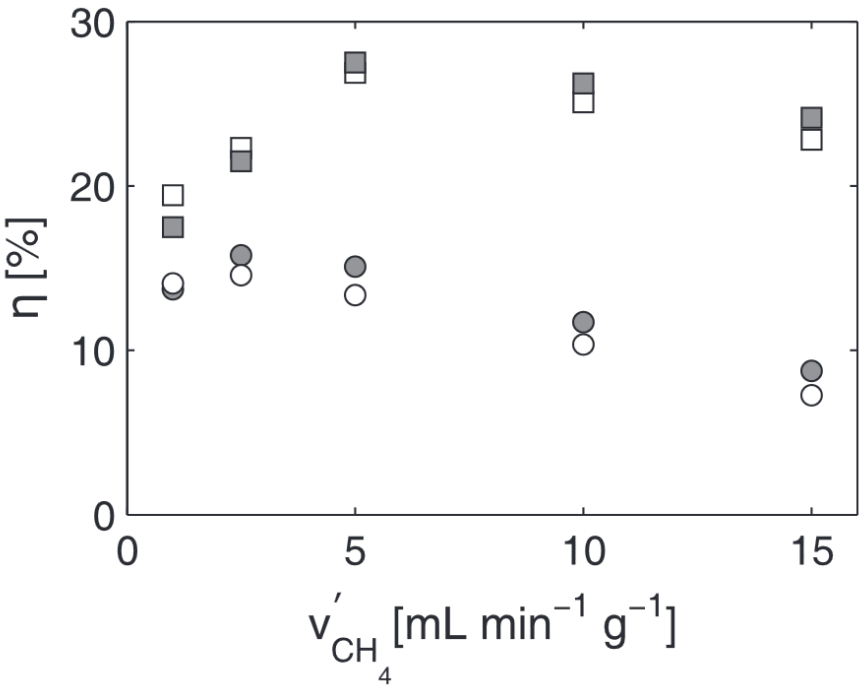

Figure 1.15 Efficiency as a function of methane flow rate for measured conversions and selectivities at 1173 K (circles) and at 1273 K (squares) with 5 mm (open symbols) and 1 mm (filled symbols) ceria particles.[135]

Catalyst-promoted ceria, such as Rh/CeO_2 or Pt/CeO_2, was demonstrated to be effective in improving methane conversion without much compromise to syngas selectivity or oxidizer conversion.[132, 133, 193, 201, 202] The catalysis is anticipated to occur

via a reverse spill-over mechanism in which H atoms trapped on Ce^{3+} spill over to a metal site where more facile recombination and/or desorption can be initiated.[133] Studies by Fathi et al. at 923 K suggest that Rh- and Pt-catalysed ceria can both improve methane conversion from 14% to 95%.[201] Rh also catalyses carbon deposition and has a lower CO selectivity than Pt. Oxidizer (CO_2) conversion achieved up to 100% at 873-973 K with Pt/CeO_2. However, the inhibiting factor is the cost associated with the precious metal catalysts that scales up quickly in an efficient commercial solar reactor requiring a mass loading of at least hundreds of kilograms of the materials.[10]

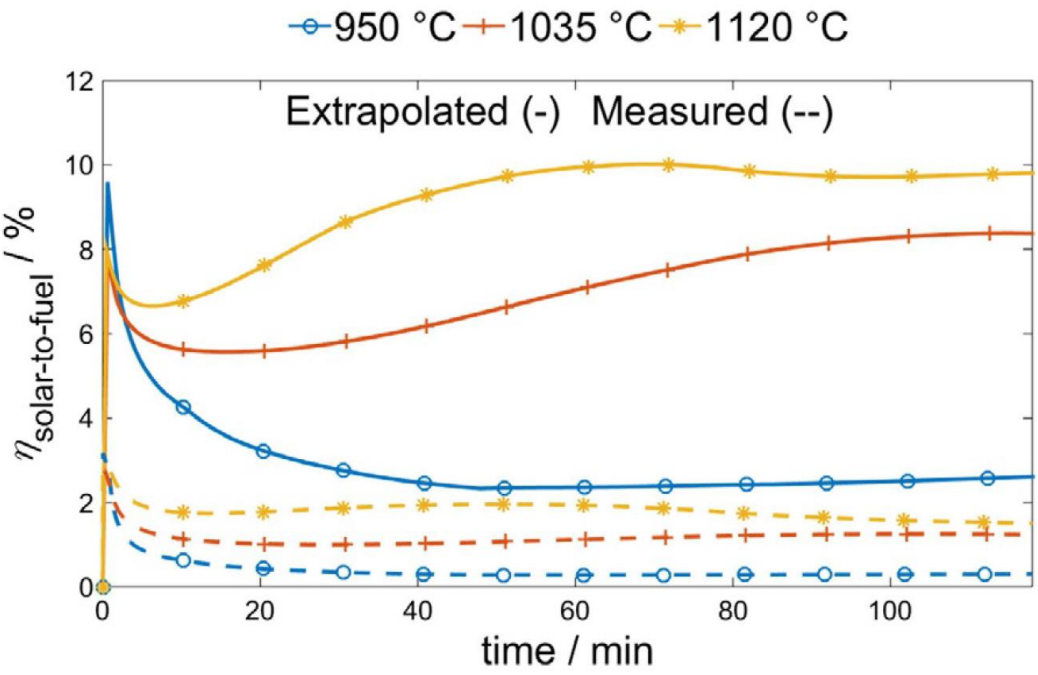

Figure 1.16 Extrapolated and measured solar-to-fuel efficiency as a function of time for each reduction test performed.[137]

Despite the fast redox kinetics, the nonstoichiometric reaction of ceria yields generally lower oxygen exchange capacity compared to stoichiometric materials, leading to lower syngas yields per cycle. Under this context, many doping studies were conducted aiming at improving the oxygen exchange capacity of ceria without detriment to its redox stability.[194, 195, 200, 230] Using Zr as a dophant by partially

substituting Ce^{4+} ions with Zr^{4+} ions in the ceria lattice has demonstrated to improve methane activity and stability of ceria. ZrO_2 has a similar fluorite structure that permits $Ce_{1-x}Zr_xO_2$ solid solutions with Zr^{4+} content up to 40%.[231] The synergetic interaction between Zr^{4+} and Ce^{4+} yields a decrease in oxygen vacancy formation enthalpy and entropy with increasing Zr content up to 20%.[232-234] However, according to the Evans-Polanyi principle, a reduction in the oxygen vacancy formation energies also leads to a reduction in the thermodynamic driving force for oxidation. Therefore, the performance of reported oxidizer splitting activities of $Ce_{1-x}Zr_xO_2$ is consistently lower than CeO_2. Otsuka et al. investigated the effect of Zr doping for methane partial oxidation at 973 K.[194] With a $Ce_{0.8}Zr_{0.2}O_2$ solid solution, syngas yields doubled compared to those of pristine CeO_2. The activation energy decreased from 137 kJ mol^{-1} for CeO_2 to 71 kJ mol^{-1} for $Ce_{0.8}Zr_{0.2}O_2$. Similar twofold increase in syngas yields was reported by Zhu et al. with a $Ce_{0.7}Zr_{0.3}O_2$ solid solution.[195] However, a decrease in H_2 selectivity and water splitting performance (Figure 1.17) was also observed. For Pt-catalysed $Ce_{1-x}Zr_xO_2$, Zr doping of up to 50% did not improve methane conversion but decreased syngas selectivity.[202]

Doping of up to 50% trivalent Fe^{3+} cations in CeO_2 also demonstrated improved methane conversion (Figure 1.18).[235] However, syngas selectivity decreases with increasing Fe content.[199, 229] Methane conversion and syngas selectivity were stable for $Ce_{0.7}Fe_{0.3}O_2$ and $Ce_{0.5}Fe_{0.5}O_2$ over 5-25 cycles. Samples with separate and poorly dispersed Fe and Ce phases with large crystal sizes produced by solid-phase synthesis exhibited lower methane conversion but higher syngas selectivity than samples prepared by hydrothermal and co-precipitation methods.[236, 237] Compared to Zr doping, Fe doping results in similar methane conversion but higher syngas selectivity and lower carbon deposition.[236] Co-doping of Zr and Fe provides a greater improvement in methane

conversion while maintaining or improving syngas selectivity.[226] However, its effect on oxidizer (H_2O or CO_2) conversion was not detailed.

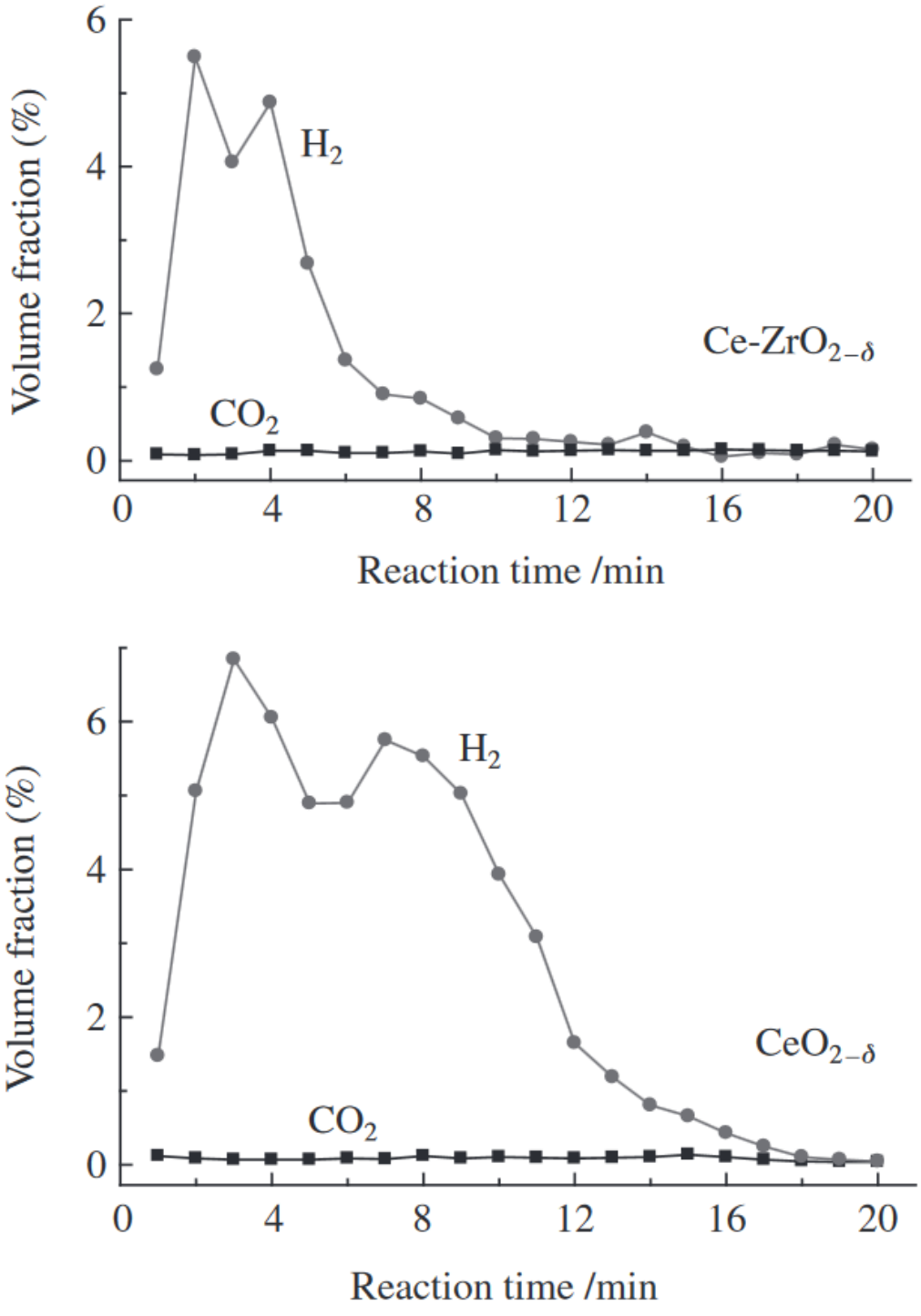

Figure 1.17 Product gas evolved volume fractions as a function of reaction time in the water splitting reaction over $CeO_{2-\delta}$ and $Ce\text{-}ZrO_{2-\delta}$ at 973 K.[195]

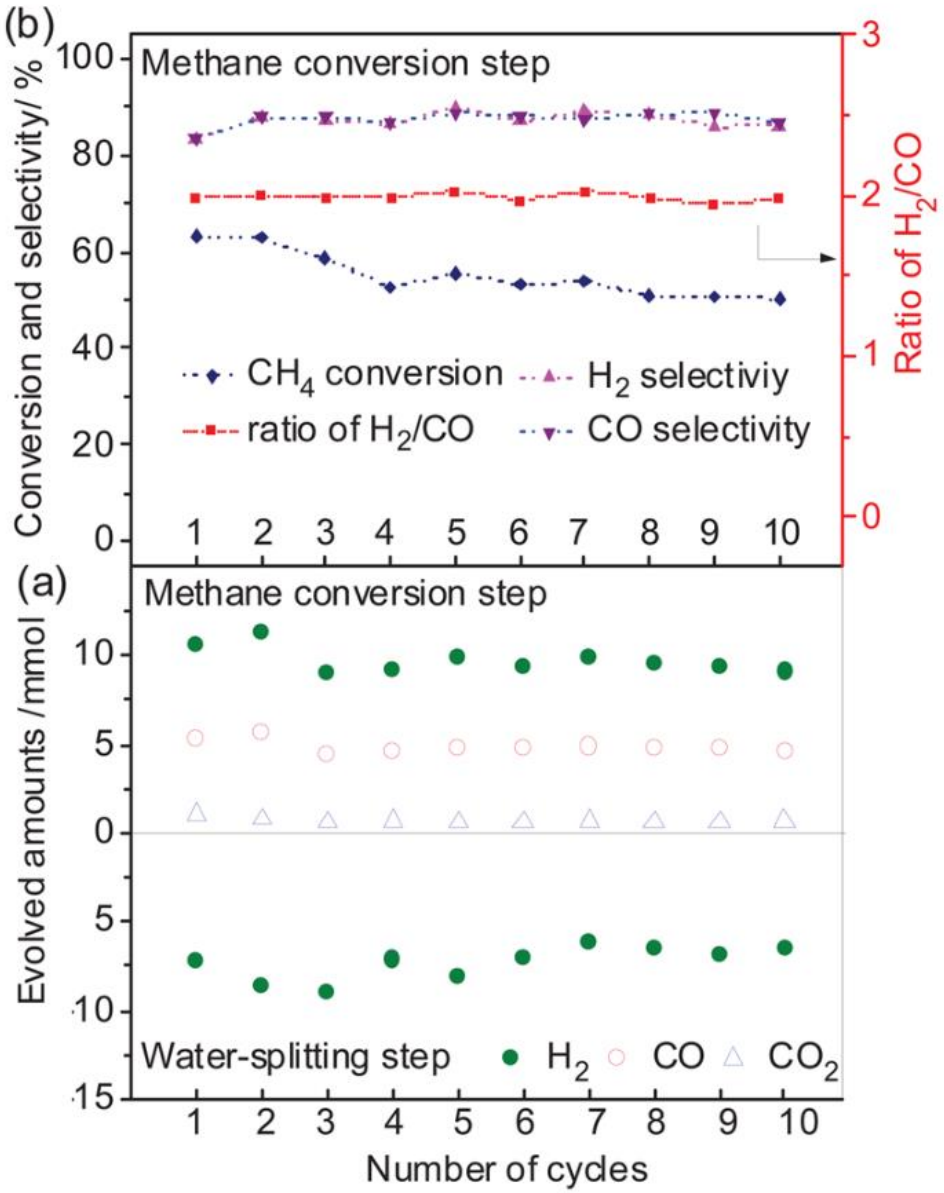

Figure 1.18 Amounts of syngas and hydrogen produced during the (a) chemical looping steam methane reforming redox process and (b) methane conversion performance over the CeO_2-Fe_2O_3 oxygen carrier at 1123 K.[235]

1.4.4 Perovskites

Perovskite denotes the class of compounds that have the same type of crystal structure explicitly expressed as $^{XII}A^{2+VI}B^{4+}X^{2-}{}_3$. Perovskite oxygen carriers generally have a cubic structure with a formula of ABO_3. The A-site ion is located on the corners of the lattice, usually from an alkaline earth or rare-earth element. The B-site ions are

located at the centre of the lattice, usually from 3d, 4d and 5d transition metal elements. These oxygen carriers exhibit excellent nonstoichiometric redox properties, high oxygen mobility, and high thermal stability. Many perovskites have been investigated for thermochemical redox cycles and chemical looping reforming, among which Fe or Mn based B-site perovskites attracted much attention because of their high syngas selectivity and methane conversion.[72, 90, 93, 96, 181, 228, 238-241] However, perovskites generally suffer from low re-oxidation capability by water or carbon dioxide due to unfavourable thermodynamics for the B-site cations to transform from trivalent (III) to tetravalent (IV) state.[239, 242]

$LaFeO_3$ was one of the first perovskites studied for chemical looping applications due to its high oxygen mobility in the bulk and the capability of hosting large concentrations of vacancies in the structure at elevated reaction temperatures.[238-240, 243] Being dependent on the operation temperature conditions, the removal of oxygen and the total amount of oxygen available for reduction by methane could lead to a reduction of $LaFeO_3$ from Fe^{3+} to Fe^{2+}, but further reduction appears to be inhibited. A kinetic study with respect to the removal of oxygen from $LaFeO_3$ reduction by CH_4 revealed a step-wise kinetic control intimately relevant to the availability of surface oxygen and vacancy site. Similar to ceria, initially the removal of oxygen generates vacancy sites on the surface, which helps to facilitate the progressing of the reaction. Subsequently, as the oxygen vacancy sites increase, diffusion of bulk lattice oxygen becomes the rate-limiting step. The maximum reaction rate for $LaFeO_3$ was found to be approximately half of the total amount of removable oxygen.[238]

The reaction mechanism which is highly dependent on mobile oxygen is usually accompanied by degradation of the structural properties of the perovskites. A morphology study by Zhao et al. with 3DOM (three-dimensionally ordered

macroporous) $LaFeO_3$ at 1123 K showed a structural deterioration after 10 cycles of chemical looping steam methane reforming (Figure 1.19), in which the specific area dropped by nearly 40%.[240] However, the average pore diameter almost remained unchanged. This is possibly caused by larger individual grains on the surface of the particles resulted from collapse of the 3DOM skeleton. The results are in agreement to prior studies of 3DOM ceria-based materials for thermochemical redox cycles driven by inert gas sweeping.[183] Sintering and loss of surface area is a concern even at 1100 K, which is detrimental to the kinetics of surface-limited gas-solid reactions (1.9) and (1.10).[139, 190, 191, 244]

$LaMnO_3$ was also found to be effective in chemical looping steam methane reforming cycles at 1273 K by Nalbandian et al. Methane conversion was 20% with a H_2 selectivity of 24% and CO selectivity of 42%, respectively, in pulse reaction experiments.[239] The subsequent H_2O splitting achieved conversions of up to 38%. However, structural evolution of the oxygen carriers during the redox cycles was not detailed in their studies.

Partial substitution of A- and B-site cations can be used to tailor the redox behaviour. Partial substitution of A-site cations in $La_{1-x}Sr_xBO_3$ (B = Fe, Mn) increases the availability of reactive oxygen, as the substitution causes electronic imbalance and requires a fraction of the B-site element to change between B^{3+} and B^{4+} and/or generation of oxygen vacancies in the lattice to compensate.[243, 245] The increase in Sr content generally leads to an increase in methane conversion and oxidizer conversion, but results in a loss of syngas selectivity.[181, 242, 246] Partial substitution of B-site Fe with aliovalent Co, Ni, Cu and Cr cations was also investigated.[239] Cr appears to be a promoting dophant that increased the methane and oxidizer conversion with H_2 selectivity of 90% for a Cr content of 10% and mixed with 5% NiO (Figure 1.20). For

$AMn_{1-y}Mn_yO_3$ (A = Ca, Ba), Ni and Fe B-site dophants increased methane conversion. Fe doping also helped increasing syngas selectivity for Fe content up to 25%.[241]

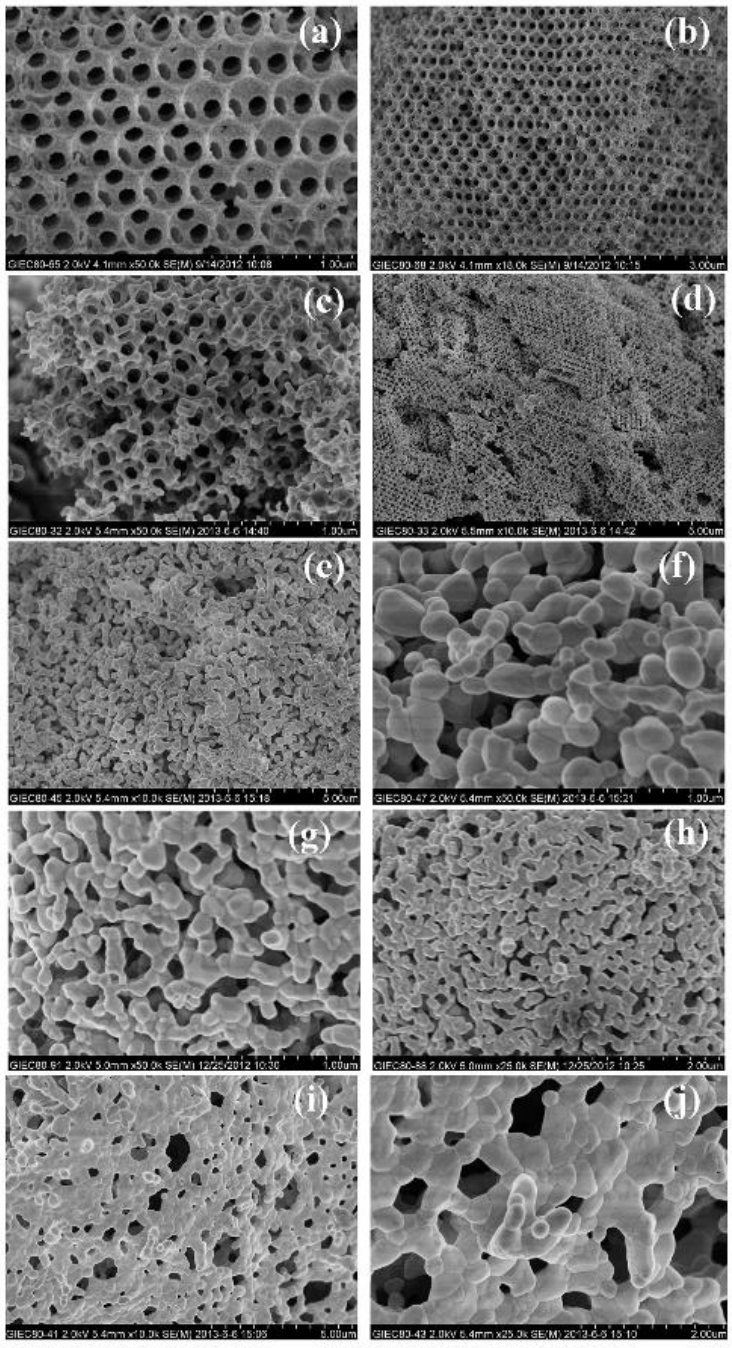

Figure 1.19 SEM images of $LaFeO_3$ (a) and (b): 3DOM-$LaFeO_3$, (c) and (d): 3DOM-$LaFeO_3$ after 1 cycle, (e) and (f): 3DOM-$LaFeO_3$ after 10 cycles, (g) and (h): nano-$LaFeO_3$, (i) and (j): nano-$LaFeO_3$ after 10 cycles.[240]

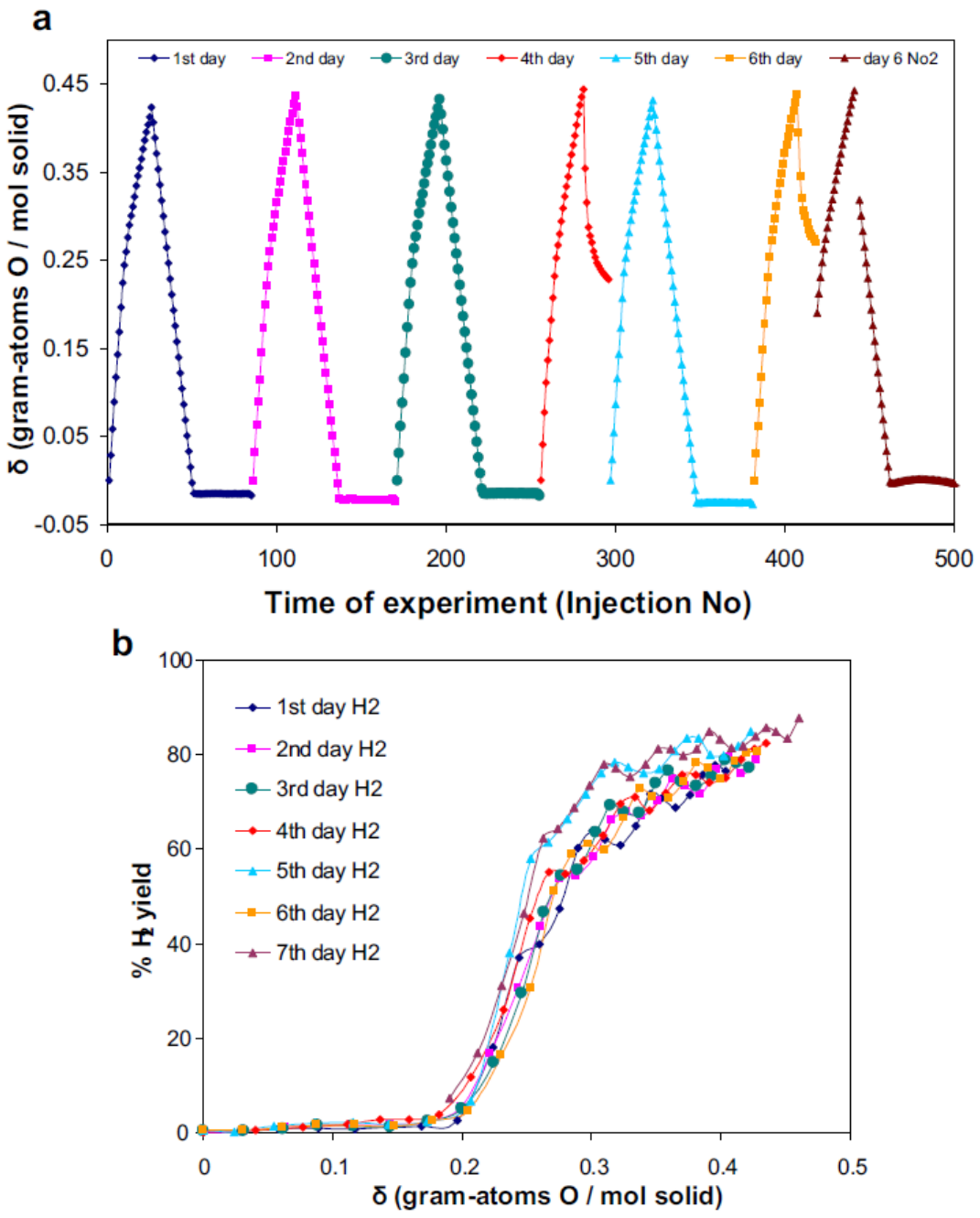

Figure 1.20 (a) Oxygen loss and uptake (b) H_2 yield vs. oxygen deficiency, during a 7 reduction-oxidation cycles stability experiment with the $La_{0.7}Sr_{0.3}Cr_{0.1}Fe_{0.9}O_3$ sample mechanically mixed with 5% NiO. Oxidation steps in 1st, 2nd, 3rd, 5th and 7th cycles with air pulses, 4th and 6th cycles with water pulses.[239]

Nevertheless, in reference to the demonstration of chemical looping reforming processes, the re-oxidation of perovskite materials by H_2O or CO_2 yields generally

lower oxidizer conversion and their long-term cyclic stability has not been explicitly reported.[228, 239, 247]

1.5 Flame spray pyrolysis

Flame spray pyrolysis (FSP) process is a well-established and versatile technique for synthesis of nanostructured materials with advanced functionalities. In FSP, the exclusive use of highly exothermic liquid precursors (mixtures of metal precursors and organic solvents) enables self-sustaining flames with temperatures up to 2500 °C.[248-250] At the same time, the high gas velocities of the FSP induce radial entrainment of surrounding gas.[251] Coupled with the radiation heat loss, this gives rise to extremely short residence times (milliseconds) with high temperature gradients (170 K cm^{-1}) along the flame axis.[249] The interplay between high temperature and large temperature gradient is one of the most important features in FSP: the high local temperature promotes the formation of homogeneous and highly crystalline materials and also promotes particle growth by sintering and coalescence,[248] while the large temperature gradient (and short residence time) preserves the nanoscale feature of the particles. This enables the synthesis and fine-tuning of complex metal oxide morphologies such as anatase TiO_2,[252] partially segregated $Si:SnO_2$,[253] and tailored $Sn_{1-x}Ti_xO_2$ solid solutions.[254]

Selection of metal precursors and solvents with suitable combustion enthalpies, melting/decomposition temperatures, miscibility and chemical stability are intrinsic to the overall particles formation in the flame, which in turn determines the resultant particle properties. The common formulations of FSP precursors are based on solid nitrates,[255, 256] acetates[257, 258] and acetylacetonates.[259, 260] Many of these precursors are economical and readily available commercially, and they can yield homogeneous morphologies comprising of fine and dense particles. The low combustion enthalpy of

some of these precursors coupled with their high melting/decomposition points can be disadvantageous, but some of these disadvantages can be circumvented by implementing the right processing conditions.

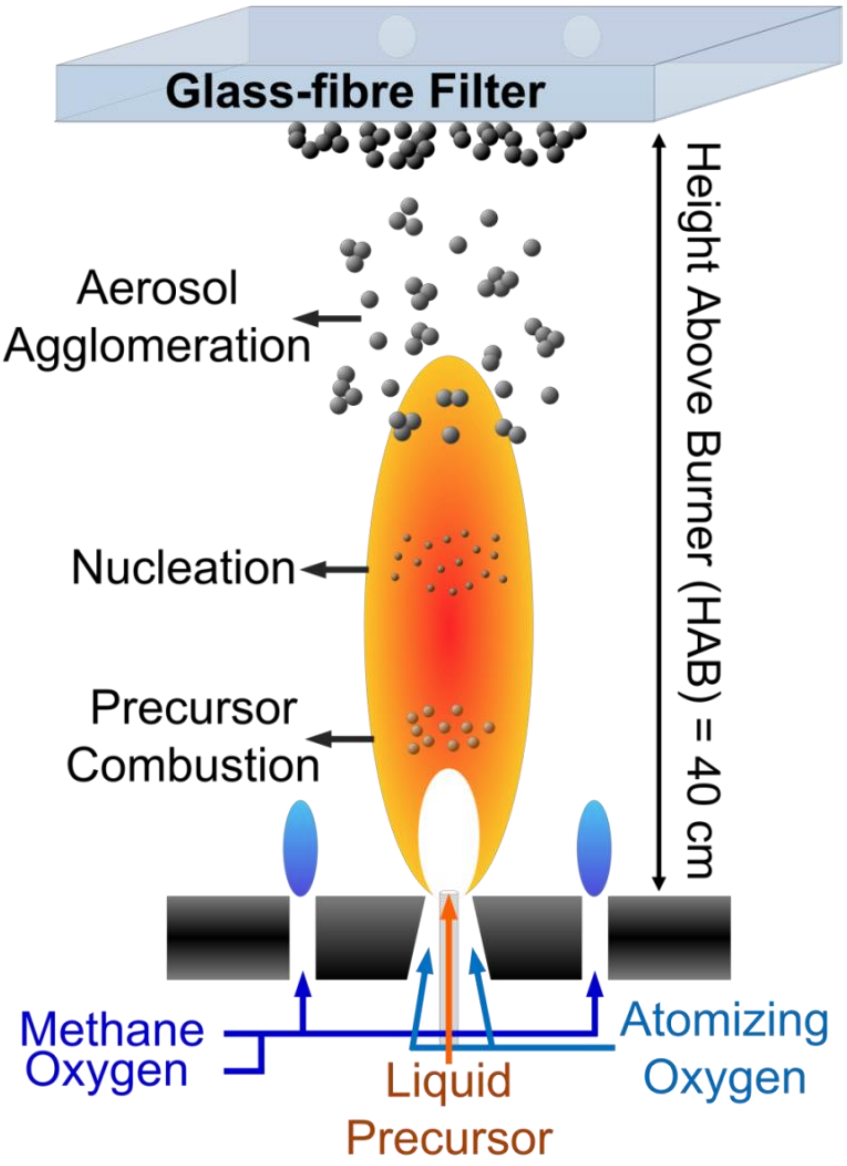

Figure 1.21 Schematic of nanoparticle synthesis by flame spray pyrolysis.[261]

The sequential stages of nanoparticle formation in FSP is illustrated in Figure 1.21. These stages consist of: (1) precursor spray evaporation/decomposition forming metal vapour; (2) nucleation as a result of supersaturation; (3) growth by coalescence and sintering; and (4) particles aggregation (forming hard agglomerates by chemical bonds) and agglomeration (forming soft agglomerates by mainly physical bonds).[262]

FSP introduces many key features and properties into the particles that other synthesis techniques may not. First of all, it is efficient, low-cost and scalable.[263-265] Liu et al. demonstrated the use of flame spray pyrolysis, to produce one-step highly pure, spinel-like Mn_3O_4 (hausmannite) nanoparticles with controllable specific surface area.[266] The enhanced surface activity introduced by FSP enabled the flame-made manganese oxide powders to exhibit an order of magnitude higher mole-specific turnover frequency than commercial nanocrystalline manganese catalysts in water oxidation tests. Secondly, the high temperature formation in the flame provides high thermal stability of the as-prepared particles as compared to other lower temperature wet techniques.[257, 267] Thirdly, highly crystalline nanoparticles are often produced by FSP, as induced by the high flame temperature crystallisation.[268, 269] Moreover, for systems where general homogeneous mixing between multiple components at intra-particle level are preferred and depending on the states as well as their nature of mixing, a wide variety of configurations could be achieved, ranging from substitutionally doped systems, solid solutions, dispersed mixed oxides, complex metal oxides (perovskite, spinel, etc.) to metal alloys. Such particle configuration is exclusive to highly miscible multi-elements. The bottom-up synthesis and high synthesis temperature in FSP can be advantageous in enhancing substitutional dopant concentrations, while its steep temperature gradient and short residence time prevent segregation of the dopants.[270] A classic example of perfect solid solutions by FSP is that of $Ce_xZr_{1-x}O_2$, which was obtainable when using high boiling point solvents to ensure good distribution of precursor in the flame.[267] Recently, FSP has also been applied to the one-step synthesis of tailored $LiMn_2O_4$ particles demonstrating potential for large-scale ultrafine manganese-oxide production.[266] A major advantage is that flame-made primary particles are usually quasi-spherical, and the crystal structure and size can be separately controlled by process parameters such as flame enthalpy and dopants.[271, 272]

1.6 Aim and scope of thesis

In the preceding chapters, the cycle mechanisms of solar chemical looping dry/steam reforming for the production of syngas in the view of the oxygen carriers are explored. Previous research of various transition metal oxides with particular focus on their oxygen exchange capacity and kinetics have been elucidated in the previous section. The cyclic redox performance of the oxygen carriers has been significantly improved over the last decades. Structural engineering played a vital role in the enhancement of syngas production rates and yields of practically all oxygen carriers. Nevertheless, the search of efficient, low-cost and sustainable metal oxides for solar chemical looping reforming still remains a challenge. The swift transition of this technology into the global market to supply reliable and renewable fuels is, on a large part, reliant on the robustness and scalability of such metal oxides and their structural engineering. Strict and consensual criteria to manifest the efficiency of the oxygen carriers also require further development in the community of concentrated solar fuels. Under this context, the aim of this thesis is to improve the benchmark standards of syngas production performance via selected metal oxides which are structurally engineered either by various facile synthesis methods or by effective lattice cationic substitution.

In Chapter 2, four distinct nano-micro structured ceria (CeO_2) powders were investigated in 10 cycles of chemical looping dry methane reforming, namely high specific surface area flame-made and flower-like nano-structured agglomerates, sol-gel sub-micro grains and commercial micro agglomerates. In particular, the synthetic techniques of choice, the physicochemical composition of the resulting powders, detailed characterization of their structural evolution and their associated syngas production performance were evaluated. The nanoparticles synthesized from flame

spray pyrolysis proved to be a highly efficient structure for chemical looping dry methane reforming, which is showcased by its highest H_2 and CO production rates and redox capacity while exhibiting lowest extent of structural deterioration upon cycling among the investigated structures. Key structural parameters determined here, including high specific surface area, low grain density and large mesopore size, provided a robust set of criteria to engineer efficient materials for enhanced high-temperature thermochemical solar fuel production.

In Chapter 3, more efficient redox pair MnO/Mn_7C_3 was developed. This was achieved by incorporating fractional amount of cerium ions in manganese oxide that enables its fast reduction to manganese carbide with an extraordinary theoretical oxygen exchange capacity of one mole of oxygen per mole of manganese. Thereafter, the significant oxidation enthalpy of the carbide was utilized to drive the CO_2 splitting reaction and achieved record high CO yields. The robustness of this Ce-promoted redox pair was consecutively tested over 46.7 hours in 100 redox cycles and revealed the repeated facile diffusion of cerium ions in an out of the host lattice in harsh thermochemical conditions. This is the first utilization of a metal oxide-carbide redox cycle in chemical looping reforming via a low-cost earth-abundant material and tentatively promises for large-scale synthesis of solar fuels via thermochemical routes.

In Chapter 4, the redox strategy to incorporate cerium ions into the Mn-based oxygen carrier was further investigated over a series of 20-cycle chemical looping steam methane reforming experiments over a broad spectrum of Ce:Mn content ratios. The fractional 3% Ce content was particularly highlighted due to its distinctively fast H_2 and CO production rates that resulted in extraordinary high yields at a commercially relevant temperature of 1173 K. Structural characterisation was carried out to

understand the role of cerium ions in activating the Mn-based oxygen carrier for its fast and reversible oxygen/carbon diffusion.

Chapter 5 represents the summary of these findings as well as their contribution to the field of solar chemical looping reforming and, in a larger sense, concentrated solar fuels. The future prospects of this field and its implication in the coming years are briefly discussed.

1.7 References

1. C. Agrafiotis, H. von Storch, M. Roeb and C. Sattler, *Renew. Sust. Energ. Rev.*, 2014, **29**, 656-682.
2. T. Kodama and N. Gokon, *Chem. Rev.*, 2007, **107**, 4048-4077.
3. A. Steinfeld, *Solar Energy*, 2005, **78**, 603-615.
4. C. Agrafiotis, M. Roeb and C. Sattler, *Renew. Sust. Energ. Rev.*, 2015, **42**, 254-285.
5. A. Steinfeld and R. Palumbo, *Encyclopedia of physical science and technology*, 2001, **15**, 237-256.
6. D. A. Wood, C. Nwaoha and B. F. Towler, *J. Nat. Gas Sci. Eng.*, 2012, **9**, 196-208.
7. R. Bader and W. Lipiński, in *Advances in Concentrating Solar Thermal Research and Technology*, ed. L. R. Santigosa, Woodhead Publishing, 2017, pp. 403-459.
8. J. R. Rostrup-Nielsen, *Catal. Today*, 2002, **71**, 243-247.
9. J. R. Rostrup-Nielsen, *Catal. Today*, 1993, **18**, 305-324.
10. P. T. Krenzke, J. R. Fosheim and J. H. Davidson, *Sol. Energy*, 2017, **156**, 48-72.
11. L. Protasova and F. Snijkers, *Fuel*, 2016, **181**, 75-93.
12. M. C. Tang, L. Xu and M. H. Fan, *Appl. Energ.*, 2015, **151**, 143-156.

13. C. L. Muhich, B. D. Ehrhart, I. Al-Shankiti, B. J. Ward, C. B. Musgrave and A. W. Weimer, *WIREs Energy Environ.*, 2016, **5**, 261-287.

14. J. R. Scheffe and A. Steinfeld, *Mater. Today*, 2014, **17**, 341-348.

15. R. J. Carrillo and J. R. Scheffe, *Sol. Energy*, 2017, **156**, 3-20.

16. K. Li, H. Wang and Y. Wei, *J. Chem.*, 2013, **2013**, 8.

17. G. Voitic and V. Hacker, *RSC Adv.*, 2016, **6**, 98267-98296.

18. Z. Wang, R. R. Roberts, G. F. Naterer and K. S. Gabriel, *Int. J. Hydrog. Energy*, 2012, **37**, 16287-16301.

19. R. E. Blankenship, D. M. Tiede, J. Barber, G. W. Brudvig, G. Fleming, M. Ghirardi, M. R. Gunner, W. Junge, D. M. Kramer, A. Melis, T. A. Moore, C. C. Moser, D. G. Nocera, A. J. Nozik, D. R. Ort, W. W. Parson, R. C. Prince and R. T. Sayre, *Science*, 2011, **332**, 805-809.

20. M. G. Walter, E. L. Warren, J. R. McKone, S. W. Boettcher, Q. Mi, E. A. Santori and N. S. Lewis, *Chem. Rev.*, 2010, **110**, 6446-6473.

21. K. Zeng and D. Zhang, *Prog. Energy Combust. Sci.*, 2010, **36**, 307-326.

22. O. Khaselev and J. A. Turner, *Science*, 1998, **280**, 425-427.

23. M. C. Hanna and A. J. Nozik, *J. Appl. Phys.*, 2006, **100**, 074510.

24. G. J. Conibeer and B. S. Richards, *Int. J. Hydrog. Energy*, 2007, **32**, 2703-2711.

25. L. Moens, D. M. Blake, D. L. Rudnicki and M. J. Hale, *J. Sol. Energy Eng.*, 2003, **125**, 112-116.

26. G. P. Smestad and A. Steinfeld, *Ind. Eng. Chem. Res.*, 2012, **51**, 11828-11840.

27. M. D. Archer and J. R. Bolton, *J. Phys. Chem.*, 1990, **94**, 8028-8036.

28. T. Markvart and P. T. Landsberg, *Physica E Low Dimens. Syst. Nanostruct.*, 2002, **14**, 71-77.

29. T. Hisatomi, J. Kubota and K. Domen, *Chem. Soc. Rev.*, 2014, **43**, 7520-7535.

30. A. Currao, *CHIMIA Int. J. Chem.* 2007, **61**, 815-819.

31. C. GRIMES, O. VARGHESE and S. RANJAN, *Light, water, hydrogen: the solar generation of hydrogen by water photoelectrolysis*, Springer Science & Business Media, 2007.

32. L. Vayssieres, *On solar hydrogen and nanotechnology*, John Wiley & Sons, 2010.

33. Y. Lijun and L. W. Woon-Fong, *Adv. Mater.*, 2011, **23**, 4559-4562.

34. K. Maeda and K. Domen, *J. Phys. Chem. Lett.s*, 2010, **1**, 2655-2661.

35. N. Fu, X. Tang and D. Li, *Appl. Phys. Lett.*, 2012, **100**, 093901.

36. S. Licht, B. Wang, S. Mukerji, T. Soga, M. Umeno and H. Tributsch, *J. Phys. Chem. B*, 2000, **104**, 8920-8924.

37. S. K. Mohapatra, M. Misra, V. K. Mahajan and K. S. Raja, *J. Phys. Chem. C*, 2007, **111**, 8677-8685.

38. R. Solarska, R. Jurczakowski and J. Augustynski, *Nanoscale*, 2012, **4**, 1553-1556.

39. S. H. Park, A. Roy, S. Beaupré, S. Cho, N. Coates, J. S. Moon, D. Moses, M. Leclerc, K. Lee and A. J. Heeger, *Nat. Photonics*, 2009, **3**, 297.

40. Y. Tachibana, L. Vayssieres and J. R. Durrant, *Nat. Photonics*, 2012, **6**, 511.

41. S. Chen and L.-W. Wang, *Chem. Mater.*, 2012, **24**, 3659-3666.

42. M. Grätzel, *J. Photochem. Photobiol. C Photochem. Rev.*, 2003, **4**, 145-153.

43. H. Hidehisa, O. Naoko, I. Takanori, M. Hiroshige and I. Tatsumi, *Angew. Chem. Int. Ed.*, 2006, **45**, 1420-1422.

44. A. Fujishima and K. Honda, *Nature*, 1972, **238**, 37.

45. A. Singh and L. Spiccia, *Coord. Chem. Rev.*, 2013, **257**, 2607-2622.

46. M. D. Kärkäs, O. Verho, E. V. Johnston and B. Åkermark, *Chem. Rev.*, 2014, **114**, 11863-12001.

47. A. Kudo and Y. Miseki, *Chem. Soc. Rev.*, 2009, **38**, 253-278.

48. C. Graves, S. D. Ebbesen, M. Mogensen and K. S. Lackner, *Renew. Sust. Energ. Rev.*, 2011, **15**, 1-23.

49. C. Perkins and A. W. Weimer, *Int. J. Hydrog. Energy*, 2004, **29**, 1587-1599.

50. N. Piatkowski, C. Wieckert, A. W. Weimer and A. Steinfeld, *Energy Environ. Sci.*, 2011, **4**, 73-82.

51. P. v. Zedtwitz and A. Steinfeld, *Energy*, 2003, **28**, 441-456.

52. M. Romero and A. Steinfeld, *Energy Environ. Sci.*, 2012, **5**, 9234-9245.

53. A. Kogan, E. Spiegler and M. Wolfshtein, *Int. J. Hydrog. Energy*, 2000, **25**, 739-745.

54. A. J. Traynor and R. J. Jensen, *Ind. Eng. Chem. Res.*, 2002, **41**, 1935-1939.

55. P. Christopher and W. A. W., *AlChE J.*, 2009, **55**, 286-293.

56. S. Abanades, P. Charvin, G. Flamant and P. Neveu, *Energy*, 2006, **31**, 2805-2822.

57. G. F. Naterer, K. Gabriel, Z. L. Wang, V. N. Daggupati and R. Gravelsins, *Int. J. Hydrog. Energy*, 2008, **33**, 5439-5450.

58. P. B. Kreider, H. H. Funke, K. Cuche, M. Schmidt, A. Steinfeld and A. W. Weimer, *Int. J. Hydrog. Energy*, 2011, **36**, 7028-7037.

59. S. Kasahara, S. Kubo, R. Hino, K. Onuki, M. Nomura and S.-i. Nakao, *Int. J. Hydrog. Energy*, 2007, **32**, 489-496.

60. T. M. Francis, P. R. Lichty and A. W. Weimer, *Chem. Eng. Sci.*, 2010, **65**, 3709-3717.

61. R. Gill, E. Bush, P. Haueter and P. Loutzenhiser, *Rev. Sci. Instrum.*, 2015, **86**, 125107.

62. W. C. Chueh, C. Falter, M. Abbott, D. Scipio, P. Furler, S. M. Haile and A. Steinfeld, *Science*, 2010, **330**, 1797-1801.

63. J. Lapp, J. H. Davidson and W. Lipiński, *Energy*, 2012, **37**, 591-600.

64. R. Bader, L. J. Venstrom, J. H. Davidson and W. Lipinski, *Energ. Fuel*, 2013, **27**, 5533-5544.

65. C. L. Muhich, B. W. Evanko, K. C. Weston, P. Lichty, X. Liang, J. Martinek, C. B. Musgrave and A. W. Weimer, *Science*, 2013, **341**, 540-542.

66. D. Marxer, P. Furler, M. Takacs and A. Steinfeld, *Energy Environ. Sci.*, 2017, **10**, 1142-1149.

67. I. Ermanoski, J. E. Miller and M. D. Allendorf, *PCCP*, 2014, **16**, 8418-8427.

68. M. Lange, M. Roeb, C. Sattler and R. Pitz-Paal, *Energy*, 2014, **67**, 298-308.

69. B. Meredig and C. Wolverton, *Phys. Rev. B*, 2009, **80**, 245119.

70. M. J. E., M. A. H. and A. M. D., *Adv. Energy Mat.*, 2014, **4**, 1300469.

71. W. C. Chueh and S. M. Haile, *Philos. T. R. Soc. A*, 2010, **368**, 3269-3294.

72. A. H. McDaniel, E. C. Miller, D. Arifin, A. Ambrosini, E. N. Coker, R. O'Hayre, W. C. Chueh and J. Tong, *Energy Environ. Sci.*, 2013, **6**, 2424-2428.

73. P. Furler, J. R. Scheffe and A. Steinfeld, *Energy Environ. Sci.*, 2012, **5**, 6098-6103.

74. Y. Hao, C.-K. Yang and S. M. Haile, *PCCP*, 2013, **15**, 17084-17092.

75. L. J. Venstrom, R. M. De Smith, Y. Hao, S. M. Haile and J. H. Davidson, *Energ. Fuel*, 2014, **28**, 2732-2742.

76. T. Nakamura, *Sol. Energy*, 1977, **19**, 467-475.

77. A. Steinfeld, S. Sanders and R. Palumbo, *Sol. Energy*, 1999, **65**, 43-53.

78. A. Steinfeld, M. Brack, A. Meier, A. Weidenkaff and D. Wuillemin, *Energy*, 1998, **23**, 803-814.

79. I. Alxneit, *Solar Energy*, 2008, **82**, 959-964.

80. M. Roeb, M. Neises, N. Monnerie, F. Call, H. Simon, C. Sattler, M. Schmucker and R. Pitz-Paal, *Materials*, 2012, **5**, 2015-2054.

81. S. Abanades, P. Charvin, F. Lemont and G. Flamant, *Int. J. Hydrog. Energy*, 2008, **33**, 6021-6030.

82. A. Steinfeld, *Int. J. Hydrog. Energy*, 2002, **27**, 611-619.

83. J. R. Scheffe, M. D. Allendorf, E. N. Coker, B. W. Jacobs, A. H. McDaniel and A. W. Weimer, *Chem. Mater.*, 2011, **23**, 2030-2038.

84. P. Charvin, S. Abanades, G. Flamant and F. Lemort, *Energy*, 2007, **32**, 1124-1133.

85. T. Kodama, Y. Nakamuro and T. Mizuno, *J. Sol. Energ. Eng.*, 2004, **128**, 3-7.

86. N. Gokon, H. Murayama, A. Nagasaki and T. Kodama, *Sol. Energy*, 2009, **83**, 527-537.

87. T. Kodama, Y. Kondoh, R. Yamamoto, H. Andou and N. Satou, *Sol. Energy*, 2005, **78**, 623-631.

88. S. Abanades, A. Legal, A. Cordier, G. Peraudeau, G. Flamant and A. Julbe, *J. Mater. Sci.*, 2010, **45**, 4163-4173.

89. A. Le Gal, S. Abanades, N. Bion, T. Le Mercier and V. Harlé, *Energ. Fuel*, 2013, **27**, 6068-6078.

90. J. R. Scheffe, D. Weibel and A. Steinfed, *Energ. Fuel*, 2013, **27**, 4250-4257.

91. D. Arifin, V. J. Aston, X. Liang, A. H. McDaniel and A. W. Weimer, *Energy Environ. Sci.*, 2012, **5**, 9438-9443.

92. B. Bulfin, F. Call, J. Vieten, M. Roeb, C. Sattler and I. V. Shvets, *J. Phys. Chem. C*, 2016, **120**, 2027-2035.

93. Q. Jiang, J. Tong, G. Zhou, Z. Jiang, Z. Li and C. Li, *Sol. Energy*, 2014, **103**, 425-437.

94. A. M. Deml, V. Stevanovic, C. L. Muhich, C. B. Musgrave and R. O'Hayre, *Energy Environ. Sci.*, 2014, **7**, 1996-2004.

95. C.-K. Yang, Y. Yamazaki, A. Aydin and S. M. Haile, *J. Mater. Chem. A*, 2014, **2**, 13612-13623.

96. A. Demont, S. Abanades and E. Beche, *J. Phys. Chem. C*, 2014, **118**, 12682-12692.

97. N. P. Siegel, J. E. Miller, I. Ermanoski, R. B. Diver and E. B. Stechel, *Ind. Eng. Chem. Res.*, 2013, **52**, 3276-3286.

98. A. Houaijia, C. Sattler, M. Roeb, M. Lange, S. Breuer and J. P. Säck, *Sol. Energy*, 2013, **97**, 26-38.

99. C. Agrafiotis, M. Roeb, A. G. Konstandopoulos, L. Nalbandian, V. T. Zaspalis, C. Sattler, P. Stobbe and A. M. Steele, *Sol. Energy*, 2005, **79**, 409-421.

100. J. Martinek, R. Viger and A. W. Weimer, *Sol. Energy*, 2014, **105**, 613-631.

101. M. Roeb, M. Neises, J.-P. Säck, P. Rietbrock, N. Monnerie, J. Dersch, M. Schmitz and C. Sattler, *Int. J. Hydrog. Energy*, 2009, **34**, 4537-4545.

102. R. Müller, P. Haeberling and R. D. Palumbo, *Sol. Energy*, 2006, **80**, 500-511.

103. L. O. Schunk, P. Haeberling, S. Wepf, D. Wuillemin, A. Meier and A. Steinfeld, *J. Sol. Energ. Eng.*, 2008, **130**, 021009-021009-021006.

104. J. R. Scheffe, M. Welte and A. Steinfeld, *Ind. Eng. Chem. Res.*, 2014, **53**, 2175-2182.

105. I. Ermanoski, *Int. J. Hydrog. Energy*, 2014, **39**, 13114-13117.

106. P. Haueter, T. Seitz and A. Steinfeld, *J. Sol. Energ. Eng.*, 1999, **121**, 77-80.

107. M. Puig-Arnavat, E. A. Tora, J. C. Bruno and A. Coronas, *Sol. Energy*, 2013, **97**, 67-84.

108. A. Abánades, C. Rubbia and D. Salmieri, *Int. J. Hydrog. Energy*, 2013, **38**, 8491-8496.

109. J. K. Dahl, K. J. Buechler, A. W. Weimer, A. Lewandowski and C. Bingham, *Int. J. Hydrog. Energy*, 2004, **29**, 725-736.

110. S. Rodat, S. Abanades and G. Flamant, *Sol. Energy*, 2011, **85**, 645-652.

111. A. Abánades, E. Ruiz, E. M. Ferruelo, F. Hernández, A. Cabanillas, J. M. Martínez-Val, J. A. Rubio, C. López, R. Gavela, G. Barrera, C. Rubbia, D. Salmieri, E. Rodilla and D. Gutiérrez, *Int. J. Hydrog. Energy*, 2011, **36**, 12877-12886.

112. A. M. Amin, E. Croiset and W. Epling, *Int. J. Hydrog. Energy*, 2011, **36**, 2904-2935.

113. E. Turpeinen, R. Raudaskoski, E. Pongrácz and R. L. Keiski, *Int. J. Hydrog. Energy*, 2008, **33**, 6635-6643.

114. D. S. A. Simakov, M. M. Wright, S. Ahmed, E. M. A. Mokheimer and Y. Roman-Leshkov, *Catal. Sci. Technol.*, 2015, **5**, 1991-2016.

115. S. A. M. Said, M. Waseeuddin and D. S. A. Simakov, *Renew. Sust. Energ. Rev.*, 2016, **59**, 149-159.

116. P. T. Krenzke and J. H. Davidson, *Energ. Fuel*, 2014, **28**, 4088-4095.

117. E. J. Sheu, E. M. A. Mokheimer and A. F. Ghoniem, *Int. J. Hydrog. Energy*, 2015, **40**, 12929-12955.

118. D. J. Wilhelm, D. R. Simbeck, A. D. Karp and R. L. Dickenson, *Fuel Process. Technol.*, 2001, **71**, 139-148.

119. Q. Zhang, W. Deng and Y. Wang, *J. Energ. Chem.*, 2013, **22**, 27-38.

120. M. C. Kung and H. H. Kung, *Surf. Sci.*, 1981, **104**, 253-269.

121. T. L. LeValley, A. R. Richard and M. H. Fan, *Int. J. Hydrog. Energy*, 2014, **39**, 16983-17000.

122. S. C. Tsang, J. B. Claridge and M. L. H. Green, *Catal. Today*, 1995, **23**, 3-15.

123. J. R. Rostrupnielsen and J. H. B. Hansen, *J. Catal.*, 1993, **144**, 38-49.

124. J. Wei and E. Iglesia, *J. Phys. Chem. B*, 2004, **108**, 4094-4103.

125. H. Wu, V. La Parola, G. Pantaleo, F. Puleo, A. M. Venezia and L. F. Liotta, *Catalysts*, 2013, **3**, 563-583.

126. C. J. Liu, J. Y. Ye, J. J. Jiang and Y. X. Pan, *Chemcatchem*, 2011, **3**, 529-541.

127. S. D. Angeli, G. Monteleone, A. Giaconia and A. A. Lemonidou, *Int. J. Hydrog. Energy*, 2014, **39**, 1979-1997.

128. S. Bhavsar and G. Veser, *RSC Adv.*, 2014, **4**, 47254-47267.

129. J. W. Snoeck, G. F. Froment and M. Fowles, *J. Catal.*, 1997, **169**, 250-262.

130. J.-W. Snoeck, G. Froment and M. Fowles, *Ind. Eng. Chem. Res.*, 2002, **41**, 4252-4265.

131. M. Annesini, V. Piemonte and L. Turchetti, *Chem. Eng.*, 2007, **11**.

132. K. Otsuka, E. Sunada, T. Ushiyama and I. Yamanaka, in *Stud. Surf. Sci. Catal.*, eds. R. L. E. C. P. N. J. H. S. M. de Pontes and M. S. Scurrell, Elsevier, 1997, vol. Volume 107, pp. 531-536.

133. K. Otsuka, Y. Wang, E. Sunada and I. Yamanaka, *J. Catal.*, 1998, **175**, 152-160.

134. P. Cho, T. Mattisson and A. Lyngfelt, *Ind. Eng. Chem. Res.*, 2005, **44**, 668-676.

135. P. T. Krenzke, J. R. Fosheim, J. Y. Zheng and J. H. Davidson, *Int. J. Hydrog. Energy*, 2016, **41**, 12799-12811.

136. A. Steinfeld, C. Larson, R. Palumbo and M. Foley, *Energy*, 1996, **21**, 205-222.

137. K. J. Warren, J. Reim, K. Randhir, B. Greek, R. Carrillo, D. W. Hahn and J. R. Scheffe, *Energ. Technol.*, 2017, **5**, 2138-2149.

138. M. Forster, *Energy*, 2004, **29**, 789-799.

139. X. Gao, A. Vidal, A. Bayon, R. Bader, J. Hinkley, W. Lipinski and A. Tricoli, *J. Mater. Chem. A*, 2016, **4**, 9614-9624.

140. X. Gao, G. Liu, Y. Zhu, P. Kreider, A. Bayon, T. Gengenbach, T. Lu, Y. Liu, J. Hinkley, W. Lipiński and A. Tricoli, *Nano Energy*, 2018, **50**, 347-358.

141. M. M. Nair and S. Abanades, *Energ. Fuel*, 2016, **30**, 6050-6058.

142. X. Gao, A. Vidal, A. Bayon, R. Bader, J. Hinkley, W. Lipiński and A. Tricoli, *2015 Asia-Pacific Solar Research Conference*, Brisbane, 2015.

143. C. Q. Lu, K. Z. Li, H. Wang, X. Zhu, Y. G. Wei, M. Zheng and C. H. Zeng, *Appl. Energy*, 2018, **211**, 1-14.

144. K. S. Go, S. R. Son, S. D. Kim, K. S. Kang and C. S. Park, *Int. J. Hydrog. Energy*, 2009, **34**, 1301-1309.

145. J. T. Jang, K. J. Yoon, J. W. Bae and G. Y. Han, *Sol. Energy*, 2014, **109**, 70-81.

146. J.-W. Snoeck, G. Froment and M. Fowles, *Int. J. Che,. React. Eng.*, 2002, **1**.

147. X.-L. Sang, K.-Z. Li, H. Wang and Y.-G. Wei, *Rare Metals*, 2014, **33**, 230-238.

148. J. W. Snoeck, G. F. Froment and M. Fowles, *J. Catal.*, 1997, **169**, 240-249.

149. P. Furler, J. Scheffe, D. Marxer, M. Gorbar, A. Bonk, U. Vogt and A. Steinfeld, *PCCP*, 2014, **16**, 10503-10511.

150. B. Bulfin, F. Call, M. Lange, O. Lubben, C. Sattler, R. Pitz-Paal and I. V. Shvets, *Energ. Fuel*, 2015, **29**, 1001-1009.

151. M. Lin and S. Haussener, *Sol. Energy*, 2017, **155**, 1389-1402.

152. T. Mancini, P. Heller, B. Butler, B. Osborn, W. Schiel, V. Goldberg, R. Buck, R. Diver, C. Andraka and J. Moreno, *J. Sol. Energ. Eng.*, 2003, **125**, 135-151.

153. L. O. Schunk, W. Lipiński and A. Steinfeld, *Chem. Eng. J.*, 2009, **150**, 502-508.

154. P. T. Krenzke and J. H. Davidson, *Energ. Fuel*, 2015, **29**, 1045-1054.

155. S. Brendelberger, M. Roeb, M. Lange and C. Sattler, *Sol. Energy*, 2015, **122**, 1011-1022.

156. K. Z. House, A. C. Baclig, M. Ranjan, E. A. van Nierop, J. Wilcox and H. J. Herzog, *P. Natl. Acad. Sci.*, 2011, **108**, 20428-20433.

157. A. Le Gal, S. Abanades, G. Flamant, D. Stolten and T. Grube, *Report Nr.: Schriften des Forschungszentrums Jülich/Energy & Environment*, 2010.

158. L. D'Souza, *Mater. Renew. Sust. Energ.*, 2013, **2**, 7.

159. M. D. Allendorf, J. E. Miller and A. H. McDaniel, *Electrochem. Soc. Interface*, 2013, **22**, 63-68.

160. M. Ortiz, L. F. de Diego, A. Abad, F. García-Labiano, P. Gayán and J. Adánez, *Energ. Fuel*, 2012, **26**, 791-800.

161. T. Abbasi and S. A. Abbasi, *Renew. Sust. Energ. Rev.*, 2011, **15**, 3034-3040.

162. A. Steinfeld, P. Kuhn and J. Karni, *Energy*, 1993, **18**, 239-249.

163. B. C. Enger, R. Lodeng and A. Holmen, *Appl. Catal. A Gen.*, 2008, **346**, 1-27.

164. T. Kodama, T. Shimizu, T. Satoh, M. Nakata and K. I. Shimizu, *Sol. Energy*, 2002, **73**, 363-374.

165. M. D. Allendorf, R. B. Diver, N. P. Siegel and J. E. Miller, *Energ. Fuel*, 2008, **22**, 4115-4124.

166. T. Suzuki, O. Nakayama and N. Okamoto, *Catal. Surv. Asia*, 2012, **16**, 75-90.

167. S. Kräupl and A. Steinfeld, *ASME Solar 2002: International Solar Energy Conference*, Nevada, 2002.

168. A. Steinfeld, A. Frei, P. Kuhn and D. Wuillemin, *Int. J. Hydrog. Energy*, 1995, **20**, 793-804.

169. T. Kodama, H. Ohtake, S. Matsumoto, A. Aoki, T. Shimizu and Y. Kitayama, *Energy*, 2000, **25**, 411-425.

170. T. Shimizu, K. Shimizu, Y. Kitayama and T. Kodama, *Sol. Energy*, 2001, **71**, 315-324.

171. T. Kodama, T. Shimizu, T. Satoh and K.-I. Shimizu, *Energy*, 2003, **28**, 1055-1068.

172. M. Johansson, T. Mattisson and A. Lyngfelt, *Chem. Eng. Res. Des.*, 2006, **84**, 807-818.

173. J. Adánez, L. F. de Diego, F. García-Labiano, P. Gayán, A. Abad and J. M. Palacios, *Energ. Fuel*, 2004, **18**, 371-377.

174. A. Bayón, V. A. de la Peña O'Shea, D. P. Serrano and J. M. Coronado, *Int. J. Hydrog. Energy*, 2013, **38**, 13143-13152.

175. J. Adanez, A. Abad, F. Garcia-Labiano, P. Gayan and L. F. de Diego, *Prog. Energy Combust. Sci.*, 2012, **38**, 215-282.

176. M. M. Hossain and H. I. de Lasa, *Chem. Eng. Sci.*, 2008, **63**, 4433-4451.

177. S. Takenaka, N. Hanaizumi, V. T. D. Son and K. Otsuka, *J. Catal.*, 2004, **228**, 405-416.

178. K.-S. Kang, C.-H. Kim, K.-K. Bae, W.-C. Cho, W.-J. Kim, Y.-H. Kim, S.-H. Kim and C.-S. Park, *Int. J. Hydrog. Energy*, 2010, **35**, 568-576.

179. K.-S. Cha, H.-S. Kim, B.-K. Yoo, Y.-S. Lee, K.-S. Kang, C.-S. Park and Y.-H. Kim, *Int. J. Hydrog. Energy*, 2009, **34**, 1801-1808.

180. K. S. Go, S. R. Son and S. D. Kim, *Int. J. Hydrog. Energy*, 2008, **33**, 5986-5995.

181. M. Rydén, A. Lyngfelt, T. Mattisson, D. Chen, A. Holmen and E. Bjørgum, *Int. J. Greenh. Gas. Con.*, 2008, **2**, 21-36.

182. O. Nakayama, N. Ikenaga, T. Miyake, E. Yagasaki and T. Suzuki, *Ind. Eng. Chem. Res.*, 2010, **49**, 526-534.

183. L. J. Venstrom, N. Petkovich, S. Rudisill, A. Stein and J. H. Davidson, *J. Sol. Energ. Eng.*, 2012, **134**, 011005.

184. S. Abanades and G. Flamant, *Sol. Energy*, 2006, **80**, 1611-1623.

185. H. Kaneko, T. Miura, H. Ishihara, S. Taku, T. Yokoyama, H. Nakajima and Y. Tamaura, *Energy*, 2007, **32**, 656-663.

186. Q. L. Meng, C. I. Lee, T. Ishihara, H. Kaneko and Y. Tamaura, *Int. J. Hydrog. Energy*, 2011, **36**, 13435-13441.

187. A. Le Gal, S. Abanades and G. Flamant, *Energ. Fuel*, 2011, **25**, 4836-4845.

188. M. Kang, J. Zhang, C. Wang, F. Wang, N. Zhao, F. Xiao, W. Wei and Y. Sun, *RSC Adv.*, 2013, **3**, 18878-18885.

189. J. R. Scheffe and A. Steinfeld, *Energ. Fuel*, 2012, **26**, 1928-1936.

190. W. T. Gibbons, L. J. Venstrom, R. M. De Smith, J. H. Davidson and G. S. Jackson, *PCCP*, 2014, **16**, 14271-14280.

191. C. D. Malonzo, R. M. De Smith, S. G. Rudisill, N. D. Petkovich, J. H. Davidson and A. Stein, *J. Phys. Chem. C*, 2014, **118**, 26172-26181.

192. H.-I. Ji, T. C. Davenport, C. B. Gopal and S. M. Haile, *PCCP*, 2016, **18**, 21554-21561.

193. K. Otsuka, T. Ushiyama and I. Yamanaka, *Chem. Lett.*, 1993, **22**, 1517-1520.

194. K. Otsuka, Y. Wang and M. Nakamura, *Appl. Catal. A Gen.*, 1999, **183**, 317-324.

195. X. Zhu, H. Wang, Y. Wei, K. Li and X. Cheng, *J. Nat. Gas Chem*, 2011, **20**, 281-286.

196. Z. Gu, K. Li, H. Wang, S. Qing, X. Zhu, Y. Wei, X. Cheng, H. Yu and Y. Cao, *Appl. Energy*, 2016, **163**, 19-31.

197. H.-S. Kim, K.-S. Cha, B.-K. Yoo, T.-G. Ryu, Y.-S. Lee, C.-S. Park and Y.-H. Kim, *J. Ind. Eng. Chem.*, 2010, **16**, 81-86.

198. A. Jha, D.-W. Jeong, W.-J. Jang, Y.-L. Lee and H.-S. Roh, *Int. J. Hydrog. Energy*, 2015, **40**, 9209-9216.

199. F. He, Y. G. Wei, H. B. Li and H. Wang, *Energ. Fuel*, 2009, **23**, 2095-2102.

200. H. H. Jeong, J. H. Kwak, G. Y. Han and K. J. Yoon, *Int. J. Hydrog. Energy*, 2011, **36**, 15221-15230.

201. M. Fathi, E. Bjorgum, T. Viig and O. A. Rokstad, *Catal. Today*, 2000, **63**, 489-497.

202. P. Pantu, K. Kim and G. R. Gavalas, *Appl. Catal. A Gen.*, 2000, **193**, 203-214.

203. R. Shannon, *Acta Crystallographica Section A*, 1976, **32**, 751-767.

204. M. Shelef, G. Graham, R. McCabe and A. Trovarelli, *Catalysis by ceria and related materials*, Imperial College Press, 2002.

205. R. Hailstone, A. DiFrancesco, J. Leong, T. Allston and K. Reed, *J. Phys. Chem. C*, 2009, **113**, 15155-15159.

206. A. Patterson, *Phys. Rev.*, 1939, **56**, 978.

207. U. M. Bhatta, D. Reid, T. Sakthivel, T. X. Sayle, D. Sayle, M. Molinari, S. C. Parker, I. M. Ross, S. Seal and G. n. Möbus, *J. Phys. Chem. C*, 2013, **117**, 24561-24569.

208. S. V. Kuchibhatla, A. S. Karakoti, D. C. Sayle, H. Heinrich and S. Seal, *Crystal Growth and Design*, 2009, **9**, 1614-1620.

209. Q. Yuan, H.-H. Duan, L.-L. Li, L.-D. Sun, Y.-W. Zhang and C.-H. Yan, *Journal of colloid and interface science*, 2009, **335**, 151-167.

210. T. X. Sayle, B. J. Inkson, A. Karakoti, A. Kumar, M. Molinari, G. Möbus, S. C. Parker, S. Seal and D. C. Sayle, *Nanoscale*, 2011, **3**, 1823-1837.

211. K. Reed, A. Cormack, A. Kulkarni, M. Mayton, D. Sayle, F. Klaessig and B. Stadler, *Environmental Science: Nano*, 2014, **1**, 390-405.

212. C. T. Campbell and C. H. Peden, *Science*, 2005, **309**, 713-714.

213. J. Zhang, H. Kumagai, K. Yamamura, S. Ohara, S. Takami, A. Morikawa, H. Shinjoh, K. Kaneko, T. Adschiri and A. Suda, *Nano letters*, 2011, **11**, 361-364.

214. C. Sun, H. Li and L. Chen, *Energy Environ. Sci.* 2012, **5**, 8475-8505.

215. F. Zhang, Q. Jin and S.-W. Chan, *J. appl. phys.*, 2004, **95**, 4319-4326.

216. H.-I. Chen and H.-Y. Chang, *Ceramics International*, 2005, **31**, 795-802.

217. K. Matsui, T. Kyotani and A. Tomita, *Adv. Mat.* 2002, **14**, 1216-1219.

218. M. Hirano and M. Inagaki, *J. Mater. Chem.*, 2000, **10**, 473-477.

219. J. M. Dowding, S. Das, A. Kumar, T. Dosani, R. McCormack, A. Gupta, T. X. Sayle, D. C. Sayle, L. von Kalm and S. Seal, *ACS nano*, 2013, **7**, 4855-4868.

220. C. Laberty-Robert, J. W. Long, E. M. Lucas, K. A. Pettigrew, R. M. Stroud, M. S. Doescher and D. R. Rolison, *Chem. mater.*, 2006, **18**, 50-58.

221. M. Niederberger, *Accounts of chemical research*, 2007, **40**, 793-800.

222. S. Patil, S. Kuiry, S. Seal and R. Vanfleet, *Journal of Nanoparticle Research*, 2002, **4**, 433-438.

223. Y. He, B. Yang and G. Cheng, *Materials letters*, 2003, **57**, 1880-1884.

224. A. S. Karakoti, P. Munusamy, K. Hostetler, V. Kodali, S. Kuchibhatla, G. Orr, J. G. Pounds, J. G. Teeguarden, B. D. Thrall and D. R. Baer, *Surface and Interface Analysis*, 2012, **44**, 882-889.

225. X. P. Dai, Q. Wu, R. J. Li, C. C. Yu and Z. P. Hao, *J. Phys. Chem. B*, 2006, **110**, 25856-25862.

226. F. X. Li, Z. C. Sun, S. W. Luo and L. S. Fan, *Energy Environ. Sci.*, 2011, **4**, 876-880.

227. Y. Zheng, Y. Wei, K. Li, X. Zhu, H. Wang and Y. Wang, *Int. J. Hydrog. Energy*, 2014, **39**, 13361-13368.

228. A. Evdou, V. Zaspalis and L. Nalbandian, *Fuel*, 2010, **89**, 1265-1273.

229. X. Zhu, Y. Wei, H. Wang and K. Li, *Int. J. Hydrog. Energy*, 2013, **38**, 4492-4501.

230. J. R. González-Velasco, M. A. Gutiérrez-Ortiz, J.-L. Marc, J. A. Botas, M. P. González-Marcos and G. Blanchard, *Appl. Catal. B Environ.*, 1999, **22**, 167-178.

231. S. Kim, Y. L. Yang, A. J. Jacobson and B. Abeles, *Solid State Ionics*, 1998, **106**, 189-195.

232. J. R. Scheffe, R. Jacot, G. R. Patzke and A. Steinfeld, *J. Phys. Chem. C*, 2013, **117**, 24104-24114.

233. Y. Hao, C.-K. Yang and S. M. Haile, *Chem. Mater.*, 2014, **26**, 6073-6082.

234. G. Zhou, P. R. Shah, T. Kim, P. Fornasiero and R. J. Gorte, *Catal. Today*, 2007, **123**, 86-93.

235. X. Zhu, K. Li, Y. Wei, H. Wang and L. Sun, *Energ. Fuel*, 2014, **28**, 754-760.

236. K. Li, H. Wang, Y. Wei and D. Yan, *Appl. Catal. B Environ.*, 2010, **97**, 361-372.

237. K. Li, H. Wang, Y. Wei and M. Liu, *Journal of Rare Earths*, 2008, **26**, 705-710.

238. O. Mihai, D. Chen and A. Holmen, *Ind. Eng. Chem. Res.*, 2011, **50**, 2613-2621.

239. L. Nalbandian, A. Evdou and V. Zaspalis, *Int. J. Hydrog. Energy*, 2011, **36**, 6657-6670.

240. K. Zhao, F. He, Z. Huang, A. Q. Zheng, H. B. Li and Z. L. Zhao, *Chinese J. Catal.*, 2014, **35**, 1196-1205.

241. A. Mishra, N. Galinsky, F. He, E. E. Santiso and F. Li, *Catal. Sci. Technol.*, 2016, **6**, 4535-4544.

242. L. Nalbandian, A. Evdou and V. Zaspalis, *Int. J. Hydrog. Energy*, 2009, **34**, 7162-7172.

243. F. He, X. Li, K. Zhao, Z. Huang, G. Wei and H. Li, *Fuel*, 2013, **108**, 465-473.

244. N. D. Petkovich, S. G. Rudisill, L. J. Venstrom, D. B. Boman, J. H. Davidson and A. Stein, *J. Phys. Chem. C*, 2011, **115**, 21022-21033.

245. H. Wei, Y. Cao, W. Ji and C. Au, *Catal. Commun.*, 2008, **9**, 2509-2514.

246. A. Evdou, V. Zaspalis and L. Nalbandian, *Int. J. Hydrog. Energy*, 2008, **33**, 5554-5562.

247. F. Mudu, U. Olsbye, B. Arstad, S. Diplas, Y. Li and H. Fjellvåg, *Appl. Catal. A Gen.*, 2016, **523**, 171-181.

248. L. Mädler, H. Kammler, R. Mueller and S. E. Pratsinis, *Journal of Aerosol Science*, 2002, **33**, 369-389.

249. H. Schulz, L. Mädler, R. Strobel, R. Jossen, S. E. Pratsinis and T. Johannessen, *J. mater. res.*, 2005, **20**, 2568-2577.

250. R. Mueller, R. Jossen, S. E. Pratsinis, M. Watson and M. K. Akhtar, *Journal of the American Ceramic Society*, 2004, **87**, 197-202.

251. M. C. Heine, L. Mädler, R. Jossen and S. E. Pratsinis, *Combustion and Flame*, 2006, **144**, 809-820.

252. A. Tricoli, A. S. Wallerand and M. Righettoni, *J. Mater. Chem.*, 2012, **22**, 14254-14261.

253. A. Tricoli, M. Graf and S. E. Pratsinis, *Adv. Func. Mater.*, 2008, **18**, 1969-1976.

254. A. Tricoli, M. Righettoni and S. E. Pratsinis, *Nanotechnology*, 2009, **20**, 315502.

255. L. Mädler and S. E. Pratsinis, *Journal of the American Ceramic Society*, 2002, **85**, 1713-1718.

256. T. Tani, K. Takatori and S. E. Pratsinis, *Journal of the American Ceramic Society*, 2004, **87**, 523-525.

257. L. Mädler, W. J. Stark and S. E. Pratsinis, *J. Mater. Res.*, 2002, **17**, 1356-1362.

258. J. Karthikeyan, C. C. Berndt, J. Tikkanen, J. Y. Wang, A. H. King and H. Herman, *Nanostructured Materials*, 1997, **8**, 61-74.

259. S. GRIMM, M. SCHULTZ, S. BARTH and R. MULLER, *J. Mater. Sci.*, 1997, **32**, 1083-1092.

260. M. Sokołowski, A. Sokołowska, A. Michalski and Z. Ziółowski, *Journal of Crystal Growth*, 1981, **52**, 274-278.

261. N. Nasiri, R. Bo, F. Wang, L. Fu and A. Tricoli, *Adv. Mater.*, 2015, **27**, 4336-4343.

262. W. Y. Teoh, R. Amal and L. Mädler, *Nanoscale*, 2010, **2**, 1324-1347.

263. S. E. Pratsinis, *Progress in Energy and Combustion Science*, 1998, **24**, 197-219.

264. M. S. Wooldridge, *Progress in Energy and Combustion Science*, 1998, **24**, 63-87.

265. A. Gutsch, H. Mühlenweg and M. Krämer, *Small*, 2005, **1**, 30-46.

266. G. Liu, J. Hall, N. Nasiri, T. Gengenbach, L. Spiccia, M. H. Cheah and A. Tricoli, *ChemSusChem*, 2015, **8**, 4162-4171.

267. W. J. Stark, M. Maciejewski, L. Mädler, S. E. Pratsinis and A. Baiker, *J. Catal.*, 2003, **220**, 35-43.

268. A. Camenzind, R. Strobel and S. E. Pratsinis, *Chemical Physics Letters*, 2005, **415**, 193-197.

269. L. Wang, A. Teleki, S. E. Pratsinis and P. I. Gouma, *Chem. Mater.*, 2008, **20**, 4794-4796.

270. W. Y. Teoh, R. Amal, L. Mädler and S. E. Pratsinis, *Catal. Today*, 2007, **120**, 203-213.

271. A. Tricoli, M. Graf, F. Mayer, S. Kuühne, A. Hierlemann and S. E. Pratsinis, *Adv. Mater.*, 2008, **20**, 3005-3010.

272. M. J. Height, L. Mädler, S. E. Pratsinis and F. Krumeich, *Chem. Mater.*, 2006, **18**, 572-578.

Chapter Two

Efficient Ceria Nanostructures for Enhanced Solar Fuel Production via High-Temperature Thermochemical Redox Cycles

Publication relevant to this chapter:

X. Gao, A. Vidal, A. Bayon, R. Bader, J. Hinkley, W. Lipiński and A. Tricoli, (2016), *Efficient ceria nanostructures for enhanced solar fuel production via high-temperature thermochemical redox cycles*. Journal of Materials Chemistry A, 4(24), 9614-9624.

Abstract

Syngas synthesis by solar energy-driven two-step thermochemical redox cycles is a promising approach for large-scale industrial production of renewable fuels. A key challenge is developing durable materials capable to provide and sustain high redox kinetics in the harsh environmental conditions required for efficient operation. Here, nanostructured ceria with high surface area and porosity was demonstrated to significantly enhance initial and long-term syngas production performance. Three types of ceria morphologies were synthesised and comparatively investigated against commercial powders in two-step thermochemical redox cycles, namely nanostructured flame-made and flower-like agglomerates, and sol-gel sub-micro particles. Their syngas production performance was assessed in terms of redox kinetics, conversion stoichiometry and structural stability. The flame-made ceria nano-powders had up to 191%, 167% and 99% higher initial average production rates than the flower-like, commercial and sol-gel ceria powders, respectively. This resulted in the highest H_2 (480 μmol min^{-1} g^{-1}) and CO (230 and 340 μmol min^{-1} g^{-1}) production rates and redox capacity ($\Delta\delta = 0.25$) so far reported for ceria. Notably, the grain morphology played a key role in the long-term performance and while the redox kinetics of the flower-like ceria rapidly decreased below that of the commercial powders, the flame-made agglomerates maintained up to 57% higher average production rate till the last cycle. These findings show that the thermochemical stabilisation of nano-scale structural features, observed in the flame-made agglomerates, is key to engineering efficient materials for enhanced thermochemical solar fuel production.

2.1 Introduction

Synthesis gas (syngas) production via thermochemical redox cycles driven by high-flux solar irradiation is a promising emerging technology for chemical storage of solar energy. The highly-endothermic reduction step of the redox cycle is typically performed by thermal reduction of a metal oxide, which requires temperatures above 1700 K[1-3]. The subsequent oxidation step for water splitting (WS) and carbon dioxide splitting (CDS) is exothermic, and can typically be operated at temperatures below 1400 K[1, 2]. The repeated temperature swings between the reduction and oxidation steps adversely affect the thermal process efficiency and provide significant challenges for maximization of heat recovery and mitigation of thermal stresses.[3-5] As a result, isothermal redox cycles have been increasingly investigated as an alternative process for solar fuel production.[5, 6]

Many metal oxide-based redox systems have been explored for WS and CDS.[3, 7-9] These include Mn oxides, Ni(II)-/Zn(II)-/Co(II)-ferrites, WO_3, CeO_2, and ZnO.[10-13] Among these, CeO_2 has attracted particular attention as it offers faster kinetics and enhanced long-term stability than many other metal oxides.[1] The isothermal cycling thermodynamics of ceria with reduction in an inert atmosphere have been recently investigated.[5] However, the required operating temperature of 1773 K for its inert gas reduction (IGR) challenges the engineering of the industrial reactors. Furthermore, even with gas-phase heat recovery, the solar-to-fuel efficiency of IGR-based cycles is relatively low with overall theoretical efficiencies of 10% and 18% for WS and CDS, respectively.[5] Coupling methane partial oxidation (MPO) to the ceria reduction step can lower the required peak temperature to 1273 K and produce syngas with solar-to-fuel efficiencies of up to 40%, without heat recovery.[14] Notably, in comparison to other methane to syngas conversion technologies such as steam and dry reforming, redox cycles with MPO can produce suitable H_2:CO ratio for downstream Fischer-Tropsch

(FT)[15] and methanol syntheses[16]. This increases the overall process efficiency by avoiding additional separation of H_2 or CO from the products.[17]

The two-step thermochemical redox cycle of ceria based on an MPO reduction and a subsequent CDS or WS oxidation consists of the following reactions[14]:

Reduction step:

$$CeO_2 + \delta CH_4 \rightarrow CeO_{2-\delta} + \delta CO + 2\delta H_2, \quad \Delta H_{298}^o = +166.2 \text{ kJ mol}^{-1} \tag{2.1}$$

Oxidation step:

$$CeO_{2-\delta} + \delta CO_2 \rightarrow \delta CO + CeO_2, \quad \Delta H_{298}^o = -22.1 \text{ kJ mol}^{-1} \tag{2.2a}$$

and/or

$$CeO_{2-\delta} + \delta H_2O \rightarrow \delta H_2 + CeO_2, \quad \Delta H_{298}^o = -63.3 \text{ kJ mol}^{-1} \tag{2.2b}$$

In the endothermic MPO step, CeO_2 is reduced in presence of CH_4 and (solar) thermal energy input with a net change in stoichiometry of δ. As ceria is able to accommodate substantial release of lattice oxygen while maintaining a stable cubic fluorite crystal phase, no phase change is expected during this reduction step.[14, 18] In the exothermic oxidation step, $CeO_{2-\delta}$ is oxidised by CO_2 or H_2O, reincorporating up to δ moles of oxygen into the lattice and producing δ moles of CO or H_2.

Studies to increase the capacity of fuel production, redox stability and thermal stability of ceria-based metal oxide systems have been performed with $Ce_xZr_{1-x}O_2$, $Ce_xHf_{1-x}O_2$, Mg-doped $Ce_xZr_{1-x}O_2$, and various rare earth elements-doped $Ce_xZr_{1-x}O_2$ systems.[19-22] A primary mechanism is the partial replacement of Ce cations in the crystal lattice with other metal cations, which facilitates diffusion of oxygen ions and decreases the oxygen vacancy formation enthalpy.[23] However, such metal doping approaches have achieved limited success in increasing the redox kinetics of ceria-based materials.[22, 24] Increased kinetics have been obtained by surface coating with rare metal catalysts such as Pt and Rh[25, 26] and exploiting morphological effects[27]. While this results in an increase in syngas production peak rates, the cycling stability and cost-

effectiveness of incorporation of noble metals is debatable.[25,28] Attempts to increase redox kinetics by increasing the specific surface area (SSA) of ceria have so far resulted in temporary improvements of peak syngas production rates, due to poor stability of the nanostructures under the harsh conditions of high temperature redox cycles[29].

Here, the syngas production performance of four distinct nano-micro structured ceria powder during two-step MPO-CDS thermochemical redox cycles was investigated. Namely, they are high specific surface area flame-made and flower-like nanostructured agglomerates, sol-gel sub-micro grains and commercial powders. These ceria morphologies were chosen for their demonstrated and potential performance in thermochemical H_2O and CO_2 splitting.[1] The evolution of the redox kinetics, total syngas production, redox capacity (δ), and thermal stability of these distinct ceria morphologies is investigated over two days in consecutive isothermal cycles under alternating CH_4 and CO_2 atmospheres. Key structural parameters for the stabilization of high redox kinetics are determined providing insights for the engineering of enhanced materials for efficient high-temperature thermochemical solar fuel production.

2.2 Experimental

2.2.1 Synthesis of Nanostructured Ceria

To synthesise flame-made ceria nanoparticles, cerium (III) acetate hydrate (Alfa Aesar, 99.995%) was dissolved in a 2-ethylhexanoic acid (SAFC, >99%) heated with 368 K oil bath to prepare the combustible liquid solution. Next, xylene of the volume equal to that of the 2-ethylhexanoic acid was added to the solution to reach a total Ce concentration of 0.2 mol L^{-1}. The solution was fed at 5 mL min^{-1} rate through a custom built nozzle[30], and atomised with an oxygen flow of 5 L min^{-1} (COREGAS grade 2.5) with a pressure drop of 4 bar. The resulting spray was ignited with a surrounding annular premixed methane ($CH_{4\text{-flamlet}}$, flow rate of 1.2 L min^{-1}, COREGAS grade 4.5)

and oxygen ($O_{2\text{-flamlet}}$, flow rate of 2 L min^{-1}, COREGAS grade 2.5) flame. Nanoparticle powders were collected with a vacuum pump (ICME Type M80B4) on water-cooled glass-fibre filters (Sartorius glass microfiber, 160-mm diameter) placed at 40 cm height above the burner (HAB).

The flower-like ceria particles were synthesised according to the procedures described by Sun et al. and started with the formation of $CeOHCO_3$ microspheres.[31] A solution was prepared by mixing glucose (Sigma Aldrich, 96%), acrylamide (Sigma Aldrich, ⩾99%) and cerium nitrate (Sigma Aldrich, 99.99%). After that, ammonia solution (VWR, 30%) was added to the solution drop-wise with stirring, and the solution turned into stiff gel. The gel was transferred into an autoclave and heated at 453 K for 72 hr. The result was an orange suspension and precipitate, which was washed with water and alcohol and dried at 353 K, obtaining $CeOHCO_3$ flower-like spheres. The as-prepared $CeOHCO_3$ powder was calcined under nitrogen atmosphere in a tubular furnace at 873 K for 6 hr. A second calcination step was carried out in air at 673 K for 4 hr. The result is CeO_2 microspheres with a flower-like structure.

To produce the sol-gel ceria by the Pechini's method[32], the following precursors were used: citric acid (CA, Sigma-Aldrich, ≥99.5%), cerium (III) nitrate hexahydrate (Sigma-Aldrich, 99%), and ethylene glycol (EG, Sigma-Aldrich, 99.8%) . All the reagents were used as received without any purification. A molar ratio of Ce:CA:EG = 1:4:20 was used for preparing the precursor solution. First, CA was added in 50 mL deionised water in a beaker and the mixture was stirred at 343 K until total dissolution. Then, cerium (III) nitrate hexahydrate was added to this solution. After further stirring for 2.5 h at 343 K, the temperature of the solution was increased to 363 K before EG was added. The resulting solution was further stirred at the same temperature to remove the excess of solvent, and the obtained resin from the polyesterification reaction[33] was

subsequently dried in an oven at 473 K for 3 h and then calcined at 673 K for 4 h in air to obtain the sol-gel ceria particles.

Potential formation of carbon deposits was evaluated by TGA (STA8000, PerkinElmer) and FTIR analysis (FTIR-EGA, PerkinElmer) of the evolved gases during temperature programmed oxidation in air (100 mL min^{-1}) at a temperature range of 800 K to 1100 K (Figure S2.4).

2.2.2 Two-Step Redox Cycles

The cyclic syngas production performance of the ceria samples was investigated in a vertical-tube reactor placed inside an electric IR furnace (P4C-VHT, Advance Riko) (Figure 2.1). The powder samples were packed between two pieces of 2 mm thick highly-porous and temperature-resistant aluminosilicate wool, located on-axis of an alumina tube. All the ceria powder samples, placed in the reactor, had a mass of 150±2 mg, resulting in a powder bed thickness of 1 - 2 mm. The inner diameter and wall thickness of the tube were 12.5 mm and 3 mm, respectively. The tube was placed in the centre of the furnace and enveloped by a quartz tube for protection of the IR lamps against thermal degradation. Gas mixtures were regulated by mass flow controllers (F-201CV, Bronkhorst) before being delivered through the top of the tube. Sample temperature was measured using an alumina sealed type-K thermocouple inside the alumina tube. The composition of the product gases was continuously monitored by a quadrupole mass spectrometer (OmniStarTM GSD 320, Pfeiffer Vacuum). All the monitored gas components were calibrated in the mass spectrometer using standard mixtures of the individual solute (CH_4, CO_2, and CO/H_2) in a carrier gas of Ar. All gas volumes were reported at 293 K and 1 atm. The average production rates of H_2 and CO were calculated over the time period when H_2 and/or CO evolution was continuous and above the calibrated detection limit of the mass spectrometer. The operating temperature for isothermal MPO-CDS ceria redox cycles, 1173 K, was derived from thermodynamic

analysis and had been experimentally evaluated in this setup from the range of 973 K to 1273 K[14] (not shown in this study) to produce H_2 and CO at a close 2:1 ratio (eq .1) while maintaining sufficient reaction rates while avoiding CH_4 thermal decomposition.

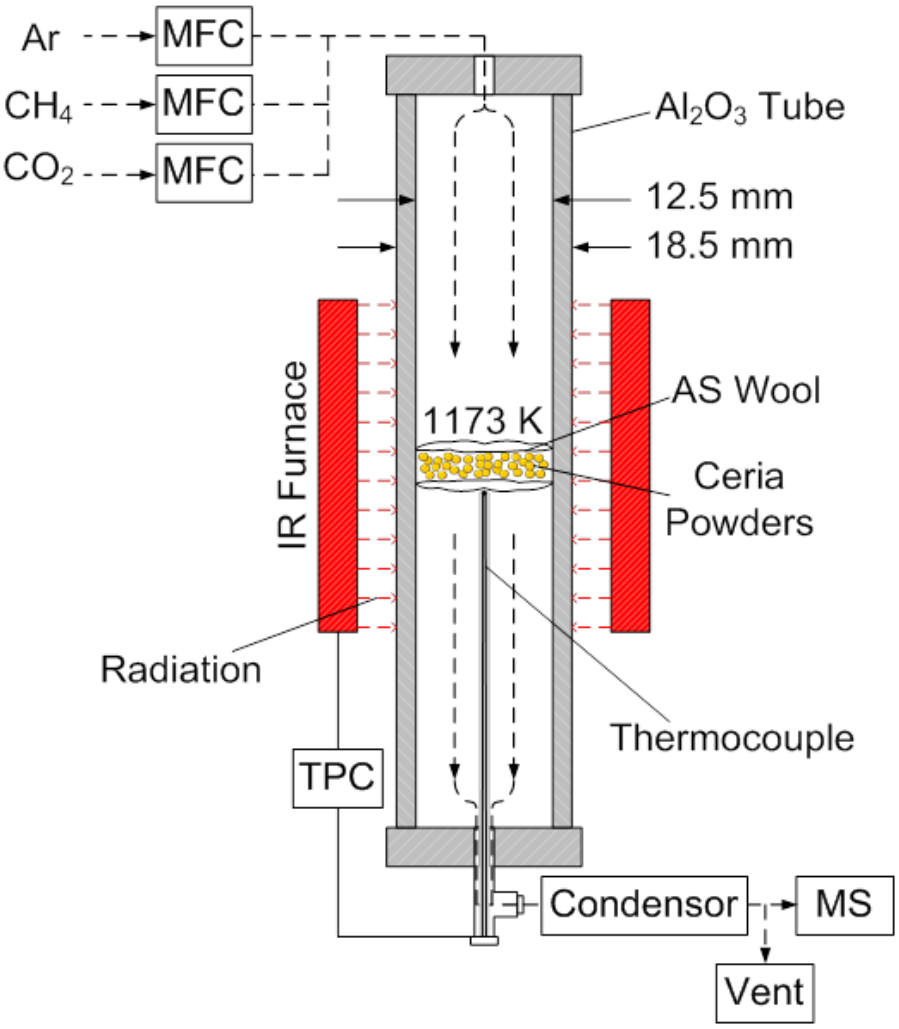

Figure 2.1 Schematic of the vertical reactor for the two-step MPO-CDS isothermal redox cycles. MFC: mass flow controller; TPC: temperature program controller; MS: mass spectrometer; AS Wool: Alumino Silicate Wool.

To simulate the operating conditions of a solar reactor, a discontinuous two-day testing was conducted for the ceria samples performing a total of 10 cycles (divided into 4 and 6 cycles over two testing days). In each testing day, the tubular reactor was initially purged of air under a 250 mL min^{-1} flow of pure Ar (COREGAS grade 5.0) at room temperature. The reactor was then heated from ambient room temperature to 1173 K at a ramp of 80 K min^{-1}. Subsequently, the sample was cyclically reduced by CH_4

(COREGAS grade 4.5) and oxidised by CO_2 (COREGAS grade 4.5). The reduction step was performed using a mixture of CH_4 in Ar (8 vol% CH_4) at a total flow rate of 250 mL min^{-1}. Each reduction step was conducted for 30 min. Then the tube was purged with Ar (250 mL min^{-1}) for 15 min. The oxidation step was initiated by delivering a mixture of CO_2 in Ar (4 vol% CO_2) at a total flow rate of 250 mL min^{-1}. Each oxidation step was conducted for 15 min. The tube was again purged with Ar (250 mL min^{-1}) for 15 min before the next cycle began. The time required for the reduction and oxidation steps was determined by preliminary tests and was sufficient for all the samples to complete the reaction until no further fuel production could be detected by the mass spectrometer. At the end of each testing day, the reactor was cooled to room temperature at 80 K min^{-1} using an external cooling system under Ar purge gas. Once the sample reached room temperature, the valves at both ends of the alumina tube were closed, and the samples were preserved in the Ar atmosphere between the testing days.

2.2.3 Sample Characterisations

Samples were characterised before and after the 10 isothermal MPO-CDS tests. X-ray diffraction (XRD) was performed using a D2 phaser diffractometer from Bruker. Each sample powder was scanned using Cu Kα (1.54 Å) radiation source with an operating voltage and current of 30 kV and 10 mA, respectively. The scanning rate of 0.75° min^{-1} was applied to record the XRD patterns in the range of 10-80° at an increment of 0.02°. The Scherrer equation was applied for the most intense peak to determine the crystal size. The Brunauer-Emmett-Teller (BET) specific surface area was measured by N_2 adsorption-desorption isotherms at 77 K, using a surface and porosity analyser (TriStar II, Micromeritics). The samples were degassed in a vacuum (0.09 mBar) at 623 K for at least 4 h prior to measurement. The Sauter mean diameters (SMD) were obtained assuming particles are spherical and non-porous with the diameter (d_{BET}) estimated by:

$$d_{\mathrm{BET}} = \frac{6}{\rho\, S_{\mathrm{BET}}} \tag{2.3}$$

where ρ is the density of ceria and S_{BET} is the specific surface area measured by the analyser. The Sauter mean diameter[34] represents the volume/surface area ratio of the samples and indicates the active surface area while the samples are experiencing structural evolutions during the cyclic reactions. The Barrett-Joyner-Halenda (BJH) pore volumes (V_{BJH}) were determined from the adsorption isotherm plots, and the corresponding pore sizes (d_{BJH}) were estimated by:

$$d_{\mathrm{BJH}} = \frac{4V_{\mathrm{BJH}}}{S_{\mathrm{BJH}}} \tag{2.4}$$

where S_{BJH} is the cumulative surface area of pores estimated by the BJH method. The samples were analysed using transmission electron microscopy (TEM, Hitachi H7100FA, operated at 125 kV) to obtain information of the particle size and morphology. Particle size distribution was obtained via the image processing software ImageJ. Field emission scanning electron microscopy was performed with a Zeiss Ultraplus FESEM to obtain information of the surface morphology and porosity.

2.3 Results and Discussion

2.3.1 Ceria Morphologies and Structural Properties

Figure 2.2 shows TEM images of all the ceria powders (Figure 2.2a-h) and an SEM image of the flower-like agglomerate structure (Figure 2.2b). The flame-made ceria consisted of disordered nanoparticles (Figure 2.2e, S2.1) of 9±3 nm in diameter (Table 2.1) agglomerated in a fractal-like porous morphology (Figure 2.2a). The as-synthesised flower-like ceria had a spherical shape made of ultra-fine dense agglomerates (Figure 2.2b, S2.2). The flower-like sphere has an agglomerate size of 3±0.5 μm in diameter, in good agreement to the morphology and agglomerate size distribution observed by Sun et al[31]. The inset of Figure 2.2b and the high magnification TEM images (Figure S2.2a) indicate that the flower-like structure had a hollow centre emphasised by the dark TEM

contrast of the edges with the bright centre[31, 35]. This structure is composed of ultra-fine primary particles of 5±2 nm that forms denser agglomerates than the flame-made particles (Figure 2.2e, 2.2f, S2.1 and S2.2). The sol-gel ceria agglomerates are shown in Figure 2.2c. The primary particles (Figure 2.2g) of the sol-gel agglomerates had a diameter of 22±7 nm (Table 2.1). The commercial ceria had coarser morphology (Figure 2.2d) with most of the grains larger than 100 nm and a dense non-porous grain surface texture. The average primary particle diameter determined from the TEM images was 63 nm (Figure 2.2h) and thus significantly larger than the sol-gel powders (Table 2.1).

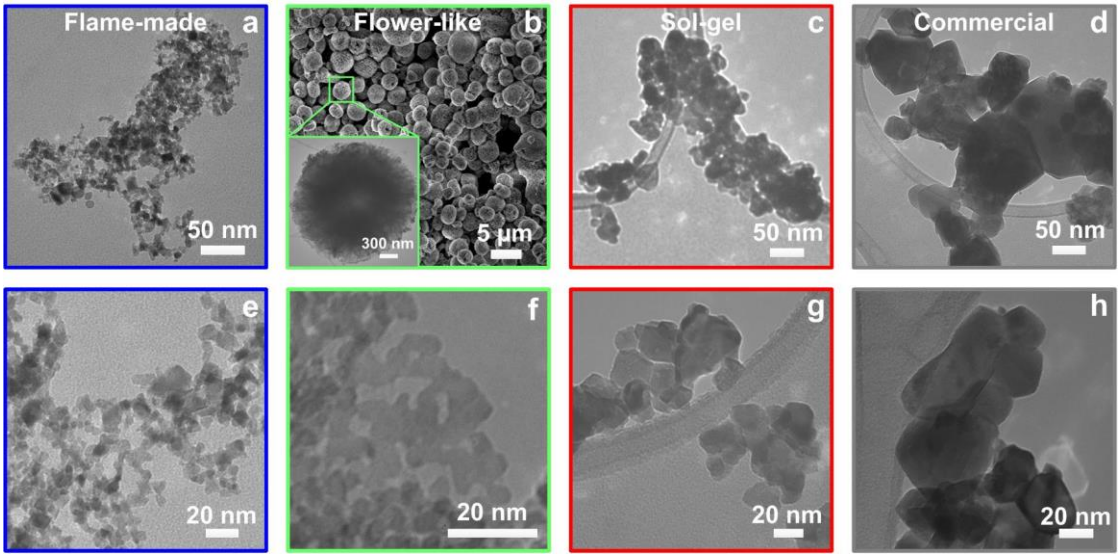

Figure 2.2 SEM and TEM micrographs of the as-prepared nano-micro ceria structures. (a, e) As-prepared flame-made agglomerates showing primary particles of 9 nm. (b, f) As-prepared flower-like 3 µm agglomerates consisted of densely agglomerated nanoparticles of 5 nm. (c, g) As-prepared sol-gel agglomerates showing primary particles of 22 nm. (d, h) As-received commercial agglomerates showing primary particles of 63 nm.

Figure 2.3 shows the XRD spectra of the ceria powders. All four structures consisted of the cubic fluorite CeO_2 phase (JCPDS 34-0394). No additional crystal and amorphous phases were detected indicating a highly crystalline and pure composition.

Notably, the crystal size of the as-prepared samples varied significantly (Table 2.1) from ca. 7 nm of the flame-made and flower-like agglomerates to 84 nm of the commercial ceria. The sol-gel structure had an intermediate crystal size of 18 nm. These crystal sizes match well the primary particle size observed by the TEM analysis (Table 2.1) with the only exception being the flower-like structures where the primary particle size was not clearly discernible.

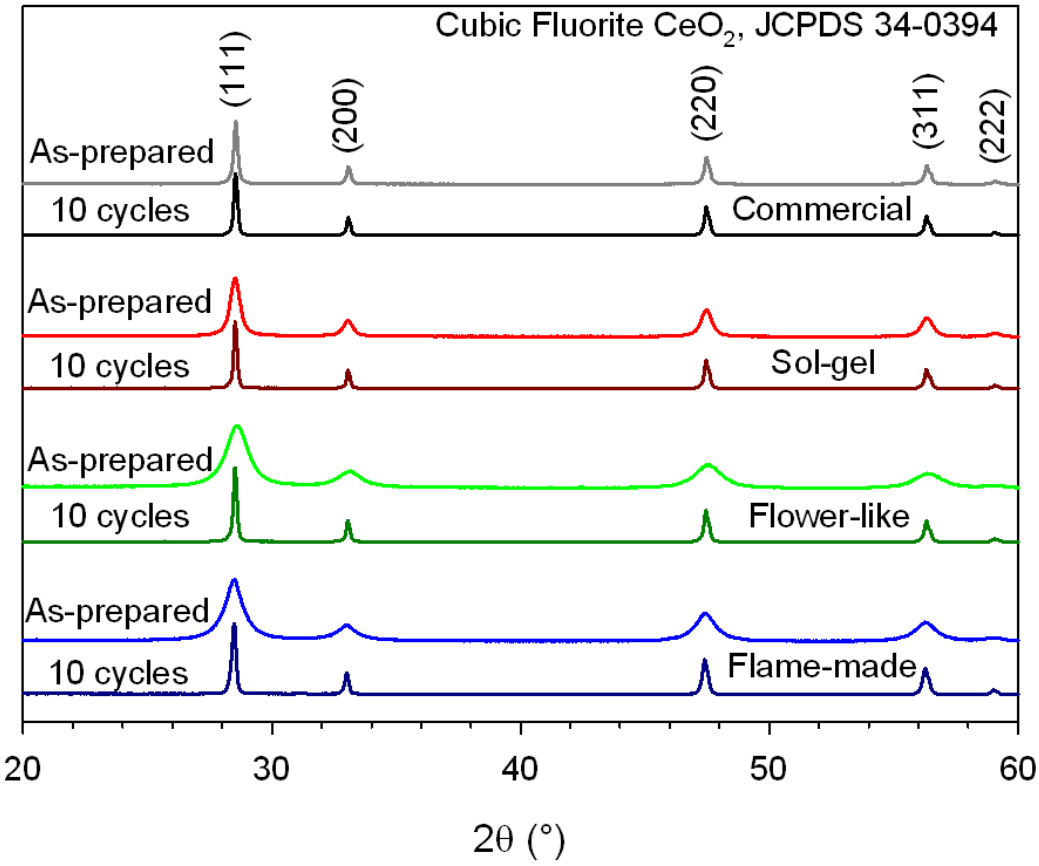

Figure 2.3 XRD patterns of the as-prepared and cycled nano-micro ceria structures and after 10 isothermal MPO-CDS cycles. All material initially had and preserved the cubic fluorite CeO_2 phase.

The N_2 adsorption-desorption analysis summarised in Table 2.1 confirmed the TEM and XRD findings while also providing insights on the specific surface area of these structures, a key parameter for high redox kinetics. The flame-made ceria agglomerates had a high specific surface area of 77 $m^2\ g^{-1}$, resulting in a Sauter mean diameter of ca. 10 nm. It also had the highest pore volume of 0.454 $cm^3\ g^{-1}$. This was 86% higher than

that of the flower-like structures and proved to be an important structural parameter in the following thermochemical cycle performance. The as-synthesised flower-like ceria had the highest SSA of 95 m^2 g^{-1}, corresponding to a Sauter mean diameter of 8.3 nm. The significant difference between the agglomerate size and the Sauter mean diameter confirms its high initial porosity, also indicated by the TEM images. In addition to its high specific surface area, the flower-like ceria had also a 3-5 times higher pore volume than the commercial sub-micro and sol-gel powders. The sol-gel ceria had a 3-4 times higher specific surface area (31 m^2 g^{-1}) than the commercial powders resulting in a Sauter mean diameter of 25.5 nm. Its pore volume was comparable (0.062 cm^3 g^{-1}) to that of the commercial ceria and in line with the TEM analysis (Figure 2.2g and 2.2h) showing mostly a sub-micro inter-grain porosity. The commercial ceria had the lowest specific surface area of 8.15 m^2 g^{-1} resulting in an equivalent Sauter mean diameter of 96 nm and a small pore volume of 0.046 cm^3 g^{-1}. This is in good agreement with their large average crystal size of 84 nm obtained by XRD and dense morphology observed by TEM.

2.3.2 CO_2 Splitting and Syngas Production Performance

The CO_2 splitting and syngas production performance of these nano and sub-micro ceria powders was investigated in a tubular IR furnace. Figure 2.4 shows the instantaneous H_2 and CO production rates per CeO_2 mass of these four distinct structures during 10 isothermal MPO-CDS cycles. To avoid potential impact from organic impurities accumulated on the surface of the ceria on the syngas production, the results of the second cycles are used here to evaluate initial material performance. During the MPO step, production of H_2 and CO was detected immediately after the introduction of CH_4. The H_2 and CO production rates increased very rapidly, reaching a maximum in approximately 3 min. Subsequently, the production rates declined to below instrument detection limits (ca. 1 ppm) in 15 min. This is attributed to depletion of

lattice oxygen resulting in reduction of CeO_2 to $CeO_{2-\delta}$. The flame-made ceria demonstrated a very high peak performance in the second cycle of over 1040 µmol min^{-1} g^{-1} and 490 µmol min^{-1} g^{-1} for H_2 and CO, respectively, twice the peak performance of the flower-like and sol-gel ceria and 3 times more than the commercial sub-micro ceria. This peak performance declined gradually over the 10 cycles, reaching ca. 420 µmol min^{-1} g^{-1} and 210 µmol min^{-1} g^{-1} for H_2 and CO, respectively, in the last cycle. This peak rate is still ca. 50% higher than that of the cycled flower-like and commercial sub-micro ceria.

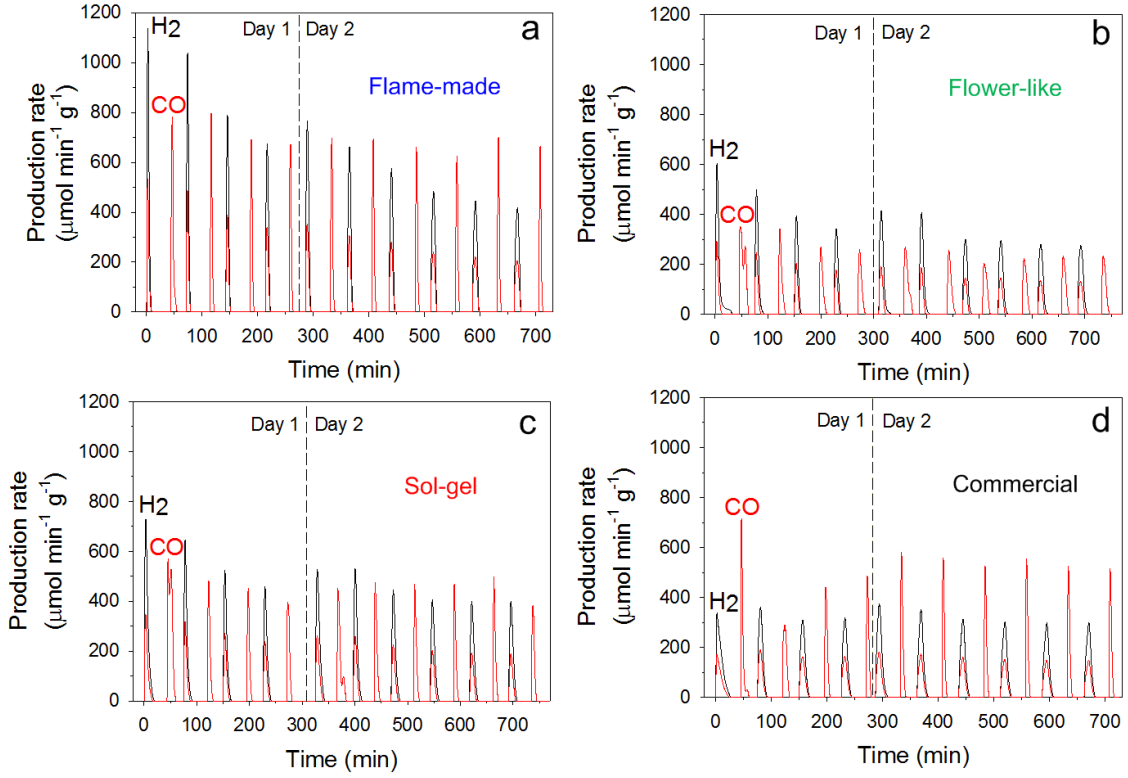

Figure 2.4 H_2 and CO production rates of the (a) flame-made ceria, (b) flower-like ceria, (c) sol-gel ceria and (d) commercial ceria during 10 isothermal MPO-CDS cycles.

During the CDS step, immediate CO production was observed upon introduction of CO_2 as the re-oxidation of the $CeO_{2-\delta}$ started. The production rate of CO (CDS) had a similar profile as that of the H_2 and CO in the MPO step. The maximum synthesis rate was reached within 2 min and declined below the limit of detection in less than 10 min. Specifically, the flame-made ceria achieved a peak production rate in the second cycle

of ca. 800 µmol min^{-1} g^{-1}. However, in contrast to the rapid declining peak rate during the MPO steps, the CDS rates remained relatively stable over the 10 cycles resulting in a CO production rate of ca. 670 µmol min^{-1} g^{-1} in the last cycle. The flower-like ceria peak CO production rate was initially less than 50% of the flame-made ceria, and was also relatively stable over the 10 cycles. The sol-gel ceria peak performance was initially ca. 60% of the flame-made ceria, and stabilised at ca. 450 µmol min^{-1} g^{-1} over the 10 cycles. The commercial sub-micro ceria had an initial CO peak production rate (2^{nd} cycle) of ca. 40% of the flame-made ceria one. However, this rate gradually increased over the 10 cycles and reached a stabilised peak performance of ca. 550 µmol min^{-1} g^{-1}.

The characteristic kinetics and CO_2 splitting performance are understandable by analysis of the redox stoichiometry and considering the following potential side reactions during the MPO-CDS cycles. Among several possible side reactions, the major ones are[36]:

$$CH_4 \rightarrow C\,(s) + 2H_2, \quad \Delta H_{298}^{o} = +\,74.9\ kJ\ mol^{-1} \tag{2.5}$$

$$2CO \leftrightarrow C\,(s) + CO_2, \quad \Delta H_{298}^{o} = -\,172.2\ kJ\ mol^{-1} \tag{2.6}$$

Eq. 2.5 represents the thermal decomposition (cracking) of CH_4, which may occur in the reduction step especially when the available metal oxide approaches its thermodynamic equilibrium (Eq. 2.1).[37] Eq. 2.6 is the Boudouard reaction[36]. It favours CO_2 and elemental carbon formation when the partial pressure of CO in the reduction step is sufficiently high. Both of these side reactions can cause the H_2:CO ratio in the reduction step to deviate from Eq. 2.1, which is undesirable for subsequent syngas processing technologies. More significantly, the resulting elemental carbon deposits on the surface of the metal oxide inhibit the reduction of ceria (Eq. 2.1). The reverse Boudouard reaction can occur in the CDS step when CO_2 is supplied, increasing the net production of CO over that expected from re-oxidation of the reduced ceria (Eq. 2.2a).

Table 2.1 Structural properties of the nano-micro CeO_2 structures before and after 10 isothermal MPO-CDS cycles.

Material	SSA [$m^2\ g^{-1}$]		d_{BET} [nm]		d_{TEM} [nm]		v_{BJH} [$cm^3\ g^{-1}$]		d_{BJH} [nm]		d_{XRD} [nm]	
	Initial	Cycled	Initial	Cycled	Initial	Cycled	Initial	Cycled	Initial	Cycled	Initial	Cycled
Flame-made	77	8	10.2	95.6	9.3±2.4	134.0±53.1	0.454	0.017	20.1	7.4	6.9	42.7
Flower-like	95	4	8.3	183.7	5.2±1.6	220.1±121.5	0.244	0.009	12.2	7.1	7.3	45.0
Sol-gel	31	3	25.5	247.4	22.2±6.8	158.8±73.5	0.062	0.020	9.4	24.6	18.2	50.0
Commercial	8	2	96.2	493.3	63.0±32.7	216.5±124.0	0.046	0.003	24.5	7.1	83.8	86.1

Specific surface area [SSA], Sauter mean diameter [d_{BET}], particle size measured from TEM micrographs [d_{TEM}], BJH adsorption pore volume [v_{BJH}], pore size [d_{BJH}], and crystal size [d_{XRD}].

Table 2.2 Comparison of syngas production rates in CeO_2-based thermochemical redox cycles.

Material and Process	**Reduction step**				**Oxidation step**					Ref.
	T_{red} [K]	$P(CH_4)$ [-]	CO production rate [μmol min^{-1} g^{-1}]	H_2 production rate [μmol min^{-1} g^{-1}]	T_{ox} [K]	$P(CO_2)$ [-]	CO production rate [μmol min^{-1} g^{-1}]	$P(H_2O)$ [-]	H_2 production rate [μmol min^{-1} g^{-1}]	
Flame-made CeO_2 MPO-CDS	1173	0.08	230.4[1]	479.5[1]	1173	0.04	339.4[1]	--	--	This work
CeO_2 MPO-WS	973	0.5	5.8[2]	13.4[2]	773	--	--	0.024	0[2]	Otsuka et al.[25]
$Ce_{0.8}Zr_{0.2}O_2$ MPO-WS	973	0.5	6.9[2]	19.3[2]	773	--	--	0.024	6.7[2]	Otsuka et al.[25]
CeO_2/SiC MPO-WS	1173	0.2	18.8[2]	54.5[2]	1173	--	--	0.455	94.0[2]	Jang et al.[38]
$Ce_{0.8}Zr_{0.2}O_2$/SiC MPO-WS	1173	0.2	19.0[2]	49.2[2]	1173	--	--	0.455	47.4[2]	Jang et al.[38]
CeO_2 MPO-WS	1123	1	40.4[2]	87.5[2]	973	--	--	0.831	16.8[2]	Zhu et al.[39]
$CeFeO_3$ Ce:Fe=7:3 MPO-WS	1123	1	177.0[2]	336.5[2]	973	--	--	0.831	80.2[2]	Zhu et al.[40]
$Ce_{0.07}Zr_{0.93}O_2$ MPO-WS	1073	0.1	6.3[2]	14.0[2]	1073	--	--	0.270	16.8[2]	Jeong et al.[41]
CeO_2 IGR-WS/CDS	1773	0	--	--	1073	0.5	174.3[2]	0.480	160.7[2]	Chueh et al.[1]
CeO_2 IGR-WS+CDS	1800	0	--	--	1100	0.08	9.3[2]	0.475	20.3[2]	Furler et al.[9]
CeO_2 IGR-CDS	1873	0	--	--	<1273	0.95	6.5[2]	--	--	Furler et al.[42]

[1] Average rate of the second cycle. [2] Highest average rate. $P(CH_4)$: partial pressure of CH_4 in the total feed gas flow; $P(CO_2)$: partial pressure of CO_2 in the total feed gas flow; $P(H_2O)$: steam partial pressure in the total feed gas flow; T_{red}: reduction temperature; T_{ox}: oxidation temperature; MPO: methane partial oxidation; CDS: carbon dioxide splitting; WS: water splitting; IGR: inert gas reduction.

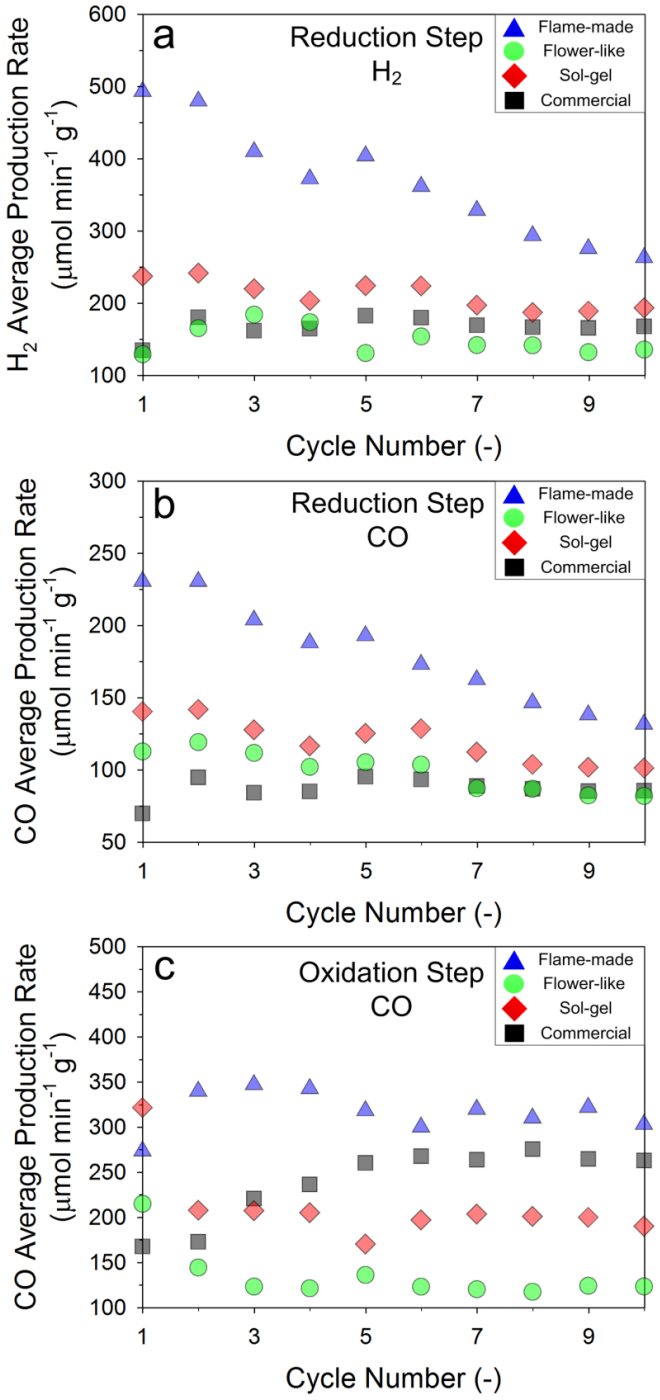

Figure 2.5 H_2 and CO average production rates of the ceria samples during 10 isothermal MPO-CDS cycles. (a) Average production rate of H_2 during the MPO steps over 10 cycles. (b) Average production rate of CO during the MPO steps over 10 cycles. (c) Average production rate of CO during the CDS steps over 10 cycles. Blue triangle: flame-made ceria. Green circle: flower-like ceria. Red diamond: sol-gel ceria. Black square: commercial ceria.

The stability of the syngas production rate of the flame-made ceria after 10 cycles was comparatively investigated against that of the commercial ceria (Figure S2.3). These results show that the performance is nearly stable after 10 cycles with a 50%, 47%, 95% higher production rate of $H_{2\ MPO}$, CO_{MPO} and CO_{CDS} for the flame-made material after 15 cycles.

Figure 2.5 shows the average H_2 and CO production rates for the different ceria structures during the reduction and oxidation steps. In the reduction step, the flame-made ceria (2nd cycle) production rates were ca. 480 µmol min^{-1} g^{-1} and 230 µmol min^{-1} g^{-1} for H_2 and CO (Figure 2.5a and 2.5b), respectively. This is 167% and 145% higher than that of the commercial sub-micro ceria. This is attributed to the higher flux of lattice oxygen reaching the surface of ceria for high SSA materials.[43,44] The initial specific surface area is one of the primary structural properties to influence the initial rate of fuel production in the MPO step. In line with this observation, while the surface area gradually decreased over the 10 cycles due to sintering of nanoparticles, the CO and H_2 production rates of the flame-made ceria declined by more than 40%. However, in the 10th cycle the production rates of the CO and H_2 stabilised and were still 57% and 40% faster than that of the commercial and sol-gel ceria, respectively.

Notwithstanding having the highest specific surface area amongst all ceria structures investigated here, the flower-like ceria had significantly lower initial average production rates than the flame-made ones reaching 165 µmol min^{-1} g^{-1} and 119 µmol min^{-1} g^{-1} for H_2 and CO, respectively, in the reduction step (2nd cycle). In a separate experiment, the as-prepared flame-made and flower-like samples were heated in an inert Ar atmosphere from room temperature to 1173 K at 80 K min^{-1} and thereafter quenched without any reduction or oxidation step. The BET measurements of the quenched samples reveal that during this heating step the specific surface area of the flower-like ceria decreased by ca. 60% (30 m^2 g^{-1} vs 95 m^2 g^{-1}) while that of the flame-made ceria was not

significantly affected (74 m^2 g^{-1} vs 77 m^2 g^{-1}). The poor thermal stability of the flower-like ceria and the related drop in specific surface area explain its surprisingly low syngas production rate in the first cycle. In Figure 2.5, the H_2 and CO average production rates of the flower-like ceria were relatively stable reaching 135 μmol min^{-1} g^{-1} and 81 μmol min^{-1} g^{-1}, respectively, in the 10^{th} cycle. This is less than the rates obtained by the sol-gel structures. This is attributed to the poor thermochemical stability of the flower-like morphology that results in a drastic decrease of its SSA and porosity during the MPO-CDS cycles. Specifically, the small pore size of the flower-like ceria relative to its high specific surface area decreased the initial surface area available for the reactions, resulting in low production rates by flower-like agglomerates since the first cycle. In fact, after 10 cycles the SSA and the pore volume of the flower-like ceria decreased from the initial 95 m^2 g^{-1} and 0.244 cm^3 g^{-1} to only 4 m^2 g^{-1} and 0.009 cm^3 g^{-1} (Table 2.1). This is significantly lower than the flame-made agglomerates that, after 10 cycles, preserved a SSA and a pore volume of 8.2 m^2 g^{-1} and 0.017 cm^3 g^{-1}, respectively.

During the identical MPO step, the H_2 and CO average production rates (2^{nd} cycle) of the sol-gel ceria were ca. 240 μmol min^{-1} g^{-1} and 140 μmol min^{-1} g^{-1}, respectively, and thus about half of the flame-made ones. However, these production rates remained stable over the 10 cycles. This is in line with their initially lower SSA and the relatively good stability of their structural properties over 10 cycles. In particular, their SSA and pore volume decreased from 31 m^2 g^{-1} and 0.062 cm^3 g^{-1} to 3 m^2 g^{-1} and 0.020 cm^3 g^{-1} after 10 cycles. This is attributed to their strongly sintered closed-neck morphology and large grain size (Figure 2.2c and 2.2g) that decrease the thermodynamic potential driving grain coagulation[45]. According to Figure 2.2c, the sol-gel agglomerates had limited surface area for the MPO reaction (Eq. 2.1) and resulted in lower reduction

kinetics. Thus, compared with the flame-made ceria, the production rates of sol-gel ceria were consistently lower.

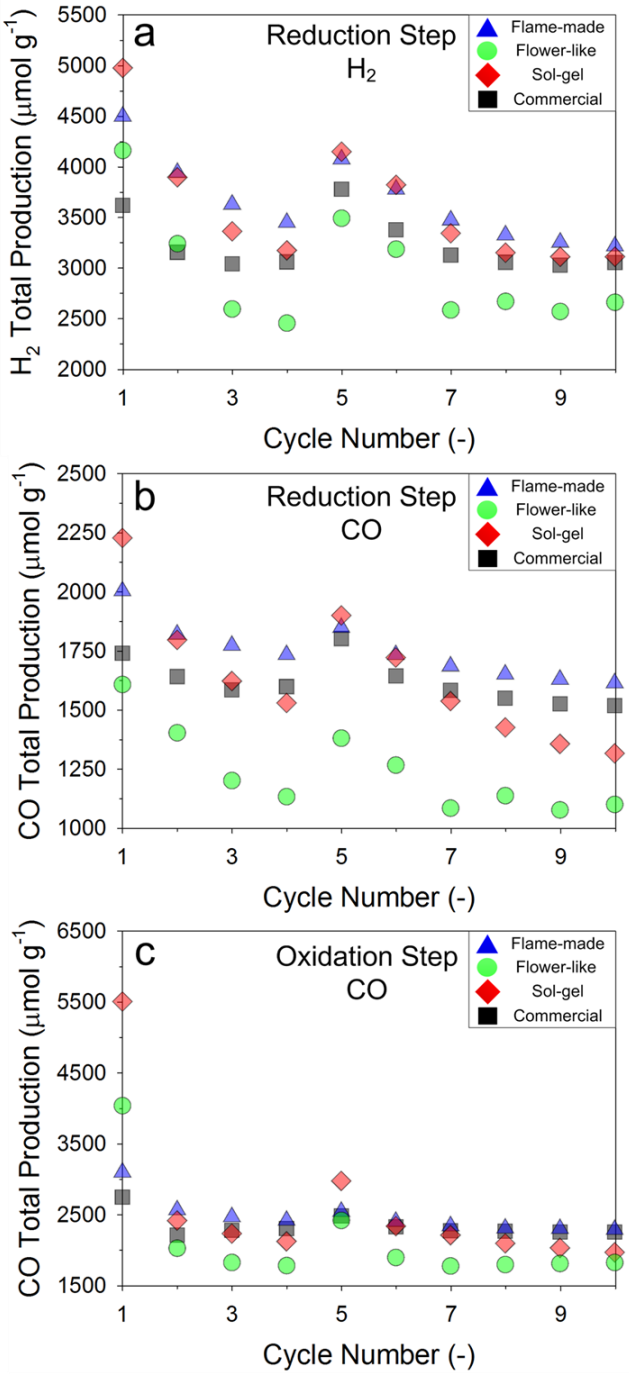

Figure 2.6 H_2 and CO total production of the ceria samples during 10 isothermal MPO-CDS cycles. (a) Total production of H_2 during the MPO steps over 10 cycles. (b) Total production of CO during the MPO steps over 10 cycles. (c) Total production of CO during the CDS steps over 10 cycles. Blue triangle: flame-made ceria. Green circle: flower-like ceria. Red diamond: sol-gel ceria. Black square: commercial ceria.

During the CDS steps (Figure 2.5c), the flame-made ceria had an initial CO production rate of ca. 340 μmol min^{-1} g^{-1} (2^{nd} cycle), which is 97% higher than that of commercial ceria. In contrast to the decline in production rates observed during the MPO steps, the CO production rate in the CDS steps was stable, converging to ca. 300 μmol min^{-1} g^{-1} over 10 cycles. In contrast, the CO production rate of the flower-like and sol-gel ceria had a sharp drop within the first 3 cycles reaching ca. 200 μmol min^{-1} g^{-1} and 125 μmol min^{-1} g^{-1}, respectively, in the last cycle.

A comparison of the syngas production rates of CeO_2-based thermochemical redox cycles is shown in Table 2.2. Here, the average production rates of H_2 and CO during the MPO step are about an order of magnitude higher than that previously reported for other CeO_2-based redox systems, and also 30-40% higher than those of $CeFeO_3$-based materials. In terms of the CDS step, here, a 95% higher CO production rate was achieved than that following an inert gas reduction step[1].

Figure 2.6 shows the total production of H_2 and CO in the MPO and CDS cycles. All ceria structures had similar and relatively stable total syngas production with small variations observed only for the flower-like ceria. Specifically, the total H_2 (MPO), CO (MPO) and CO (CDS) productions averaged over 10 MPO-CDS cycles were 3659.4 μmol g^{-1}, 1748.3 μmol g^{-1}, and 2470.0 μmol g^{-1} for the flame-made ceria; 2956.2 μmol g^{-1}, 1237.7 μmol g^{-1}, and 2115.2 μmol g^{-1} for the flower-like ceria; 3605.0 μmol g^{-1}, 1642.4 μmol g^{-1}, and 2586.7 μmol g^{-1} for the sol-gel ceria; and 3224.2 μmol g^{-1}, 1617.5 μmol g^{-1}, and 2337.3 μmol g^{-1} for the commercial ceria. In the 10^{th} cycle, the H_2 (MPO), CO (MPO) and CO (CDS) production converged towards 3005.2±242.4 μmol g^{-1}, 1386.0±228.3 μmol g^{-1}, and 2080.5±224.3 μmol g^{-1}, respectively, for all structures. This results in a change of stoichiometry (δ) of 0.25±0.01 based on the H_2 (MPO) and CO (MPO) production. The stoichiometry reduction from CeO_2 to $CeO_{1.75}$ obtained here is in agreement to the theoretical thermodynamic calculations[14] indicating a maximum δ of

0.25 during methane-induced reduction of the ceria cubic fluorite crystal structure. Therefore, in this work, the reaction equilibrium is reached for all samples within the redox steps and ceria was fully reduced and oxidised within the thermodynamic stoichiometry value. In comparison to previous isothermal reduction of ceria at 973 K[25], the H_2 and CO productions, here, were up to 401% and 415% higher. This is attributed to both the higher SSA and higher isothermal temperature utilized here. In terms of the CO total production during the CDS step, a significant enhancement was observed here over that reported for the inert gas reduction (IGR) process[1]. Specifically, at a higher isothermal temperature of 1773 K, CDS of ceria following an IGR step resulted in a total production of CO of 455±215 μmol g^{-1}. Here, the CO total production of the flame-made ceria, during the CDS step, are approximately 400% (2271.4±23.3 μmol g^{-1}) higher. This is in agreement with the theoretical thermodynamic potential indicating that at 1773 K conventional IGR is only capable to provide a change in stoichiometry δ of 0.06.[5] Here, by incorporating MPO in the reduction step, the obtainable reduction in stoichiometry was significantly increased by more than four times.

The flame-made ceria had a nearly constant H_2:CO ratio of 2.1±0.1 in the MPO step over the 10 cycles (Figure 2.7a). This is in good agreement with the theoretical ratio of 2 expected by the complete MPO reaction (Eq. 2.1). The slightly increased H_2 content (ca. 5%) may be attributed to the thermal decomposition of methane (Eq. 2.5). Noticeably, this effect was only significant in the initial cycles of the day and the ratios converged toward the theoretical value of 2 rapidly. The elevated H_2:CO ratios observed at the beginning of the second testing day are tentatively attributed to adsorption of atmospheric carbonaceous species during the cooling down step in the previous day. The flower-like and sol-gel ceria had systematically higher H_2:CO ratios than the theoretical and flame-made ones with a value of 2.4±0.1 and 2.2±0.1, respectively. The commercial ceria had a H_2:CO ratio of 2.0±0.1, which is also close to the theoretical

prediction. Most notably, the H_2:CO ratios of the flower-like, sol-gel and commercial ceria increased in the last 3 cycles, indicating a growing contribution of undesired reactions (Eq. 2.5).

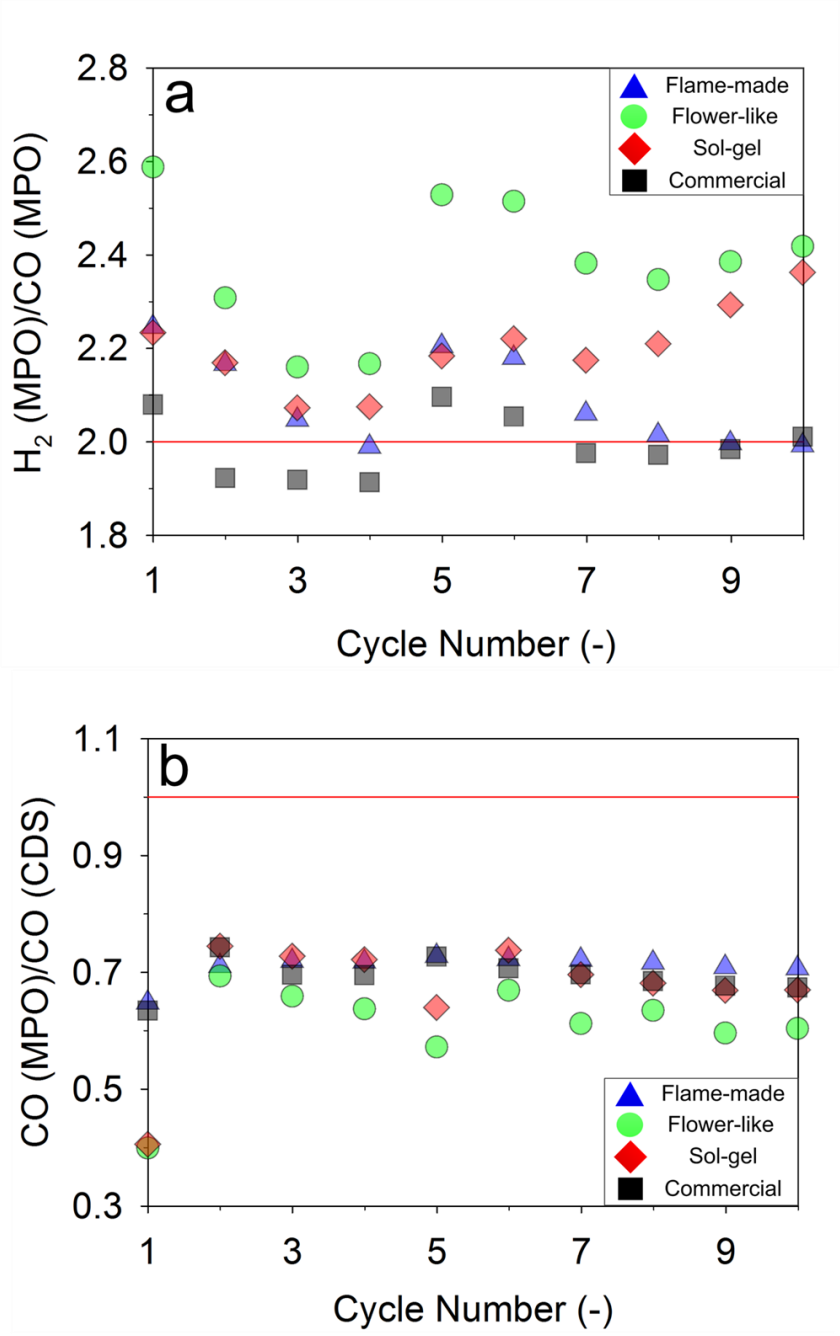

Figure 2.7 Product ratios of the flame-made (blue triangles), flower-like (green circles), sol-gel (red diamonds) and commercial (black square) ceria during 10 isothermal MPO-CDS cycles. Red lines show the theoretical values. (a) H_2:CO ratios during the MPO steps. (b) Per cycle ratios of CO produced from the MPO and CDS steps.

Figure 2.7b shows the ratio of CO produced during the MPO and CDS steps (CO_{MPO}/CO_{CDS}). According to reactions Eq. 2.1 and 2.2a, a theoretical value of 1 is expected for a perfect MPO-CDS cycle with no side reactions (Eq. 2.5 and Eq. 2.6). Notably, all ceria powders resulted in CO_{MPO}/CO_{CDS} below 1. The flame-made ceria had the closest ratio to the theoretical one with a CO_{MPO}/CO_{CDS} of 0.71±0.02. The flower-like, sol-gel and commercial ceria had lower ratios and higher cycle to cycle deviations of 0.60±0.08, 0.67±0.10, and 0.69±0.03, respectively. According to Eq. 2.5, during the MPO step formation of carbon can decrease the total production of CO. As a result, during the subsequent CDS step, oxidation of the elemental carbon accumulated during the reduction step can increase the total CO production according to the reverse Boudouard reaction (Eq. 2.6).[46] Additionally, the isothermal temperature of 1173 K, utilized here, favours CO vs CO_2 formation.[46, 47] As a result, the enhanced CO production in the oxidation step indicates that the reverse Boudouard reaction may contribute to maintain the activity of the ceria surface by removing some of the deposited carbon formed in the reduction step, although this is a potential source of inefficiency in the overall process.

According to the TGA-FTIR analysis (Figure S2.5), all the 10-cycled samples had a weight loss that can be attributed to the oxidation of carbon deposits. Specifically, the weight percentage of carbon mass per sample is 3.7%, 6.2%, 4.4% and 4.5% for the flame-made, flower-like, sol-gel and commercial ceria, respectively. The higher amount of carbon deposition observed for the cycled flower-like ceria is in agreement to its H_2:CO (MPO) and CO_{MPO}:CO_{CDS} ratios (Figure 2.7), where both ratios deviate the most from the theoretical ratios. The flame-made ceria had the smallest carbon content (ca. 3.7%).

2.3.3 Thermochemical Stability and Cycling Performance

TEM, XRD and N_2 adsorption-desorption isotherms of the cycled nanostructured ceria and the commercial sub-micro ceria powders were investigated to assess the impact of the structural stability on the redox kinetics and syngas production performance. Figure 2.8 shows that, compared to as-prepared structures, all ceria morphologies underwent a distinct extent of restructuring during the MPO-CDS cycles. For example, the ultrafine flame-made agglomerates underwent significant growth resulting in strongly sintered sub-micro primary particles of ca. 134±53 nm. In fact, after 10 cycles the flame-made particles had a specific surface area of 8.3 $m^2 g^{-1}$ (Table 2.1), and thus a fraction of the initial one (94.9 $m^2 g^{-1}$). Concurrently, the flame-made ceria experienced significant crystal growth from 7 nm to 43 nm (Table 2.1). This higher degree of sintering resulting in 89% loss in specific surface area and 96% loss in pore volume, reduces the solid surface available for the redox reactions (Eq. 2.1 and 2.2a), and explains the ca. 40% drop in CO and H_2 production rates in the MPO step. Notably, the flame-made agglomerates had still the largest SSA amongst all the cycled structures. This partially explains their higher H_2 and CO production rate after 10 cycles (Figure 2.4). Furthermore, the larger fraction of pore volume (Table 2.1) maintained by the flame-made structures after cycling (0.017 $m^2 g^{-1}$) also contributes to increased oxygen transport during the MPO step.

The flower-like ceria agglomerates underwent the most intense sintering (Figure 2.8b), shrinking in size by 60% and losing the hollow morphology of the as-prepared samples (Figure 2.2b). Their morphology restructured from the porous agglomerates of nanoparticles (Figure 2.2f) to centred micro grains formed by sub-micro agglomerates. According to the Ostward ripening mechanism,[48] smaller crystals and particles tend to dissociate and redeposit on the surfaces of larger structures in order to minimise the overall surface energy. Each flower-like agglomerate was initially ca. 3 μm in diameter, whereas the individual particles forming the agglomerates of the structure were less than

10 nm in size. Eventually, all particles of the flower-like agglomerate collapsed filling the hollow centre and leading to a substantial 96% decrease in specific surface area and pore volume (Table 2.1) reducing redox kinetics.

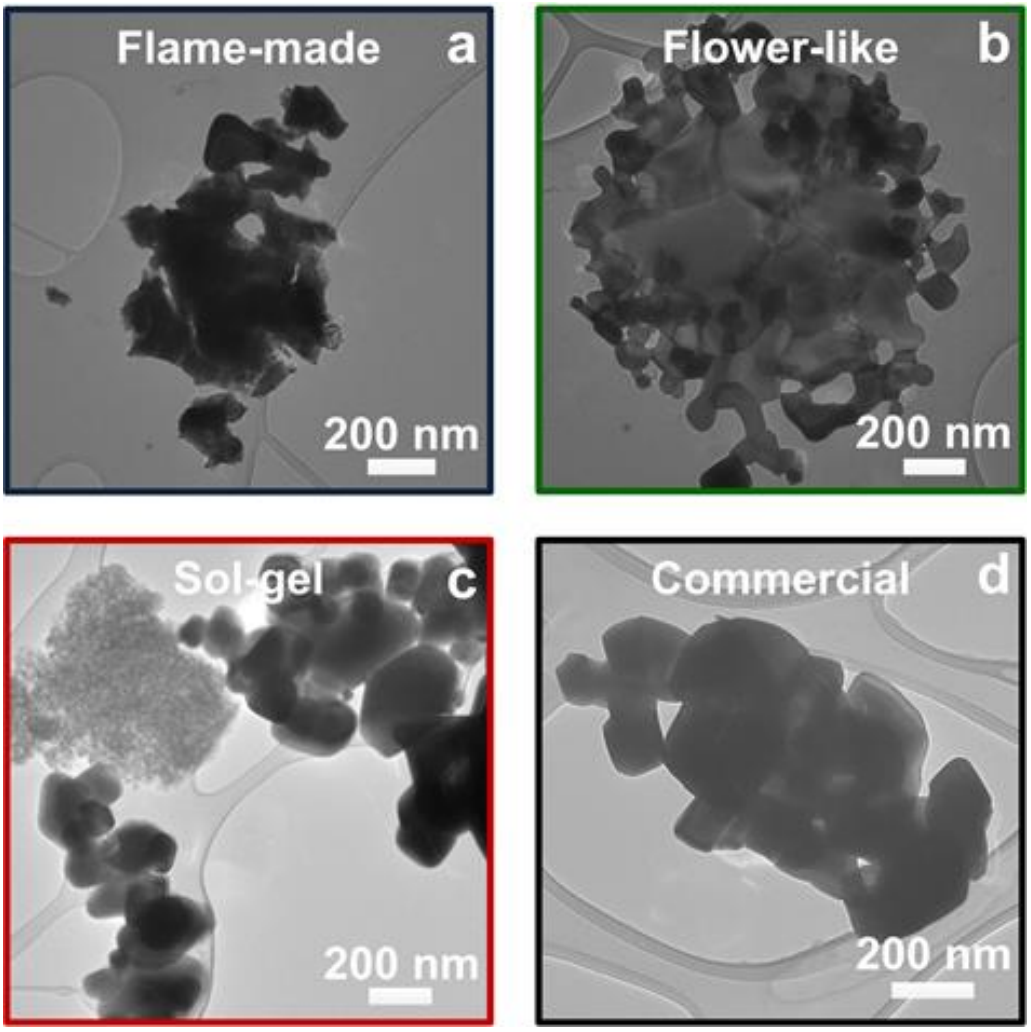

Figure 2.8 TEM micrographs of the nano-micro ceria structures after 10 isothermal MPO-CDS cycles. (a) Cycled flame-made agglomerates showing sintered particles of 130 nm. (b) Cycled flower-like 1 µm agglomerates showing centred micro grains formed by sub-micro agglomerates. (c) Cycled sol-gel agglomerates showing primary particles of 160 nm. (d) Cycled commercial agglomerates showing primary particles of 220 nm.

In contrast to high SSA materials, the sol-gel ceria (Figure 2.8c) shows less variation in morphology with growth in particle size from 22±7 nm to 159±74 nm. Interestingly, the sol-gel particles were less sintered than the flame-made, flower-like and commercial

sub-micro ones. This leads to a last-cycle pore volume of 0.020 cm^3 g^{-1} (Table 2.1), the largest among all structures. The retained porosity of the sol-gel ceria is expected to enhance the gas transport of gas molecules to the ceria surface. As a result the sol-gel ceria had a better cycling stability over the 10 cycles. Nevertheless, the sol-gel ceria had a large decrease in specific surface area of ca. 90%, and its crystals grew from 18 nm to 50nm, leading to slower reaction kinetics than the flame-made structures.

Similarly to the sol-gel ceria, the commercial sub-micro ceria (Figure 2.8d) had no significant structural variation after the reaction tests, with only minor growth in particle size. The initial larger particles of the commercial sub-micro ceria with low specific surface area, low porosity and limited grain boundaries resulted in a lower thermodynamic potential for sintering and grain growth.[49] Accordingly, the specific surface area of the commercial sub-micro ceria shrunk from 8.15 m^2 g^{-1} to 1.89 m^2 g^{-1} and its crystal size remained almost constant growing from 84 nm to 86 nm. However, as the commercial ceria had the lowest SSA and pore volume of 0.003 cm^3 g^{-1} it had also consistently the slowest redox kinetics during the MPO and CDS cycles.

Overall, the less agglomeration of flame-made ceria compared to the other three counterparts after 10 redox cycles is not surprising. As was discussed in Section 1.5, compared to other lower temperature hydrothermal synthesis techniques, FSP features high synthesis temperature (2600-2800 K) and rapid thermal quenching which enables the high crystallinity of the ceria nanoparticles and minimizes carbon soot and/or hydroxyl group surface deposits. The relatively stabilized surface chemistry of flame-made ceria tentatively attributes to its stable structural performance in harsh thermochemical conditions.

2.4 Conclusions

The impact of ceria structural features on its syngas production performance during two-step isothermal redox cycles for four different nano and micro morphologies was

investigated. Highly porous flame-made agglomerates composed of small crystalline particles were determined as the best performing morphology with initial production rates of H_2 and CO up to 167% higher than that of commercial sub-micro ceria. Upon 10 isothermal redox cycles at 1173 K, these flame-made structures still maintained at up to 57% faster production rates. It was shown that the high porosity of the flame-made agglomerates was important in inhibiting sintering and grain growth. Notably, higher specific surface area flower-like morphologies collapsed and densified rapidly, and exhibited the slowest kinetics. Overall, these flame-made nanostructured agglomerates demonstrated the highest H_2 and CO production rates so far reported for ceria in two-step thermochemical cycles while utilization of a MPO reduction step resulted in the highest redox capacity of 0.25. These findings provide a robust set of structural properties, namely high specific surface area, low grain density and large mesopore size, to engineer efficient materials for enhanced solar fuel production by high temperature thermochemical cycles. Future work is recommended to evaluate the difference in ceria reducibility among these morphologies using chemisorption experiments, such as H_2 or CH_4 temperature programmed reductions. Surface XPS characterization of the as-prepared particles may provide some further insights of their chemical composition that could affect initial performance in the thermochemical cycles. Additionally, XPS characterization of the reduced and oxidized ceria samples may also reveal the degree of reduction and the relative oxygen vacancy concentration that give rise to the stable performance by flower-like and sol-gel ceria in the later stage of the 10 cycles.

2.5 Supplementary Information

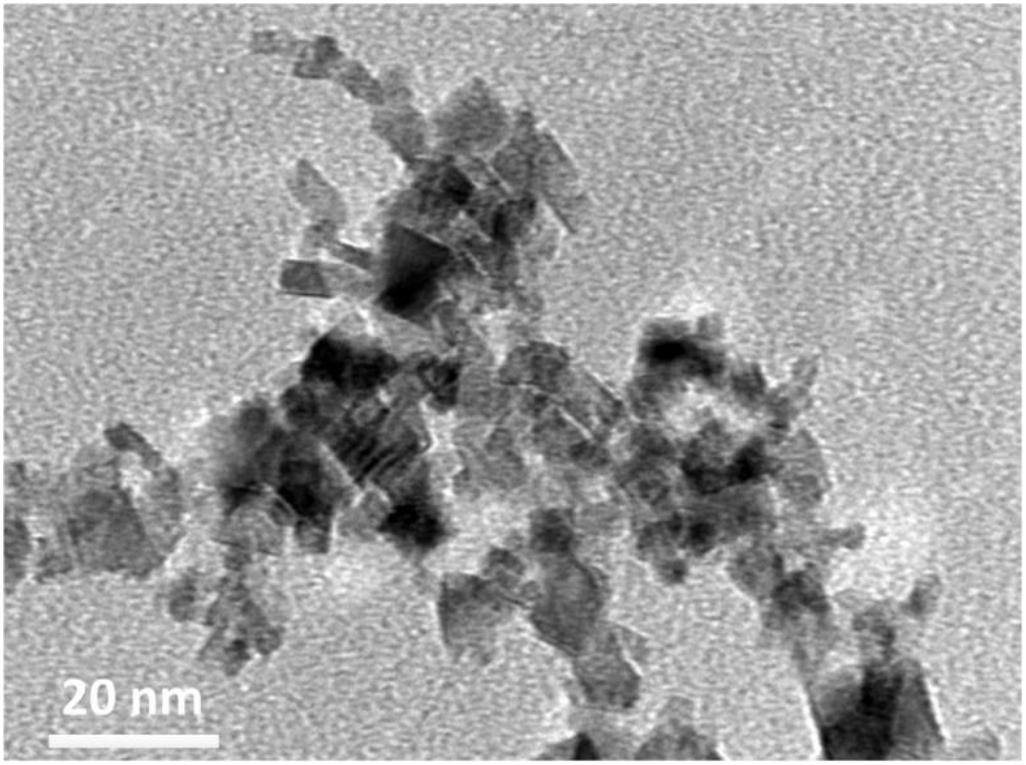

Figure S2.1 TEM images of the as-prepared flame-made agglomerates showing primary particles of 6-13 nm.

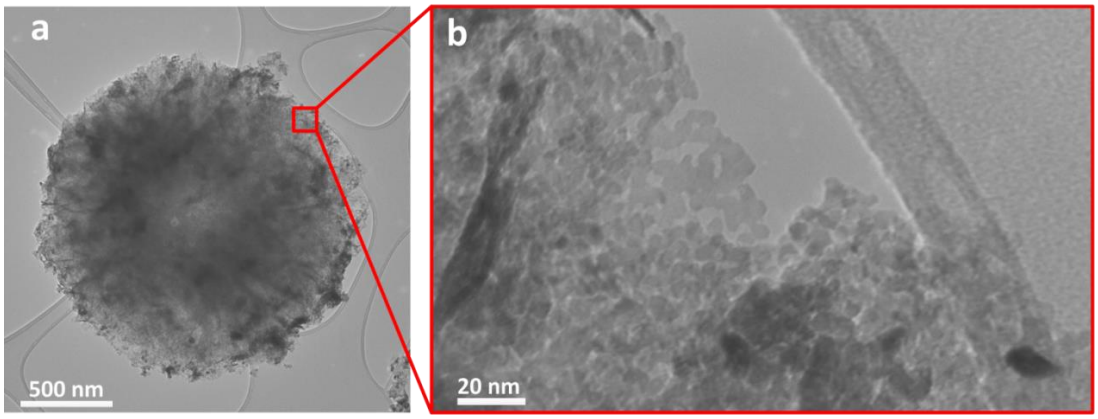

Figure S2.2 TEM micrographs of the as-prepared flower-like agglomerates showing (a) a single flower-like spherical agglomerate, and (b) the primary particles.

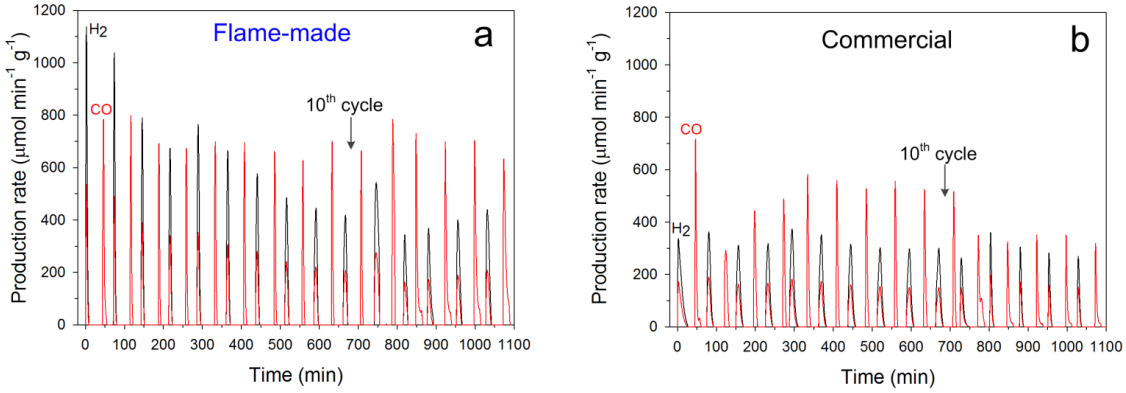

Figure S2.3 H_2 and CO production rates of the (a) flame-made ceria and (b) commercial ceria during 15 isothermal MPO-CDS cycles at 1173 K.

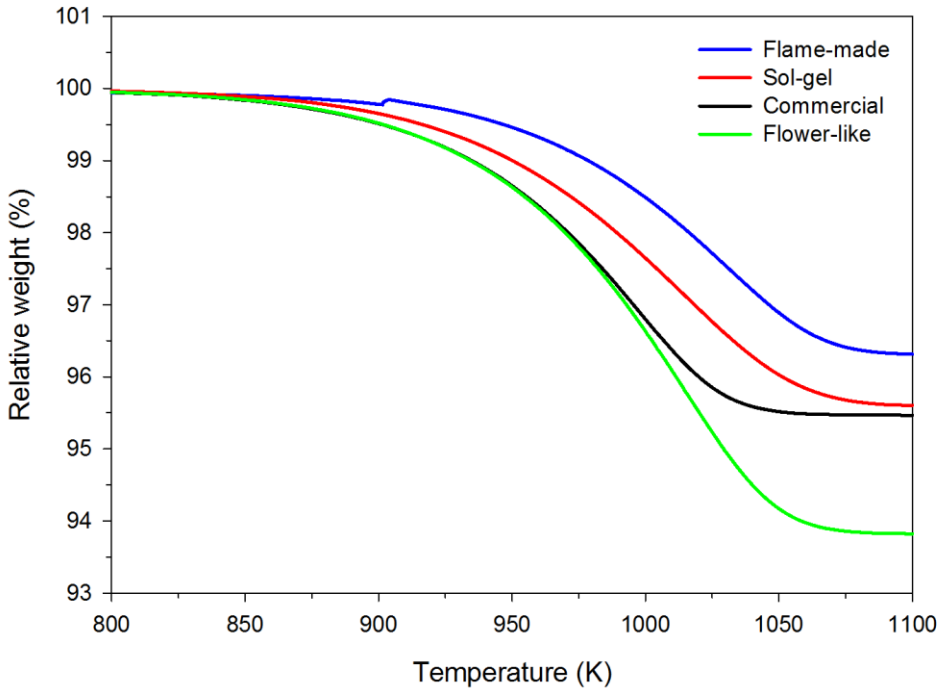

Figure S2.4 TGA profile in air of the flame-made (blue), flower-like (green), sol-gel (red) and commercial (black) ceria after 10 MPO-CDS cycles. Measurement conditions: heating rate 5 K min^{-1}, air flow rate 100 mL min^{-1}, sample size 25-35 mg.

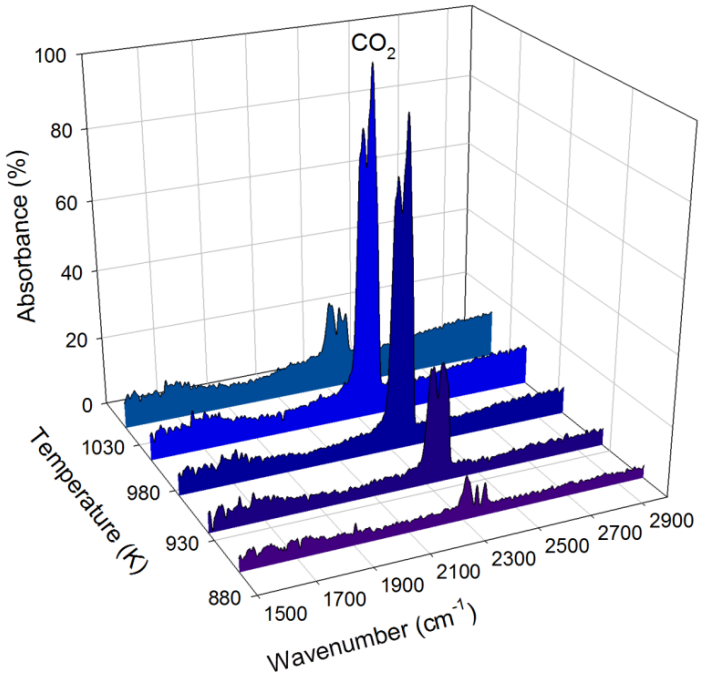

Figure S2.5 FTIR-EGA profile of CO_2 evolution during the temperature programmed oxidation of the flame-made ceria after 10 MPO-CDS cycles. CO_2 production is attributed to oxidation of the carbon deposits.

2.6 References

1. W. C. Chueh, C. Falter, M. Abbott, D. Scipio, P. Furler, S. M. Haile and A. Steinfeld, *Science*, 2010, **330**, 1797-1801.
2. L. J. Venstrom, R. M. De Smith, Y. Hao, S. M. Haile and J. H. Davidson, *Energ. Fuel*, 2014, **28**, 2732-2742.
3. C. L. Muhich, B. D. Ehrhart, I. Al-Shankiti, B. J. Ward, C. B. Musgrave and A. W. Weimer, *WIREs Energ. Environ.*, 2016, **5**, 261-287.
4. B. Bulfin, F. Call, M. Lange, O. Lubben, C. Sattler, R. Pitz-Paal and I. V. Shvets, *Energ. Fuel*, 2015, **29**, 1001-1009.
5. R. Bader, L. J. Venstrom, J. H. Davidson and W. Lipinski, *Energ. Fuel*, 2013, **27**, 5533-5544.
6. C. L. Muhich, B. W. Evanko, K. C. Weston, P. Lichty, X. Liang, J. Martinek, C. B. Musgrave and A. W. Weimer, *Science*, 2013, **341**, 540-542.

7. M. Roeb, M. Neises, N. Monnerie, F. Call, H. Simon, C. Sattler, M. Schmucker and R. Pitz-Paal, *Materials*, 2012, **5**, 2015-2054.

8. J. R. Scheffe and A. Steinfeld, *Mater. Today*, 2014, **17**, 341-348.

9. P. Furler, J. R. Scheffe and A. Steinfeld, *Energy Environ. Sci.*, 2012, **5**, 6098-6103.

10. T. Kodama, T. Shimizu, T. Satoh, M. Nakata and K. I. Shimizu, *Sol. Energy*, 2002, **73**, 363-374.

11. T. Kodama, T. Shimizu, T. Satoh and K.-I. Shimizu, *Energy*, 2003, **28**, 1055-1068.

12. K. Otsuka, Y. Wang, E. Sunada and I. Yamanaka, *J. Catal.*, 1998, **175**, 152-160.

13. A. Steinfeld, M. Brack, A. Meier, A. Weidenkaff and D. Wuillemin, *Energy*, 1998, **23**, 803-814.

14. P. T. Krenzke and J. H. Davidson, *Energ. Fuel*, 2014, **28**, 4088-4095.

15. H. Schulz, *Appl. Catal. A Gen.*, 1999, **186**, 3-12.

16. K. Waugh, *Catal. Today*, 1992, **15**, 51-75.

17. A. P. York, T. Xiao and M. L. Green, *Top. Catal.*, 2003, **22**, 345-358.

18. W. C. Chueh and S. M. Haile, *Philos. T. R. Soc. A*, 2010, **368**, 3269-3294.

19. A. Le Gal, S. Abanades and G. Flamant, *Energ. Fuel*, 2011, **25**, 4836-4845.

20. J. R. Scheffe, R. Jacot, G. R. Patzke and A. Steinfeld, *J. Phys. Chem. C*, 2013, **117**, 24104-24114.

21. M. Kang, J. Zhang, C. Wang, F. Wang, N. Zhao, F. Xiao, W. Wei and Y. Sun, *RSC Adv.*, 2013, **3**, 18878-18885.

22. H. P. Dasari, K. Ahn, S. Y. Park, H. I. Ji, K. J. Yoon, B. K. Kim, H. J. Je, H. W. Lee and J. H. Lee, *Int. J. Hydrog. Energy*, 2013, **38**, 6097-6103.

23. Q.-L. Meng, C.-i. Lee, T. Ishihara, H. Kaneko and Y. Tamaura, *Int. J. Hydrog. Energy*, 2011, **36**, 13435-13441.

24. B. Bulfin, F. Call, J. Vieten, M. Roeb, C. Sattler and I. V. Shvets, *J. Phys. Chem. C*, 2016, **120**, 2027-2035.

25. K. Otsuka, Y. Wang and M. Nakamura, *Appl. Catal. A Gen.*, 1999, **183**, 317-324.

26. H. Cordatos, T. Bunluesin, J. Stubenrauch, J. M. Vohs and R. J. Gorte, *J. Phys. Chem.*, 1996, **100**, 785-789.

27. L. J. Venstrom, N. Petkovich, S. Rudisill, A. Stein and J. H. Davidson, *J. Sol. Energ. Eng.*, 2012, **134**, 011005.

28. M. Fathi, E. Bjorgum, T. Viig and O. A. Rokstad, *Catal. Today*, 2000, **63**, 489-497.

29. A. Tricoli, M. Graf and S. E. Pratsinis, *Adv. Funct. Mater.*, 2008, **18**, 1969-1976.

30. N. Nasiri, R. H. Bo, F. Wang, L. Fu and A. Tricoli, *Adv. Mater.*, 2015, **27**, 4336-4343.

31. C. W. Sun, J. Sun, G. L. Xiao, H. R. Zhang, X. P. Qiu, H. Li and L. Q. Chen, *J. Phys. Chem. B*, 2006, **110**, 13445-13452.

32. *US Pat.*, 3330697, 1967.

33. P. Jana, A. Víctor, J. M. Coronado and D. P. Serrano, *Int. J. Hydrog. Energy*, 2010, **35**, 10285-10294.

34. F. Scala, *Fluidized bed technologies for near-zero emission combustion and gasification*, Elsevier, 2013.

35. W. Xu, J. Li and J. Sun, *RSC Adv.*, 2015, **5**, 81407-81414.

36. B. C. Enger, R. Lodeng and A. Holmen, *Appl. Catal. A Gen.*, 2008, **346**, 1-27.

37. J. H. Kwak, G. Y. Han and K. J. Yoon, *Int. J. Hydrog. Energy*, 2013, **38**, 8293-8305.

38. J. T. Jang, K. J. Yoon, J. W. Bae and G. Y. Han, *Sol. Energy*, 2014, **109**, 70-81.

39. X. Zhu, H. Wang, Y. Wei, K. Li and X. Cheng, *J. Nat. Gas Chem.*, 2011, **20**, 281-286.

40. Z. Xing, W. Hua, W. Yonggang, L. Kongzhai and X. Cheng, *J. Rare Earth.*, 2010, **28**, 907-913.

41. H. H. Jeong, J. H. Kwak, G. Y. Han and K. J. Yoon, *Int. J. Hydrog. Energy*, 2011, **36**, 15221-15230.

42. P. Furler, J. Scheffe, D. Marxer, M. Gorbar, A. Bonk, U. Vogt and A. Steinfeld, *PCCP*, 2014, **16**, 10503-10511.

43. H. Wang, W. Yang, C. Tablet and J. Caro, *Diffusion Fundamentals, J. Kärger, P. Heitjans, F. Grinberg, G. Schütz, www. diffusion-fundamentals. org*, 2005.

44. C. T. Campbell and C. H. Peden, *Science*, 2005, **309**, 713-714.

45. A. Kobata, K. Kusakabe and S. Morooka, *AIChE J.*, 1991, **37**, 347-359.

46. J.-W. Snoeck, G. Froment and M. Fowles, *Ind. Eng. Chem. Res.*, 2002, **41**, 4252-4265.

47. J. B. Claridge, M. L. H. Green, S. C. Tsang, A. P. E. York, A. T. Ashcroft and P. D. Battle, *Catal. Lett.*, 1993, **22**, 299-305.

48. A. D. McNaught and A. D. McNaught, *Compendium of chemical terminology*, Blackwell Science Oxford, 1997.

49. C. T. Campbell, S. C. Parker and D. E. Starr, *Science*, 2002, **298**, 811-814.

Chapter Three

Earth-Abundant Transition Metal Oxides with Extraordinary Reversible Oxygen Exchange Capacity for Efficient Thermochemical Synthesis of Solar Fuels

Publication relevant to this chapter:

X. Gao, G. Liu, Y. Zhu, P. Kreider, A. Bayon, T. Gengenbach, T. Lu, Y. Liu, J. Hinkley, W. Lipiński and A. Tricoli, (2018), *Earth-Abundant Transition Metal Oxides with Extraordinary Reversible Oxygen Exchange Capacity for Efficient Thermochemical Synthesis of Solar Fuels*. Nano Energy, 50, 347-358.

Abstract

Efficient storage of solar and wind power is one of the most challenging tasks still limiting the utilization of the prime but intermittent renewable energy sources. The direct storage of concentrated solar power in renewable fuels via thermochemical splitting of water and carbon dioxide on a redox material is a scalable approach with up to 54% solar-to-fuel conversion efficiency. Despite progress, the search for earth-abundant materials that can provide and maintain high H_2 and CO production rates over long period of high-temperature cycles continues. Here, a strategy to unlock the use of manganese was reported. As the 12th most abundant element in the Earth's crust, manganese can be used for thermochemical synthesis of solar fuels, achieving superior thermochemical stability, oxygen exchange capacity, and up to seven times higher mass-specific H_2 and CO yield than cerium dioxide. Incorporation of a small fraction of cerium ions in the manganese (II,III) oxide crystal lattice drastically increases its oxygen ion mobility, allowing its reduction from oxide to carbide during methane partial oxidation with simultaneous Ce exsolution. High CO_2 and H_2O splitting rates are achieved by re-oxidation of the carbide to manganese (II) oxide with simultaneous reincorporation of the cerium ions. The oxide to carbide reaction is highly reversible, achieving remarkable CO_2 splitting rates over 100 thermochemical cycles of methane partial oxidation and CO_2 splitting, and preserving the initial oxygen exchange capacity of 0.65 mol_O mol_{Mn}^{-1} and 89% of the fuel production rates. Due to this extraordinarily high reversible oxygen exchange capacity, the 3% Ce-doped manganese oxide achieves an average mass-specific CO yield for CO_2 splitting of 17.72 $mmol_{CO}$ g^{-1}, which is significantly higher than that previously achieved in thermochemical redox cycles. More generally, these findings suggest that incorporation of small soluble amounts of cerium in earth-abundant transition metal oxides like manganese oxide is a powerful approach to enable solar thermochemical fuel synthesis.

3.1 Introduction

Reduction of anthropogenic carbon emissions is a pivotal task requiring significant progress in renewable energy conversion and storage technologies. Direct synthesis of renewable fuels via solar thermochemical splitting of water and carbon dioxide can enable the use of this prime renewable energy source for transport, off-the-grid power generation and storage as well as production of numerous commodities. Extensive efforts have been devoted to find efficient processes that can reduce the excessively high temperatures (> 3300 K) required for direct thermal dissociation of CO_2 and H_2O into CO, H_2 and O_2, and facilitate the separation of these gases[1, 2]. Two-step reduction-oxidation (redox) cycles using a metal oxide as an intermediate oxygen exchange material are one of the most promising processes for large-scale water and carbon dioxide splitting[2-4]. Recently, it was shown that by promoting the reduction of the metal oxide material with methane partial oxidation (MPO) rather than by inert gas sweeping (IGS), it is possible to decrease the required reaction temperature from 1600 K to less than 1200 K[5-7]. This MPO-driven metal oxide reduction also increases the solar-to-fuel conversion efficiency limit from 19% for the IGS-driven cycles to 54%[1, 7-9]. Notably, the resulting CO and H_2 products can be adjusted to match the required composition ratio for production and downstream processing of syngas, providing a simple pathway for large-scale synthesis of liquid fuels via established industrial solutions such as the Fischer–Tropsch process.

A major challenge of solar thermochemical redox cycles is the search for earth-abundant low-cost materials that can provide high oxygen exchange capacity and fast fuel production rates over thousands of high temperature cycles in harsh environmental conditions. Many binary, ternary, and complex oxides such as ferrites and perovskites have been explored, with the highest performing materials including CeO_2[10-12], $Ce_xZr_{1-x}O_2$[13], $FeAl_2O_4$[14] and $La_xSr_{1-x}Mn_yAl_{1-y}O_3$[15-17]. Nanostructured cerium dioxide (CeO_2)

remains the benchmark material for thermochemical cycles, featuring high mass-specific production rates of H_2 and CO[12]. Despite the fast reaction kinetics, CeO_2 provides only low oxygen exchange capacities of below 0.25 mol_O mol_{Ce}^{-1}[7, 12], while maintaining its cubic fluorite crystal structure. Additionally, CeO_2 has been reported to suffer from a decline in production rates, due to loss of surface area after the initial cycles at moderate temperatures (1173 K) [1, 12, 18, 19]. Enhancement of the initial oxygen exchange capacity and morphological stability by using support materials such as MgO has resulted in a maximum of only 0.43 mol_O mol_{Ce}^{-1} at 1273 K. Since the oxygen exchange capacity provides the upper limit for the fuel production of each cycle, it is critical to develop materials that provide and maintain higher oxygen exchange capacity than CeO_2 in harsh thermochemical environments. In addition, cerium is a rare earth element, and while it is the most abundant of the lanthanides with a content in the Earth's crust of around 70 ppm, its extraction from natural deposits is laborious posing limitations for its future use in such large-scale energy conversion processes[20].

In search of higher oxygen exchange capacities and more earth-abundant cations, numerous transition metals have been explored as alternative to cerium, including $BaMn_xFe_{1-x}O_3$[15], $Ni_xFe_{3-x}O_4$[21], and $La_xSr_{1-x}MnO_3$[16]. Notwithstanding their extraordinary abundancy, iron-based metal oxides suffer from even faster deactivation than CeO_2[15, 22]. As an alternative, manganese is the 12th most abundant element in the Earth's crust with a concentration of 1000 ppm, and its oxides can be readily obtained by refining low-cost minerals such as pyrolusite and hausmannite[23-25]. Small fractions of manganese ions have been incorporated into benchmark metal oxides, such as CeO_2[26] and perovskites[17], demonstrating improved oxygen exchange capacity and overall H_2 yield in thermochemical water splitting[26]. However, there are currently no studies reporting the direct use of manganese oxide for thermochemical water or CO_2 splitting, due to thermodynamic limitations. An indirect three-step cycle for H_2 generation was

demonstrated by utilizing MnO and NaOH, subsequent hydrolysis of the birnessite mineral phase to generate Mn_2O_3 and regenerate NaOH, followed by high-temperature reduction of Mn_2O_3 to MnO[27-31]. The latter approach suffers from energy losses due to the significant temperature swings (ca. 750 K) between the reduction and the hydrolysis steps, and incomplete recovery of sodium during hydrolysis.

Here, a strategy to enhance the reaction rates and drastically increase the oxygen exchange capacity of manganese oxide is presented. It unlocks the use for efficient direct synthesis of solar fuels. The incorporation of soluble amount of cerium ions in manganese oxide enables its reduction to manganese carbide with an extraordinary theoretical oxygen exchange capacity of one mole of oxygen per mole of manganese. Thereafter, the significant oxidation enthalpy of the carbide can be utilized to drive the carbon dioxide and water splitting reactions with unprecedentedly high CO and H_2 yields. Here, it is hypothesised that incorporation of the cerium ions drastically increases the oxygen ion mobility in the manganese oxide lattice enabling the thermodynamically favourable formation of an intermediate transition metal carbide, and its re-oxidation during water and carbon dioxide splitting. Importantly, while the cerium exsolutes during the reduction step, it is fully reincorporated during the oxidation step allowing long-term cyclability. The potential of this material is demonstrated by the production of valuable syngas, a mixture of CO and H_2, at record-high yields over 100 CO_2 splitting cycles with harsh methane-driven reduction steps. These findings may be applied to many members of the large family of earth-abundant transition metals setting the basis to overcome one of the longstanding challenges for the efficient thermochemical synthesis of solar fuels.

3.2 Experimental

3.2.1 Synthesis of Nanostructures

The ultra-fine pure Mn_3O_4 and 3% (atomic) Ce-doped Mn_3O_4 (3% Ce Mn_3O_4) nanoparticles were synthesised using a custom built flame spray pyrolysis setup[12, 32, 33]. The precursor liquid solution for synthesising pure Mn_3O_4 was prepared by dissolving manganese (III) acetylacetonate (Sigma Aldrich, technical grade) in 2-ethylhexanoic acid (Sigma Aldrich, purity ≥ 99%) with a total atomic concentration of Mn ions at 0.4 mol L^{-1}. Similarly, the precursor solution for synthesising 3% Ce Mn_3O_4 was prepared by mixing cerium (III) acetate hydrate (Sigma Aldrich, purity 99.9%) with manganese acetylacetonate at a Ce:Mn atomic ratio of 3:97, and dissolving the mixture in 2-ethylhexanoic acid with a total atomic concentration of the metal ions at 0.4 mol L^{-1}. Both solutions were heated in 368 K oil bath and subsequently added with equal volumetric amount of xylene to reach a total metal ion concentration of 0.2 mol L^{-1}. The final combustible solutions were fed at 5 mL min^{-1} rate through a custom-built nozzle, and atomised with an oxygen flow of 5 SLPM (grade 4.0) with a pressure drop of ca. 4 bar. The resulting spray was ignited with a surrounding annular premixed methane (flow rate of 1.2 SLPM, grade 4.5) and oxygen (flow rate of 2 SLPM, grade 4.0) flame. Nanoparticle powders were collected with a vacuum pump (ICME Type M80B4) on water-cooled glass-fibre filters (Sartorius glass microfiber, 150 mm diameter) placed at ca. 40 cm height above the burner.

3.2.2 Setup for Methane Partial Oxidation and CO_2 Splitting Cycles

The cyclic MPO and CO_2 splitting performance of pure Mn_3O_4 and 3% Ce Mn_3O_4 was investigated in a vertical-tube reactor placed inside an infrared gold image furnace(P4C-VHT, Advance Riko) illustrated in a previous work[12]. The powder samples were packed between two pieces of 2 mm thick highly porous and temperature-resistant alumina-based fibres (ALBF-1, 97% Al_2O_3 and 3% SiO_2, ZIRCAR), located on-axis of the vertical alumina tube to allow for a nearly uniform mass flow distribution on the gas-solid interface. All the samples had a mass of 200 ± 2 mg, resulting in a

powder layer thickness of 1-2 mm. The mass of the samples and the packing fibres were measured before and after the redox cycles. No apparent mass loss was observed except up to 7% mass change of the samples induced by the cycle chemistry. Increasing the sample mass to 300 mg and 500 mg resulted in lower material activity, due to mass transfer-limited reactions during the redox cycles. Gas flow rates were regulated by mass flow controllers (F-201CV, Bronkhorst) before being delivered through the top of the tube. Sample temperature was measured using an alumina sealed type-K thermocouple located directly under the packed samples. The composition of the product gases was continuously monitored by a quadrupole mass spectrometer (OmniStarTM GSD 320, Pfeiffer Vacuum). All gas volumes were reported at SATP conditions (298 K, 1 bar).

To find the effective redox stoichiometry of the materials, the tubular reactor was initially purged of air under a flow of pure Ar (grade 5.0) at room temperature. The reactor was then heated from ambient room temperature to the optimised isothermal operating temperature of 1173 K at a ramp of 80 K min^{-1}. Subsequently, the sample was cyclically reduced by CH_4 (grade 4.5) and oxidized by CO_2 (grade 4.5). The reduction step was performed using a mixture of CH_4 in Ar (8 vol%) at a total flow rate of 250 mL min^{-1} for 90 min. Then the tube was purged with Ar (250 mL min^{-1}) for 10 min. The oxidation step was initiated by delivering a mixture of CO_2 in Ar (4 vol%) at a total flow rate of 250 mL min^{-1} for 75 min. The tube was again purged with Ar (250 mL min^{-1}) for 10 min before the next cycle began. The time set for the reduction steps was determined from preliminary tests by monitoring the instantaneous H_2:CO evolution ratios. The deviation of the H_2:CO ratios caused by thermal cracking of CH_4 began to dominate after ca. 120 min into the reduction step, and compromised the credibility of the desirable products produced via the major redox reactions. Therefore, the full reduction of the samples was not investigated in this study. The subsequent oxidation

steps were kept sufficiently long enough to reoxidize as much of the samples as possible. For H_2O splitting, steam vapour was generated from a bubbler filled with DI water and kept at the targeted temperature selected between 348 and 378 K. An Ar gas flow at 20 mL min^{-1} passed through the bubbler and was further diluted with 230 mL min^{-1} of Ar before delivering steam vapour into the reactor tube.

To demonstrate the intermediate cyclic stability of 3% Ce Mn_3O_4, a 100-cycle 1173 K isothermal test with 6 min for reduction and 12 min for oxidation using the same input gas flow composition as above was performed. The Ar purge gas was increased to 500 mL min^{-1} and kept for 5 min after each reduction and oxidation step. Automated gas switch and flow rate control was operated using an in-house developed LabVIEW (National InstrumentsTM) application integrated with the mass flow controllers and pneumatically actuated valves (1315R, Swagelok). As a comparative study, commercial CeO_2 powders (Alfa Aesar, purity 99.995%) was also tested for 100 cycles with the same conditions.

3.2.3 Sample Characterisation

Samples were characterised before and after the cyclic MPO and CO_2 splitting tests. X-ray diffraction (XRD) was performed using a D2 phaser diffractometer (Bruker). Each sample powder was scanned using Cu Kα (1.54 Å) radiation source with an operating voltage of 30 kV and a current of 10 mA. The scanning rate of 0.75° min^{-1} was applied to record the XRD patterns in the 2θ range of 10–80° at an increment of 0.02°. The Scherrer equation was applied for the most intense peaks to determine the crystalline domain size. The quantitative analysis was performed based on parabolic fitting using pseudo-Voigt profile parameters.

Information of the particle morphology and lattice plane spacing was analysed using a high-resolution transmission electron microscope (HR-TEM, JEOL 2100F) operated at 200 kV. Samples were deposited on 200-mesh carbon-filmed copper grids for

imaging. Primary particle size and lattice plane spacing were obtained via the image processing software ImageJ. Additional energy dispersive X-ray spectroscopy (EDX) was performed using the scanning transmission electron microscopy (STEM) mode on the JEOL 2100F. Elemental mapping was carried out by scanning a STEM probe over the area of interest and acquiring EDX spectra at every beam positions. Atomic resolution STEM imaging and electron energy loss spectroscopy (EELS) was carried out on an aberration-corrected FEI Titan STEM operated at 300 kV.

X-ray photoelectron spectroscopy (XPS) analysis was performed using an AXIS Nova spectrometer (Kratos Analytical Inc., Manchester, UK) with a monochromatic Al Kα source at a power of 180 W (15 kV × 12 mA) with a hemispherical analyser operating in the fixed analyser transmission mode and the standard aperture (analysis area: 0.3 mm × 0.7 mm). The total pressure in the main vacuum chamber during analysis was typically around 10^{-8} mbar. Samples were loaded into shallow wells of custom-built sample holders. One batch of each sample was prepared. Two different locations were analysed on each sample at a nominal photoelectron emission angle of 0º with respect to the surface normal. As the actual emission angle is ill-defined in the case of powders (ranging from 0º to 90º), the sampling depth may range from 0 nm to ca. 10 nm. Survey spectra were acquired at pass energy of 160 eV. To obtain more detailed information about chemical structure and oxidation states, high resolution spectra were recorded from individual peaks at 40 eV pass energy. Data processing was performed using CasaXPS processing software version 2.3.15 (Casa Software Ltd., Teignmouth, UK). All elements present were identified from survey spectra. Binding energies were referenced to the C 1s peak at 284.8 eV for aliphatic hydrocarbon.

The carbon content of the samples formed after the reduction and oxidation was evaluated by TG-DSC analysis in a STA8000 Simultaneous Thermal Analyser

(PerkinElmer). Samples were calcined in air (100 mL min^{-1}) in the temperature range of 303 K to 1273 K at 5 K min^{-1}. Evolution of sample mass and heat flow were recorded.

The BET specific surface area was measured by N_2 adsorption-desorption isotherms at 77 K, using a surface and porosity analyser (TriStar II, Micromeritics), upon 4 h degassing at 423 K.

3.2.4 Reaction Equilibrium and Thermodynamic Analysis

The proposed reactions and the equilibriums were evaluated using the FactSage thermochemical analysis software[34]. The databases used in the calculations include FACT pure substances (FactPS), oxides (FToxid, including solid solution phases[35]) and miscellaneous (FTmisc) databases. The Gibbs free energy change (ΔG) of each reaction as a function of the equilibrium temperature were calculated between 473 K and 1573 K. All ΔG values were normalised as per unit mol of Mn in each equation. To obtain the equilibrium composition as a function of the temperature, the initial products were set as the stoichiometric molar amount according to the reaction equations shown in Figure S3.2. All gases were treated as ideal gases under 1 bar.

3.3 Results and Discussion

To investigate the feasibility of doping the manganese oxide crystal lattice with cerium ions, composite nanoparticles with Ce concentration varying from 3% to 50% of the total metal atom content were synthesised by flame spray pyrolysis. The synthesis method was chosen as a scalable method capable of synthesizing high purity manganese oxide nanocrystals with well-controlled structural properties in one step[24]. All of the as-prepared nanocomposites consisted of Mn_3O_4 crystals with a mixed Mn(II) and Mn(III) oxidation state (Figure S3.1). Incorporation of up to 10% of Ce resulted in a solid solution with the Mn_3O_4 matrix, while further increasing the Ce content resulted in its segregation and formation of a separated CeO_2 crystal phase. Upon initial trials, it was

found that the 3% Ce provided an optimal enhancement of the reduction and oxidation kinetics of the manganese oxide. This optimal composition was further comparatively investigated with the pure manganese oxide, and benchmarked against CeO_2.

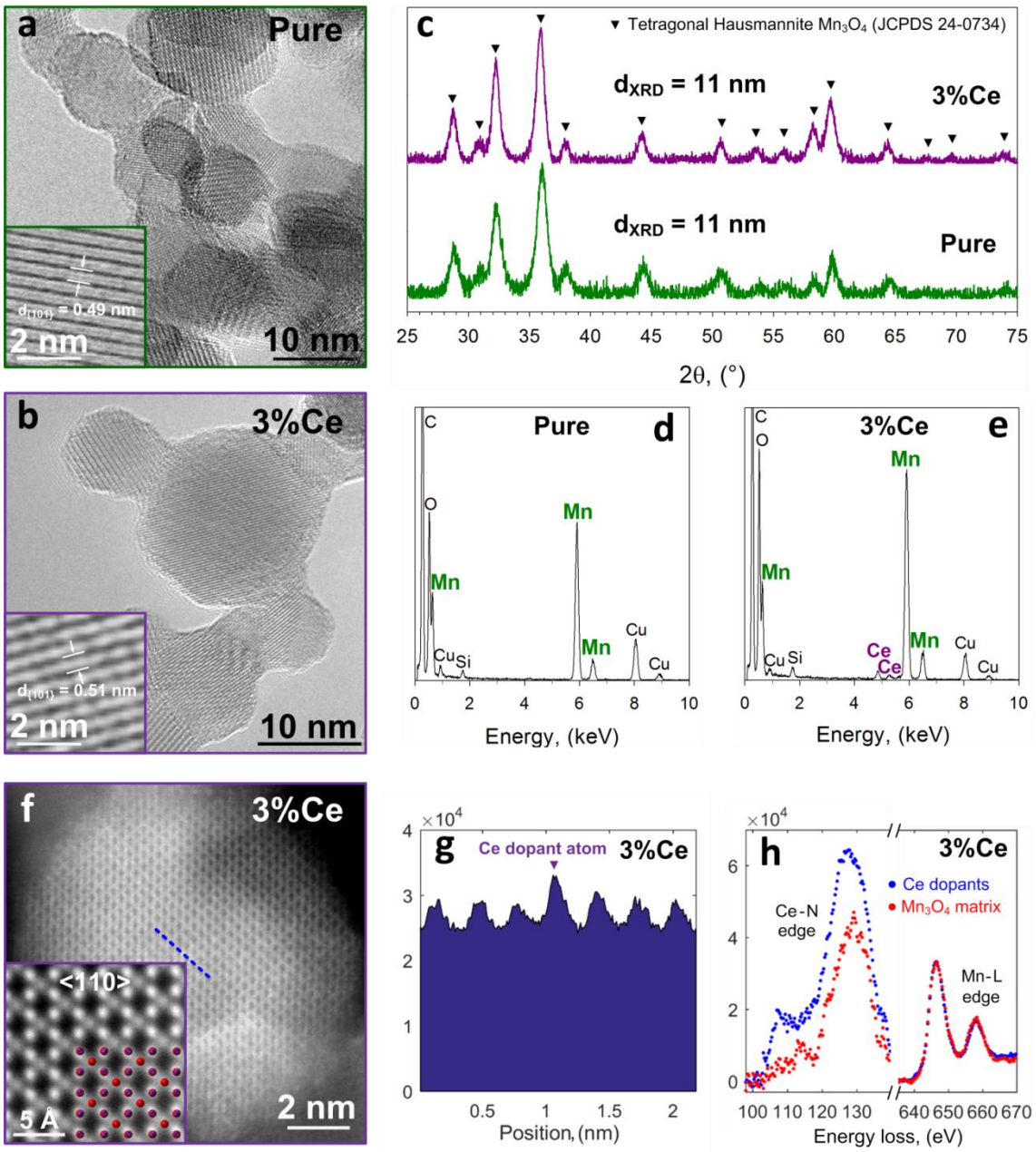

Figure 3.1 Morphological characterization of the cerium-doped manganese oxide. HR-TEM micrographs (a and b), XRD patterns (c) and EDX (d and e) of the as-prepared Pure and 3% Ce Mn_3O_4 nanostructures. HR-STEM micrograph (f) showing a primary 3% Ce Mn_3O_4 nanoparticle with associated ADF detection profile (g) and EELS (h) along the dotted line.

Figure 3.1 shows a structural comparison of the as-prepared pure and 3% Ce Mn_3O_4 nanoparticles. Both materials show similar nanoscale morphology consisting of agglomerated quasi-spherical primary particles with an average diameter of 11.2 nm and a geometric standard deviation of 1.7 (Figure S3.3). High-resolution transmission electron microscopic (HR-TEM) analysis of these samples reveals similar hexagonally-shaped monocrystalline nanoparticles and exposed (101) facets for both materials (Figure 3.1 a,b). However, while the fringe spacing of the pure Mn_3O_4 (Figure 3.1a, inset) matches well the 0.49 nm lattice spacing of the (101) Mn_3O_4 plane[24, 36], the 3% Ce one is broader (0.51 nm) suggesting a distortion of the tetragonal hausmannite crystal structure (Figure 3.1b, inset). These results were further corroborated by X-ray diffraction (XRD) analysis (Figure 3.1c), which confirms the same Mn_3O_4 phase (JCPDS No.24–0734) and average crystallite size of approx. 11 nm for both pure and 3% Ce Mn_3O_4, but a shift of the (101) plane spacing from 0.49 nm of the former to 0.51 nm of the latter. The successful incorporation of the cerium ions was confirmed by energy-dispersive X-ray spectroscopy (EDX) analysis (Figure 3.1e), showing characteristic Ce emission energies, in addition to the Mn, for the 3% Ce Mn_3O_4 samples. The EDX of the pure manganese oxide reveals only Mn, and the presence of carbon and copper from the TEM grid (Figure 3.1d). The increase in lattice spacing, observed in the Ce-doped samples, is tentatively attributed to the incorporation of the cerium ions that have larger ionic radii (Ce^{4+}: 0.097 nm; Ce^{3+}: 0.114 nm) than manganese (Mn^{4+}: 0.053 nm; Mn^{3+}: 0.065 nm; Mn^{2+}: 0.083 nm)[37]. The surface potentials of pure Mn_3O_4 and 3% Ce Mn_3O_4 was further investigated by Kelvin probe force microscopy and presented no significant contact potential difference (ca. 50 mV) (Figure S3.8), suggesting a similar surface affinity to reaction products.

The atomic distribution of the cerium ions was further investigated by annular dark-field imaging (ADF) and electron energy loss spectroscopy (EELS) analysis across the

(110) plane of the Ce-doped samples. Figure 3.1f shows a high-resolution scanning transmission electron microscopic (HR-STEM) image of a monocrystalline 3% Ce Mn_3O_4 particle and a high-magnification (inset) of the lattice image matching well the Mn_3O_4 structure model at the <110> zone axis[24]. EELS line scanning (Figure 3.1h) and its associated ADF detection profile (Figure 3.1g) show localized and increased intensities, which are associated with the presence of the Ce dopants and further confirm the formation of a substitutional $(Mn_{0.97}Ce_{0.03})_3O_4$ solid solution with no detectable segregation or clustering of the Ce inside the grains. The oxidation state of the cerium ions and possible variation in the electronic structure of the Mn were investigated by X-ray photoelectron spectroscopy (Figure 3.2). The Ce 3d spectrum observable in the 3% Ce Mn_3O_4 samples confirms the presence of tetravalent cerium (Figure 3.2a). In particular, the Ce^{4+} oxidation state is associated with a dominant peak at 917.0 eV[38]. The same spectrum with the broad Mn LMM Auger peak subtracted in the same spectral region (875 – 925 eV binding energy) to present the pure Ce 3d spectrum is shown in Figure S3.5. The Ce^{4+} presence in the Mn_3O_4 lattice appears to decrease the oxidation state of the manganese cations; this partial reduction of Mn is evidenced by a stronger intensity contribution to the Mn 2p spectrum at lower binding energy (641 eV; Figure 3.2b), and an increased multiplet splitting of the Mn 3s doublet (Figure 3.2c)[39]. It is hypothesised that the cerium ions may act as electron donor weakening the Mn-O bonds.

To investigate the overall impact of these structural reorganization on the oxygen exchange capacity and redox kinetics of the manganese oxide matrix, four sequential reduction and oxidation cycles were conducted comparatively with the pure and 3% doped manganese oxide (Figure 3.3 a,b). To increase the overall thermal energy-to-fuel efficiency limit and decrease the required reaction temperature, methane partial oxidation was utilized in the reduction step. A temperature of 1173 K was chosen as

close to the lowest (1150 K) possible for the thermodynamically favourable partial oxidation of methane with small amount of CH_4 cracking and carbon formation (Figure S3.2 a, c). Furthermore, this is also a suitable temperature to activate the subsequent exothermic oxidation step allowing the execution of the whole two-step cycle isothermally[40-42]. This decreases thermal losses that are associated with the temperature swings, required with inert gas reduction steps[14]. The re-oxidation kinetics was investigated in detail for CO_2 splitting (Figure 3.3 a,b), and further validated also for H_2O splitting (Figure 3.3c).

The overall thermodynamic reaction stoichiometry for this redox cycle (Figure S3.2) indicates favourable formation of manganese carbide (Mn_7C_3) by methane partial oxidation in the first step (Eq. 3.1, 3.2), and complete re-oxidation to manganese (II) oxide by CO_2 splitting during the second step (Eq. 3.3) [43-45]:

$$Mn_3O_4 + CH_4 \rightarrow 3\ MnO + CO + 2\ H_2,\ \Delta H^o_{298} = +196.1\ kJ\ mol^{-1} \quad (3.1)$$

$$7\ MnO + 10\ CH_4 \rightarrow Mn_7C_3 + 7\ CO + 20\ H_2,\ \Delta H^o_{298} = +2557.7\ kJ\ mol^{-1} \quad (3.2)$$

$$Mn_7C_3 + 10\ CO_2 \rightarrow 7\ MnO + 13\ CO,\ \Delta H^o_{298} = -84.4\ kJ\ mol^{-1} \quad (3.3)$$

Notably, this alternative metal oxide to carbide redox cycle has a theoretical oxygen exchange capacity of 1 $mol_O\ mol_{Mn}^{-1}$ (Eq. 3.2). This is up to four times the theoretical oxygen exchange capacity of pure ceria maintaining its cubic fluorite crystal structure[7, 12]. A temporary oxygen exchange capacity of 0.379 was reported by reducing CeO_2 to Ce_2O_3, however, the CO_2 splitting rates decreased rapidly in the first two cycles[11]. The theoretical fuel production yields in this work are unprecedentedly high with 2.86 $mol_{H2}\ mol_{Mn}^{-1}$ and 1 $mol_{CO}\ mol_{Mn}^{-1}$ (Eq. 3.2) during methane partial oxidation. In comparison, the highest theoretical H_2 and CO yields from methane partial oxidation reported for cerium dioxide, while maintaining its cubic fluorite crystal structure, are 0.5 $mol_{H2}\ mol_{Ce}^{-1}$ and 0.25 $mol_{CO}\ mol_{Ce}^{-1}$. Similarly, the potential CO_2 splitting capacity for the 3% Ce-doped manganese oxide during the oxidation step is 1.86 $mol_{CO}\ mol_{Mn}^{-1}$ (Eq. 3.3)

and thus more than 7 times higher than that potentially achievable with cerium dioxide (0.25 mol_{CO} mol_{Ce}^{-1}), while maintaining its cubic fluorite crystal structure.

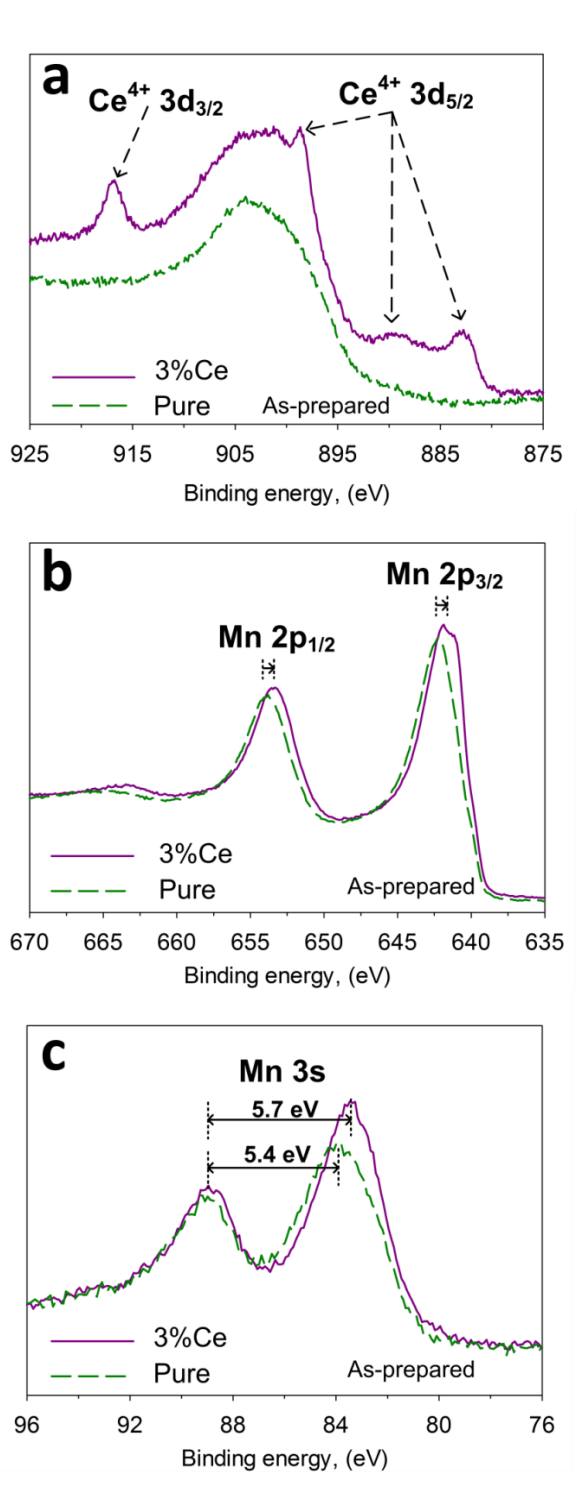

Figure 3.2 Structural characterization of the cerium-doped manganese oxide. XPS of the as-prepared Pure and 3% Ce Mn_3O_4 showing the characteristic spectra of (a) Ce 3d, (b) Mn 2p and (c) Mn 3s.

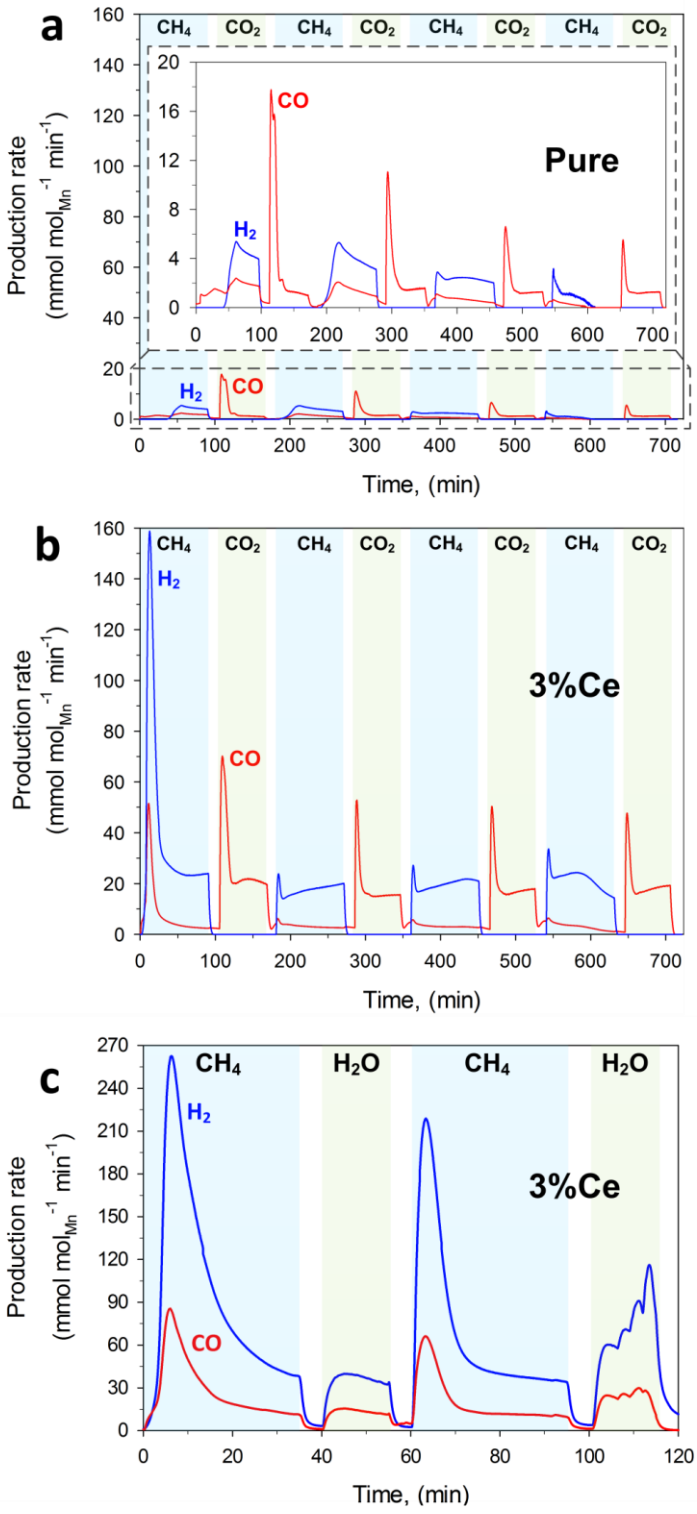

Figure 3.3 Efficient carbon dioxide splitting via the oxide-carbide cycle. H_2 and CO production rates of the (a) Pure and (b) 3% Ce Mn_3O_4 during 4 isothermal cycles of methane partial oxidation and CO_2 splitting at 1173 K. (c) H_2 and CO production rates of 3% Ce Mn_3O_4 during 2 isothermal cycles of methane partial oxidation and H_2O splitting at 1173 K.

Steinfeld et al. [46] successfully proposed the Fe_3O_4/Fe-based CLR concept achieving a full reduction of the iron oxide from Fe_3O_4 to Fe. While this is equivalent to an initial oxygen exchange capacity of 1.33 mol_O mol_{Fe}^{-1}, this was limited to the reduction step (from Fe_3O_4 to Fe), and the re-oxidation (from Fe to Fe_xO_y or possibly Fe_3O_4) to determine whether the oxygen exchange capacity was reversible and could be sustained for more than one cycle was not investigated. Currently, state-of-the-art iron oxide-based CLRs of methane rely on the Fe_3O_4/FeO redox pair due to the multi-cycle stability requirements [47, 48]. The latter yields an oxygen exchange capacity of 0.33 mol_O mol_{Fe}^{-1}, which is below the reversible one of 1 mol_O mol_{Mn}^{-1}, investigated in this study. To the best of my knowledge, such a high reversible oxygen exchange capacity in CLR has not been previously reported.

Despite this favourable thermodynamics, Figure 3.3a shows that the pure Mn_3O_4 is unable to perform this oxide–carbide redox cycle (Eq. 3.1-3.3) and only demonstrates small amounts of H_2 and CO during the reduction step (< 0.32 mol_{H2} mol_{Mn}^{-1} and 0.16 mol_{CO} mol_{Mn}^{-1}), and CO during oxidation step (< 0.24 mol_{CO} mol_{Mn}^{-1}). More specifically, in the first reduction cycle with the pure Mn_3O_4, production of a small amount of CO and CO_2 was simultaneously observed after 5 min, while detectable H_2 was only measured after 45 min and accompanied by a distinct increase in CO production rate. Evolution of CO_2 is an undesirable side reaction indicating complete oxidation of methane. In the subsequent reduction cycles, the amount of evolved CO_2 decreased rapidly. These reduction profiles suggest that while a certain amount of reduction from Mn_3O_4 into MnO and perhaps from MnO to Mn_7C_3 according to Eq. 3.1 and Eq. 3.2 may be occurring, the reaction rates are likely too slow to advance significantly. This was further supported by the CO evolution profiles during the oxidation steps. A very small and rapidly decreasing yield and production rate of CO was observed. Overall, these results further corroborate previous studies indicating that,

despite its low-cost and earth-abundancy, pure manganese oxide cannot be efficiently employed for either IGS of MPO-driven thermochemical CO_2 and H_2O splitting cycles. In fact, the highest mass-specific CO production rate measured here with the pure Mn_3O_4 was 2.3×10^{-4} mol_{CO} g^{-1} min^{-1}, and thus 71% lower than that of the state-of-the-art CeO_2[12], which at the same conditions reaches a CO production rate of 8×10^{-4} mol_{CO} g^{-1} min^{-1}.

Notably, incorporation of 3% cerium ions in the Mn_3O_4 matrix drastically enhanced reduction and oxidation kinetics, unlocking this promising metal oxide-carbide redox cycle (Eq. 3.2-3.3). Figure 3.3b shows four exemplary redox cycles with the 3% Ce Mn_3O_4. In the reduction steps, the onset of the H_2 and CO evolution was simultaneous and immediate. The H_2 and CO production rates peaked at 1.6×10^{-1} mol_{H2} mol_{Mn}^{-1} min^{-1} and 0.5×10^{-1} mol_{CO} mol_{Mn}^{-1} min^{-1}, respectively, upon 10 min into the first reduction step. These rates are more than 20 times higher than that achieved with the pure Mn_3O_4. After 35 min of the first reduction step, the production rates entered a tailing stage, stabilizing at 0.3×10^{-1} mol_{H2} mol_{Mn}^{-1} min^{-1} and 0.04×10^{-1} mol_{CO} mol_{Mn}^{-1} min^{-1}, respectively. The slight increasing tail of H_2 production during the reduction steps (Figure 3.3b) is attributed to an increased selectivity toward methane partial oxidation to H_2 and CO over full oxidation to H_2O and CO_2 with increasing reduction time (Table 3.1). This is possibly caused by the decline in oxygen partial pressure during reduction from the metal oxide to metal carbide. Another possible mechanism is methane cracking to carbon and H_2. The latter may also be facilitated by the lower oxygen content with the progress of the reduction step and may lead to an increase in H_2 production rate. In fact, a certain fraction of methane cracking is confirmed by the carbon deposits observed on the metal carbides by TGA and TEM (Figure 3.4 c, f). The increasing tail of CO production rates during the oxidation steps is possibly attributed by the increase of oxygen diffusion rates at the porous domains after the carbon contents are reacted. Over

the last 3 reduction steps, the peak rates decreased, while the tail production rates were quite stable resulting in an average of $0.22\pm0.01\times10^{-1}$ mol_{H2} mol_{Mn}^{-1} min^{-1} and $0.05\pm0.008\times10^{-1}$ mol_{CO} mol_{Mn}^{-1} min^{-1}, respectively. Furthermore, non-negligible production of CO_2 was only observed in the first cycle (Figure S3.6). The high CO/CO_2 production ratios show an inverse scenario to that observed for the pure Mn_3O_4. As summarized in Figure S3.6, increasing H_2 tail production rates accompanied by a fast decline in CO_2 evolution rates were observed over the 4 redox cycles, indicating an increased selectivity for methane partial over full oxidation (Table 3.1). Neglecting the first cycle, the average H_2 and CO yields were 2.32 ± 0.21 mol_{H2} mol_{Mn}^{-1} and 0.52 ± 0.07 mol_{CO} mol_{Mn}^{-1}, and thus comparable to those (2.86 mol_{H2} mol_{Mn}^{-1} and 1 mol_{CO} mol_{Mn}^{-1}) expected for the complete metal oxide to carbide reaction (Eq. 3.2).

The CO_2 splitting kinetics of the reduced Ce-doped manganese oxide showed fast CO evolution profiles with sharp initial peaks and sustained tail rates. While the peak CO production rate decreased from 0.7×10^{-1} to 0.5×10^{-1} mol_{CO} mol_{Mn}^{-1} min^{-1} from the first to the fourth cycle, the tail production rates were quite stable at $0.2\pm0.02\times10^{-1}$ mol_{CO} mol_{Mn}^{-1} min^{-1}. In line with the reduction steps, these CO production rates were also more than one order of magnitude higher than that of the pure manganese oxide. The CO yield of 1.89 mol_{CO} mol_{Mn}^{-1}, measured in the first cycle, is in good agreement with the theoretical yield predicted by Eq. 3.3 (1.86 mol_{CO} mol_{Mn}^{-1}), which predicts 0.43 mol_{CO} mol_{Mn}^{-1} (ca. 23%) of CO produced from oxidation of Mn_7C_3 and 1.43 mol_{CO} mol_{Mn}^{-1} of CO produced from CO_2 splitting. A further contribution of 0.03 mol_{CO} mol_{Mn}^{-1} is attributed to the reverse Boudouard reaction. This is in line with the thermodynamic analysis (Figure S3.2d), which predicts the full oxidation of Mn_7C_3 to CO and MnO during CO_2 splitting at above 1150 K. The average CO yield of 1.44 ± 0.04 mol_{CO} mol_{Mn}^{-1} in the last three CO_2 splitting steps is comparable to that of 1.86 mol_{CO} mol_{Mn}^{-1} expected from complete re-oxidation of the carbide to the metal oxide (Eq. 3.3).

Notably, the mass-specific CO yield of this 3% Ce Mn_3O_4 was 8 times higher than cerium dioxide[12], while featuring comparable CO_2 splitting kinetics.

A first demonstration of the possibility to split H_2O with the 3% Ce Mn_3O_4 is shown in Figure 3.3c. An approximately 60% and 70% higher H_2 and CO peak production rates, respectively, were observed after 7 min in the first reduction step of the MPO-H_2O splitting cycles (Figure 3.3c), than that of MPO-CO_2 splitting cycles (Figure 3.3b). This is attributed to the batch-to-batch variation in the specific surface area between the 3% Ce-doped samples. The fluctuations observed in the second oxidation step (Figure 3.3c) were induced by increasing the steam vapour pressure via increasing the bubbler temperature sequentially from 348 K to 378 K during the second H_2O splitting step. This was done to investigate the effect of the steam concentration on the production rate. The results indicate that the H_2 and CO production rates were increased from 0.06 $mol_{H2}\ mol_{Mn}^{-1}\ min^{-1}$ to 0.12 $mol_{H2}\ mol_{Mn}^{-1}\ min^{-1}$ and 0.03 $mol_{CO}\ mol_{Mn}^{-1}\ min^{-1}$ to 0.04 $mol_{CO}\ mol_{Mn}^{-1}\ min^{-1}$, respectively, by increasing the steam vapour pressure from 0.38 atm to 1 atm.

To understand the role of the cerium ions in enhancing the redox kinetics and overall thermochemical performance of manganese oxide, the structural properties of the pure and 3% Ce Mn_3O_4 were mapped along the four two-step cycles. The evolution of the XRD patterns reveals that while presenting the same crystal phase, particle size and nanoscale morphology, these two materials have very distinct redox behaviours (Figure 3.4 a,b). As suggested by the H_2 and CO evolution profiles (Figure 3.3a), the quantitative XRD analysis confirms that the pure Mn_3O_4 fails to complete its reduction to metal carbide. Upon the first reduction step only 14 wt% of Mn_7C_3 is formed, while the residual 86 wt% is slightly reduced to MnO. During the first CO_2 splitting step, this Mn_7C_3-MnO composite is partially re-oxidized to 32 wt% Mn_3O_4 and 68 wt% MnO.

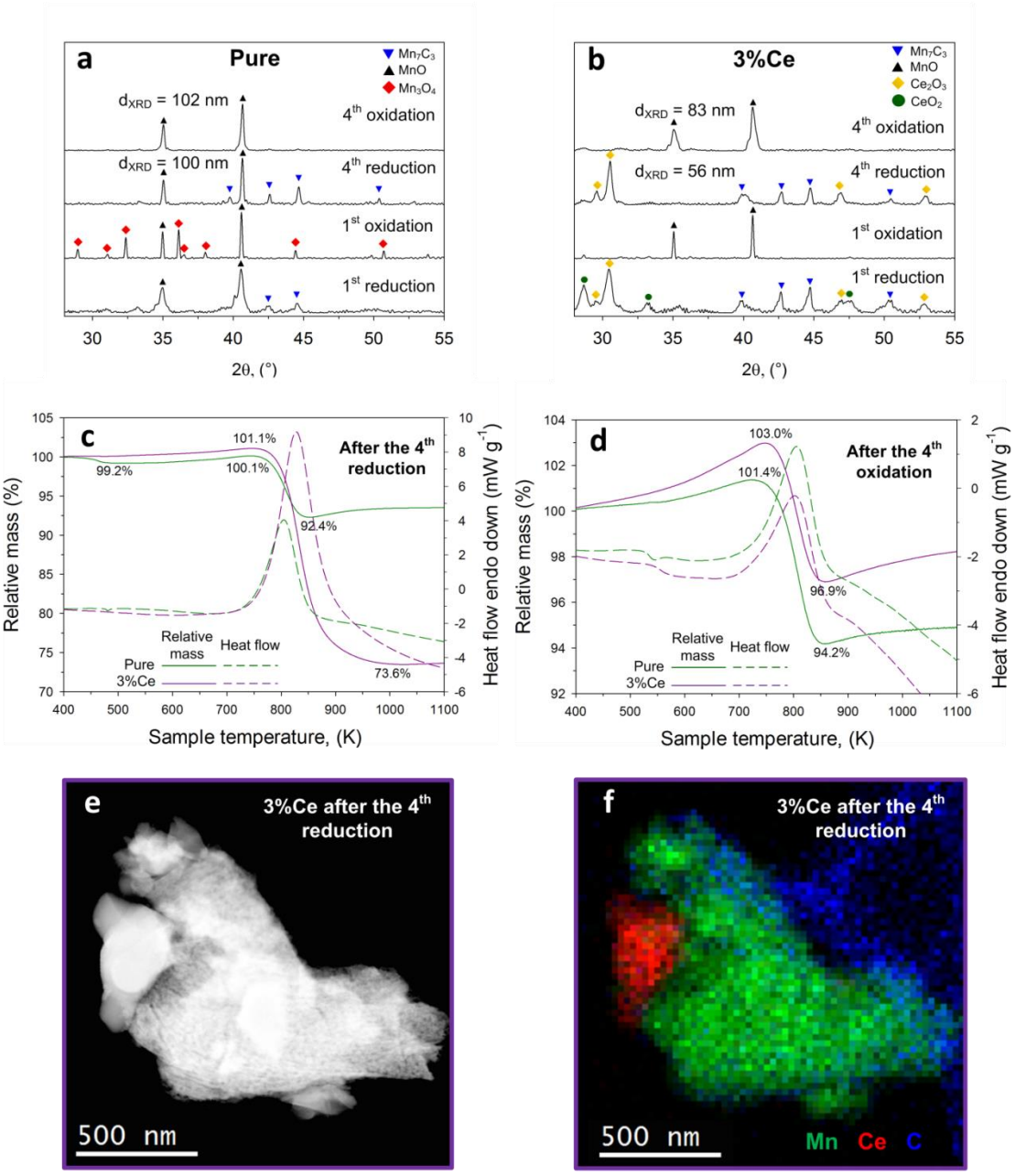

Figure 3.4 Evolution of the cerium-doped manganese oxide composition during the redox cycles. XRD patterns of the (a) Pure and (b) 3% Ce Mn_3O_4 during the 1st and 4th cycles of methane partial oxidation and CO_2 splitting. TG-DSC analysis of calcination in air at 100 mL min^{-1} showing relative mass change and heat flow of the Pure and 3% Ce Mn_3O_4 after (c) the 4th reduction step and (d) the 4th oxidation step. STEM micrograph (e) showing nanoporous 3% Ce Mn_3O_4 after the 4th reduction step and its associated elemental mapping (f) showing segregated carbon-rich Mn domains and carbon-free Ce domains.

Table 3.1 Syngas yields and CO selectivity between pure Mn_3O_4 and 3% Ce Mn_3O_4 over 4 cycles of methane partial oxidation and CO_2 splitting.

		Reduction (MPO)				Oxidation (CDS)
Material	Cycle	H_2 yield [mol mol_{Mn}^{-1}]	CO yield [mol mol_{Mn}^{-1}]	CO_2 yield [mol mol_{Mn}^{-1}]	S_{CO} [%]	CO yield [mol mol_{Mn}^{-1}]
Mn_3O_4	1	0.22	0.16	0.17	48.4	0.24
	2	0.32	0.12	0.06	67.1	0.17
	3	0.21	0.07	0.02	78.3	0.12
	4	0.07	0.02	0.02	52.3	0.10
3% Ce Mn_3O_4	1	3.71	1.05	0.28	78.9	1.89
	2	2.09	0.56	0.07	88.8	1.39
	3	2.37	0.56	0.05	91.8	1.47
	4	2.51	0.43	0.03	93.4	1.46

However, after the fourth CO_2 splitting step, only MnO is present with no Mn_3O_4 formed (Figure 3.4a). This indicates that while initially there is some cycling between Mn_3O_4 and MnO, this path is rapidly deactivated during the first few cycles. The deactivation of this path is attributed to the essential role of the nanoparticle surface for the Mn_3O_4-MnO redox cycle. As soon as the high specific surface area is lost due to sintering, the oxygen ions in the MnO lattice do not have enough mobility to re-oxidize it to Mn_3O_4. Furthermore, while this is the first demonstration of thermochemical syngas production with pure manganese oxide, the reduction from Mn_3O_4 to MnO (Eq. 3.1) has an oxygen exchange stoichiometry of only 0.33 mol_O mol_{Mn}^{-1}, and thus is not significantly higher than that of cerium dioxide (0.25 mol_O mol_{Ce}^{-1}), while maintaining

its cubic fluorite crystal structure. Here, it is proposed that the small amount of H_2 and CO evolved during the pure manganese oxide redox cycles arise mostly from the MnO to carbide pathway (Eq. 3.2 and 3.3). However, the poor mobility of the oxygen ions in the manganese oxide lattice limits the carbide formation to a small surface fraction, thus not allowing to attain the thermodynamic equilibrium (Figure S3.2c).

In stark contrast to the pure Mn_3O_4, upon the first reduction step, the XRD spectrum of the 3% Ce Mn_3O_4 reveals the presence of only Mn_7C_3 with no trace of MnO or other manganese oxides (Figure 3.4b). A small fraction of ca. 3-5 wt% CeO_2 and Ce_2O_3 was also observable in the XRD patterns, indicating exsolution of the cerium from the manganese carbide phase. After the first CO_2 splitting step, the manganese carbide was completely oxidized to MnO with no trace of segregated cerium oxides indicating its re-incorporation into the manganese oxide lattice. Notably, a high extent of the reduction and oxidation was observed also in the fourth cycle (Figure 3.4b), and explains the very high H_2 and CO yields measured also during the last three redox cycles (Figure 3.3b). The shoulders in the MnO spectra are tentatively attributed to bimodal crystal size distribution [49], due to cyclic redox reactions as there are no other Mn_7C_3 peaks visible. The thermodynamic feasibility of these results was assessed by comparing the Gibbs free energy of formation of possible reduction and oxidation reactions against the reaction temperature. The Ellingham diagram for the reduction (Figure S3.2a) shows spontaneous conversion of Mn_3O_4 into MnO under methane-rich environments. When Mn_3O_4 is completely consumed, MnO is spontaneously converted into Mn_7C_3 at temperatures above 1150 K (Eq. 3.2). For the re-oxidation by CO_2 splitting (Figure S3.2b), conversion from Mn_7C_3 to MnO (Eq. 3.3) is spontaneous, but further conversion from MnO to Mn_3O_4 is not thermodynamically favourable. Upon the first cycle starting from Mn_3O_4, this leads to the observed reversible MnO-Mn_7C_3 cycling described in Eq. 3.2 and Eq. 3.3. As a result, the MnO to Mn_7C_3 redox cycle is thermodynamically

reversible and followed closely the dictated stoichiometry in Eq. 3.2-3.3. The unsatisfactory attempts to cycle the pure manganese oxides are attributed to kinetics constraints in line with the poor oxygen mobility in manganese oxides[50, 51].

To verify the amount of manganese carbide formed, the pure and 3% Ce doped samples were analysed by thermogravimetric differential scanning calorimetry (TG-DSC) under calcination in air at 100 mL min^{-1}. Figure 3.4c shows the relative mass change and heat flow during air calcination of the pure and 3% Ce Mn_3O_4 after the fourth reduction step. Upon calcination in air a main Mn_2O_3 phase was detected for both the 3% Ce and pure Mn_3O_4 samples (Figure S3.4). Formation of Mn_2O_3 is in line with previous results obtained by calcination of nanostructured manganese oxide in air[24]. Most importantly, a mass loss was observed for both materials with increasing temperature from 800 to 870 K. This is in contrast to the expected mass gain due to oxidation from Mn_7C_3 or MnO to Mn_2O_3, which would lead to mass gains for the pure and 3% Ce Mn_3O_4 samples, respectively. This mass loss (Figure 3.4c) is attributed to the combustion of carbon deposits formed on the nanoparticle surface via methane cracking. An estimate of the mass balance based on the XRD compositions and gravimetric variations suggests that upon the fourth reduction the pure manganese oxide samples consisted of 17 wt% Mn_7C_3, 63 wt% MnO and 20 wt% carbon deposits. In contrast, the reduced 3% Ce Mn_3O_4 consisted of 58 wt% Mn_7C_3 and ca. 42 wt% carbon deposits. The TG-DSC analysis of the re-oxidized pure and 3% Ce Mn_3O_4 samples (Figure 3.4d) shows a smaller but noticeable mass loss of 8% and 3%, respectively, indicating that after 90 min in the oxidation cycle there are still some small amounts of carbon deposit (12-15 wt%). The initial mass gain is attributed to the oxidation of MnO to higher valence states (first Mn_3O_4 and then Mn_2O_3) before the on-set (ca. 800-870 K) of the carbon deposits oxidation to CO_2. The latter mass loss overshadows the 11.3% increase in mass expected for oxidation of the MnO to the final Mn_2O_3, which was

detected by XRD in the calcined samples (Figure S3.4). Similar amount of methane cracking and carbon deposit have also been reported for the benchmark cerium dioxide in thermochemical CO_2 and H_2O splitting cycles with MPO reduction[6, 52, 53]. While carbon formation by methane cracking decreases the amount of CO produced in the reduction step, the CO deficit can be recovered in the oxidation step during CO_2 splitting by the reverse Boudouard reaction. Minimizing carbon formation and deposition can be pursued by optimizing the methane concentration, reaction temperature and cycle step time[5].

Electron microscope analysis of the reduced 3% Ce Mn_3O_4 particles provides some further insights on the role of the cerium ions and the redox mechanism of these composites. After the fourth reduction step, the 3% Ce Mn_3O_4 particles have a segregated morphology composed of mostly nanoporous Mn-rich particles and some dense Ce domains (Figure 3.4 e,f). The nanoporous domains are also rich in carbon, while the Ce domains are carbon free. These structures correspond well to the segregated manganese carbide and cerium dioxide crystal phases observed by XRD. Some segregated carbon is also identified outside of the Mn-containing particles. In line with the TGA analysis (Figure 3.4c), this is attributed to the carbon deposits formed via methane cracking. It is hypothesized that the cyclic migration of cerium ions in and out of the manganese domains results in a cyclic contraction and expansion of the crystal structure, which possibly results in a nanoporous morphology. The latter has extensive grain boundary and defects available for oxygen and reactant diffusion during the reduction and oxidation steps. This is supported by the strong 48% variation in crystal size of the 3% Ce Mn_3O_4 during the fourth cycle (Figure 3.4b) from 56 nm of the reduction to 83 nm of the oxidation steps. In comparison, the crystal size of the pure Mn_3O_4 varied only by ca. 2% from 100 nm to 102 nm between the reduction and oxidation steps (Figure 3.4a). After four redox cycles, the BET analysis revealed a

specific surface area of 28 ± 2 m^2 g^{-1} and 36 ± 2 m^2 g^{-1} for the pure Mn_3O_4 and 3% Ce Mn_3O_4, respectively, indicating a 75-85% drop with respect to the ones of the as-prepared samples of 117 ± 10 m^2 g^{-1} and 169 ± 37 m^2 g^{-1}, respectively. This is in agreement with previous literatures reporting a drop in specific surface area after redox cycles with ceria [12, 18, 54, 55].

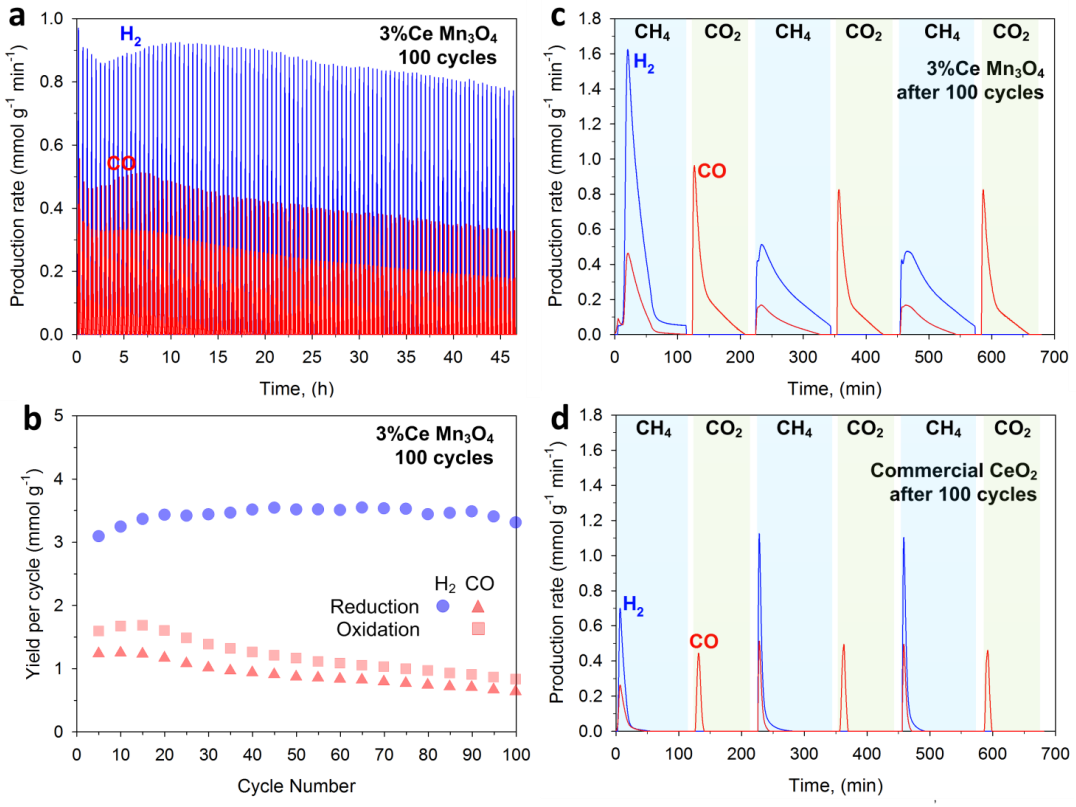

Figure 3.5 Investigation of the mid-term CO_2 splitting kinetics and mid-term stability over consecutive 100 redox cycles. (a) H_2 and CO production rates of the 3% Ce Mn_3O_4 during 100 isothermal cycles of methane partial oxidation and CO_2 splitting and its (b) H_2 and CO yields in every 5th cycle. H_2 and CO production rates of the (c) 3% Ce Mn_3O_4 and (d) commercial CeO_2 over 3 extended cycles after 100 cycles of methane partial oxidation and CO_2 splitting.

To evaluate the thermochemical stability of this material, the CO_2 splitting kinetics of the 3% Ce Mn_3O_4 was investigated over 100 continuous redox cycles with MPO-driven reduction. A comparative experiment was conducted with cerium dioxide to

provide reference values for the overall material performance (Figure S3.7). Minimization of methane cracking was achieved by decreasing the reduction and oxidation step times from 90 and 75 min (Figure 3.3) to 6 and 12 min. Figure 3.5a shows the H_2 and CO evolution rates for the 3% Ce Mn_3O_4 over these 100 redox cycles. After some initial oscillations and decline in peak CO production rate for both the reduction and oxidation step, the step-yields stabilized from the 50th cycle onward with an average yield of $3.5\pm0.07\times10^{-3}$ mol_{H2} g^{-1}, $0.8\pm0.08\times10^{-3}$ mol_{CO} g^{-1}, and $1\pm0.09\times10^{-3}$ mol_{CO} g^{-1} during methane partial oxidation and CO_2 splitting, respectively (Figure 3.5b). The initial decrease in the peak rates for methane partial oxidation and CO_2 splitting is attributed to the sintering of the nanoparticles, which decreases the available surface area slowing the reduction and oxidation kinetics. This initial surface area decrease is comparable to the behaviour observed with the nanostructured Mn_3O_4. However, the impact on the H_2 and CO yield is significantly smaller as the noteworthy bulk-diffusivity of the oxygen ions in both the 3% Ce Mn_3O_4 and CeO_2 keeps driving the redox reactions toward the thermodynamic equilibrium. The slight decline in performance can likely be mitigated by optimisation of the operating mode in a fluidised bed reactor or through the inclusion of a compatible secondary phase, as discussed in previous works[56, 57].

Table 3.2 Comparison of syngas production in two-step thermochemical redox cycles.[a)]

Material	Process	t_c [h]	N_c [#]	Reduction			Oxidation			Reference
				T_R [K]	Y_{H2} [10^{-3} mol g^{-1}]	Y_{CO} [10^{-3} mol g^{-1}]	T_O [K]	Y_{H2} [10^{-3} mol g^{-1}]	Y_{CO} [10^{-3} mol g^{-1}]	
3% Ce Mn_3O_4	MPO-CDS	11.7	4	1173	28.6	6.39	1173	--	17.7	This work
3% Ce Mn_3O_4	MPO-WS	2	2	1173	37.8	11.3	1173	11.2	3.63	This work
3% Ce Mn_3O_4	MPO-CDS	46.7	100	1173	3.44	0.90	1173	--	1.30	This work

CeO_2	MPO-CDS	46.7	100	1173	1.97	0.72	1173	--	1.55	This work
$Ce_{0.8}Zr_{0.2}O_2$	MPO-WS	>2.7	1	973	1.29	0.62	773	0.84	--	Otsuka et al.[58]
$Ce_{0.7}Fe_{0.3}O_3$	MPO-WS	>6.3	10	1123	1.19	0.63	973	1.02	--	Xing et al.[59]
CeO_2/SiC	MPO-WS	0.7	3	1273	1.75	0.43	1273	1.22	--	Nair et al.[11]
$LaFeO_3$	MPO-WS	>27	30	1073	2.00	0.27	1073	3.37	--	Zheng et al.[60]
$LaFe_{0.9}Ni_{0.1}O_3$	MPO-WS	--	10	1123	--	--	1123	6.69	--	Shen et al.[61]
Fe_3O_4	MPO-WS	15.5	6	1223	7.09	3.55	1123	5.25	--	Lu et al.[47]
CeO_2	IGS-WS	166.7	500	1773	--	--	1073	0.61	--	Chueh et al.[1]
CeO_2	IGS-WS+CDS	>8	10	1700	--	--	1100	0.09	0.04	Furler et al.[62]
$Sr_{0.6}La_{0.4}Mn_{0.6}Al_{0.4}O_3$	IGS-CDS	40	80	1623	--	--	1273	--	0.14	McDaniel et al.[17]
$CoFe_2O_4/Al_2O_3$	IGS-WS	4.6	3	1623	--	--	1623	0.10	--	Muhich et al.[14]
$La_{0.6}Ca_{0.4}MnO_3$	RWGS	3.3	5	823	--	--	823	--	1.24	Maiti et al.[63]

[a] t_c: operating time; N_c: number of cycles; T_R: reduction temperature; T_O: oxidation temperature; Y_{H2}: H_2 yield; Y_{CO}: CO yield; MPO: methane partial oxidation; CDS: carbon dioxide splitting; WS: water splitting; IGS: inert gas sweeping; RWGS: reverse water gas shift.

Overall, the cerium-doped manganese oxide achieved 75% higher H_2 and 25% higher CO yields during the methane partial oxidation step and comparable yields during the CO_2 splitting step than the commercial CeO_2. The H_2 and CO production rates during the redox steps were comparable to those of CeO_2, which is the current benchmark material for fast redox reaction kinetics in thermochemical redox cycles. Table 3.2 reports a comparative summary of the cyclic performance of the 3% Ce Mn_3O_4 against that of commercial ceria and other high-performing materials reported for thermochemical CO_2 or H_2O splitting with inert gas and MPO-driven reductions. It should be noted that MPO-driven reduction is expected to lead to higher syngas yields, due to its capability to induce higher reduction of the material than inert gas reduction.

Notably, mass-specific CO production capacity achieved here for CO_2 splitting is 17.72 $mmol_{CO}$ g^{-1}. This mass-specific CO production capacity is significantly higher (Table 3.2) than that reported in other recent studies (e.g. >10 times that of recently reported $La_{0.6}Ca_{0.4}MnO_3$[63]), and is attributed to the extraordinary reversible oxygen exchange capacity of the 3% Ce Mn_3O_4. This is also one of the highest CO production capacities from CO_2 splitting so far reported with an earth-abundant metal oxide material for thermochemical synthesis of solar fuels.

The long-term stability of the Ce-doped manganese oxide was further investigated in a separate experiment by measuring the residual oxygen exchange capacity after the 100 redox cycles. Figure 3.5c and d show three MPO-driven reduction and CO_2 splitting oxidation cycles for the cycled 3% Ce Mn_3O_4 and commercial CeO_2. The higher production peak rates in the first step of the following 3-cycle investigation (Figure 3.5c) are attributed to the longer reaction times, which enable the material to reach its peak production rates. Notably, neglecting the first cycle, the oxygen exchange capacity and H_2 and CO yields of the 3% Ce Mn_3O_4 was largely unchanged. The latter maintained comparable MPO and CO_2 splitting rates and yields to the as-prepared material (Figure 3.3). However, it should be noted that the ceria reduction and oxidation terminated significantly earlier in each cycle step than those of the 3% Ce sample did, and thus a comparison of the overall production rates would require a separate optimization of the cycling times for both materials independently as observed for the 100 redox cycles. The 3% Ce revealed up to 7 and 5 times higher H_2 and CO yields, respectively, during the reduction steps, and 4–6 times higher CO yield during the CO_2 splitting steps than the commercial CeO_2. After 100 redox cycles, the oxygen exchange capacity of the Ce-doped manganese oxide, estimated from the average CO yield during the MPO steps, was 0.61 mol_O mol_{Mn}^{-1} and thus close to the as-prepared material (0.65 mol_O mol_{Mn}^{-1}) despite an 81% decrease in specific surface area. This is attributed to the drastic

improvement in oxygen ion mobility achieved by incorporation of the Ce^{4+} in the manganese oxide lattice, which may reduce the Mn-O binding energy and also create a microporous morphology.

3.4 Conclusions

In conclusion, doping earth-abundant metal oxides with soluble amounts of high oxygen conductivity materials, such as cerium, may lead to a broadly applicable strategy to improve the redox kinetics and unlock the use of the outstanding oxygen exchange capacity of this broad family of low-cost materials for solar thermochemical fuel synthesis. The cerium-doped manganese oxide, developed here, demonstrates the first metal oxide to carbide redox cycle and efficient use of manganese, one of the most earth-abundant elements, for thermochemical carbon dioxide and water splitting. The incorporation of a fractional amount of cerium ions improved significantly the reduction and oxidation kinetics, resulting in 15 times higher CO_2 splitting rates than the undoped manganese oxide, and also 8 times higher CO yields than cerium oxide. The long-term cyclic performance revealed that this is not a short-lived enhancement and that the cerium ions are able to easily diffuse in and out of the host lattice over hundreds of reduction and oxidation cycles in harsh thermochemical conditions. As an immediate result, these findings provide a novel low-cost earth-abundant material for the large-scale synthesis of solar fuels via efficient thermochemical routes.

3.5 Supplementary Information

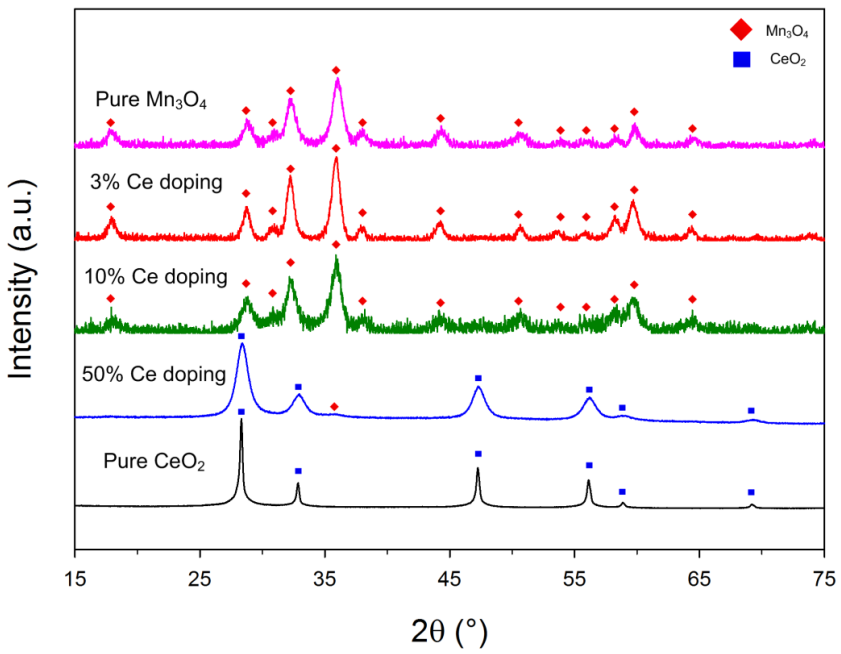

Figure S3.1 XRD patterns of as-prepared cerium-doped manganese oxides showing 0%, 3%, 10%, 50%, and 100% atomic Ce content.

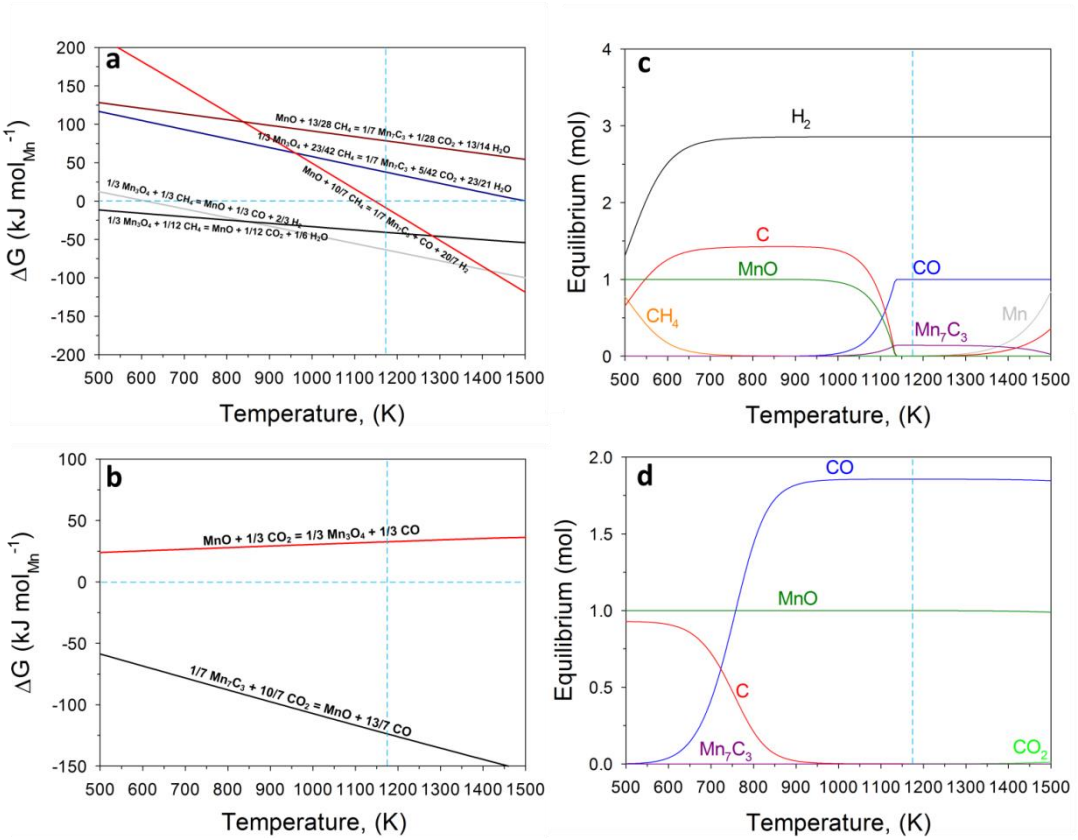

Figure S3.2 Gibbs free energy of the evaluated (a) reduction equations of manganese oxides by CH_4 and (b) oxidation equations of manganese monoxide and carbide by CO_2, normalised as per unit mol of Mn in each equation. The equilibrium composition of (c) 1 mol MnO and 1.4286 mol CH_4 and (d) 0.1429 mol Mn_7C_3 and 1.4286 mol CO_2 from 500 K to 1500 K, with all gases treated as ideal gases under 1 bar.

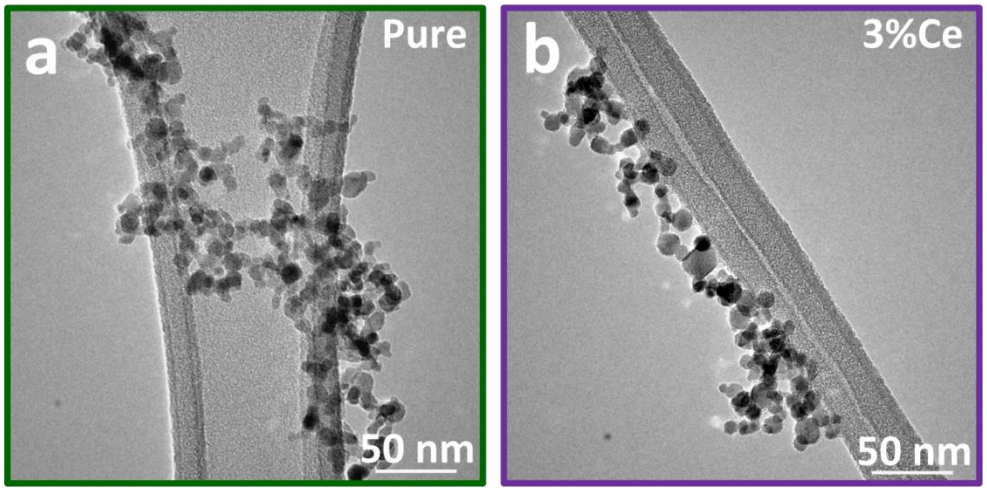

Figure S3.3 TEM micrographs showing the as-prepared (a) Pure and (b) 3% Ce Mn_3O_4 with primary particle size of ca. 10nm.

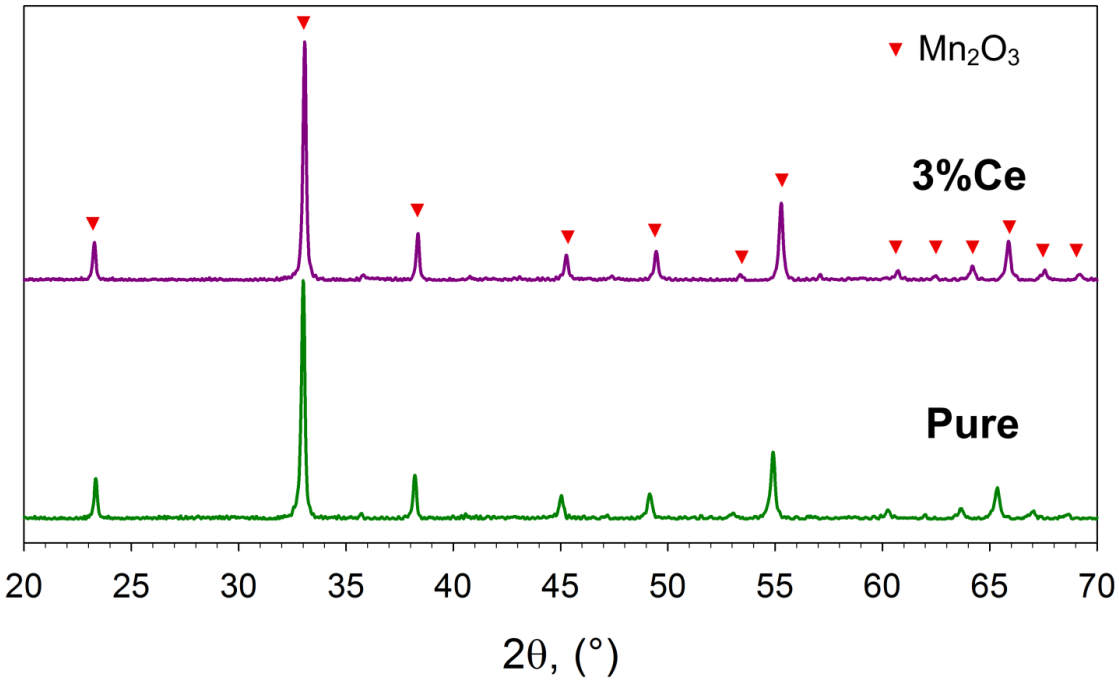

Figure S3.4 XRD patterns of the cycled (a) Pure and (b) 3% Ce Mn_3O_4 after calcination in air at up to 1273 K during TG-DSC experiments.

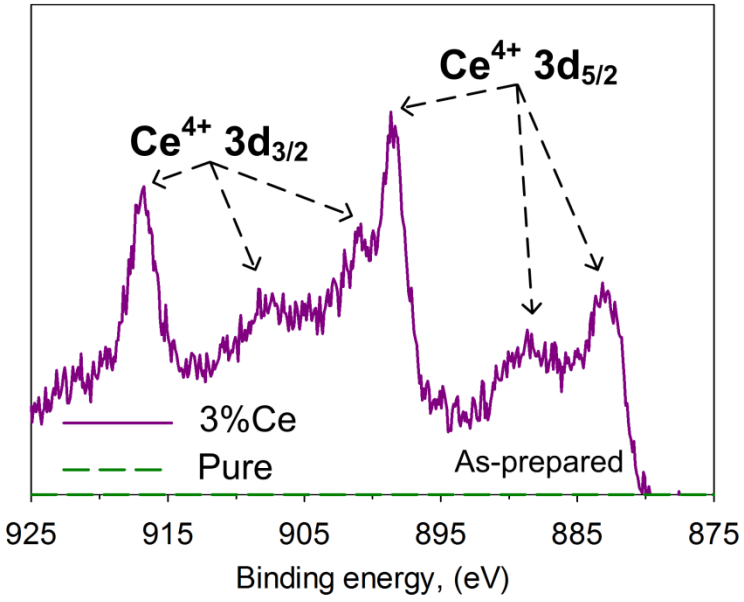

Figure S3.5 XPS of the as-prepared Pure and 3% Ce Mn_3O_4 showing the characteristic spectra of Ce 3d. A broad Mn LMM Auger peak in the same spectral region (875–925 eV binding energy) has been subtracted in order to present the pure Ce 3d spectrum.

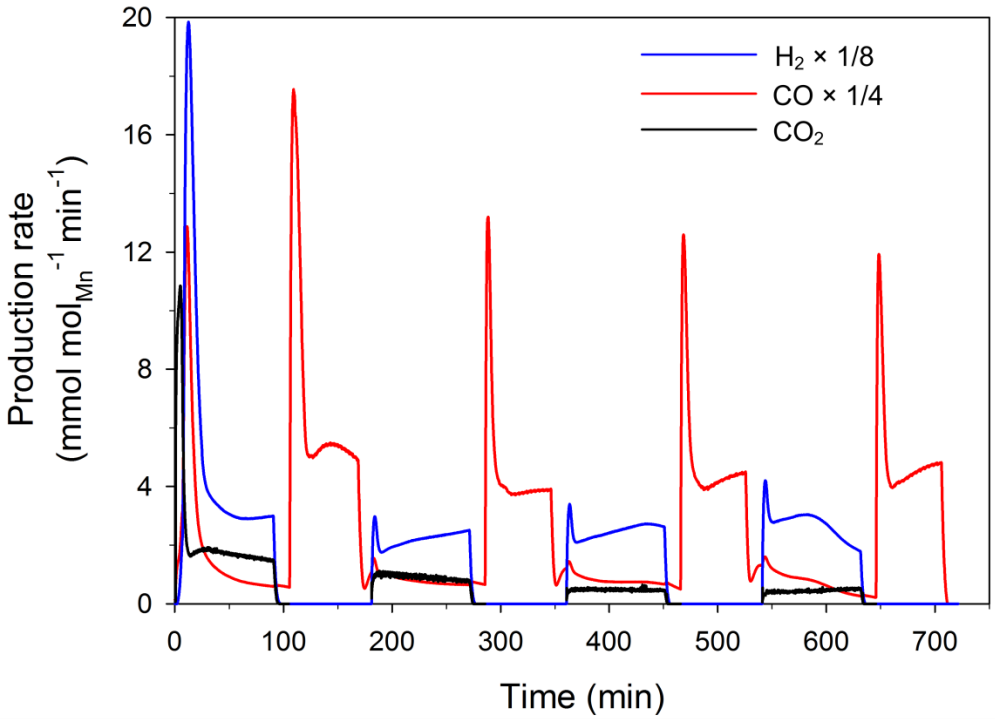

Figure S3.6 H_2 (divided by 8), CO (divided by 4) and CO_2 production rates during the 4 isothermal cycles of methane partial oxidation and CO_2 splitting via 3% Ce Mn_3O_4 at 1173 K.

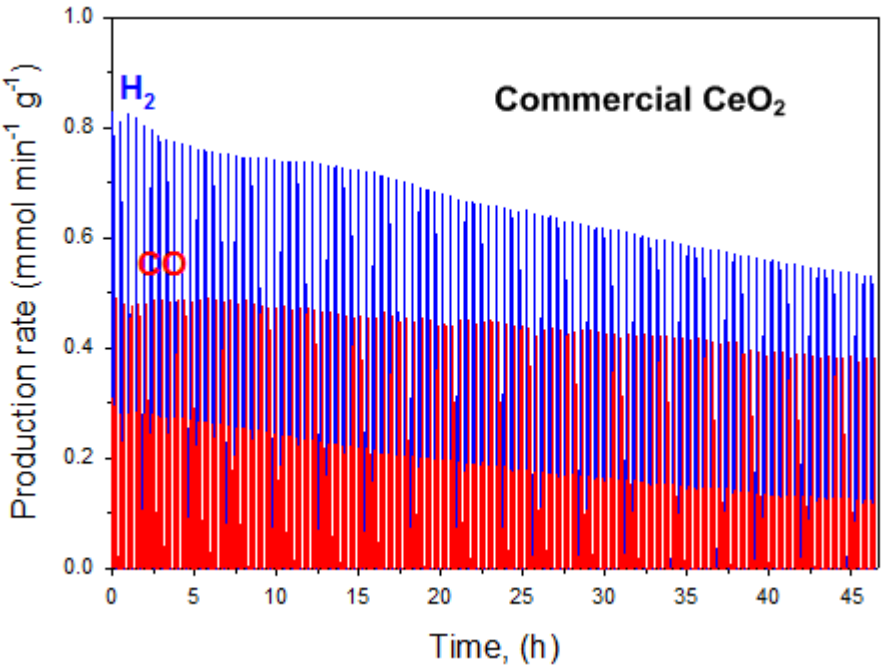

Figure S3.7 Syngas production of commercial ceria over 100 consecutive redox cycles.

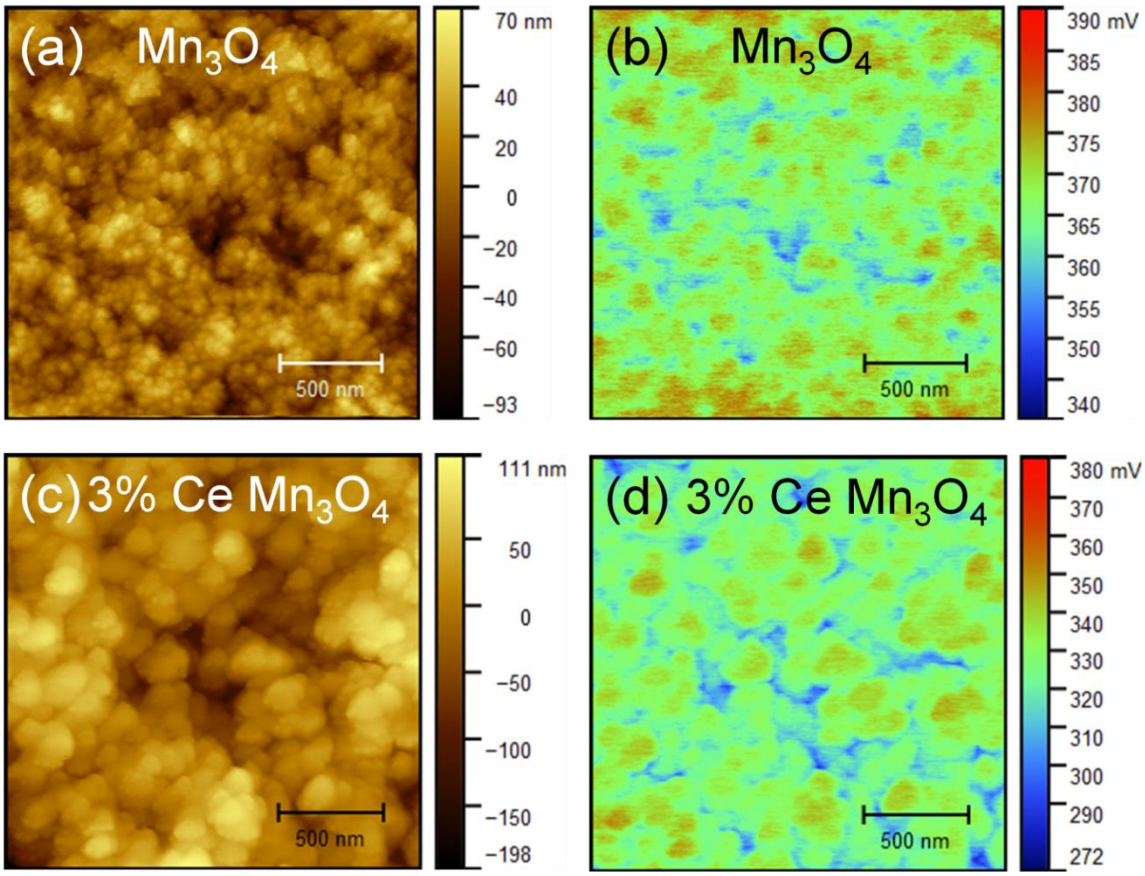

Figure S3.8: (a) Morphology and (b) surface potential of the pure Mn_3O_4 and (c,d) 3% Ce Mn_3O_4 sample.

Selectivity of CO during MPO steps were calculated by:

$$S\ (CO) = \frac{n(CO)_{MPO}}{n(CO)_{MPO} + n(CO_2)_{MPO}} \times 100\% \qquad \text{(S3.1)}$$

$n(i)_{MPO}$ denotes the total amount of evolution of species i during MPO steps.

3.6 References

1. W. C. Chueh, C. Falter, M. Abbott, D. Scipio, P. Furler, S. M. Haile and A. Steinfeld, *Science*, 2010, **330**, 1797-1801.
2. C. Agrafiotis, M. Roeb and C. Sattler, *Renew. Sust. Energ. Rev.*, 2015, **42**, 254-285.
3. C. L. Muhich, B. D. Ehrhart, I. Al-Shankiti, B. J. Ward, C. B. Musgrave and A. W. Weimer, *WIREs Energ. Environ.*, 2016, **5**, 261-287.
4. A. Steinfeld, *Sol. Energy*, 2005, **78**, 603-615.
5. C. Agrafiotis, H. von Storch, M. Roeb and C. Sattler, *Renew. Sust. Energ. Rev.*, 2014, **29**, 656-682.
6. K. Otsuka, Y. Wang, E. Sunada and I. Yamanaka, *J. Catal.*, 1998, **175**, 152-160.
7. P. T. Krenzke and J. H. Davidson, *Energ. Fuel*, 2014, **28**, 4088-4095.
8. R. Bader, L. J. Venstrom, J. H. Davidson and W. Lipinski, *Energ. Fuel*, 2013, **27**, 5533-5544.
9. P. T. Krenzke, J. R. Fosheim and J. H. Davidson, *Sol. Energy*, 2017, **156**, 48-72.
10. P. T. Krenzke, J. R. Fosheim, J. Y. Zheng and J. H. Davidson, *Int. J. Hydrog. Energy*, 2016, **41**, 12799-12811.
11. M. M. Nair and S. Abanades, *Energ. Fuel*, 2016, **30**, 6050-6058.
12. X. Gao, A. Vidal, A. Bayon, R. Bader, J. Hinkley, W. Lipinski and A. Tricoli, *J. Mater. Chem. A*, 2016, **4**, 9614-9624.
13. A. Le Gal, S. Abanades and G. Flamant, *Energ. Fuel*, 2011, **25**, 4836-4845.
14. C. L. Muhich, B. W. Evanko, K. C. Weston, P. Lichty, X. Liang, J. Martinek, C. B. Musgrave and A. W. Weimer, *Science*, 2013, **341**, 540-542.
15. A. Mishra, N. Galinsky, F. He, E. E. Santiso and F. Li, *Catal. Sci. Technol.*, 2016, **6**, 4535-4544.
16. H. Wei, Y. Cao, W. Ji and C. Au, *Catal. Commun.*, 2008, **9**, 2509-2514.

17. A. H. McDaniel, E. C. Miller, D. Arifin, A. Ambrosini, E. N. Coker, R. O'Hayre, W. C. Chueh and J. Tong, *Energy Environ. Sci.*, 2013, **6**, 2424-2428.

18. L. J. Venstrom, N. Petkovich, S. Rudisill, A. Stein and J. H. Davidson, *J. Sol. Energ. Eng.*, 2012, **134**, 011005.

19. W. T. Gibbons, L. J. Venstrom, R. M. De Smith, J. H. Davidson and G. S. Jackson, *PCCP*, 2014, **16**, 14271-14280.

20. F. Xie, T. A. Zhang, D. Dreisinger and F. Doyle, *Miner. Eng.*, 2014, **56**, 10-28.

21. T. Kodama, T. Shimizu, T. Satoh, M. Nakata and K. I. Shimizu, *Sol. Energy*, 2002, **73**, 363-374.

22. F. He, Y. G. Wei, H. B. Li and H. Wang, *Energ. Fuel*, 2009, **23**, 2095-2102.

23. M. Wiechen, M. M. Najafpour, S. I. Allakhverdiev and L. Spiccia, *Energy Environ. Sci.*, 2014, **7**, 2203-2212.

24. G. Y. Liu, J. Hall, N. Nasiri, T. Gengenbach, L. Spiccia, M. H. Cheah and A. Tricoli, *ChemSusChem*, 2015, **8**, 4162-4171.

25. F. Y. Cheng, J. A. Shen, B. Peng, Y. D. Pan, Z. L. Tao and J. Chen, *Nat. Chem.*, 2011, **3**, 79-84.

26. H. Kaneko, T. Miura, H. Ishihara, S. Taku, T. Yokoyama, H. Nakajima and Y. Tamaura, *Energy*, 2007, **32**, 656-663.

27. T. M. Francis, P. R. Lichty and A. W. Weimer, *Chem. Eng. Sci.*, 2010, **65**, 3709-3717.

28. M. Sturzenegger, J. Ganz, P. Nuesch and T. Schelling, *J. Phys. IV*, 1999, **9**, 331-335.

29. P. B. Kreider, H. H. Funke, K. Cuche, M. Schmidt, A. Steinfeld and A. W. Weimer, *Int. J. Hydrog. Energy*, 2011, **36**, 7028-7037.

30. A. Bayón, V. A. de la Peña O'Shea, D. P. Serrano and J. M. Coronado, *Int. J. Hydrog. Energy*, 2013, **38**, 13143-13152.

31. A. Bayón, V. A. de la Peña O'Shea, J. M. Coronado and D. P. Serrano, *Int. J. Hydrog. Energy*, 2016, **41**, 113-122.

32. N. Nasiri, R. H. Bo, F. Wang, L. Fu and A. Tricoli, *Adv. Mater.*, 2015, **27**, 4336-4343.

33. G. Liu, W. S. Wong, N. Nasiri and A. Tricoli, *Nanoscale*, 2016, **8**, 6085-6093.

34. C. W. Bale, E. Belisle, P. Chartrand, S. A. Decterov, G. Eriksson, K. Hack, I. H. Jung, Y. B. Kang, J. Melancon, A. D. Pelton, C. Robelin and S. Petersen, *Calphad-Computer Coupling of Phase Diagrams and Thermochemistry*, 2009, **33**, 295-311.

35. M. D. Allendorf, R. B. Diver, N. P. Siegel and J. E. Miller, *Energ. Fuel*, 2008, **22**, 4115-4124.

36. C. C. Hu, Y. T. Wu and K. H. Chang, *Chem. Mater.*, 2008, **20**, 2890-2894.

37. P. Zhang, H. Lu, Y. Zhou, L. Zhang, Z. Wu, S. Yang, H. Shi, Q. Zhu, Y. Chen and S. Dai, *Nat. Commun.*, 2015, **6**, 8446.

38. D. R. Mullins, S. H. Overbury and D. R. Huntley, *Surf. Sci.*, 1998, **409**, 307-319.

39. M. C. Biesinger, B. P. Payne, A. P. Grosvenor, L. W. M. Lau, A. R. Gerson and R. S. Smart, *Appl. Surf. Sci.*, 2011, **257**, 2717-2730.

40. A. Serrano-Lotina and L. Daza, *Int. J. Hydrog. Energy*, 2014, **39**, 4089-4094.

41. K. Zhao, F. He, Z. Huang, A. Q. Zheng, H. B. Li and Z. L. Zhao, *Chinese J. Catal.*, 2014, **35**, 1196-1205.

42. A. Serrano-Lotina and L. Daza, *Appl. Catal. A Gen.*, 2014, **474**, 107-113.

43. N. Anacleto, O. Ostrovski and S. Ganguly, *ISIJ Int.*, 2004, **44**, 1480-1487.

44. O. Ostrovski and G. Q. Zhang, *AIChE J.*, 2006, **52**, 300-310.

45. C. H. Eom and D. J. Min, *Met. Mater. Int.*, 2016, **22**, 129-135.

46. A. Steinfeld, P. Kuhn and J. Karni, *Energy*, 1993, **18**, 239-249.

47. C. Q. Lu, K. Z. Li, H. Wang, X. Zhu, Y. G. Wei, M. Zheng and C. H. Zeng, *Appl. Energy*, 2018, **211**, 1-14.

48. K. S. Go, S. R. Son, S. D. Kim, K. S. Kang and C. S. Park, *Int. J. Hydrog. Energy*, 2009, **34**, 1301-1309.

49. T. Rudin, K. Wegner and S. E. Pratsinis, *J. Nanoparticle Res.*, 2011, **13**, 2715-2725.

50. M. Nolan, J. E. Fearon and G. W. Watson, *Solid State Ionics*, 2006, **177**, 3069-3074.

51. G. Zhou, P. R. Shah and R. J. Gorte, *Catal. Lett.*, 2008, **120**, 191-197.

52. J. T. Jang, K. J. Yoon, J. W. Bae and G. Y. Han, *Solar Energy*, 2014, **109**, 70-81.

53. H. H. Jeong, J. H. Kwak, G. Y. Han and K. J. Yoon, *Int. J. Hydrog. Energy*, 2011, **36**, 15221-15230.

54. A. C. Gladen and J. H. Davidson, *Sol. Energy*, 2016, **139**, 524-532.

55. C. D. Malonzo, R. M. De Smith, S. G. Rudisill, N. D. Petkovich, J. H. Davidson and A. Stein, *J. Phys. Chem. C*, 2014, **118**, 26172-26181.

56. A. Shafiefarhood, J. C. Hamill, L. M. Neal and F. Li, *PCCP*, 2015, **17**, 31297-31307.

57. N. L. Galinsky, A. Shafiefarhood, Y. G. Chen, L. Neal and F. X. Li, *Appl. Catal. B Environ.*, 2015, **164**, 371-379.

58. K. Otsuka, Y. Wang and M. Nakamura, *Appl. Catal. A Gen.*, 1999, **183**, 317-324.

59. Z. Xing, W. Hua, W. Yonggang, L. Kongzhai and X. Cheng, *J. Rare Earth.*, 2010, **28**, 907-913.

60. Y. Zheng, K. Li, H. Wang, D. Tian, Y. Wang, X. Zhu, Y. Wei, M. Zheng and Y. Luo, *Appl. Catal. B Environ.*, 2017, **202**, 51-63.

61. Y. Shen, K. Zhao, F. He and H. Li, *J. Energ. Inst.*, 2018.

62. P. Furler, J. R. Scheffe and A. Steinfeld, *Energy Environ. Sci.*, 2012, **5**, 6098-6103.

63. D. Maiti, B. J. Hare, Y. A. Daza, A. E. Ramos, J. N. Kuhn and V. R. Bhethanabotla, *Energy Environ. Sci.*, 2018, **11**, 648-659.

Chapter Four

Role of Cerium Ions in Activating Solar Fuels Production by Manganese-based Oxygen Carriers via Chemical Looping Steam Methane Reforming

Publication relevant to this chapter:

X. Gao, I. di Bernardo, P. Kreider, T. Tran-Phu, W. S. Y. Wong, G. Zhao, Y. Zhu, X. Cai, N. Wang, N. Motta, A. Bayon, W. Lipiński and A. Tricoli, *Role of Cerium Ions in Activating Solar Fuels Production by Manganese-based Oxygen Carriers via Chemical Looping Steam Methane Reforming.* (internal review, submission to *Journal of Materials Chemistry A* soon).

Abstract

Solar chemical looping steam methane reforming is an attractive technology to supply synthesis gas for reliable production of transportation fuels on a global scale in the near future. Manganese oxide has the potential to act as a low-cost oxygen carrier in this solar thermochemical redox cycle. However, the process has not been commercially demonstrated yet due to kinetic limitations at a commercially competitive temperature. Here, the role of cerium ions in activating the efficient production of solar fuels via a MnO/Mn_7C_3-based chemical looping reforming cycle is investigated. At an optimal fractional molar content of 3% Ce, the surface of the oxygen carrier can be effectively covered with Ce-rich nanoparticles that efficiently dissociate the chemisorbed species into H_2 and CO during methane reforming and water splitting. XPS and XRD characterisation revealed the abundant bulk lattice diffusion of oxygen and carbon in 3% Ce. As a result, over 13 hours of continuous demonstration at 1173 K, 3% Ce produced high per-cycle synthesis gas yields of 45.38 $mmol_{H2}$ g^{-1} and 21.02 $mmol_{CO}$ g^{-1} during methane reforming, and 8.33 $mmol_{H2}$ g^{-1} and 1.29 $mmol_{CO}$ g^{-1} during water splitting. The experimentally derived benchmark performance in chemical looping steam methane reforming and the comprehensive rationalization by structural characterization provides a stepping stone for the 3% Ce MnO/Mn_7C_3 oxygen carrier towards practical viability.

4.1 Introduction

The increasing global energy demand in the expanding transport sector calls for the development of sustainable and reliable alternatives to produce liquid fuels in the near future. One approach to meet this demand is to upgrade the vast global reserves of natural gas to liquid hydrocarbons using renewable energy. The current industrial conversion of CH_4 is almost exclusively limited to producing syngas from steam methane reforming and subsequent processing of the syngas into liquid fuels via Fischer–Tropsch synthesis.[1,2] Due to the increasing concerns with carbon emissions, conventional steam methane reforming has been criticized for combusting nearly 40% of the methane feedstock to supply required process heat,[3] resulting in a 24% downgrade of energy content for the process.[4] In this context, solar-driven chemical looping reforming (CLR) of methane has been considered as competitive, near-term alternative. Solar CLR involves a two-step thermochemical cycle that converts methane into syngas via oxygen carriers according to the following reactions, where required process heat is supplied by concentrated solar energy rather than via the combustion of methane feedstock

$$MeO_x + \delta\, CH_4 \rightarrow MeO_{x-\delta} + \delta\, CO + 2\delta\, H_2,\ \Delta H^o_{298} > 0 \quad (4.1)$$

$$MeO_{x-\delta} + \delta\, H_2O\ (g) \rightarrow MeO_x + \delta\, H_2,\ \Delta H^o_{298} < 0 \quad (4.2)$$

Specifically, in the endothermic reduction step (Eq. 4.1), CH_4 is partially oxidized into H_2 and CO while the oxygen carrier is reduced to a lower valency state with less oxygen content. In the exothermic oxidation step (Eq. 4.2), steam is introduced to regenerate the oxygen carrier, while simultaneously being split into H_2. More importantly, solar energy is stored as the chemical bonds in the syngas products, effectively resulting in an up to 28% energetic upgrade compared to the methane feedstock.[5] The carbon footprint of this solar thermochemical process is essentially 41%

less than conventional steam methane reforming, paving the way for a low-carbon and sustainable industrial practice.[4]

Current solar chemical looping steam methane reforming material studies almost exclusively focus on finding efficient oxygen carriers that can be reduced to their metallic components during the redox cycles.[6-11] The sought-after characteristics of oxygen carriers are low-cost, high and reversible oxygen exchange capacity, fast reaction kinetics and sustained physicochemical properties. Fe-based oxygen carriers operate within a Fe_3O_4/FeO redox pair, yielding limited syngas selectivity and reversibility.[7,8] Nonstoichiometric oxygen carriers such as $LaFeO_3$-based perovskites demonstrates efficient reaction kinetics but suffered from low oxygen exchange capacity.[12-14] Ni, Cu-ferrite oxygen carriers yielded low H_2O splitting activity.[15-19] Nonstoichiometric ceria has been widely investigated in recent years in solar thermochemical redox cycles due to its fast oxygen transport.[20-31] Efforts to exploit higher syngas yields in ceria have been mainly achieved by doping with trivalent and tetravalent cations, but have not successfully reduced ceria beyond Ce_2O_3 to access a higher reversible oxygen exchange capacity.[32-36] On the other hand, ceria has demonstrated noteworthy capability in redox catalysis where reversible migration of oxygen on the surface of the catalysts is of utmost importance for the reaction kinetics.[37] In such a context, earth-abundant manganese oxide as an alternative has not attracted much attention. This is mostly due to the fact that research has primarily focused on the transition among different stoichiometric states of manganese oxides such as Mn_2O_3, Mn_3O_4 and MnO. This has yielded very limited success as a direct one-step oxidation with H_2O being thermodynamically impossible in such redox strategies.[38-41] A recent study has explored an alternative redox pathway by accessing the MnO/Mn_7C_3 redox pair that has the potential for large-scale synthesis of solar fuels via thermochemical routes.[42]

Here, the strategy to incorporate Ce ions into a Mn-based oxygen carrier in order to achieve efficient production of solar fuels is investigated. A series of 20-cycle CLR using Ce-Mn oxide solid solutions over a broad spectrum of Ce:Mn content ratios is showcased.. A fractional 3% Ce content that can activate the MnO/Mn_7C_3 redox pair with distinctively fast production rates and high yields of syngas at a commercially relevant temperature of 1173 K is highlighted. Structural characterisation is carried out to determine the role of Ce ions in activating the Mn-based oxygen carrier for fast and reversible oxygen/carbon diffusion.

4.2 Experimental

4.2.1 Synthesis of the Oxygen Carriers

The Ce-Mn oxide solid solutions were synthesized from a custom-built flame spray pyrolysis setup illustrated in previous work[21,43,44]. First, cerium (III) acetate hydrate (purity 99.9%, Sigma Aldrich) was mixed with manganese (III) acetylacetonate (technical grade, Sigma Aldrich) at Ce/(Mn+Ce) atomic ratios of 0, 0.01, 0.03, 0.05, 0.1, 0.25, 0.5, 0.75 and 1. Each atomic ratio mixture was dissolved in 2-ethylhexanoic acid (purity ≥ 99%, Sigma Aldrich) with a total metal atomic concentration at 0.4 mol L^{-1}. The solutions were heated in a 368 K oil bath and subsequently mixed with equal volumetric amounts of m-Xylene (purity ≥ 99%, Sigma Aldrich) to reach a total metal atomic concentration of 0.2 mol L^{-1}. The final combustible solutions were supplied at a rate of 5 mL min^{-1} through a syringe pump, and dispersed into a fine spray with 7 L min^{-1} oxygen at a constant pressure drop of 4 bar. The spray was ignited by supporting premixed methane (1.8 L min^{-1}) and oxygen (2 L min^{-1}) flames. The nanoparticles were collected on water-cooled glass-fibre filters placed 40 cm above the burner.

4.2.2 Materials Characterization

The crystal phases, crystallite sizes (d_{XRD}) and interplanar spacings ($d_{(hkl)}$) were characterized by X-ray diffraction (XRD, D2 Phaser, Bruker) with a Cu Kα radiation source (γ = 0.15406 nm). Particle specific surface area (SSA) was measured by N_2 adsorption at 77 K in a surface and porosity analyser (TriStar II, Micromeritics), after degassing at 423 K for 4 h. Sample morphology was investigated by field-emission scanning electron microscopy (FESEM, Zeiss UltraPlus) at 3 kV. The backscattered electron (BSE) images were obtained by an Electron Backscattered Diffraction system (EBSD, Oxford Instruments) equipped by Zeiss UltraPlus FESEM. The elemental mapping evaluated by Energy-dispersive X-ray spectroscopy (EDX) was obtained from a 10 mm^2 silicon drift detector (Oxford Instruments). X-ray photoelectron spectra (XPS) were collected in a Thermofisher Kratos Axis Supra photoelectron spectrometer, with Al kα radiation (1486.7 eV) at pass energy 20. The high-resolution transmission electron microscopy images were acquired by JEOL JEM 2010F under 200 kV accelerating voltage with camera's drift-correction. The (101) lattice interplanar spacing was measured by averaging 150 line profiles across 10 lattice planes using the same camera calibration. The inverse fast Fourier transform was extracted from (101) spots in fast Fourier transform patterns of each particle to highlight the measured lattice fringes.

4.2.3 Setup for chemical looping steam methane reforming cycles

The synthesized active material performance in cyclic solar CLR of methane was investigated in a vertical tubular reactor placed inside an electric IR gold image furnace (P4C-VHT, Advance Riko).[21] Approximately 0.2 g of each oxygen carrier was packed between two pieces of 2 mm thick alumina-based fibres and situated on-axis of the vertical tubular reactor. The product gases were measured by a quadrupole mass spectrometer (OmniStarTM GSD 320, Pfeiffer Vacuum) after passing through a chilled

condenser filled with desiccant to remove the remaining steam. All gas volumes were reported at SATP conditions (298 K, 1 bar).

The tubular reactor was initially purged of air under a flow of high-purity Ar (grade 5.0, Coregas) and heated to the isothermal operating temperature of 1173 K at a ramp of 100 K min^{-1}. The methane reforming step was performed using 20 mL min^{-1} of CH_4 (grade 4.5, Coregas) entrained in 230 mL min^{-1} of Ar for 20 min. Then the reactor was purged with Ar (500 mL min^{-1}) for 5 min. For the water splitting step, steam vapour was generated from a bubbler filled with deionized water and kept at a constant 373 K. 20 mL min^{-1} of Ar passed through the bubbler and was entrained in 230 mL min^{-1} of Ar before delivering steam vapour into the reactor for 10 min. The reactor was again purged with Ar (500 mL min^{-1}) for 5 min before the next cycle began. 20 cycles of chemical looping steam methane reforming were carried out with each oxygen carrier, from which H_2 and CO production rates and yields were calculated.

The kinetic analysis for methane reforming was investigated in separate experiments after the materials were cycled as above. The same 20 mL min^{-1} of CH_4 entrained in 230 mL min^{-1} of Ar was used and each sample was reduced under a temperature program from 973 K to 1273 K with a ramp of 5 K min^{-1}. The Friedman isoconversional method was used to give model-free estimation of the activation energies.[45,46] The extent of conversion was calculated from the instantaneous H_2 and CO concentrations measured by the mass spectrometer.

4.3 Results and Discussion

Ce-Mn oxygen carriers with varying Ce/(Mn+Ce) nominal atomic content of 0% Ce, 1% Ce, 3% Ce, 5% Ce, 10% Ce, 25% Ce, 50% Ce, 75% Ce and 100% Ce were prepared by flame spray pyrolysis. This scalable and facile method is capable of synthesizing well-controlled Ce-Mn oxide solid solutions with enhanced solubility and

structural stability.[21,43,44] Here, the 3% Ce refers to the same 3% Ce Mn_3O_4 investigated in Chapter 3. TEM analysis of the as-prepared oxygen carriers showed similar particle morphology and distribution. As an example, the TEM micrographs of the 1% Ce, 3% Ce and 5% Ce are shown in Figure 4.1a. Here, all the three as-prepared samples exhibited agglomerates of 10–15 nm nanoparticles. The lattice interplanar spacings measured on the Mn_3O_4 (101) plane were 5.02 Å, 5.07 Å and 5.07 Å, respectively. These lattice spacings conform to that of 4.92 Å in pure Mn_3O_4 but are slightly larger due to lattice expansion by substitutional incorporation of Ce ions that have a larger ionic radii than Mn ions.[47] The XRD patterns of the as-prepared oxygen carriers confirm this analysis and are shown in Figure 4.1b. Oxygen carriers with Ce content up to 10% resulted in solid solutions with a Mn_3O_4 matrix and no apparent segregation of Ce-containing species. With increasing Ce content, the lattice expansion resulted in a shift of the spectra towards lower diffraction angles. This is demonstrated by the most intense Mn_3O_4 peaks on the (211) plane showing a gradual shift of 2θ from 36.08° in 0% Ce to 35.81° in 10% Ce (Figure 4.1c). This is confirmed by the interplanar spacing of the Mn_3O_4 (211) plane calculated from the XRD patterns, showing an increasing $d_{(211)}$ from 2.486 Å in 0% Ce to 2.491 Å in 10% Ce (Table 4.1). Further increasing the Ce content to 100% resulted in XRD spectra showing an increasing presence of CeO_2 with fluorite structure. At 25% Ce, a secondary segregation suggested by the peak located at 36.44° was also observed. This is attributed to ex-solution of a Mn-containing phase from the CeO_2 crystal structure. The most intense CeO_2 peaks on the (111) plane show a gradual shift of this peak from 28.49° in 100% Ce to 29.03° in 25% Ce with increasing Mn substitution in the CeO_2 structure (Figure 4.1c). As a result, the corresponding interplanar spacing of the CeO_2 (111) plane also decreased from 3.125 Å in 100% Ce to 3.075 Å in 25% Ce (Table 4.1). Additionally, the crystallite size of 25% Ce is 9 nm (Table 4.1), which is the smallest in all the investigated oxygen carriers and suggests an

increasing extent of lattice distortion when the Ce:Mn ratio in the precursor approaches 1:3. The complete XRD patterns of the as-prepared oxygen carriers are shown in Figure S4.4.

The SSA of the as-prepared oxygen carriers was evaluated by N_2 adsorption via the BET method (Table 4.1). Notably, 3% Ce has the highest SSA (343 m^2 g^{-1}) among the investigated oxygen carriers with more than 3 times enhancement from the baseline SSA (approximately 100 m^2 g^{-1}). Deviation of Ce content from 3% reduced the SSA rapidly towards the baseline value, as shown by the apparent decrease of 15% in 5% Ce (293 m^2 g^{-1}) and 50% in 1% Ce (170 m^2 g^{-1}), respectively, compared to that of 3% Ce.

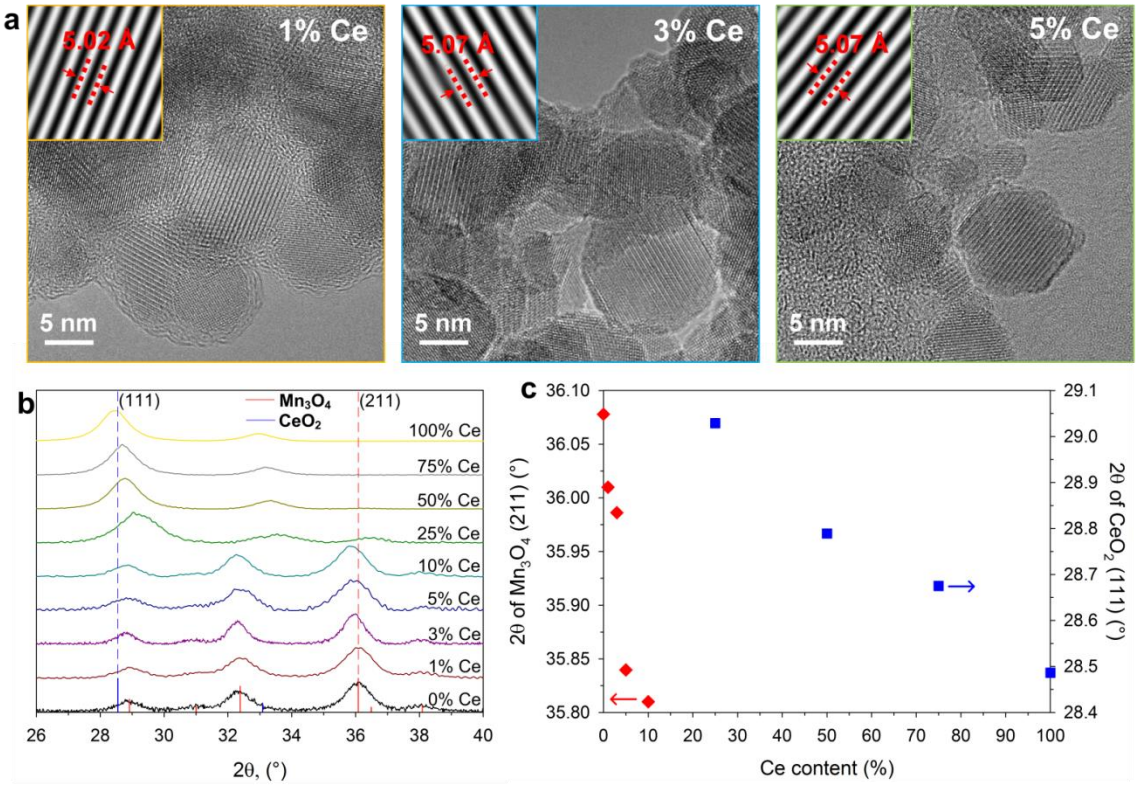

Figure 4.1 Structural characterization of the as-prepared Ce-Mn oxygen carriers. **(**a) TEM micrographs of 1% Ce, 3% Ce and 5% Ce showing the lattice interplanar spacings on the Mn_3O_4 (101) plane. (b) XRD patterns and the ICDD reference spectra of Mn_3O_4 (80-0382) and CeO_2 (75-0120). (c) XRD diffraction angles of the Mn_3O_4 (211) plane and the CeO_2 (111) plane with increasing Ce content.

Table 4.1 Structural properties of CMO oxygen carriers over 20 cycles of chemical looping steam methane reforming.[a)]

Material	As-prepared				After 20 Cycles			
	S_{BET} (m^2 g^{-1})	d_{XRD} (nm)	CeO_2 $d_{(111)}$ (Å)	Mn_3O_4 $d_{(211)}$ (Å)	S_{BET} (m^2 g^{-1})	d_{XRD} (nm)	CeO_2 $d_{(111)}$ (Å)	MnO $d_{(200)}$ (Å)
0% Ce	115	14		2.486	0.8	50		2.222
1% Ce	170	12		2.487	0.6	51		2.223
3% Ce	343	15		2.489	2.0	42	3.124	2.240
5% Ce	293	11		2.490	1.2	55	3.123	2.231
10% Ce	103	12		2.491	0.4	62	3.122	2.233
25% Ce		9	3.075			40	3.124	2.228
50% Ce	96	11	3.101		0.3	49	3.123	
75% Ce		10	3.117			53	3.124	
100% Ce	106	10	3.125		1.5	42	3.124	

[a)] S_{BET}: specific surface area; d_{XRD}: crystallite size; CeO_2 $d_{(111)}$: interplanar spacing of the CeO_2 (111) plane; Mn_3O_4 $d_{(211)}$: interplanar spacing of the Mn_3O_4 (211) plane; MnO $d_{(200)}$: interplanar spacing of the MnO (200) plane.

A calculation of the Gibbs free energy of reaction in Figure S4.1a shows that a MnO/Mn_7C_3 redox pair is thermodynamically favourable above 1150 K to drive the chemical looping steam methane reforming reactions according to the following equations:

$$7\ MnO + 10\ CH_4 \rightarrow Mn_7C_3 + 7\ CO + 20\ H_2,\ \Delta H^o_{298} = +2558\ kJ\ mol^{-1} \quad (4.3)$$

$$Mn_7C_3 + 10\ H_2O\ (g) \rightarrow 7\ MnO + 3\ CO + 10\ H_2,\ \Delta H^o_{298} = -497\ kJ\ mol^{-1} \quad (4.4)$$

At 1173 K, selected as the isothermal operating temperature of this study, chemical equilibriums show almost 100% selectivity to H_2 and CO (as opposed to H_2O and CO_2) during reduction (Figure S4.1b), and 99.1% to H_2 and 99.3% to CO, respectively,

during oxidation (Figure S4.1c). Additionally, all the materials investigated in this work were subjected to a 20-cycle redox pathway in Eq. 4.3 and 4.4.

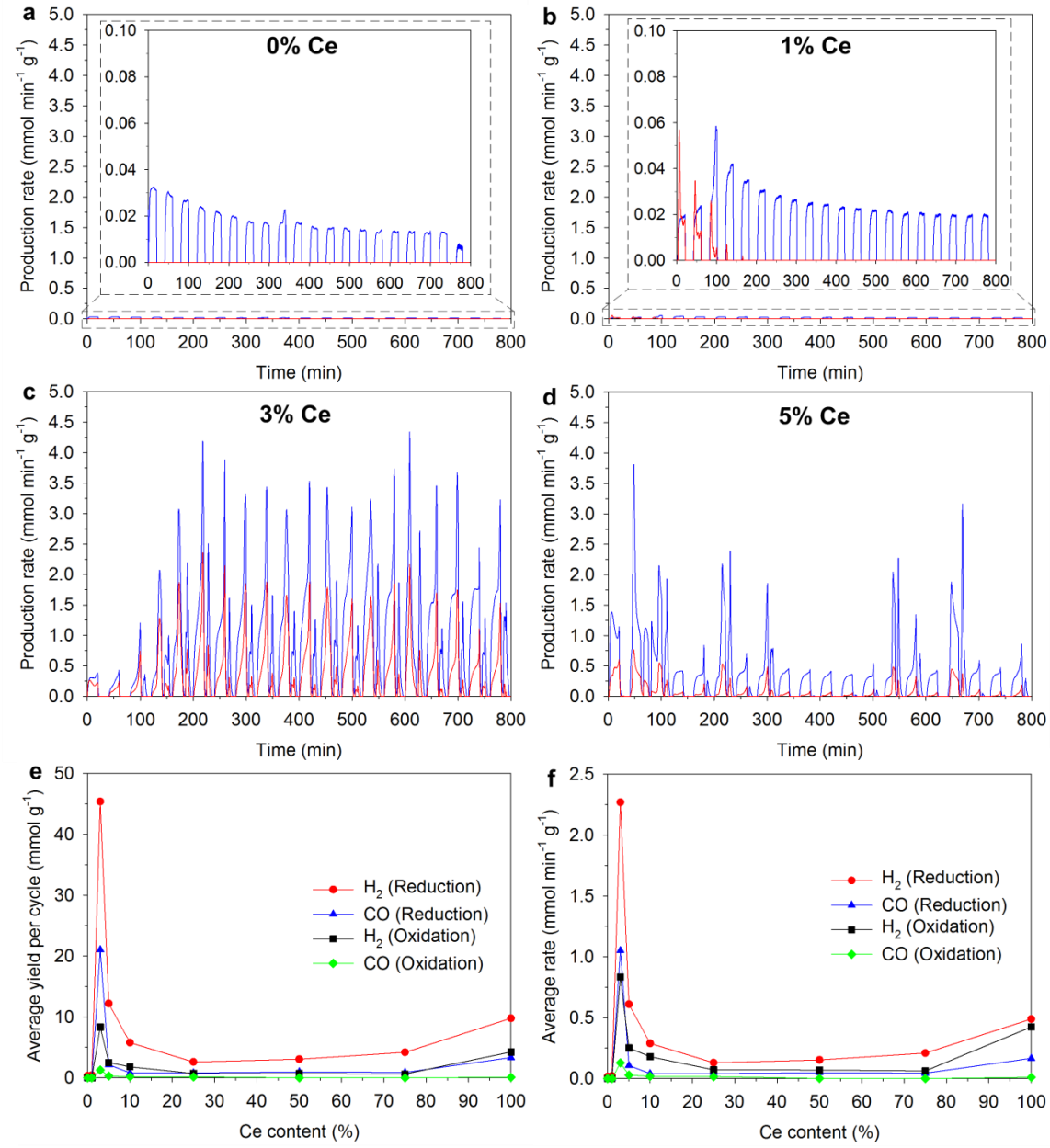

Figure 4.2 Syngas production over 20 cycles of chemical looping steam methane reforming. H_2 (blue) and CO (red) production by (a) 0% Ce, (b) 1% Ce, (c) 3% Ce and (d) 5% Ce at 1173 K. (e) Average syngas yield and (f) average production rate with increasing Ce content over 20 cycles.

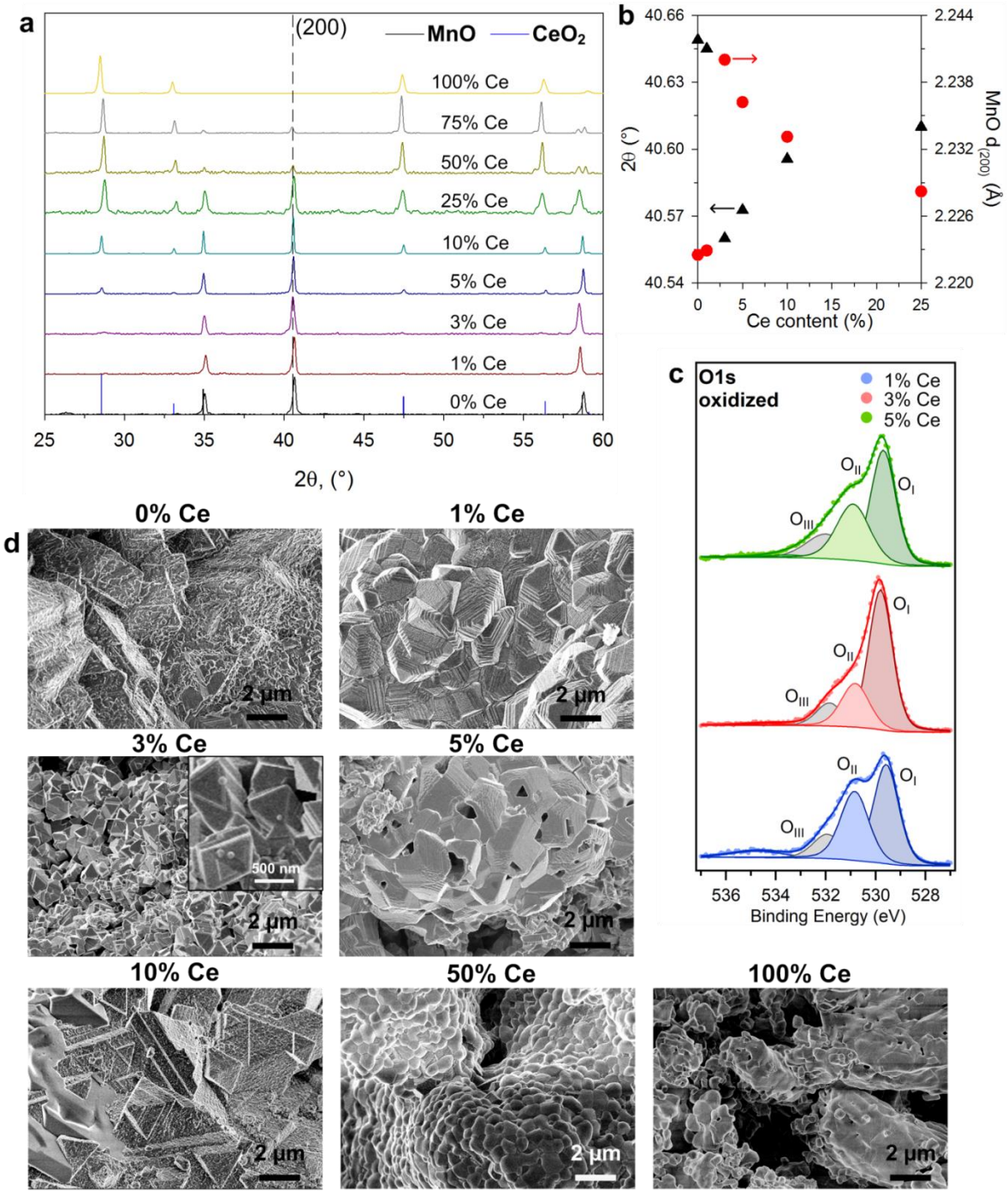

Figure 4.3 Structural characterization of the Ce-Mn oxygen carriers after 20 cycles of chemical looping steam methane reforming. (a) XRD patterns and the ICDD reference spectra of MnO (75-1090) and CeO_2 (75-0120). (b) XRD diffraction angles and interplanar spacings of the MnO (200) plane with increasing Ce content. (c) XPS of the O 1s spectra. O_I: lattice oxygen. O_{II}: lattice oxygen near vacancies. O_{III}: oxygen in surface hydroxides and carbonates. (d) SEM images.

Syngas production performance for a majority of the oxygen carriers investigated here (75% Ce, 50% Ce, 25% Ce and 10% Ce) is shown in Figure S4.2 b–e. At the end of the 20 cycles, these samples demonstrated slower reaction rates compared to pure ceria (100% Ce, Figure S4.2a) and no significant improvement from pure manganese oxide (0% Ce, Figure 4.2a). However, notably high H_2 and CO production peak rates were observed with 10% Ce in the 3rd and 5th cycle (Figure S4.2e) and indicated that an optimal kinetic enhancement can be reached by further lowering the Ce content.

The H_2 and CO production rates demonstrated by 1% Ce, 3% Ce and 5% Ce (Figure 4.2 b–d) confirm the optimal Ce content for kinetic enhancement at 3%. In particular, the enhanced reduction and oxidation kinetics was noticeably observed in cycles with 3% Ce (Figure 4.2c). The initial 2 cycles showed syngas production rates lower than 0.5 $mmol_{H2}$ min^{-1} g^{-1} and 0.25 $mmol_{CO}$ min^{-1} g^{-1}, respectively, attributed to reduction from Mn_3O_4 to MnO, and accompanied by no H_2O splitting. From the 3rd cycle the syngas production rates during reduction significantly ramped up by up to 100% per cycle and reached peak production rates of 4.2 $mmol_{H2}$ min^{-1} g^{-1} and 2.3 $mmol_{CO}$ min^{-1} g^{-1} in the 6th cycle. These rates indicate a distinct and effective kinetic enhancement by 3% Ce. Notably, the corresponding H_2 and CO evolution during the oxidation steps also simultaneously began from the 3rd cycle and ramped up to peak production rates of 2.5 $mmol_{H2}$ min^{-1} g^{-1} and 0.8 $mmol_{CO}$ min^{-1} g^{-1} in the 6th cycle. This improvement was not short-lived as the later 14 cycles sustained high peak production rates and approximately 3.1 $mmol_{H2}$ min^{-1} g^{-1} and 1.5 $mmol_{CO}$ min^{-1} g^{-1} were observed during reduction, while those of 1.3 $mmol_{H2}$ min^{-1} g^{-1} and 0.2 $mmol_{CO}$ min^{-1} g^{-1} were observed during oxidation.

In contrast, a slight deviation of the Ce content from 3% involved a significant drop of the redox kinetics, demonstrated by the performance of the 1% Ce and 5% Ce. In

particular, 1% Ce (Figure 4.2b) was not able to efficiently perform in the oxide-carbide redox cycle (Eq. 4.3 and 4.4). The initial CO evolution was attributed to the reduction of Mn_3O_4 to MnO and diminished after 3 cycles as no further reduction from MnO to Mn_7C_3 was initiated. The reduction steps in the rest of the cycles showing no CO production and a steady H_2 production rate of 0.025 $mmol_{H2}$ min^{-1} g^{-1} may be due to methane cracking[11,48], resembling that demonstrated by 0% Ce (Figure 4.2a). Note that these production rates are two orders of magnitude slower than those of 3% Ce. More significantly, no syngas production was observed in the oxidation steps, indicative of no H_2O splitting activity by 1% Ce. The low activity of 1% Ce indicates an optimal Ce content to provide any kinetic improvement had not been reached in this oxygen carrier to activate the redox cycle of Eq. 4.3 and Eq. 4.4. On the other hand, the 5% Ce (Figure 4.2d) demonstrated overall irregular kinetic improvement with the majority of the investigated cycles showing low syngas production rates compared to 3% Ce. Initially, the 5% Ce enabled a faster reduction from Mn_3O_4 to MnO, demonstrated by the higher peak production rates of 1.3 $mmol_{H2}$ min^{-1} g^{-1} and 0.6 $mmol_{CO}$ min^{-1} g^{-1} in the first reduction step compared to those of 3% Ce. Additionally, the onset of redox cycle by Eq. 4.3 and Eq. 4.4 also occurred from the 2nd cycle, suggested by the production of H_2 and CO in the oxidation step, and thus earlier than that which occurred for 3% Ce. However, a kinetic enhancement in 5% Ce was not constantly retained. This is demonstrated by the irregular spikes of H_2 and CO production rates which were only observed in the 2nd, 3rd, 6th, 8th, 14th, 15th and 17th cycles, while the rest of the cycles exhibit slow kinetics with significant methane cracking activity. Although the high performing cycles showed peak syngas production rates comparable to those of 3% Ce, the intermittent activity and reduced performance of 5% Ce limits its promise as a long-term efficient oxygen carrier in solar chemical looping steam methane reforming cycles.

The average syngas yields (Figure 4.2e) and production rates (Figure 4.2f) per cycle especially highlight the optimal kinetic enhancement for chemical looping steam methane reforming by 3% Ce. Although large variations of performance per cycle need to be considered when evaluating the results of 5% Ce (Figure 4.2c), 10% Ce (Figure S4.2e), 25% Ce (Figure S4.2d) and 50% Ce (Figure S4.2c), the calculated averages here provide an indication of the overall reversible oxygen exchange capacity accessed per each Ce content in the given time due to the various extent of enhancement on the redox kinetics. Here, 3% Ce has demonstrated exceptionally high syngas yields of 45.38 $mmol_{H2}$ g^{-1} and 21.02 $mmol_{CO}$ g^{-1} during 20 min of methane reforming (Figure 4.2e), due to fast syngas production rates of 2.27 $mmol_{H2}$ min^{-1} g^{-1} and 1.05 $mmol_{CO}$ min^{-1} g^{-1}, respectively (Figure 4.2f). This is in contrast to 9.77 $mmol_{H2}$ g^{-1} and 3.32 $mmol_{CO}$ g^{-1} achieved by 100% Ce, and 0.32 $mmol_{H2}$ g^{-1} and 0.01 $mmol_{CO}$ g^{-1} achieved by 0% Ce. During 10 min of water splitting, cycles with 3% Ce also produced H_2 at 8.33 $mmol_{H2}$ g^{-1}. This is approximately twice as much as 100% Ce while no apparent syngas yields were produced by 0% Ce. The noticeable CO production of 1.29 $mmol_{CO}$ g^{-1} during water splitting by 3% Ce adds to the oxidizer conversion efficiency due to additional carbon from methane introduced into the redox cycle according to Eq. 4.3 and 4.4. It is also worth noting that the significant decrease in syngas yields and production rates demonstrated by 5% Ce and 1% Ce suggest the importance of keeping the Ce content close to 3% in order to optimize the effect of kinetic enhancement.

To identify the cause for the optimal enhancement in redox kinetics, the structural properties of the oxygen carriers after the methane reforming step following 20 complete CLR cycles were first characterized by XRD, as shown in Figure 4.3a. Clear segregation of MnO and CeO_2 phases were observed in all the cycled Ce-Mn oxygen carriers. Particularly from 1% Ce to 25% Ce, where various degrees of kinetic enhancement were observed, the most intense peaks at MnO (200) planes shifted

towards a lower 2θ compared to 0% Ce, with the maximum shift occurring in 3% Ce (Figure 4.3b). The corresponding interplanar spacing also shows that 3% Ce had the highest $d_{(200)}$ of 2.240 Å (Table 4.1), indicative of the largest expansion of the lattice cells. This is due to the presence of residual Ce ions in the MnO matrix that increased the interplanar spacing, and 3% Ce may have reincorporated the greatest amount of Ce ions. Additionally, all the oxygen carriers typically had 3 to 5 times growth in crystallite size after the redox cycles (Table 4.1) due to thermal sintering and grain growth. This is corroborated by the BET measurements showing more than 99% loss in SSA for all the investigated oxygen carriers (Table 4.1) after 13.3 h of operation at 1173 K. Although the SSA of 3% Ce (2.0 m^2 g^{-1}) still remained the largest among the cycled oxygen carriers, the drastic loss in SSA is in contrast to its sustained high syngas production activity demonstrated in Figure 4.2b and suggests that the initial high surface area had a limited contribution to the enhanced redox kinetics in the later cycles.

An insight of the lattice oxygen occupancy after the 20th oxidation step of steam methane reforming is shown in Figure 4.3c with 1% Ce, 3% Ce and 5% Ce via the XPS spectra of the O1s orbital. Three peaks at 529.5, 531.0 and 532.0 eV were deconvoluted from the O1s spectra. Among them, the peak at 529.5 eV (O_I) originates from lattice oxygen. The peak with a higher binding energy of 531.0 eV (O_{II}) is associated with oxygen atoms close to vacancy-rich regions. The third peak at 532.0 eV (O_{III}) is attributed to surface H_2O and/or –OH species adsorbed onto the sample.[47,49,50] The relative peak intensity between O_I and O_{II} reveals that the O_I content in 3% Ce is distinctively higher than for 1% Ce and 5% Ce, which resulted from a greater net consumption of vacancies during the H_2O splitting reaction (Eq. 4.4).[51] The complete XPS analysis including the Mn2p, Ce3d and C1s of 1% Ce, 3% Ce and 5% Ce after 20 redox cycles is provided in Figure S4.3.

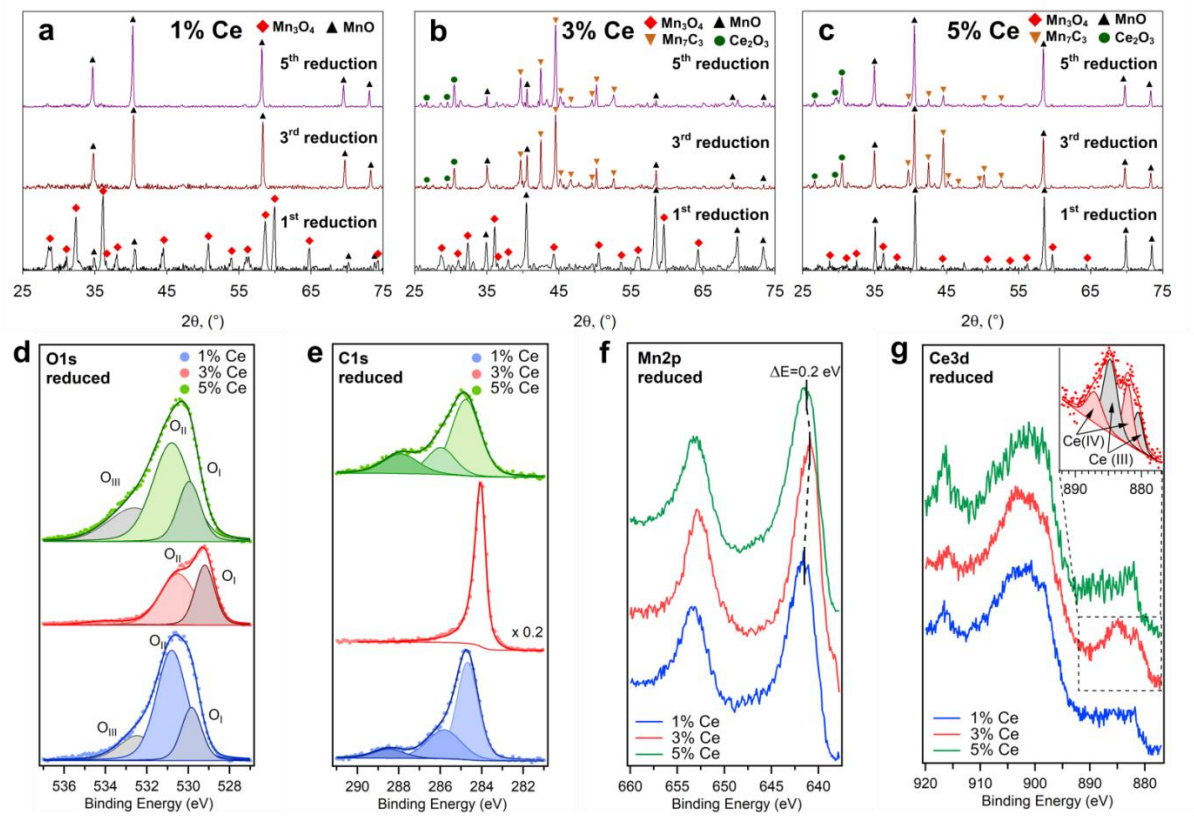

Figure 4.4 Structural evolution of the Ce-Mn oxygen carriers during the chemical looping steam methane reforming cycles. XRD patterns of the (a) 1% Ce, (b) 3% Ce and (c) 5% Ce after the 1st, 3rd and 5th reduction steps. XPS of the 1% Ce, 3% Ce and 5% Ce showing the (d) O 1s, (e) C 1s, (f) Mn 2p and (g) Ce 3d patterns after the 21st reduction step.

The structural enhancement introduced by 3% Ce was observed in the SEM images (Figure 4.3d) showing 0% Ce, 1% Ce, 3% Ce, 5% Ce, 10% Ce, 50% Ce and 100% Ce. In particular, the cycled 0% Ce showed highly dense and crystalline grains which suggest a high degree of sintering and corresponds well to the growth in crystallite size observed in Figure 4.3a and the significant loss of SSA shown in Table 4.1. Additionally, the surface of the 0% Ce grains was covered with amorphous adsorbents. This is not observed in the cycled 1% Ce, where only aggregated polyhedrons with sizes larger than 2 µm were present. The cycled 1% Ce crystals were densely packed and showed low porosity. In contrast, the cycled 3% Ce showed highly crystalline and

interconnected polyhedrons with less than 500 nm in size. Notwithstanding the increased Ce content, the cycled 5% Ce did not show smaller granules, but resembled that of 1% Ce with densely packed polyhedrons that were larger than 2 µm in grain size. Further increasing the Ce content resulted in a more pronounced segregation of a second phase. In the case of 50% Ce and 100% Ce, the cycled oxygen carriers showed monolithic interconnected aggregates of this second phase due to high-temperature sintering.

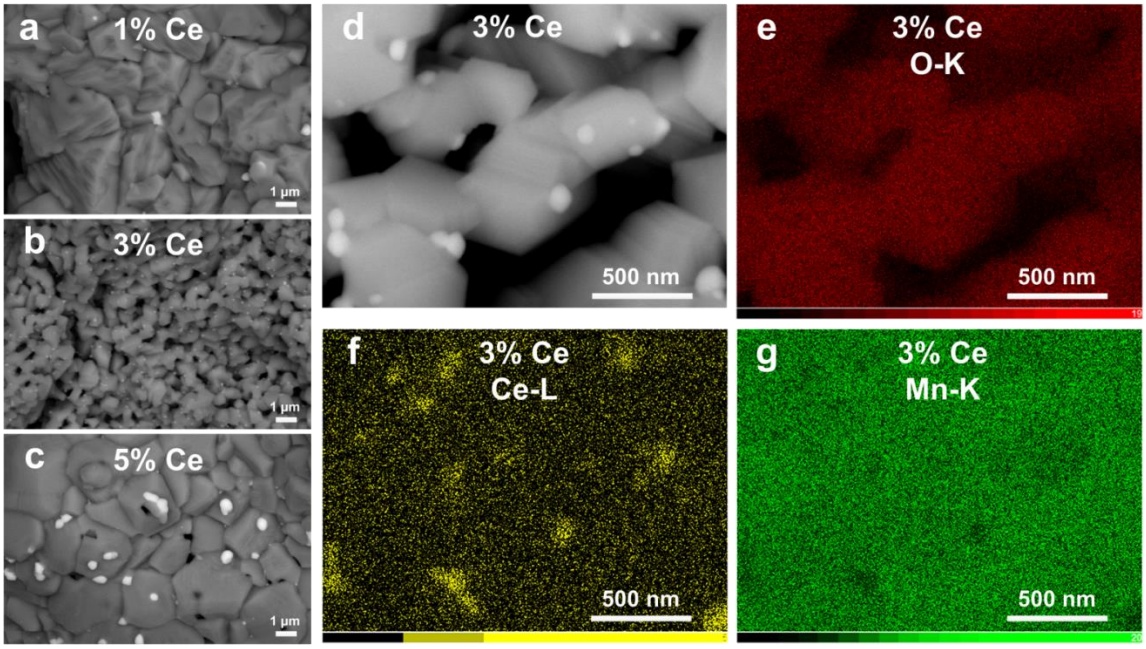

Figure 4.5 Morphology of the Ce-Mn oxygen carriers after 20 cycles of chemical looping steam methane reforming. SEM images obtained with backscattered electrons showing the (a) 1% Ce, (b) 3% Ce and (c) 5% Ce. EDX elemental mapping of 3% Ce over an area of interest (d) showing 300 nm polyhedrons with 50 nm secondary phase on the surface and their composition of (e) O, (f) Ce and (g) Mn.

To understand the role of Ce ions in the optimal kinetic enhancement and forming the distinctive structural properties of 3% Ce, the structural states after the reduction steps were investigated in detail by step-wise XRD analysis (Figure 4.4 a-c) for 1% Ce, 3% Ce and 5% Ce. Upon the 1st reduction by methane, all three oxygen carriers were in

transition from Mn_3O_4 to MnO with no apparent segregation of CeO_2 or Ce_2O_3 phases, demonstrated by the coexistence of only Mn_3O_4 and MnO phases shown in Figure 4.4 a-c. This is consistent with the 1st cycle demonstrations in Figure 4.2 b–d showing no H_2O splitting activity in the 1st oxidation steps by all the three oxygen carriers, as a Mn_3O_4-to-MnO reduction is not thermodynamically reversible by H_2O. The difference in relative intensity between Mn_3O_4 and MnO after the 1st reduction in Figure 4.4 a–c suggests the kinetics for the reduction of Mn_3O_4 to MnO increases with increasing Ce content, and is confirmed by the increasing H_2 and CO production rates from 1% Ce to 5% Ce in Figure 4.2 b–d. Upon the initial reduction from Mn_3O_4 to MnO, 1% Ce remained structurally unchanged in the subsequent redox cycles, demonstrated by a single MnO phase appearing after the 3rd and 5th reduction steps in Figure 4.4a. The presence of only MnO explains why no CO was produced in the later reduction steps in Figure 4.2a and further confirms that the low amount of H_2 evolution was not due to active redox reactions with 1% Ce, but rather due to methane cracking. On the other hand, the high kinetics by 3% Ce in the later cycles (Figure 4.2c) were associated with fast redox cycling via Eq. 4.3 and Eq. 4.4, confirmed by the prevalent formation of Mn_7C_3 after the 3rd and 5th reduction steps (Figure 4.4b). The increasing peak intensity of Mn_7C_3 from the 3rd to the 5th reduction also corresponds to the increasing peak H_2 and CO production rates between the two reduction steps. Notably, Ce dopants were segregated from the matrix upon reduction, shown as the Ce_2O_3 phase after the 3rd and the 5th reduction steps. Lastly, in Figure 4.4c, the formation of Mn_7C_3 in 5% Ce was more pronounced in the 3rd reduction than in the 5th, correlating to the randomly high syngas production rates observed in the 3rd cycle but not in the 5th cycle in Figure 4.2d.

The high activity of lattice oxygen diffusion and carbide formation in 3% Ce during methane reforming was further confirmed by XPS analysis in Figure 4.4 d–g obtained upon a further reduction of 1% Ce, 3% Ce and 5% Ce after 20 cycles. Here, when

comparing Figure 4.4d with Figure 4.3c showing the O1s binding energies, a relative shift of intensity from O_I to O_{II} is shown in all the three samples, indicative of oxygen vacancies formed during reduction. The presence of surface O_{III} species in 1% Ce and 5% Ce in Figure 4.4d indicates that the migrated oxygen atoms did not have sufficient energy to oxidize the chemisorbed carbon and hydrogen cleaved from CH_4.[20,52,53] These oxygen atoms remain on the surface of 1% Ce and 5% Ce and are confirmed by the higher relative intensity of O_{II} species when compared to 3% Ce. This also corresponds to the low activity of 1% Ce and 5% Ce in producing CO during reduction steps demonstrated in Figure 4.2b and d. In contrast, upon reduction the spectrum centroid of O1s in 3% Ce is at lower binding energy despite a consumption of lattice oxygen (O_I). Notably, the lower relative intensity of O_I/O_{II} in this sample points a reduced relative amount of lattice oxygen, suggesting the vacancies generated during reduction were filled by non-oxygen species, such as carbon. Additionally, the absence of O_{III} species in 3% Ce indicates that the migrated oxygen atoms had dissociated from the metal oxide surface and corresponds to the formation of CO during reduction as was shown in Figure 4.2c. In Figure 4.4e, the C1s spectra give more information about the different interactions of carbon atoms in the three oxygen carriers. The three peaks observed in 1% Ce and 5% Ce are ascribed to adventitious C–C bonds (284.9 eV), surface C–O bonds (285.9 eV), and surface C=O bonds (> 288 eV), respectively.[54-56] The latter two types of carbon-oxygen bonds correspond to the O_{III} species observed in Figure 4.4d, confirming the low activity of oxygen in 1% Ce and 5% Ce to dissociate from the surface. In contrast, the C1s spectra of reduced 3% Ce showed one sharp and intense peak at a lower binding energy of 284.0 eV, corresponding to the metal-carbide bond[54,55] arising from the formation of Mn_7C_3, which suggests that the oxygen vacancies created during reduction from the O1s spectra are filled by carbon. Here in 3% Ce, the absence of C1s peaks associated with surface C–O or C=O bonds is in agreement with the absence of

O_{III} species in Figure 4.4d, further supporting the ability of 3% Ce to promote the dissociation of chemisorbed species. In terms of the metallic ions, the Mn2p doublet in Figure 4.4f shows that in 3% Ce there is a 0.2 eV shift towards lower binding energy. This may be attributed to the abundance of Mn–C bonds[57] in the reduced 3% Ce that are weaker than Mn–O bonds[58]. In Figure 4.4g the Ce3d spin-orbit multiplets from 880 eV to 920 eV is shown, overlapping the Mn Auger peak in the background. The characteristic peaks at 917 eV and 882 eV correspond to Ce^{4+}, and the peak at 885 eV is attributed to Ce^{3+}.[59,60] In general, all the reduced oxygen carriers exhibited a mix of Ce^{4+} and Ce^{3+}, with Ce^{3+} as the relatively larger fraction in 3% Ce compared to 1% Ce and 5% Ce. This suggests that on the surface atomic layers the segregation of Ce in the form of Ce_2O_3 upon reduction (Figure 4.4b and c) was only partial, and there were residual Ce^{4+} and/or Ce^{3+} ions in the manganese oxide matrix. The abundance of Ce^{3+} in 3% Ce is the result of a higher extent of reduction during methane reforming.

To identify the relationship of phase segregation in regard to the redox performance demonstrated by 1% Ce, 3% Ce and 5% Ce in Figure 4.2 b–d, backscattered electron (BSE) images were obtained from the three oxygen carriers after 20 chemical looping steam methane reforming cycles, shown in Figure 4.5 a–c, respectively. Here, the morphologies are in agreement with Figure 4.3d, where 3% Ce consists of primarily 500 nm interconnected polyhedrons that are distinctive from the large and sintered polycrystalline grains in 1% Ce and 5% Ce. In particular, the elemental mapping of the same 3% Ce via energy-dispersive X-ray spectroscopy (EDX) over a general area of interest (Figure 4.5d) is shown in Figure 4.5 e-g, and suggests that these polyhedrons mainly consist of MnO with a homogeneous incorporation of Ce ions in a low amount, confirming the residual Ce ions in the MnO matrix. Additionally, the surface of the MnO polyhedrons in 3% Ce (Figure 4.5b) was uniformly distributed with separated nanoparticles as a secondary phase that were less than 50 nm in size (Figure 4.5d),

which was in contrast to the larger than 300 nm and partially sintered secondary phase observed in 1% Ce and 5% Ce (Figure 4.5a and c). Elemental analysis (Figure 4.5 e–g) suggests that these metal oxide nanoparticles on the surface of 3% Ce are rich in Ce and deficient in Mn. Here, it is hypothesized that the distinctively porous and interconnected polyhedrons with uniformly-distributed surface-abundant ceria-rich nanoparticles observed in the steady-state 3% Ce have a direct structural effect on its optimal kinetic enhancement in chemical looping steam methane reforming redox cycles.

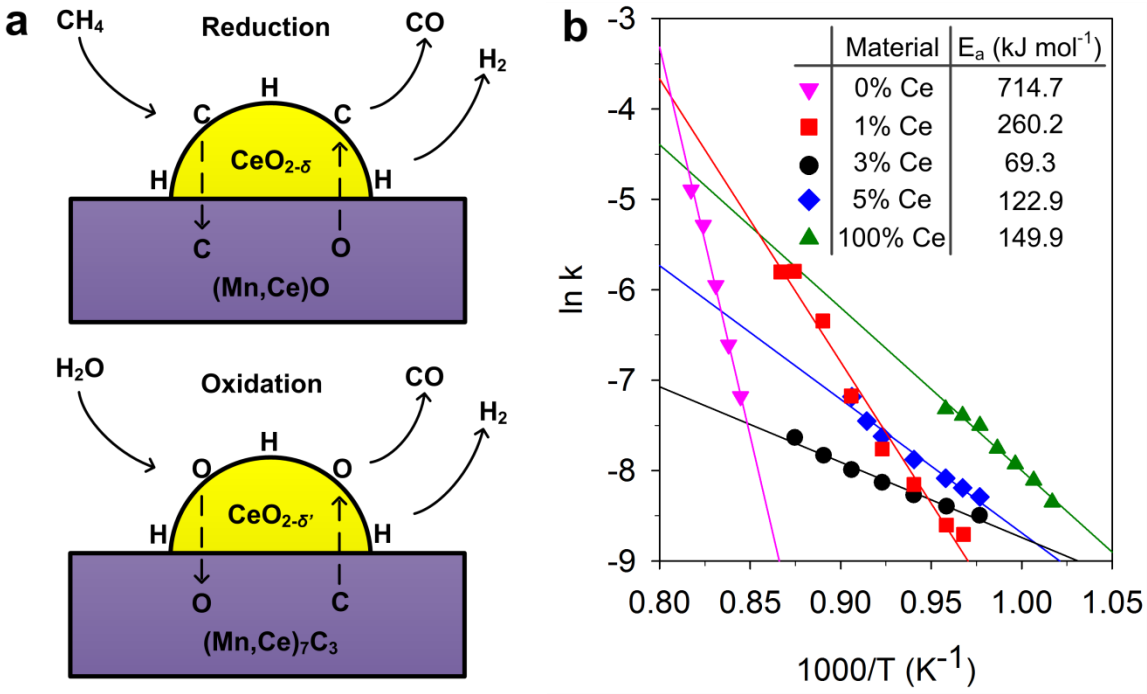

Figure 4.6 Redox mechanism of the Ce-Mn oxygen carriers in solar chemical looping steam methane reforming. (a) CH_4/H_2O dissociation and oxygen/carbon diffusion over a Ce-rich region. (b) Activation energy of the oxygen carriers for reduction by methane.

The above step-wise structural analysis and characterisation of the steady-state oxygen carriers (Figure 4.3–4.5) provides a foundation to understand the mechanism of oxygen carriers in a redox cycle based on Eq. 4.3 and Eq. 4.4. The mechanism is depicted in Figure 4.6a. Here, a hypothesis is that the surface Ce-rich region is where Eq. 4.3 (reduction) and Eq. 4.4 (oxidation) are kinetically promoted. This region includes

the surface ceria segregates and their interface with the Ce-enriched Mn-based oxygen carrier. At the initiation of reduction, surface oxygen is abundant in the Ce-rich region. Dissociation of CH_4 molecules supplies carbons that are chemisorbed onto the surface of the oxygen carrier.[20,53,61] However, only in the Ce-rich regions are the chemisorbed carbons partially oxidized into CO, creating vacancies as the bulk oxygens diffuse into the surface and combine with the carbons.[20,52,53,61] Once sufficient vacancies are generated, the chemisorbed carbons are able to diffuse into the bulk lattice. Similarly, during oxidation, dissociation of H_2O molecules supplies oxygens that are chemisorbed onto the surface of the reduced oxygen carrier and soon released into CO by combining with the carbons diffused from the bulk material. Upon that the chemisorbed oxygens are able to diffuse into the bulk. Notably, the Ce content plays a vital role in this redox mechanism. In 1% Ce, insufficient Ce content could not ensure a high coverage of Ce-rich regions on the oxygen carrier to provide effective kinetic enhancement. On the other hand, in 5% Ce, excessive Ce content resulted in bulk-size segregation of ceria-rich phases that do not provide effective promotion due to the fact that most of these phases were too far away from the oxygen carrier's interface. However, in 3% Ce (Figure 4.5b), highly dispersed ceria-rich nanoparticles were in close contact to the surface of the oxygen carrier, and effectively provide a large coverage of Ce-rich region to activate the redox cycle. Additionally, an abundance of Ce ions in the bulk lattice of 3% Ce (Figure 4.3b) also enhances the diffusion of oxygen and carbon.

The optimized kinetics in 3% Ce effectively lowered its activation energy for the reduction by methane, calculated in Figure 4.6b via the Friedman isoconversional method. Here, based on the model-free estimation, the 3% Ce achieved an activation energy of 69.3 kJ mol^{-1}, which is more than 90% lower than that of 0% Ce (714.7 kJ mol^{-1}), effectively bringing down the energy barrier to drive a manganese-based chemical looping steam methane reforming into a practically relevant solar-to-chemical

conversion cycle with efficient kinetics. Note that this activation energy of 3% Ce is also approximately half of that of 100% Ce (149.9 kJ mol^{-1}), resulting in its benchmark performance demonstrated in Figure 4.2c.

4.4 Conclusions

The syngas production via chemical looping steam methane reforming over a series of Ce-Mn oxygen carriers was carried out to investigate the dependency of redox kinetics on cerium ions. An optimized fractional Ce content of 3% was demonstrated to activate the vast potential of reversible oxygen exchange capacity in earth-abundant manganese oxide. This resulted in an efficient Ce-promoted MnO/Mn_7C_3 redox cycle for solar fuels production at a commercially competitive temperature of 1173 K from chemical looping steam methane reforming. Step-wise structural analysis and characterisation of the steady-state oxygen carriers revealed that the enhanced redox kinetics in 3% Ce is due to the intense surface distribution of Ce-rich regions and the abundance of Ce ions in the bulk lattice. The Ce-rich regions efficiently dissociate the chemisorbed species into H_2 and CO during methane reforming and water splitting. The bulk Ce ions, supported by XRD and XPS analysis, effectively unlock the oxygen carrier's reversible diffusion of oxygen and carbon in a vacancy-based redox mechanism.

The outstanding capability for methane reforming and water splitting by 3% doped Ce and its distinctive structural and morphological properties calls for further investigation of the role of cerium ions in altering the vacancy formation energy of a MnO/Mn_7C_3 redox cycle at a quantum scale. Such a study may reveal valuable strategies to enhance the long-term thermochemical stability of this efficient and low-cost oxygen carrier, expediting its transition into the expanding renewable energy market.

4.5 Supplementary Information

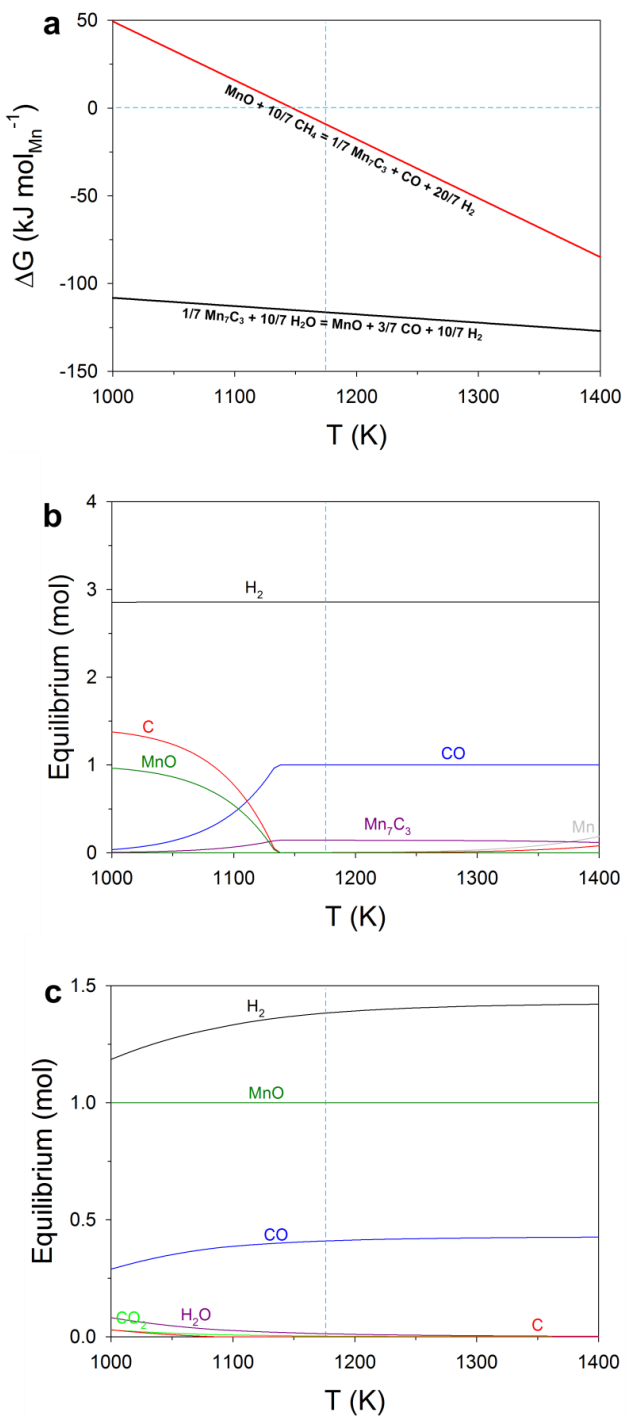

Figure S4.1 (a) Gibbs free energy of the chemical looping steam methane reforming by a MnO/Mn_7C_3 redox pair, normalised as per unit mol of Mn in each equation. The equilibrium composition of (b) 1 mol MnO and 1.4286 mol CH_4 and (c) 0.1429 mol Mn_7C_3 and 1.4286 mol H_2O from 1000 K to 1400 K, with all gases treated as ideal gases under 1 bar.

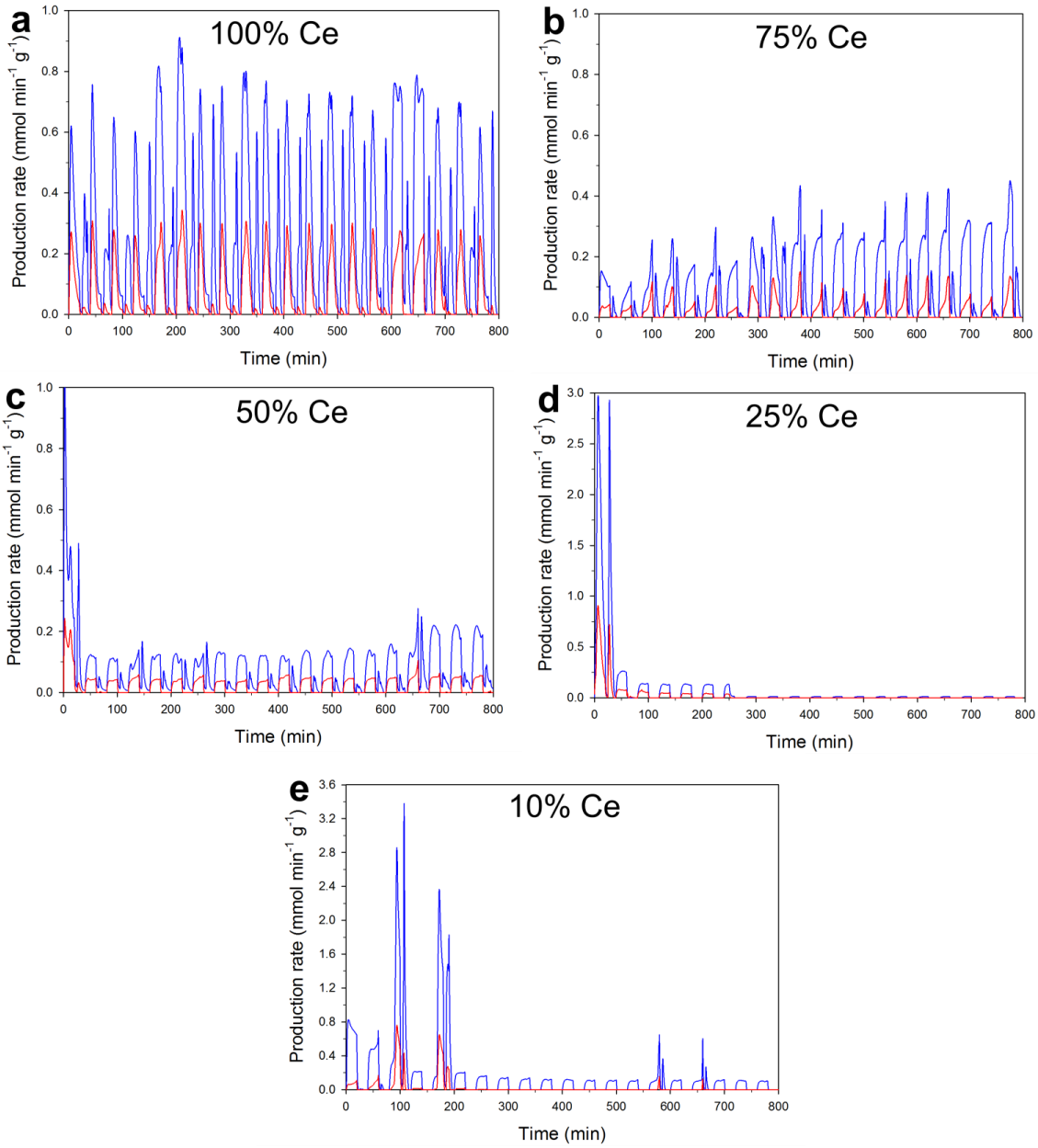

Figure S4.2 H_2 (blue) and CO (red) production over 20 cycles of chemical looping steam methane reforming by (a) 100% Ce, (b) 75% Ce, (c) 50% Ce, (d) 25% Ce and (e) 10% Ce at 1173 K.

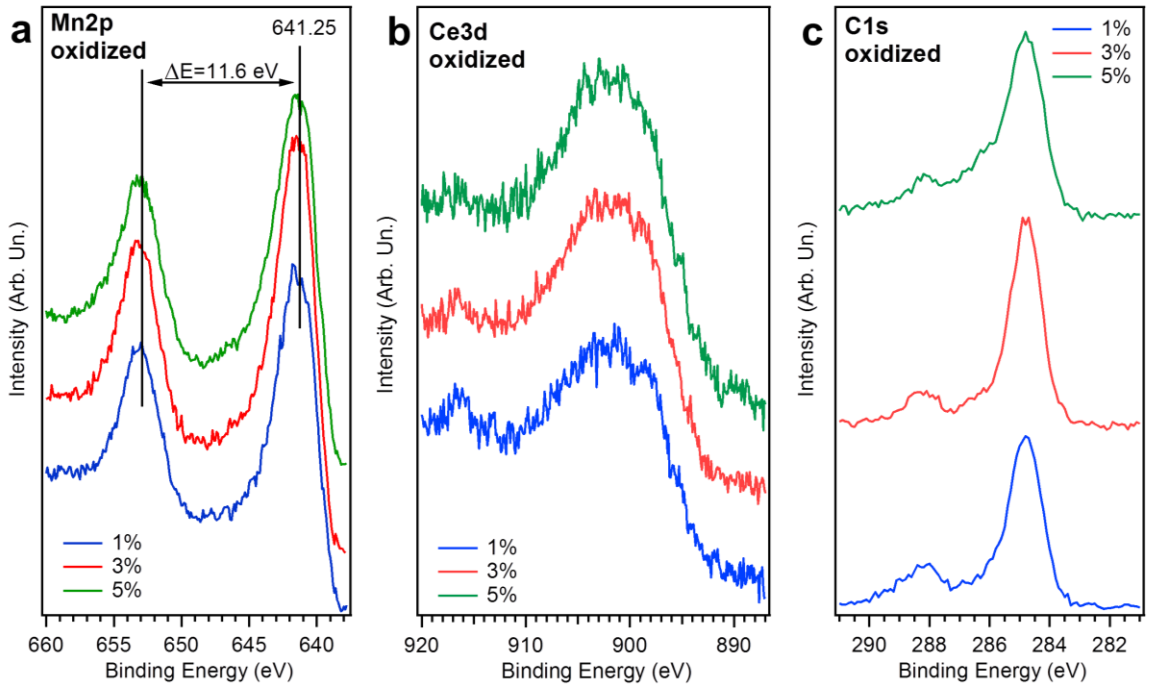

Figure S4.3 XPS of the 1% Ce, 3% Ce and 5% Ce showing (a) Mn 2p, (b) Ce 3d, (c) C 1s spectra after 20 cycles of chemical looping steam methane reforming.

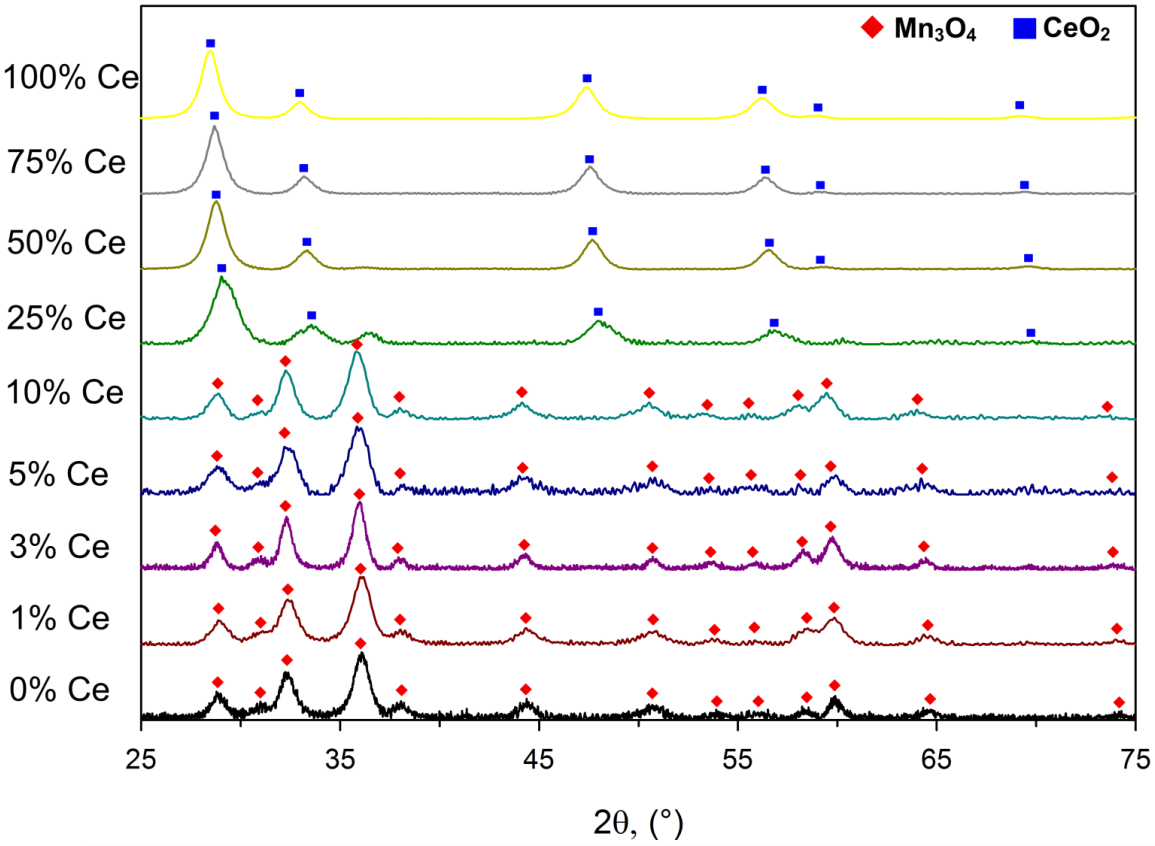

Figure S4.4 XRD patterns of the as-prepared Ce-Mn oxygen carriers.

4.6 References

1. C. Agrafiotis, H. von Storch, M. Roeb and C. Sattler, *Renew. Sust. Energ. Rev.*, 2014, **29**, 656-682.
2. R. Bader and W. Lipiński, in *Advances in Concentrating Solar Thermal Research and Technology*, ed. L. R. Santigosa, Woodhead Publishing, 2017, pp. 403-459.
3. D. S. A. Simakov, M. M. Wright, S. Ahmed, E. M. A. Mokheimer and Y. Roman-Leshkov, *Catal. Sci. Technol.*, 2015, **5**, 1991-2016.
4. P. T. Krenzke, J. R. Fosheim and J. H. Davidson, *Sol. Energy*, 2017, **156**, 48-72.
5. P. T. Krenzke and J. H. Davidson, *Energ. Fuel*, 2014, **28**, 4088-4095.
6. M. C. Tang, L. Xu and M. H. Fan, *Appl. Energy*, 2015, **151**, 143-156.
7. A. Steinfeld, P. Kuhn and J. Karni, *Energy*, 1993, **18**, 239-249.
8. K. S. Go, S. R. Son, S. D. Kim, K. S. Kang and C. S. Park, *Int. J. Hydrog. Energy*, 2009, **34**, 1301-1309.
9. T. Kodama, T. Shimizu, T. Satoh, M. Nakata and K. I. Shimizu, *Sol. Energy*, 2002, **73**, 363-374.
10. T. Kodama, T. Shimizu, T. Satoh and K.-I. Shimizu, *Energy*, 2003, **28**, 1055-1068.
11. J. T. Jang, K. J. Yoon, J. W. Bae and G. Y. Han, *Sol. Energy*, 2014, **109**, 70-81.
12. A. Evdou, V. Zaspalis and L. Nalbandian, *Fuel*, 2010, **89**, 1265-1273.
13. X. P. Dai, Q. Wu, R. J. Li, C. C. Yu and Z. P. Hao, *J. Phys. Chem. B*, 2006, **110**, 25856-25862.
14. L. Nalbandian, A. Evdou and V. Zaspalis, *Int. J. Hydrog. Energy*, 2011, **36**, 6657-6670.
15. K.-S. Cha, H.-S. Kim, B.-K. Yoo, Y.-S. Lee, K.-S. Kang, C.-S. Park and Y.-H. Kim, *Int. J. Hydrog. Energy*, 2009, **34**, 1801-1808.

16. K.-S. Kang, C.-H. Kim, K.-K. Bae, W.-C. Cho, W.-J. Kim, Y.-H. Kim, S.-H. Kim and C.-S. Park, *Int. J. Hydrog. Energy*, 2010, **35**, 568-576.

17. T. Suzuki, O. Nakayama and N. Okamoto, *Cata.s Surv. Asia*, 2012, **16**, 75-90.

18. O. Nakayama, N. Ikenaga, T. Miyake, E. Yagasaki and T. Suzuki, *Ind. Eng. Chem. Res.*, 2010, **49**, 526-534.

19. M. Ortiz, L. F. de Diego, A. Abad, F. García-Labiano, P. Gayán and J. Adánez, *Energ. Fuel*, 2012, **26**, 791-800.

20. K. Otsuka, Y. Wang, E. Sunada and I. Yamanaka, *J. Catal.*, 1998, **175**, 152-160.

21. X. Gao, A. Vidal, A. Bayon, R. Bader, J. Hinkley, W. Lipinski and A. Tricoli, *J. Mater. Chem. A*, 2016, **4**, 9614-9624.

22. P. T. Krenzke, J. R. Fosheim, J. Y. Zheng and J. H. Davidson, *Int. J. Hydrog. Energy*, 2016, **41**, 12799-12811.

23. M. M. Nair and S. Abanades, *Energ. Fuel*, 2016, **30**, 6050-6058.

24. R. Bader, L. J. Venstrom, J. H. Davidson and W. Lipinski, *Energ. Fuel*, 2013, **27**, 5533-5544.

25. L. J. Venstrom, N. Petkovich, S. Rudisill, A. Stein and J. H. Davidson, *J. Sol. Energy Eng.*, 2012, **134**, 011005.

26. S. Abanades and G. Flamant, *Sol. Energy*, 2006, **80**, 1611-1623.

27. A. Le Gal, S. Abanades and G. Flamant, *Energ. Fuel*, 2011, **25**, 4836-4845.

28. J. R. Scheffe and A. Steinfeld, *Energ. Fuel*, 2012, **26**, 1928-1936.

29. W. C. Chueh, C. Falter, M. Abbott, D. Scipio, P. Furler, S. M. Haile and A. Steinfeld, *Science*, 2010, **330**, 1797-1801.

30. K. J. Warren, J. Reim, K. Randhir, B. Greek, R. Carrillo, D. W. Hahn and J. R. Scheffe, *Energy Technol.*, 2017, **5**, 2138-2149.

31. D. Marxer, P. Furler, M. Takacs and A. Steinfeld, *Energy Environ. Sci.*, 2017, **10**, 1142-1149.

32. X. Zhu, Y. Wei, H. Wang and K. Li, *Int. J. Hydrog. Energy*, 2013, **38**, 4492-4501.

33. X. Zhu, H. Wang, Y. Wei, K. Li and X. Cheng, *J. Nat. Gas Chem.*, 2011, **20**, 281-286.

34. J. R. Scheffe, R. Jacot, G. R. Patzke and A. Steinfeld, *J. Phys. Chem. C*, 2013, **117**, 24104-24114.

35. K. Otsuka, Y. Wang and M. Nakamura, *Appl. Catal. A: Gen.*, 1999, **183**, 317-324.

36. H. H. Jeong, J. H. Kwak, G. Y. Han and K. J. Yoon, *Int. J. Hydrog. Energy*, 2011, **36**, 15221-15230.

37. J. A. Rodriguez, D. C. Grinter, Z. Liu, R. M. Palomino and S. D. Senanayake, *Chem. Soc. Rev.*, 2017, **46**, 1824-1841.

38. A. Bayón, V. A. de la Peña O'Shea, J. M. Coronado and D. P. Serrano, *Int. J. Hydrog. Energy*, 2016, **41**, 113-122.

39. P. B. Kreider, H. H. Funke, K. Cuche, M. Schmidt, A. Steinfeld and A. W. Weimer, *Int. J. Hydrog. Energy*, 2011, **36**, 7028-7037.

40. S. Dey, S. Rajesh and C. N. R. Rao, *J Mater Chem A*, 2016, **4**, 16830-16833.

41. A. Bayón, V. A. de la Peña O'Shea, D. P. Serrano and J. M. Coronado, *Int. J. Hydrog. Energy*, 2013, **38**, 13143-13152.

42. X. Gao, G. Liu, Y. Zhu, P. Kreider, A. Bayon, T. Gengenbach, T. Lu, Y. Liu, J. Hinkley, W. Lipiński and A. Tricoli, *Nano Energy*, 2018, **50**, 347-358.

43. G. Y. Liu, J. Hall, N. Nasiri, T. Gengenbach, L. Spiccia, M. H. Cheah and A. Tricoli, *Chemsuschem*, 2015, **8**, 4162-4171.

44. G. Liu, W. S. Wong, N. Nasiri and A. Tricoli, *Nanoscale*, 2016, **8**, 6085-6093.

45. M. Venkatesh, P. Ravi and S. P. Tewari, *J. Phys. Chem. A*, 2013, **117**, 10162-10169.

46. P. Šimon, *J. Therm. Anal. Calorim.*, 2004, **76**, 123.

47. P. Zhang, H. Lu, Y. Zhou, L. Zhang, Z. Wu, S. Yang, H. Shi, Q. Zhu, Y. Chen and S. Dai, *Nat. Commun.*, 2015, **6**, 8446.

48. N. Anacleto, O. Ostrovski and S. Ganguly, *ISIJ Int.*, 2004, **44**, 1480-1487.

49. Y. Yang, Y. Jin, H. He and Z. Ye, *CrystEngComm*, 2010, **12**, 2663-2665.

50. Y. Adnan, C. Dewei and L. Sean, *J. Phys. D: Appl. Phys.*, 2012, **45**, 355101.

51. S. Dama, S. R. Ghodke, R. Bobade, H. R. Gurav and S. Chilukuri, *Appl. Catal. B: Environ.*, 2018, **224**, 146-158.

52. X. P. Dai, R. J. Li, C. C. Yu and Z. P. Hao, *J. Phys. Chem. B*, 2006, **110**, 22525-22531.

53. P. Pantu, K. Kim and G. R. Gavalas, *Appl. Catal. A: Gen.*, 2000, **193**, 203-214.

54. A. Shchukarev and D. Korolkov, *Open Chem.*, 2004, **2**, 347-362.

55. A. Naumkin, A. Kraut-Vass, S. Gaarenstroom and C. Powell, *srdata. nist. gov/xps/. Date of access*, 2013, **7**.

56. T. L. Barr and S. Seal, *J. Vac. Sci. Technol. A*, 1995, **13**, 1239-1246.

57. G. Panzner and W. Diekmann, *Surf. Sci.*, 1985, **160**, 253-270.

58. J. Foord, R. Jackman and G. Allen, *Philos. Mag. A*, 1984, **49**, 657-663.

59. S. Kato, M. Ammann, T. Huthwelker, C. Paun, M. Lampimaki, M.-T. Lee, M. Rothensteiner and J. A. van Bokhoven, *PCCP*, 2015, **17**, 5078-5083.

60. W. Xiao, Q. Guo and E. G. Wang, *Chem. Phys. Lett.*, 2003, **368**, 527-531.

61. M. Fathi, E. Bjorgum, T. Viig and O. A. Rokstad, *Catal. Today*, 2000, **63**, 489-497.

Chapter Five

Conclusions and Future Work

5.1 Summary, Conclusions and Future Work

Currently, a widespread transition from fossil fuels to clean fuels is still hampered by the high cost and low efficiency of bulk renewable fuel production via sustainable resources. In light of this challenge, solar chemical looping reforming of natural gas provides one of the most promising approaches to achieve an economical and reliable shift towards the sustainable fuels. Embodying solar energy thermochemically into syngas overcomes many limitations, enabling solar energy to be stored and transported at ambient conditions and utilized outside daylight hours. The upgraded energy content in the natural gas feedstock also leads to much lower carbon footprints. However, finding efficient redox materials with ideal properties for solar chemical looping reforming still remains a major challenge in this area of research.

In this work, the latest research in solar fuel production was first summarized, particularly focusing on solar thermochemical approaches. Thereafter, the role of solar chemical looping reforming was highlighted and its fundamental thermodynamics was briefly covered. Following this, detailed review of the most recent and significant advancements in the field of material research for solar chemical looping reforming was provided. The critical review of the state of the art paved essential foundations for the aim of this thesis, which is to improve the benchmark standards of syngas production performance in solar chemical looping reforming via structural engineering of transition metal oxides.

First, structural enhancement of the current benchmark metal oxides was explored by employing facile synthesis methods. In Chapter 2, the physicochemical evolution of flame-made, flower-like, sol-gel as well as commercial ceria powders was evaluated in details over 10 cycles of chemical looping dry methane reforming. The adaptation of flame spray pyrolysis has provided a scalable, time- and cost-efficient approach to fabricate ceria powders with high-performing structural parameters, namely high

specific surface area, low grain density and large mesopore size. Finding these structural properties offered a robust set of benchmark standards for engineering efficient redox materials in solar chemical looping reforming.

I then moved into the regime of structural enhancement via effective lattice cationic substitution. From here I explored manganese oxides, potential oxygen carriers that are earth-abundant, inexpensive and environmentally benign, but largely undervalued in solar fuel synthesis via thermochemical routes due to the intrinsically inhibiting thermodynamics for reversible transition among different manganese oxides. As an alternative pathway, in Chapter 3, a MnO/Mn_7C_3 redox pair was showcased for the first time to be thermodynamically possible and can be utilized in a chemical looping reforming process. This redox pair processes extraordinary reversible oxygen exchange capacity, but is largely inaccessible due to low reaction kinetics of pure manganese oxides at commercially relevant temperatures. At this point, a strategy to unlock this vast potential of reversible oxygen exchange capacity by incorporating fractional amount of cerium ions into the manganese oxide crystal lattice was introduced. As a result, the Ce-promoted manganese oxide achieved record-high syngas production and CO_2 splitting capacities as well as benchmark kinetics in chemical looping dry methane reforming cycles. This robust structural enhancement, demonstrated over 100 cycles, was further delved into in Chapter 4. Here, I endeavoured to understand the role of cerium ions in activating the Mn-based oxygen carrier for its fast and reversible oxygen/carbon diffusion by investigating the structural evolution of an array of Ce-Mn oxides over a series of chemical looping steam methane reforming cycles. The distinct performance of the oxygen carrier with a particular 3% Ce content was observed, and an explanation of the cycle chemistry was provided, backed up by robust structural characterizations to understand the synergetic “balance of power” that resulted in the extraordinary optimal enhancement. This work tentatively promises for large-scale

synthesis of solar fuels via chemical looping reforming by manganese oxides, and prompts further research efforts to explore the powerful approach of lattice cationic substitution in the oxygen carriers to enhance solar fuel production via thermochemical routes.

The work here has demonstrated my journey through versatile engineering techniques for exploring a novel Ce-Mn oxide system in solar fuel production via chemical looping reforming. Regardless of the progress, much work still remains to be achieved in this field. For instance, the proposed cycle mechanism to explain the outstanding performance of 3% Ce still requires further validation. Investigation of surface Ce-rich regions and bulk cerium ions and their effect on oxygen mobility in the manganese oxide lattice could be benefited by a deeper understanding and application of quantum mechanical modelling methods, such as density functional theory (DFT). Additionally, more insightful information could be obtained if in situ characterizations could be applied to more accurately capture and profile the evolution of the structural properties in the Ce-Mn oxide system during redox reactions.

The experience garnered here from the Ce-Mn oxide system prompts further exploration into other binary or ternary multi-valent transition metal oxide solid solutions that may exhibit enhanced oxygen exchange capacity upon fine tuning of the dopant ratios. Such systems with enhanced oxygen mobility would be highly suitable for other important research topics including chemical polishing, industrial catalysis, fuel additives, fuel cells and chemical looping combustion.

5.2 Postscript

The transition into a future powered by renewable and sustainable resources is inevitable if we are to preserve and continue the glory of human civilization on the earth. The ever more frequent and drastic climate events and the forthcoming energy crisis is a wake-up call that imposes us to step into changes here and now. Hydrogen and

renewably synthesized fuels provide a clear, reliable and efficient alternative for this transition.

Despite remarkable accomplishments in the past few decades, much technological and social progress still remains to be achieved in this march of energy revolution through the path of solar fuels. For instance, the technological breakthrough calls for a much deeper understanding of the working mechanism of solar thermochemical processes at both quantum and systematic scales. Additionally, a more unified global effort is required to industrialize the production of solar fuels and subsidize the deployment of renewable energy. These endeavours are challenging but not insurmountable, as long as the community strives to eventually depart from the economy based on fossil-fuels.

Appendix

Structural Performance of Micro and Nano-structured Ceria for Solar Thermochemical Fuel Production

Publication relevant to this chapter:

X. Gao, A. Vidal, A. Bayon, R. Bader, J. Hinkley, W. Lipiński and A. Tricoli, (2015), *Structural Performance of Micro and Nano-structured Ceria for Solar Thermochemical Fuel Production*. 2015 Asia-Pacific Solar Research Conference, ed. R. Egan, R. Passey, Australian Photovoltaic Institute, Canberra.

Abstract

Flame-made nano-structured and commercial micro-structured ceria powders are assessed for two-step carbon dioxide splitting (CDS) driven by a reduction step of methane partial oxidation (MPO). The MPO and CDS reaction rates are strongly dependent on the structural properties of the ceria powders. The nano-structured material shows up to 167% and 144% higher H_2 and CO average production rates during MPO, respectively, and 97% higher CO average production rate during CDS than the micro-structured commercial ceria. After 10 consecutive cycles, the rates are still 57%, 54% and 15% higher, respectively. The higher reaction rates for the nano-structured ceria are attributed to the initially 10 times higher specific surface area of the flame-made nano-structured ceria (76.6 m^2g^{-1}) than that of commercial micro-structured powders (7.3 m^2g^{-1}). These findings indicate that thermal and chemical stabilization of nano-scale structural features is the key to achieving long-term cyclability of ceria in high temperature solar thermochemical fuel production.

A.1 Introduction

Solar production of fuels via high-temperature thermochemical processing is a promising approach to the chemical storage of solar energy for stationary and mobile applications. An industrially viable process is the solar production of synthesis gas (syngas), a mixture of hydrogen and carbon monoxide. Syngas can be directly used for efficient power generation via gas power cycles, or further transformed into hydrocarbon fuels or carbonaceous commodity materials via synthesis processes such as Fischer–Tropsch and methanation.

Two-step thermochemical metal-oxide redox cycles have been demonstrated as an efficient pathway for hydrogen and carbon monoxide production via water (WS) and carbon dioxide (CDS) splitting, respectively. A desired stoichiometric ratio H_2:CO in the syngas is achieved through controlled mixing of the products of WS and CDS cycles. Conventional two-step redox cycles rely on the direct thermal reduction of metal oxides. This approach requires high operating temperatures, typically above 1673 K, and low oxygen partial pressures.[1] However, high process temperature requires sophisticated reactor designs and materials to maintain reactor durability and acceptable thermal losses. Furthermore, the overall process efficiency is negatively affected by the requirement of large quantities of inert sweep gas.[1] An alternative approach, reduction under vacuum, requires mechanical energy input and is challenging for implementation at the high operating reactor temperatures. Yet another alternative approach is to employ a carbothermal reduction process of a metal oxide with a carbonaceous reducing agent such as the methane partial oxidation (MPO). A thermodynamic study performed by Krenzke and Davidson suggested that coupling MPO to the reduction step of the solar ceria redox cycle enables production of high-quality syngas.[2] The predicted solar-to-fuel efficiencies are 39% and 40% for the CDS and WS step, respectively, without

accounting for additional heat recovery. The carbothermal CDS/WS cycles, in particular with MPO, are considered as a short- to mid-term strategy for solar fuel production.

A large number of metal-oxide redox systems have been investigated for the production of syngas by MPO-CDS/WS cycles including Fe_3O_4/FeO, Cu(II)-ferrites[3], Ni(II)-, Zn(II)-, and Co(II)-ferrites[4], WO_3/W[5], CeO_2/$CeO_{2-\delta}$[6], and $La_{1-x}Sr_xFeO_3$ perovskites[7]. CeO_2 has attracted some particular attention as it offers faster kinetics and more enhanced long-term stability than other metal oxides. The MPO-CDS/WS two-step solar thermochemical redox cycle of CeO_2 is written as:

1st, endothermic step:

$$\mathrm{CeO_2} + \delta\mathrm{CH_4} \rightarrow \mathrm{CeO_{2-\delta}} + \delta\mathrm{CO} + 2\delta\mathrm{H_2}, \Delta H^{\circ}_{298\mathrm{K}} = +166.23\mathrm{kJ\ mol^{-1}} \quad \text{(A.1)}$$

2nd, exothermic step:

$$\mathrm{CeO_{2-\delta}} + \delta\mathrm{CO_2} \rightarrow \mathrm{CeO_2} + \delta\mathrm{CO}, \Delta H^{\circ}_{298\mathrm{K}} = -22.09\mathrm{kJ\ mol^{-1}} \quad \text{(A.2a)}$$

and/or

$$\mathrm{CeO_{2-\delta}} + \delta\mathrm{H_2O} \rightarrow \mathrm{CeO_2} + \delta\mathrm{H_2}, \Delta H^{\circ}_{298\mathrm{K}} = -63.29\mathrm{kJ\ mol^{-1}} \quad \text{(A.2b)}$$

During the first step ceria is reduced by CH_4 with a net change in oxygen stoichiometry of δ. No phase change occurs during the reduction as ceria is able to accommodate substantial release of lattice oxygen (δ < 0.25 at 1273 K) while maintaining a stable cubic crystal phase.[8] In the second step ceria reacts with CO_2 or H_2O reincorporating up to δ of oxygen into the lattice. Both steps can be run isothermally in the temperature range of 873–1273 K.

This (A.1)–(A.2) cycle has been experimentally demonstrated with pure ceria. Several ceria-based mixed oxides have been tested to improve the cyclic performance

including CeO_2-ZrO_2[9] and CeO_2-FeO_2[10]. Morphology studies of pure ceria including specific surface area and porosity has also been shown to significantly improve peak fuel production rates by up to 175% for two-step thermochemical metal-oxide redox cycles with direct thermal reduction under inert gas.[11] Flame synthesis was employed to produce pure CeO_2 with high specific surface area and crystallinity.[12] Flame-made ceria nanoparticles were demonstrated to improve thermal stability and oxygen exchange capacity. However, studies on improving thermochemical performance of pure ceria in MPO-WS/CDS cycling by introducing nano-scale structural features are not reported in literature.

Here, the performance of micro- and nano-scale structured pure ceria for solar fuel production via two-step MPO-CDS thermochemical redox cycles is reported. The performance of commercial micro-structured and flame-made nano-structured ceria is evaluated comparatively using an IR furnace setup with a vertical-tube packed-bed reactor. The performance metrics are the instantaneous and total amounts of H_2 and CO produced during isothermal MPO-CDS cycling at 1173 K. The structural changes of ceria samples during 10 testing cycles are evaluated by characterising crystal size, specific surface area and TEM morphology before and after cycling.

A.2 Experimental

A.2.1 Material Synthesis

To synthesize nano-structured ceria particles using flame spray pyrolysis, cerium (III) acetate hydrate (Alfa Aesar, 99.995%) is dissolved in a 2-ethylhexanoic acid (SAFC, purity >99%) heated with 368 K oil bath to prepare the combustible liquid solution. Next, xylene of the volume equal to that of the 2-ethylhexanoic acid is added to the solution to reach a total Ce-atom concentration of 0.2 mol L^{-1}. The solution is fed at 5 mL min^{-1} rate through a custom built nozzle[13], and atomized with an oxygen flow

of 5 L min^{-1} (COREGAS grade 2.5) with a pressure drop of 4 bar. The resulting spray is ignited with a surrounding annular premixed methane ($CH_{4\text{-flamlet}}$, flow rate of 1.2 L min^{-1}, COREGAS grade 4.5) and oxygen ($O_{2\text{-flamlet}}$, flow rate of 2 L min^{-1}, COREGAS grade 2.5) flame. Nanoparticle powders are collected with a vacuum pump (ICME Type M80B4) on water-cooled glass-fiber filters (Sartorius glass microfiber, 160-mm diameter) placed at 38 cm height above burner (HAB). This material is referred to in the following text as nano-structured ceria.

Commercially available ceria micro-structured powders (Alfa Aesar, 99.9%) are used in this study as an alternative material for the purpose of comparative evaluation of thermochemical performance in syngas production. This material is referred to in the following text as micro-structured ceria.

A.2.2 Material Characterization

Samples of micro and nano-structured ceria are characterized by X-ray diffraction (XRD, D2 phaser diffractometer, Bruker). Each sample powder is scanned using Cu Kα (1.54 Å) radiation source with an operating voltage and current of 30 kV and 10 mA, respectively. The scan rate of 0.75° min^{-1} is applied to record the XRD patterns in the range of 10–80° at an increment of 0.02°. The Scherrer equation is applied for the most intense peak to determine the crystal size. The Brunauer–Emmett–Teller (BET) specific surface area is measured by N_2 adsorption–desorption isotherms at 77 K, using a surface and porosity analyser (TriStar II, Micromeritics). The samples are degassed at 623 K for 4 hours prior to measurement. The samples are also analysed using transmission electron microscopy (TEM, Hitachi H7100FA, operated at 125 kV). Specimens are dispersed in ethanol (200 proof, Sigma Aldrich) and sonicated for 1 h at 318 K and 60 W (1.5 L capacity) before deposited on 200-mesh holey carbon filmed copper grids.

A.2.3 Reaction Testing

The cyclic syngas production performance of the ceria samples is investigated in a vertical-tube reactor placed inside an electric IR furnace (P4C-VHT, Advance Riko) depicted in Figure . The powder samples are sandwiched between two 2-mm thick highly-porous and temperature-resistant alumina wool disks, located on-axis of an alumina tube. The ceria sample thickness is varied between 1 mm and 2 mm which allows for a nearly-uniform temperature distribution in the sample. The inner diameter and wall thickness of the tube are 12.5 mm and 3 mm, respectively. The tube is placed in the centre of the furnace and enveloped by a quartz tube for protection of IR lamps against thermal degradation. The tube is sealed to stainless steel connectors with Kalrez O-rings, and closed with mechanic valves (Swagelok) at both ends. Gas mixtures are regulated by mass flow controllers (Bronkhorst) before delivered through the top of the tube. Sample temperature is measured using a type-K thermocouple inside the alumina tube. The composition of the effluent gases is continuously monitored by a quadrupole mass spectrometer (OmniStar^{TM} GSD 320, Pfeiffer Vacuum). All the monitored gas components are calibrated in the mass spectrometer using standard mixtures of the individual solute (CH_4, CO_2, and CO/H_2) in a reference Ar gas. All gas volumes are reported at 293 K and 1 atm. The average production rates of H_2 and CO are calculated over the 2-100% peak production rate time period.

The operating temperature for isothermal MPO-CDS ceria redox cycles, 1173K, is derived from thermodynamic analysis and has been experimentally evaluated (not shown in this study) to produce H_2 and CO at a close 2:1 ratio while maintaining sufficiently fast reaction kinetics. To simulate the operation conditions of a solar reactor, a discontinuous two-day testing was conducted for both samples performing a total of 10 cycles (divided into 4 and 6 cycles in the two testing days). In each testing day, the tubular reactor was initially purged of air under a 250 mL min^{-1} flow of pure Ar

(COREGAS grade 5.0). The reactor was then heated from 293 K to 1173 K at a ramp of 80 K min^{-1}.

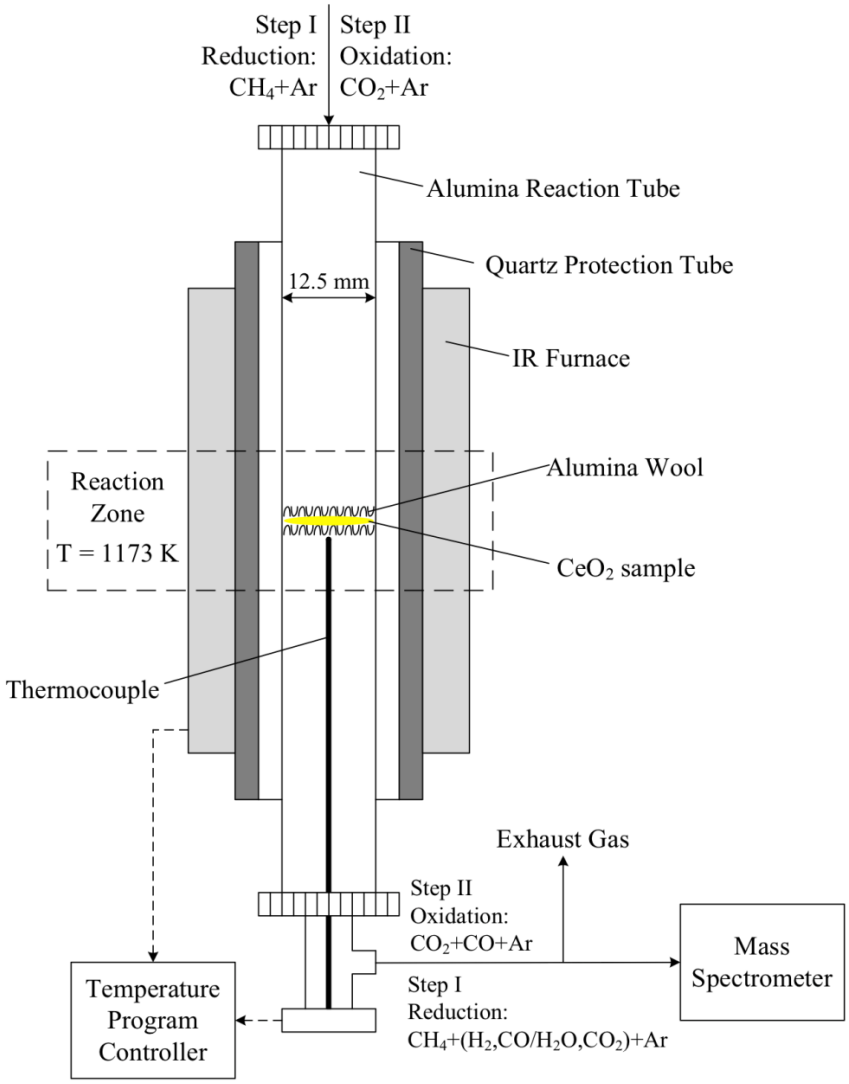

Figure A.1 Schematic of the experimental setup for the two-step MPO-CDS cycling.

Subsequently, the sample was cyclically reduced and oxidized with CH_4 (COREGAS grade 4.5) and CO_2 (COREGAS grade 4.5). The reduction step was performed using a mixture of CH_4 in Ar (8 vol% CH_4) at a total flow rate of 250 mL min^{-1}. The sample was allowed to reduce for 30 min. Between the cycle steps and the cycles, the tube was purged with Ar (250 mL min^{-1}) for 15 min. The oxidation was then initiated by delivering a mixture of CO_2 in Ar (4 vol% CO_2) at a total flow rate of 250 mL min^{-1}. Each oxidation step was allowed for 15 min. The time required for the

reduction and oxidation steps was determined by preliminary tests and was sufficient for both samples to complete the reaction until no further fuel production could be detected from the mass spectrometer. At the end of each testing day, the reactor was cooled to 293 K at 80 K min^{-1} using an external cooling system and under Ar purge gas. Once the sample reached room temperature, the valves at both ends of the alumina tube were closed, and the samples were preserved in the Ar atmosphere between the testing days.

A.3 Results and Discussion

The results of the nitrogen adsorption–desorption and XRD crystal size measurements are summarized in Table A.. The XRD spectra are displayed in Figure A. and correspond to the spectra of cubic ceria (JCPDS No. 34-0394) with a displacement of 0.009°. The most intense peak was located at 28.540°, and the average crystal size of micro-structured ceria increased from 83.8 nm (as-prepared) to 86.1 nm after 10 MPO-CDS cycles (Table A.). The nano-structured ceria consists of 9.4 nm crystals in diameter and grow to 51.3 nm after 10 MPO-CDS cycles (Table A.). These results show that the size of the crystals of the micro-structured powder remains nearly constant during thermochemical cycling. The crystals size of the nanostructured ceria, on the contrary, increases by a factor of 5.

Table A.1 Physical and chemical properties of the commercial and flame-made CeO_2.

Material	SSA (m^2 g^{-1})		d_{BET} (nm)		d_{XRD} (nm)	
	As-Prepared	10 cycles	As-Prepared	10 cycles	As-Prepared	10 cycles
Micro-CeO_2	7.34	1.59	106.9	493.3	83.8	86.1
Nano-CeO_2	76.63	1.58	10.2	496.4	9.4	51.3

The as-prepared BET surface area of the micro-structured ceria was 7.34 m^2 g^{-1} and decreased to 1.59 m^2 g^{-1} after the 10 MPO-CDS thermal cycles (Table A.). Although, for these commercial samples a similar irregular faceted shape is observed before and after cycling, the decrease in surface area can still be associated with changes in the grain TEM morphology a fractal-like and disordered morphology constituted by partially sintered nanoparticle agglomerates. After the 10 MPO-CDS cycles, the specific surface area of nano-structured ceria decreased by 98%. Figure d confirms that the nano-structured ceria experienced significant sintering after cyclic thermochemical reactions and prolonged residence time at high temperatures. Nano-structured ceria particles have a higher potential to cluster and agglomerate to minimize the surface energy than micro-structured ceria, hence more severe sintering is expected.

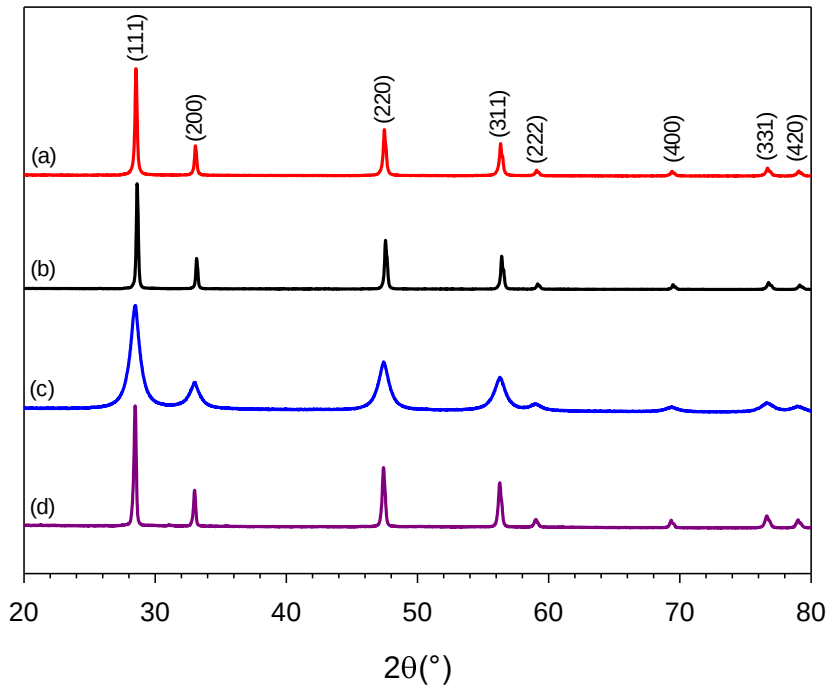

Figure A.2 XRD patterns of the commercial micro-structured and flame-made nano-structured ceria powders: (a) micro-structured before cycling, (b) micro-structured after cycling, (c) nano-structured before cycling, (d) nano-structured after cycling.

Figure shows the H_2 (MPO), CO (MPO), and CO (CDS) production rates of the micro and nano-structured ceria as a function of time during an exemplary 10 MPO-CDS cycles experiment. During the MPO reduction step, CO and H_2 are produced immediately after the introduction of CH_4. Their production rates increase very fast, reaching a maximum in 3 to 5 minutes, and then the production rates decay. This is tentatively attributed to the combined effects of solid-state diffusion of oxygen and deposition of carbon. Upon depletion of the ceria surface oxygen, solid-state diffusion of O_2 from the lattice becomes the rate-limiting step for the MPO reaction.

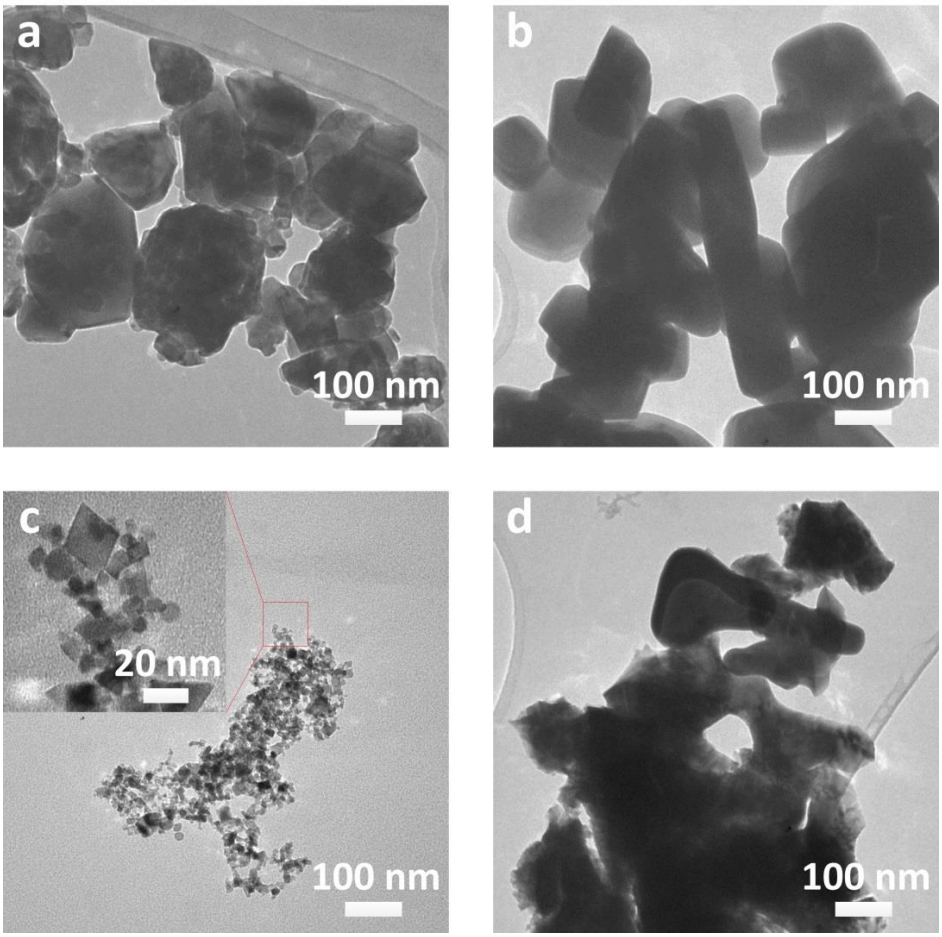

Figure A.3 TEM micrographs of the micro-structured and nano-structured ceria powders: (a) micro-structured before cycling, (b) micro-structured after cycling, (c) nano-structured before cycling, (d) nano-structured after cycling.

Similar production rates profiles are also observed during the CDS oxidation steps. However, the pronounced spike in CO production rate during the first oxidation step of the micro-structured ceria (Figure a) is unexpected. This is tentatively attributed to the volatilisation of organic impurities at high temperature that may have been present on the commercial ceria surface. Thus, the results of the second cycle are used to evaluate initial peak production performance. Specifically, micro-structured ceria achieved peak production rates of 362.0 µmol min^{-1} g^{-1}, 190.1 µmol min^{-1} g^{-1} and 291.1 µmol min^{-1} g^{-1} for H_2 (MPO), CO (MPO) and CO (CDS), respectively. For the nano-structured ceria,

the corresponding rates are 1038.1 µmol min^{-1} g^{-1}, 489.2 µmol min^{-1} g^{-1} and 798.7 µmol min^{-1} g^{-1}, which constitute increases of 187%, 157% and 174%, respectively.

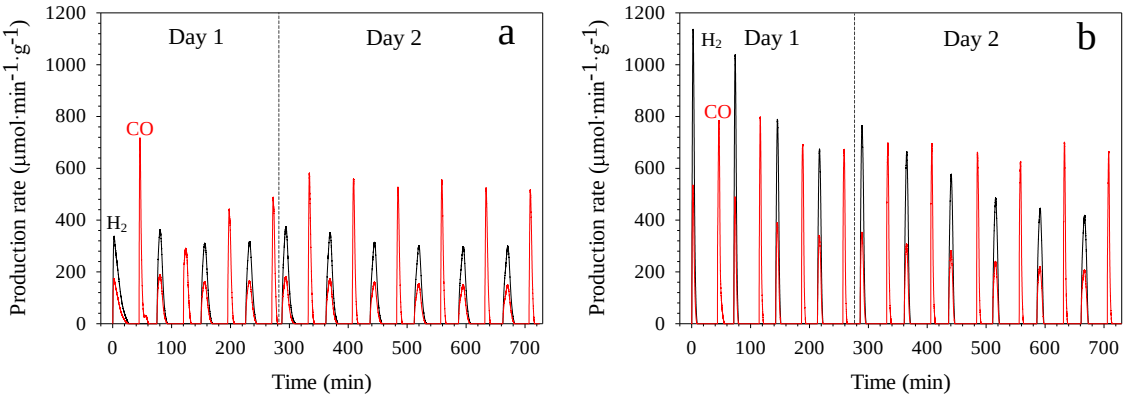

Figure A.4 H_2 and CO production rates during thermal cycling for (a) the micro-structured and (b) the nano-structured ceria powders.

Figure a and b show the average H_2 and CO production rates of the micro-structured and nano-structured ceria powders. In the second cycle (Figure a and b), during MPO the nano-structured ceria had 167% and 144% higher average H_2 and CO production rates, respectively, and during the CDS 97% higher average CO production rate than the micro-structured ceria. In the 10th cycle, these results are still 57%, 54% and 15% faster, respectively. This suggests that the nano-structured ceria still reduces and oxidises significantly faster than commercial ceria even after 11 hours of accumulated MPO-CDS cycling.

In Figure a, it is noticeable that while the production rates of micro-structured ceria remained relatively stable throughout the cycles, the CO and H_2 production rates of the nano-structured ceria declined by more than 40% and have nearly converged to a constant performance only after 10 cycles. This is in line with Figure b that suggests a declining trend of peak production rates for nano-structured sample during reduction, while the lower rates of micro-structured ceria remained relatively stable (Figure a). This is attributed to the significantly higher sintering of the nano-structured ceria, which

drastically reduces the surface area available for the MPO and CDS reactions. Therefore, in order to maintain the superior initial performance of the flame-made ceria, the high specific surface area of the flame-made ceria must to be maintained.

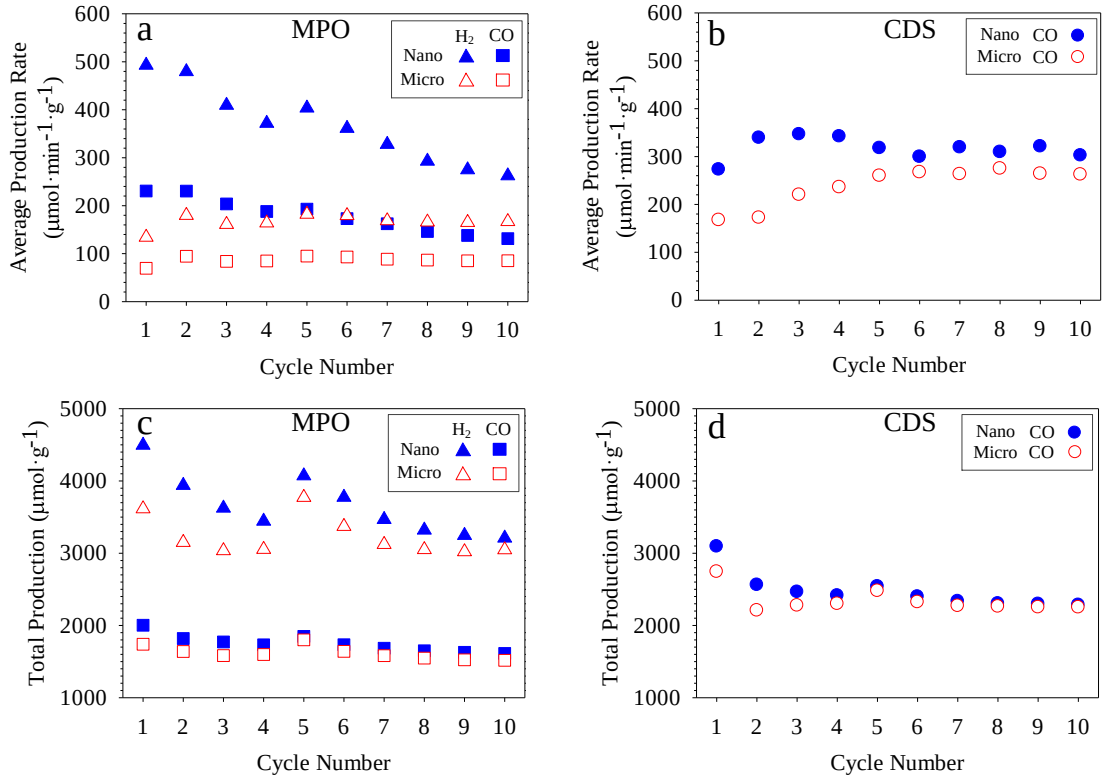

Figure A.5 Average production rates (a, b) and total amount produced (c, d) of H_2 (MPO), CO (MPO) and CO (CDS) for micro-structured and nano-structured powders.

Figure c and d show the total production of H_2 and CO per MPO and CDS cycle. The average amounts of H_2 (MPO), CO (MPO) and CO (CDS) produced over 10 MPO-CDS cycles are 3224.2 μmol g^{-1}, 1617.5 μmol g^{-1}, and 2337.3 μmol g^{-1} for the micro-structured ceria, and 3659.4 μmol g^{-1}, 1748.3 μmol g^{-1}, and 2470.0 μmol g^{-1} for the nano-structured ceria. While nano-structured ceria leads to significantly higher CO and H_2 production rates compared to micro-structured ceria, the amounts of CO and H_2 produced per cycle are comparable. The averaged production rates were obtained over the time periods with an H_2 and CO production rate above 2% of the maximum production rates for each single MPO and CDS step as explained earlier. These time

periods vary slightly but are consistently shorter than the total step time (30 min for MPO and 15 min for CDS). This is also visible in Figure A.4, where all reactions finish before the total step time, and the nano-structured ceria finishes much faster than micro-structured ceria. As a consequence, even though the total productions between the two structured ceria do not show much difference, this is due to the very large step times. Notably, the nano-structured ceria completes the redox reactions in significantly shorter time than the micro-structured ceria and can be operated with much shorter step times.

According to experimental studies, at an isothermal temperature of 973 K, the H_2 and CO production during the MPO reduction step using commercially available ceria were approximately 730 µmol g^{-1} at 8.5 µmol min^{-1} g^{-1} and 339 µmol g^{-1} at 3.0 µmol min^{-1} g^{-1}, respectively.[6] These values are comparable to the results obtained here with the micro-structured ceria considering the more favourable experimental conditions such as higher operating temperatures, higher feed gas flow rates, and targeted structural enhancement that improve the overall MPO reaction performance. In terms of the amount of CO produced during the CDS oxidation step, here significant improvement was observed with both micro and nano-structured ceria over that reported for the inert gas reduction (IGR) process.[14, 15] Specifically in these works, at an isothermal temperature of 1073–1200 K, following the IGR reduction, the CDS oxidation step resulted in only 455±215 µmol g^{-1} of CO or H_2, with average production rates at 45.5±29.5 µmol min^{-1} g^{-1}. Notably, here, the amount of CO produced during the CDS oxidation step is ca 5 times higher (2403.5±66.5 µmol g^{-1}) with a 6 times higher average production rate of 267.5±100.5 µmol $min^{-1}g^{-1}$. Theoretical analysis has suggested that at 1773 K conventional IGR is only capable to provide a change in stoichiometry for ceria of 0.06.[1] By using the MPO for the reduction step, the obtainable reduction in stoichiometry is significantly increased. Further analysis shows that a stoichiometry variation of 0.2693±0.0076 was achieved in this study. Compared to theoretical

thermodynamic calculations indicating a maximal stoichiometry variation of 0.25 for the MPO reduction of the cubic fluorite crystal structure of ceria[2], the values obtained in this work is comparable and only slightly exceeding this limit. Further in-situ characterisation is required to determine if other crystalline phases are formed during the reduction step.

The reaction stoichiometry in Eq. A.1 and A.2a indicates a H_2:CO product ratio in the MPO step of 2:1. The total production of CO in the CDS step should be equal to that in the MPO step. However, according to the measured total productions (Figure A.5c and d), the H_2 to CO ratio in the MPO steps is larger than 2. Furthermore, the total CO production in the CDS step is larger than the total CO production in the MPO step. These results are attributed to formation of some carbon during the MPO step. In fact, thermal cracking of CH_4 during MPO can produce solid carbon and H_2. During CDS this carbon can be oxidized by CO_2, resulting in additional CO production.

Figure c and d show that the total fuel production for the micro-structured and nano-structured ceria converge to 3132.1±113.6 μmol g^{-1}, 1570.5±58.1 μmol g^{-1}, and 2271.4±23.3 μmol g^{-1} for H_2 (MPO), CO (MPO) and CO (CDS), respectively. This suggests limited effects of the structural features on the solid-state redox equilibrium of ceria. This is also confirmed by evaluating the stoichiometry of the last cycle between the micro-structured and nano-structured ceria, in contrast to the drastic difference of 15–57% in average production rates, the achieved stoichiometry variation from flame-made nano-structured ceria (0.2769±0.0007) is only 5–7% higher than that of commercial micro-structured ceria (0.2617±0.0006). This indicates that while structural properties of ceria influence the kinetics of fuel production, its influence on the chemical equilibrium of the system is limited.

A.4 Conclusion

This study investigated the impact of nano-scale structural features of pure ceria on its syngas production performance during two-step MPO-CDS isothermal redox cycles. Specifically, production rates and total amount of produced H_2 and CO in each cycle for the micro and nano-structured ceria samples are comparatively evaluated and analysed with respect to the evolution of their key structural parameters such as specific surface area, crystal size and TEM morphology.

Initially, the reaction rates of flame-made nano-structured ceria are at least 97% higher than the micro-structured commercial ceria during the MPO-CDS cycles at 1173 K isothermal redox conditions. Even after 10 cycles, the nano-structured ceria has still at least 15% faster reaction rates compared with micro-structured ceria. This is attributed to its initial higher specific surface area of 76.63 m^2 g^{-1} that accelerate the solid-state O_2 diffusion kinetic. The potential of nano-structured ceria to benefit the kinetics of syngas production is suggested.

While the initial syngas production rates of the nano-structured ceria are the highest among those reported in literature, the rates decline by more than 40% after 10 cycles. The rapid deterioration of the activity of nano-structured ceria suggests that the ability to maintain the structural features in the material is crucial for long-term solar thermochemical fuel production. Hence, a research challenge is to find means to avoid sintering of such fine nano-scale structural features during long-term exposure to a high temperature reducing environment. Based on the TEM images, the as-synthesized flame-made nano-structured ceria presents agglomerated individual nanoparticles. These particles are prone to form necking with adjacent particles at high operating temperatures and initiate further sintering [16]. From this perspective, future studies will examine feasible options for optimizing the nano-structures of ceria, in order to retain the very high initial reaction rates.

A.5 Reference

1. R. Bader, L. J. Venstrom, J. H. Davidson and W. Lipinski, *Energ. Fuel*, 2013, **27**, 5533-5544.
2. P. T. Krenzke and J. H. Davidson, *Energ. Fuel*, 2014, **28**, 4088-4095.
3. K.-S. Kang, C.-H. Kim, K.-K. Bae, W.-C. Cho, W.-J. Kim, Y.-H. Kim, S.-H. Kim and C.-S. Park, *Int. J. Hydrog. Energy*, 2010, **35**, 568-576.
4. T. Kodama, T. Shimizu, T. Satoh, M. Nakata and K. I. Shimizu, *Sol. Energy*, 2002, **73**, 363-374.
5. T. Kodama, H. Ohtake, S. Matsumoto, A. Aoki, T. Shimizu and Y. Kitayama, *Energy*, 2000, **25**, 411-425.
6. K. Otsuka, Y. Wang, E. Sunada and I. Yamanaka, *J. Catal.*, 1998, **175**, 152-160.
7. A. Evdou, V. Zaspalis and L. Nalbandian, *Fuel*, 2010, **89**, 1265-1273.
8. W. C. Chueh and S. M. Haile, *Philos. T. R. Soc. A*, 2010, **368**, 3269-3294.
9. K. Otsuka, Y. Wang and M. Nakamura, *Appl. Catal. A Gen.*, 1999, **183**, 317-324.
10. K. Li, H. Wang, Y. Wei and D. Yan, *Appl. Catal. B Environ.*, 2010, **97**, 361-372.
11. L. J. Venstrom, N. Petkovich, S. Rudisill, A. Stein and J. H. Davidson, *J. Sol. Energ. Eng.*, 2012, **134**, 011005.
12. L. Mädler, W. Stark and S. Pratsinis, *J. Mater. Res.*, 2002, **17**, 1356-1362.
13. N. Nasiri, R. H. Bo, F. Wang, L. Fu and A. Tricoli, *Adv. Mater.*, 2015, **27**, 4336-4343.
14. W. C. Chueh, C. Falter, M. Abbott, D. Scipio, P. Furler, S. M. Haile and A. Steinfeld, *Science*, 2010, **330**, 1797-1801.
15. P. Furler, J. R. Scheffe and A. Steinfeld, *Energy Environ. Sci.*, 2012, **5**, 6098-6103.
16. A. Tricoli, M. Graf and S. E. Pratsinis, *Adv. Funct. Mater.*, 2008, **18**, 1969-1976.